Fracture in polycrystalline diamond.

Investigating cracking and toughness behaviour using a miniature double torsion technique.

Serguei Igorevich Petrov

This thesis is submitted for the degree of Doctor of Philosophy in the Department of Mechanical Engineering
University of Cape Town

February 2019

Abstract

This thesis project studied the crack initiation and controllable propagation of cracks in four grades of polycrystalline diamond (PCD) employing a miniature double torsion (DT) technique. The extremely high stiffness and relatively low toughness of the PCD material make controllable crack propagation and fracture parameter studies very difficult. Therefore, the research project investigated the ability of the DT technique to **controllably** initiate and propagate cracks, followed by the development of the in-situ SEM miniature DT rig. Development of such a rig permitted the live observation of the cracking process, while capturing the load displacement data. In addition to the in-situ SEM experiments, the fracture process was also observed outside the SEM by digital image correlation (DIC), a full field surface displacement measurement technique. The DIC experiments were performed in both 2D and 3D configurations. The DIC data was processed employing the JMAN routine – a numerical method for the calculation of the J-integral from the DIC measured displacement field. The combination of the DIC and JMAN techniques enabled non-contact characterization of the surface stress intensity around the propagating crack. In addition to the abovementioned techniques, electron backscatter diffraction (EBSD) was employed to investigate the effect of the microstructural features on the behaviour of the various grades of PCD.

The miniature DT technique enabled controllable initiation, unloading, analysis and subsequent propagation from “atomically” sharp condition which avoided the notch toughness phenomena. The miniature DT technique enabled clear, repeatable differentiation of the fracture toughness properties of the four grades of PCD studied. In-situ observation of the fracture process, coupled with the fractographic studies of the broken specimens, revealed clear differences in crack propagation behaviour of the specimens with different grain size. The transgranular crack propagation component increased with increasing grain size and contiguity, while the fine grain specimens revealed more secondary damage in the wake of the crack. That is to say that the fine grain specimens revealed a larger fracture process zone (FPZ) than the coarse grain specimens. PCD toughness increased with increasing grain size and increasing contiguity. The non-contact 2D DIC/JMAN experiments characterised the surface stress intensity factor (SIF) around the crack with a good level of accuracy. The non-contact SIF measurements were within 6-8% of those determined by employing the load-

displacement data and the classical DT formulations. The EBSD characterization of the specimen surface proved very useful in the observation of the crack path as a function of the microstructure.

The application of the techniques and methodologies developed and presented in the current research project provide robust new tools in the development of the understanding of the fracture mechanisms in PCD material. The techniques presented can be used to quantify, observe and understand the fracture mechanisms in PCD materials made by new sintering methodologies and new binder/catalyst compositions. The ability to observe and understand the effects microstructural features have on crack resistance, may enable the development of functionally graded materials which employ the principles of biomimicry to develop toughening mechanisms resembling those found in nature.

Declaration

1. I know that plagiarism is wrong. Plagiarism is to use another's work and pretend that it is one's own.
2. I have used the IEEE convention for citation and referencing. Each contribution to, and quotation in, this project from the work(s) of other people has been attributed, and has been cited and referenced.
3. This project is my own work.
4. I have not allowed, and will not allow, anyone to copy my work with the intention of passing it off as his or her own work.

Signature: … Signed by candidate

Date: 26/06/19

Acknowledgements

The author would like to express his sincere appreciation to his supervisors, Professor R.B. Tait (University of Cape Town), Professor T.H. Becker (University of Stellenbosch) and Dr. S. Ozbayraktar (Element 6 (Pty)Ltd), for their facilitation of this project and continued encouragement, guidance and support during the course of the project. Special thanks go out to Professor Robert Tait for once upon a time suggesting that I consider postgraduate studies in the field of fatigue and fracture mechanics, a field that has now formed my professional life. To Professor Thorsten Becker, for his amazing ability to grasp a research topic and break it down into a clear and logical research plan which yields results. I would like to thank Dr. Serdar Ozbayraktar for enabling this project, the sponsorship, production of the unique specimens and for his patience.

The author would like to express his thanks to Dr. Johan Westraad (Nelson Mandela Metropolitan University HRTEM Centre) for his assistance with specialist imaging techniques as well as his understanding of the PCD materials which led to a number of very interesting discussions. Special thanks go out to Mrs. Miranda Waldron (University of Cape Town Imaging Centre) for SEM training and continued support.

The author would like to express his gratitude to the colleagues who provided great discussion, ideas, shared their knowledge and coffee. The special thanks go out to Richard Huchzermeyer, Matt Molteno, Melody van Rooyen and, last but not least, Ivan Tchekashkine for his assistance with the electronics.

I would like to express my appreciation to my family and friends. Very special thanks go out to my parents, Dr. Vera Petrova and Dr. Igor Petrov for always supporting me in my academic endeavours and always believing in me. To Janet and Bradley, for helping me stay focused when it was most needed. Finally, I would like to thank my wife Ekaterina for always supporting me and my children Andrey and Iaroslava for always putting a smile on my face.

Thank you to everyone who was part of this journey but is not specifically mentioned here.

Table of contents

Page

Abstract ..... **i**

Declaration ..... **iii**

Acknowledgements ..... **iv**

Table of contents ..... **v**

List of figures ..... **ix**

List of tables ..... **xxv**

List of abbreviations and symbols ..... **xxvi**

1 Introduction **1**

1.1 Background 1

1.2 Structural integrity of polycrystalline diamond compact 5

1.3 Aims of the project 6

1.4 Thesis document layout 7

2 Literature review of PCD and testing in brittle materials **9**

2.1 Development of synthetic diamond 10

2.1.1 PCD material key properties 11

2.1.2 PDC insert performance evaluation methods 14

2.1.3 Summary 15

2.2 Fracture mechanics and its applicability to brittle materials 15

2.2.1 Linear elastic fracture mechanics (LEFM) energy principle 16

2.2.2 Crack face displacement modes during fracture 19

2.2.3 Strain energy release rate *G* 20

2.2.4 Strain energy release rate during Mode I crack extension 21

2.2.5 Stress Intensity Factor (*SIF, K*) 23

2.2.6 Elastic Plastic Fracture Mechanics (EPFM) considerations in brittle materials 24

2.2.7 The J contour integral 25

2.2.8 Equivalence of fracture mechanics parameters 26

2.2.9 Standard test geometries 27

2.3 The double torsion technique 30

2.3.1 Double torsion geometry and formulation 30

2.3.2 Crack length independence 34

2.3.3 Specimen thickness effects 35
2.3.4 Crack path effects 36
2.3.5 In-situ microscope studies employing double torsion 37
2.4 Digital image correlation 44
2.4.1 Introduction 44
2.4.2 Background theory 44
2.4.3 Speckle pattern analysis and accuracy estimates 48
2.4.4 Extracting material properties from DIC 51
2.5 Electron backscatter diffraction (EBSD) 54
2.5.1 Introduction to EBSD 54
2.5.2 The unit cell and Miller indices 56
2.5.3 EBSD analysis of polycrystalline diamond (PCD) 57
2.6 Summary 58

3 Previous studies in PCD damage mechanisms 60

3.1 Fracture and fatigue studies in PCD 62
3.1.1 Fracture toughness and mechanical properties of PCD 62
3.1.2 Application of standard FM geometries to PCD 65
3.1.3 Fatigue testing of PCD employing custom methodologies 70
3.1.4 Indentation techniques 74
3.1.5 Double torsion 76
3.2 Discussion of the current understanding of fatigue and fracture in PCD 78
3.3 Aims and objectives of this thesis 80
3.3.1 Introduction 80
3.3.2 Objectives 81
3.4 Summary 83

4 Experimental methodology 85

4.1 Experimental procedure overview 86
4.2 Test specimens 87
4.2.2 Polycrystalline diamond (PCD) specimens 89
4.3 Miniature Double Torsion Methodology 91
4.3.1 Overview of the design requirements 91
4.3.2 Design constraints 92
4.3.3 Existing miniature double torsion rig 93
4.3.4 Evaluation of the existing double torsion rig 96
4.3.5 Miniature rig development for PCD applications 98
4.4 Evaluation of the miniature DT rig 106
4.4.1 Testing in polymethyl methacrylate (PMMA) 106
4.4.2 Testing in polycrystalline diamond (PCD) 109
4.5 In-situ SEM fracture process observation 110

4.5.1 Overview of the experimental procedure....110
4.5.2 Fracture phenomena observation 113
4.6 Full field deformation methods 113
4.6.1 Digital image correlation approach....114
4.6.2 Speckle pattern....115
4.6.3 System calibration 116
4.6.4 Application of JMAN to a theoretical displacement field. 119
4.6.5 Extracting fracture toughness from 2D DIC data employing JMAN 121
4.6.6 Extracting PMMA fracture toughness parameters from 3D DIC data 127
4.7 Surface grain orientation mapping by EBSD 130
4.7.1 Surface finish and EBSD mapping 131
4.7.2 Mapping approach 132
4.8 Summary 135

5 Results of fracture observations in PCD 136

5.1 PCD specimen characteristics 136
5.1.1 Cobalt content....136
5.1.2 Diamond particle grain size....140
5.1.3 Diamond phase contiguity 142
5.2 Classic DT formulation results....144
5.3 Extracting fracture toughness parameters employing optical techniques....148
5.3.1 Extracting PCD fracture toughness parameters from 2D and 3D DIC data 148
5.4 In-situ observation of the fracture process 154
5.4.1 General experimental considerations....155
5.4.2 4µm starter particle PCD....155
5.4.3 12µm starter particle size 164
5.4.4 30µm starter particle size 170
5.4.5 30-4µm starter particle size 178
5.5 Fractography 185
5.5.1 Broken specimen fractography 185
5.5.2 Surface cobalt mapping....192
5.6 EBSD mapping of the propagation regions....193
5.6.1 Pre-mapping 193
5.6.2 EBSD mapping of crack paths....195
5.6.3 Microstructural observations in coarse grain specimens 196
5.6.4 EBSD mapping of unloaded cracked specimens 197

6 Discussion 201

6.1 Miniature double torsion methodology 201
6.1.1 System concept overview 201
6.1.2 Miniature DT system parameters 202
6.1.3 Miniature DT testing of PMMA specimens 203
6.1.4 In-situ SEM experimental approach 204
6.2 PCD fracture toughness properties 205
6.2.1 Miniature DT fracture toughness results obtained in-situ SEM tests of PCD materials 205
6.2.2 Microstructural effects on fracture toughness 207
6.3 Fracture process observations 211
6.3.1 In-situ SEM live process observations 211
6.3.2 Fractographic observations 213
6.4 Characterising toughness by DIC and JMAN routine 215
6.4.2 3D DIC-JMAN based results 220
6.5 EBSD based microstructural observations 220
6.5.1 Pre-mapping 221
6.5.2 Post-mapping 221
6.6 Results in the context of the current state of the art 222
6.6.1 Fracture toughness results 222
6.6.2 Experimental solutions 223
6.6.3 Improving PCD material toughness 224

7 Conclusions and Recommendations 228
7.1 Conclusions 228
7.2 Recommendations 230

References 232

Appendix A Miniature DT rig drawings and control circuit diagrams. 240

Appendix B Images employed in the analyses. 258

Appendix C –HPHT Sintering and Leaching of PCD 267

List of figures

Page

Figure 1.1 – Backscatter electron micrograph depicting a typical microstructure of polycrystalline diamond (PCD) material. 2

Figure 1.2 –Photograph depicting a PDC “button” cutter, highlighting the thin wafer of PCD sintered onto a support body of tungsten carbide-cobalt WC/Co. 3

Figure 2.1 – Plot depicting the percentage of total footage drilled, breakdown in accordance with the respective brill bit types [9]. 11

Figure 2.2 – The diamond graphite equilibrium diagram[36]. 12

Figure 2.3 – A large loaded plate of an elastic material containing a crack-like defect of width 2a [49]. 17

Figure 2.4 – The three modes of crack development under the application of the various loading geometries [55]. 19

Figure 2.5 – A load vs. displacement plot describing the system energy during Mode I incremental crack extension *da* [47]. 21

Figure 2.6 – (a) – diagram describing the energy release rate in a non-linear elastic material with an advancing crack, (b) – an arbitrary contour around the crack tip. 25

Figure 2.7 – Three-point bend specimen geometry (SENB)[55] 27

Figure 2.8 – Compact tension specimen (CT)[55] 28

Figure 2.9 – Double cantilever beam specimen (DCB)[55] 28

Figure 2.10 – Centre notched diametral compression specimen otherwise known as centre notched Brazilian disc specimen (CNBDS)[21]. 28

Figure 2.11 – Schematic diagrams of the – a) short rod specimen and b) short bar specimens. 29

Figure 2.12 – Schematic representation of the DT specimen and the associated loading geometry. 31

Figure 2.13 – Plot depicting the critical stress intensity, K_{IC}, as a function of the crack length normalised by the specimen length[65]. 35

Figure 2.14 – Graphical representation of the valid thickness concept. 36

Figure 2.15 – Plot depicting the effect of the crack plane misalignment on the apparent critical stress intensity level obtained. 37

Figure 2.16 – Examples of purpose built equipment for in-situ SEM double torsion studies which are locatable in the specimen chamber of an SEM and used for fracture testing in cement mortar, polymethyl methacrylate (PMMA) and nuclear graphite – (a) Tait and Garrett [71], (b) Tait and Rosie [74]. 39

Figure 2.17 - Micrographs reproduced from Tait [71] depicting crack paths in concrete double torsion specimens which were controllably fractured in-situ in the SEM. (a) Highlights a crack path which had shut down due to a discontinuous “crack jump” and (b) depicts an example of crack branching. 40

Figure 2.18 – Micrograph reproduced from Tait [71] depicting crack paths in concrete double torsion specimens which were controllably fractured in-situ in the SEM. The main crack propagated from the top right (T-tip). Significant “process zone” microcracking was observed preceding the crack as highlighted by letters A-D. 40

Figure 2.19 – Micrographs reproduced from Rosie [74] depicting a crack propagating (bottom to top) in a miniature DT specimen of nuclear graphite. The initial crack path which initiates a particle pull out (a) is changed as the crack develops, causing the particle to fracture (b) as the new path becomes preferential in terms of energy required. 41

Figure 2.20 – Test rig employed by Becker et. al. for in-situ DIC investigation into the fracture mechanisms in nuclear graphite [57]. 41

Figure 2.21 – Images depicting the results capturing the fracture process zone by ESPI techniques, Becker [57]. The three images depicting three stages of crack propagation associated with three discrete events being (a) crack arrest at a pore, (b) crack branching and (c) crack bridging. The general size of the ESPI fringes provides an indication of the fracture process zone (FPZ) around the crack tip. 42

Figure 2.22 – Maximum normal strain mapping during crack propagation in nuclear graphite, employing DIC, reproduced from Becker [57]. The strain level of 0.35% was considered as the threshold for the formation of a microcrack. As can be seen, significant microcracking occurs ahead of the crack tip but partially closes up with passage of crack tip strain field. Some of the damage is permanent as microcrack closure in the crack wake is incomplete. 43

Figure 2.23 – A figure depicting an example of a region of interest which has been meshed into small subsets (the blocks of the yellow grid) 45

Figure 2.24 – An illustration of a reference image subset (left) and a deformed image subset (right) where some displacement and deformation of the subset has occurred. 46

Figure 2.25 – An illustration of the displacement field obtained from calculating the displacements of each individual subset. 48

Figure 2.26 - Pictured are three levels of speckle sizing, generated by selecting various digress of magnification of the same physical pattern, scaling over equivalent pixel domain. These three levels of speckle size were compared to study the influence of speckle size on homogeneous and heterogeneous strain fields. Results depicted in Figure 2.27 and Figure 2.28. 49

Figure 2.27 - Plot collage depicting the relative influence of speckle size (horizontal axis) and subset size (vertical axis), on the accuracy of DIC identification of a theoretically imposed uniaxial strain. It is evident that in general small speckle and larger subsets are useful for increased accuracy. The plot further highlights that in general, larger subsets improve global accuracy but would lose local resolution [81]. 50

Figure 2.28 - Plot collage depicting the relative influence of speckle size (horizontal axis) and subset size (vertical axis), on the accuracy of DIC identification of a theoretically imposed heterogeneous strain. It is evident how complex strain fields require good speckle patterns[81]. 51

Figure 2.29 - Schematic depicting a typical sample orientation and the general system components associated with EBSD mapping [83]. 55

Figure 2.30 - Schematic depicting the electron beam interaction with the crystallographic plane of the sample and the resulting Kikuchi bands forming due to the scattered electron luminescence of the phosphor screen [83]. 55

Figure 2.31 – An illustration of a simple square unit cell of atoms with superimposed examples of the Miller indices describing the shaded planes[84]. 56

Figure 2.32 – An example of an EBSD scan of a region of abnormal diamond crystal growth where the inverse pole figure visualisation approached is employed to differentiate the orientation of different crystals [86]. 57

Figure 2.33 – An example of crack propagation related to the crystallographic orientation of the individual grains – (a) an SEM micrograph depicting a sudden change in the direction of the crack and (b) highlighting that a high angle grain boundary resulted in the crack path deviation into a crystal which is preferentially orientated in terms of the energy required for cleavage[93]. 58

Figure 3.1 – Plots depicting the transverse rupture strength vs. grain size dependence in PCD. 64

Figure 3.2 – Plot depicting the relationship between fracture toughness and PCD grain size. 64

Figure 3.3 – Disk shaped compact tension specimen geometry employed by Achilles[19]. 66

Figure 3.4 – Example of the crack initiation and growth by fatigue mechanisms[19]. 66

Figure 3.5 – Photographs depicting the SEVNB notch geometry (left) and the CNB notch cross-sectional geometry after fracture (right). 68

Figure 3.6 – Normalised fracture toughness results highlighting the sensitivity of the PCD material measurement to the notch root radius dimension[16]. 69

Figure 3.7 – Effect of the residual metal removal depth (RMRD) on the fracture toughness result obtained[16]. 69

Figure 3.8 – PCD fracture toughness as a function of starter particle grain size (each point represents an average of 10 fracture toughness measurements) [18]. 70

Figure 3.9 – Schematic view of the fixture developed for the cyclic compression loading of PDC cutters [22]. 71

Figure 3.10 – The contact geometry between the PDC cutter and the tungsten carbide cylinder[22]. 72

Figure 3.11 – Plot depicting the maximum load versus the number of cycles leading to failure[22]. 72

Figure 3.12 – Test rig developed by Kanyanta et. al. [23] to investigate the impact fatigue lives of PDC cutters (left) and the geometry of the impact zone between the carbide anvil and the Syndril cutter (right). 73

Figure 3.13 – Cyclic impact S-N fatigue life curves developed for two different cutters of undisclosed composition[23]. 74

Figure 3.14 – (a) Schematic representation of the key elements required to determine fracture toughness from the Vickers indentation test, (b) cracks emanating from the corners of a Vickers indent in polycrystalline CVD diamond [15]. 76

Figure 3.15 – The illustration on the left (a-c), show the specimen geometry, loading geometry as well as the schematic of the crack front in the Lin et. al. experiments while (d) shows the experimental arrangement of the Davies and Field experiments[29,91]. 77

Figure 4.1 - Sketch depicting the PMMA specimen, highlighting the general dimensions of the specimen. 88

Figure 4.2 – Drawing depicting the geometry of the PCD specimens. 90

Figure 4.3- No part of the rig could protrude more than 25mm above the plane of the sample as such protrusions could impact the SEM column/detector during the panning process and cause damage to the microscope. 92

Figure 4.4 - Photograph depicting the general layout of the miniature double torsion rig employed in the nuclear graphite research project. The key components are labelled. 95

Figure 4.5 - Photograph depicting the general layout of the miniature double torsion rig employed in the nuclear graphite research project, highlighting the loading geometry employed. 95

Figure 4.6 - Photograph depicting the layout of the load sensing bridge geometry, highlighting the composite approach where a half bridge strain gauge setup is applied to the load sensing beam and an aluminium saddle is employed to “float” the inner reaction balls over the upper gauge. 96

Figure 4.7 - Photograph depicting the miniature DT rig as installed in the Leo S400 SEM, highlighting the internal rig position and the external motor drive application via a rotary manipulator. 96

Figure 4.8 – Optical micrograph (a) depicting the wide open crack at the tip of the starter notch after propagation has been achieved through approximately 50% of the sample length. The degree of closure and lack of any discernible features after load removal are highlighted in micrograph (b). This highlights the difficulty in the tracking of the crack. 98

Figure 4.9 – SEM micrographs highlighting the initiation region (left) and the propagation region (right) in the first in-situ SEM PCD experiment. . 98

Figure 4.10 - Photograph depicting the in-situ DT rig, highlighting the new actuation approach (left), where the motor is placed “on-board” the rig to prevent the need for complex cardan shaft arrangements and expensive rotary throughput development. The native Z-axis stage adjustment and “stage touching” alarms have been removed from the SEM to facilitate optimized working distances. 100

Figure 4.11 – Plot depicting the load bridge calibration data, highlighting the linear behaviour. 101

Figure 4.12 - Chart plotting an example of the calibration data for the cross-head displacement gauge, highlighting the linearity and resolution of the displacement gauge. 102

Figure 4.13 – Plot highlighting the noise and drift performance of the load measuring system. 103

Figure 4.14 - EDM machined load bridge geometry, highlighting the fact that the bridge load- deflection coefficient cannot be easily calculated employing theoretical calculations. 104

Figure 4.15 – Plot depicting the vertical bridge deflection under load. 104

Figure 4.16 – Exploded CAD view of the miniature rig. 106

Figure 4.17 – Plot depicting the load displacement data obtained during a fracture test of a 2 mm PMMA miniature DT specimen. 107

Figure 4.18 – Plot depicting the stress intensity values calculated from the load displacement data presented in Figure 4.17. 108

Figure 4.19 – Plot depicting the SIF results of ten crack propagation experiments in 2 mm PMMA material. 108

Figure 4.20 – Plot depicting the SIF-displacement data for a test carried out in CTM502 PCD, highlighting the notch toughness effect (red arrow) as well as controllable propagation in the constant stress intensity region. 110

Figure 4.21 – Layout of the components employed during the in-situ SEM miniature double torsion fracture experiments. 111

Figure 4.22 – Micrograph depicting the root of the starter notch prior to the initiation of loading. 112

Figure 4.23 – Micrograph depicting the initiation of the crack. Note the arrows as the crack is difficult to observe. 112

Figure 4.24 – Micrograph depicting a crack deflection feature caused by microstructural features in 30 µm PCD specimen. 113

Figure 4.25 – Photograph depicting the stereo camera rig employed to capture the images for the DIC analysis. 115

Figure 4.26 – Diagram depicting the components making the in-situ DIC miniature double torsion fracture experiments. 115

Figure 4.27 – Photograph depicting two PMMA specimens, highlighting the speckle pattern obtained by the described paint spraying method. 116

Figure 4.28 – Pinhole camera model described by Sutton [77] for the purposes of calibration of a stereo DIC system. 118

Figure 4.29 – Theoretical displacement field calculated employing the Williams analysis solution for the stress intensity level of 1MPa√m. The position of the crack tip has to be selected from the plotted field (in the theoretical case the position is at the origin of the plot). 120

Figure 4.30 – Plot depicting a square integration region (grey square region) applied to the displacement field with elements adjacent to the crack faces masked out to prevent the use of erroneous data associated with the crack. An example of an area integral contour is also shown. 120

Figure 4.31 – Plot depicting the stress intensity value calculated by the application of the JMAN code to the theoretical displacement field. 121

Figure 4.32 - Chart plotting the load-displacement behaviour for the 2 mm PMMA specimen in the DT experiment. It is noteworthy that the sample thickness selection results in a similar critical load level as that for 0.5 mm PCD sample, Figure 4.36. Processing that load data employing the classical DT formulations, the stress intensity results are obtained, plotted in Figure 4.33. 123

Figure 4.33 - Chart plotting the stress intensity factor for the 2 mm PMMA DT specimen calculated employing classical DT equations. The numbered balloons correlate the positions at which stress intensity was evaluated employing JMAN routine as presented in Figure 4.35. 123

Figure 4.34 - The speckle pattern applied to the otherwise transparent PMMA sample is depicted on the left. Analysing the speckle pattern deformation employing DIC techniques, material displacement field is extracted.....124

Figure 4.35 - Charts plotting the area contour employed to calculate the stress intensity parameter (left) as well as the plot of the stress intensity solution for each of the seven contours (right, starting at the notch tip and progressing outward). Comparing the results depicted above to those calculated and plotted in Figure 4.33, good level of correlation is revealed. 124

Figure 4.36 - Chart plotting the load-displacement behaviour for the 0.5 mm PCD sample in the DT experiment. Processing the load data employing the classical DT formulations, the stress intensity results are obtained, plotted in Figure 4.37. 125

Figure 4.37 - Chart plotting the stress intensity for the 0.5 mm PCD DT specimen as calculated employing classical DT equations. 125

Figure 4.38 - The natural pattern of the PCD sample is depicted on the left (addition of white spray pattern was performed to aid the DIC analysis). Analysing the surface deformation data employing DIC techniques, the displacement field was extracted. 126

Figure 4.39 - Charts plotting the area contour employed to calculate the stress intensity parameter (left) as well as the plot of the stress intensity solution for each of the 25 contours (right, starting at notch tip and progressing outward). Comparing the results depicted above to those calculated and plotted in Figure 4.35, a good level of correlation is revealed. 126

Figure 4.40 – Plot of the load-displacement data for a 2 mm PMMA DT experiment.....128

Figure 4.41 – Plot of the stress intensity-displacement data for the 2 mm PMMA DT experiment. 128

Figure 4.42 – Images depicting the surface deformation of the specimen prior to initiation (left) and once the crack is in the constant stress intensity range (right). 129

Figure 4.43 – Plot depicting the specimen deformation data as imported into MATLAB, highlighting the crack tip position (red circle), masked noisy data adjacent to the crack faces (crosses) and the field of data (grey area) over which the area J-integral is calculated.....129

Figure 4.44 – Plot depicting the stress intensity value obtained in the constant stress intensity region by the non-contact optical approach. 130

Figure 4.45 - EBSD plot (a) depicts the results of a scan performed over a smaller region (200x200 µm), highlighting improved resolution of the constituent's orientation. The surface finish in the region of the map is highlighted in SEM micrograph (b).....131

Figure 4.46 - Schematic representation of the two EBSD mapping approaches employed. On the left, a specimen is shown with a region being highlighted for pre-mapping. On the right, a specimen containing an arrested crack is shown, highlighting small regions of interest identified for mapping. 133

Figure 4.47 - Scanning electron micrograph depicting the region to be mapped, highlighting the focused ion beam (FIB) marks at the perimeter of the region. 133

Figure 4.48 – EBSD Euler angle map highlighting the crack path as a function of orientation of the various diamond grains. Crystallographic preference can be observed at the bottom of the map. 134

Figure 4.49 - BSD micrograph highlighting the crack path as a function of the diamond particles (dark phase) and the cobalt binder pools (grey phase). The bright speckles are believed to be particles of tungsten residual from the sintering process. 134

Figure 5.1 – SEM backscatter micrographs depicting the microstructures of the 4 µm PCD material (left) and the 12 µm PCD material (right). The dark phase is diamond while the bright phase is cobalt with small inclusions of tungsten which is characterised by the brightest speckles. 137

Figure 5.2 - SEM backscatter micrographs depicting the microstructures of the 30 µm PCD material (left) and the 30/4 µm bi-modal PCD material (right). The dark phase is diamond while the bright phase is cobalt with small inclusions of tungsten which is characterised by the brightest speckles. 137

Figure 5.3 - Two phase composition analysis (bottom) of the BSD image (top) of the cobalt phase in a 4µm specimen. All data below the intensity level equal to 50 is considered to be diamond and is highlighted red, the remaining areas are considered to be cobalt. 139

Figure 5.4 – BSD micrograph depicting the microstructure of the 4 µm grade PCD specimen, highlighting the regions where measurements were taken. 141

Figure 5.5 – Backscatter micrograph depicting the microstructure of the 30-4 µm PCD specimen, highlighting an example of the line intercepts employed to determine the diamond phase contiguity. Where the boundary contact is diamond-diamond, a red dot is placed, while a green dot is placed at the diamond-cobalt interface. 144

Figure 5.6 – SIF-displacement plot for the 4 µm PCD specimen during the in-situ SEM experiment (raw data). 146

Figure 5.7 - SIF-displacement plot for the 12µm PCD specimen during the in-situ SEM experiment (raw data). 146

Figure 5.8 - SIF-displacement plot for the 30 µm PCD specimen during the in-situ SEM experiment (raw data). 147

Figure 5.9 - SIF-displacement plot for the 30-4 µm PCD specimen during the in-situ SEM experiment (raw data). 147

Figure 5.10 – Stereo micrograph depicting the surface of the leached PCD specimen, with an application of white paint speckles aimed at improving the surface contrast. 149

Figure 5.11 – Load displacement data for leached 0.5 mm leached PCD experiment performed in-situ stereomicroscope. 149

Figure 5.12 – DIC output plot of the maximum normal strain field around the developed crack. 150

Figure 5.13 – Image depicting the JMAN integration contour superimposed onto the displacement field (vector length) generated by the DIC software. 150

Figure 5.14 – Stress intensity level as evaluated employing the JMAN methodology. 151

Figure 5.15 – The global displacement field on the speckle painted surface of the DT specimen. The specimen is positioned horizontally with the crack propagating from the left to the right. 153

Figure 5.16 – Local displacement field (vector length) around the crack tip, allowing for more accurate selection of the crack tip position. 153

Figure 5.17 – Chart plotting the stress intensity calculated by employing the JMAN routine applied to the displacement field data in Figure 5.16. The SIF data is plotted against the contour number. Note that the first contour SIF values will typically be zero as these data points are masked out to prevent erroneous data around the crack tip where displacements cannot be accurately evaluated by DIC. 154

Figure 5.18 – SEM micrograph depicting the starter notch of the 4µm-1 specimen, highlighting its bluntness relative to a sharp crack. Note the pitting/erosion damage adjacent to the root of the starter notch (arrows). 156

Figure 5.19 – SEM micrograph depicting the starter notch of the 4µm-2 specimen, highlighting an appearance different to that observed in Specimen 1, Figure 5.18. 157

Figure 5.20 – SEM micrograph collage depicting the position of crack initiation in specimen 4µm-1. 157

Figure 5.21 - SEM micrograph collage depicting the position of crack initiation in specimen 4µm-2. 158

Figure 5.22 – SEM micrograph collage depicting the developed crack in specimen 4µm-1. The insert on the right depicts x2.5 magnification of the region highlighted by the dashed rectangle. The surface breaking portion of the crack plane can be seen deflecting due to the microstructural features. 159

Figure 5.23 – SEM micrograph depicting a broken out ligament of the PCD surface material. The crack initially propagated to the right of the ligament and subsequently, the ligament fractured under the local stresses resulting in the crack jump to the left. 160

Figure 5.24 – SEM micrograph depicting the EBSD pre-mapped region highlighted by the FIB marks. The crack is entering the region from the bottom, highlighted by the arrow. The propagation of the crack is depicted in Figure 5.25. 160

Figure 5.25 – SEM micrograph sequence depicting the crack propagation within the EBSD pre-mapped region. 161

Figure 5.26 – SEM micrograph depicting the surface of specimen 4µm-2, highlighting the crack path (red arrow). The insert on the right depicts a x2.5 magnification of the crack path region highlighted by the dashed rectangle. 162

Figure 5.27 – SEM micrograph collage displaying a global view of that crack propagation path in the 4µm-1 specimen. The crack remained slightly open after the load was removed. 163

Figure 5.28 - SEM micrograph depicting the starter notch of the 12µm-1 specimen, highlighting its bluntness relative to a sharp crack. Some pitting/erosion, similar to that observed in the 4µm specimens, is evident around the EDM machined notch. 164

Figure 5.29 - SEM micrograph depicting the starter notch of the 12µm-2 specimen, highlighting an appearance different to that observed in Specimen 1. The specimen experienced significant deposition during the EBSD process which made crack detection difficult. The FIB marks are highlighted by arrows. 165

Figure 5.30 – SEM micrograph highlighting the region of crack initiation. The x2.5 magnification inset at the top right corner highlights that initiation coincided with pits believed to be the result of EDM machining process. 165

Figure 5.31 – SEM micrograph depicting the initiation notch of specimen 12µm-2. Imaging was complicated by charging the source of which was not well understood as specimens 12µm-1 and 12µm-2 were prepared employing the same procedure. The accelerating voltage had to be reduced to 2.5 kV in order to generate the initiation images. 166

Figure 5.32 – SEM micrograph depicting the crack propagation in specimen 12µm-1. It is believed that the crack deflects along the preferential microstructural features. 167

Figure 5.33 – SEM micrograph depicting the crack propagating through the EBSD pre-mapped region of specimen 12µm-2. Due to the difficulties with imaging the magnified view insert is not clear. However, the features resemble those observed in specimen 12µm-1. 167

Figure 5.34 – SEM micrograph collage depicting the global view of the crack in the 12µm specimen after unloading of the miniature DT specimen. The crack appears more tortuous than the crack observed in the finer grained 4µm specimen. 169

Figure 5.35 - SEM micrograph depicting the starter notch of specimen 30µm-1. 170

Figure 5.36 – SEM micrograph depicting the starter notch of specimen 30µm-2. 171

Figure 5.37 – SEM micrograph depicting the initiation observed in specimen 30µm-1. This was the only instance where the crack initiated away from the centre, as highlighted by the x2.5 magnification insert (the crack is highlighted with arrows). 171

Figure 5.38 – SEM micrograph depicting the crack initiation region in specimen 30µm-2. 172

Figure 5.39 – SEM micrograph depicting the propagation of the crack in the 30µm-1, highlighting the fact that the crack is propagating from left to right. 173

Figure 5.40 – SEM micrograph collage depicting three stages of crack propagation through the EBSD mapped region (green arrows highlight FIB marks and red arrows highlight the crack tip position). 174

Figure 5.41 – SEM micrograph depicting the crack propagation in specimen 30µm-2, highlighting a crack “jump” feature. The crack terminates in what appears to be a diamond crystal and re-initiates along an energetically preferential path (arrow). 175

Figure 5.42 – SEM micrograph depicting further crack “jumps” during propagation in specimen 30µm-2. 175

Figure 5.43 – SEM micrograph depicting a crack branching feature in specimen 30µm-2 (arrows). 176

Figure 5.44 – SEM micrograph collage depicting the global view of the crack after specimen 30µm-2 unloading. 177

Figure 5.45 - SEM micrograph depicting the propagation features in specimen 30µm-2 after unloading. The red arrows highlight the positions where the crack propagates through diamond grains. The green arrow highlights a deviation of the crack to the left, seeking a preferential path in the binder pool – between diamond grains. ... 178

Figure 5.46 - SEM micrograph depicting the starter notch of specimen 30-4µm-1. The root of the notch had irregular geometry. Regions of cobalt pool

removal due to EDM machining were observed adjacent to the notch (red arrows). 179

Figure 5.47 - SEM micrograph depicting the starter notch of specimen 30-4µm-2. The root of the notch had irregular geometry with regions of cobalt pool removal due to EDM machining (red arrows). 179

Figure 5.48 - SEM micrograph depicting the crack initiation region in specimen 30-4µm-1. The crack initiated at the root of the notch, adjacent to an EDM erosion defect. 180

Figure 5.49 - SEM micrograph depicting the starter notch of specimen 30-4µm-2. Crack initiation occurred at one of the EDM machining defects in the root of the starter notch (red arrow). The magnification was halved in order to frame the FIB marks. 180

Figure 5.50 - SEM micrograph collage depicting three stages of crack propagation through the EBSD mapped region of specimen 30-4µm-2 (green arrows highlight FIB marks and red arrows highlight the crack tip position). 182

Figure 5.51 - SEM micrograph depicting a crack branching feature in specimen 30-4µm-1 (arrow). Significant crack path deflection was also observed (green arrow, main image). 183

Figure 5.52 - SEM micrograph depicting a crack deflection feature in specimen 30-4µm-1 (arrow). The feature appears to have been generated by a relative slip between two diamond grains (green arrow) with subsequent fracture of a grain along a preferential cleavage plane (red arrow). 183

Figure 5.53 – Micrograph collage depicting the crack in specimen 30-4µm after unloading. 184

Figure 5.54 – SEM micrograph depicting the fracture surfaces of specimens 4µm-1 and 30µm-1. The specimens are mounted adjacent to each other, held in by a grub screw visible in the top left corner of the micrograph. 187

Figure 5.55 - SEM micrograph depicting the fracture surfaces of specimens 12µm-1 and 30-4µm-1. The specimens are mounted adjacent to each other, held in by a grub screw visible in the top left corner of the micrograph. 187

Figure 5.56 – SEM micrograph depicting the fracture surfaces of specimens 4µm-1 and 30µm-1. The red arrows highlight the contour of the arrest mark believed to be consistent with the shape of the crack front. .188

Figure 5.57 – SEM micrograph depicting the arrest boundary in specimen 4µm-1, highlighting the change in the appearance of the fractographic

features of the diamond grains as well as the appearance of the cobalt pools. The red arrow shows the direction of crack propagation.....188

Figure 5.58 – SEM micrograph depicting the fracture surface of the 4µm-1 specimen, highlighting the morphology of the cobalt pools (white constituent) and the diamond phase (grey constituent). 189

Figure 5.59 – SEM micrograph depicting the fracture surface of the 12µm-1 specimen, highlighting the morphology of the cobalt pools (white constituent) and the diamond phase (grey constituent). Compared to the 4 µm specimen, distinct diamond grains are better defined with a clear reduction in the number of cobalt pool features.....189

Figure 5.60 – SEM micrograph depicting the fracture surface of the 30µm-1 specimen, highlighting the morphology of the cobalt pools (white constituent) and the diamond phase (grey constituent). The cobalt pool positions can be attributed to the boundary regions of adjacent diamond grains. 190

Figure 5.61 - SEM micrograph depicting the fracture surface of the 30-4µm-1 specimen, highlighting the morphology of the cobalt pools (white constituent) and the diamond phase (grey constituent). Similar to 30 µm specimen, the cobalt pools are isolated at the grain boundaries, showing further reduction in cobalt phase. 190

Figure 5.62 – SEM micrograph depicting the fracture surface of specimen 30-4µm-1, highlighting the cobalt phase (white constituent) clearly isolated at the grain boundaries between diamond particles (grey phase).....191

Figure 5.63 – SEM micrograph depicting the fracture surface of specimen 30µm-1, highlighting a diamond grain (bounded by the green dashed line) and the diamond-to-diamond connections (red arrows) separated by intermittent grain boundary cobalt pools. 191

Figure 5.64 – SEM micrograph depicting a step in the fracture surface (in the plane of the page) of specimen 30µm-2, caused by internal porosity defects.....192

Figure 5.65 – EBSD map in the starter region of the 30 µm specimen containing an overlaid crack path (yellow line) obtained during the in-situ SEM fracture experiments. It appears that the crack path coincides with regions of finer/crushed grains (yellow arrows). 194

Figure 5.66 - EBSD map in the starter region of the 30-4 µm specimen containing an overlaid crack path (yellow line) obtained during the in-situ SEM fracture experiments. No preferential features are evident from the map and crack path overlay. 194

Figure 5.67 – EBSD map collage for the 4 µm specimen (left) and 30-4 µm (right). The 4µm specimen is difficult to index due to the very small grains as well as the intergranular cobalt pools which have high a degree of deformation. The 30-4 µm map has better indexing and the crack path is clearly visibly as a function of the microstructure. 195

Figure 5.68 - EBSD map collage for the 12 µm specimen (left) and 30 µm (right). The indexing in 12 µm specimen is improved when compared to the 4 µm but it still lacks the quality obtained in the case of the 30 µm and 30-4 µm specimens.....196

Figure 5.69 - EBSD map collage depicting the 30 µm specimen (left) and the 30-4 µm specimen (right). Red arrows highlight regions where the crack paths tend to avoid the grain boundaries to preferentially pass through the diamond crystals. 197

Figure 5.70 – Transmission electron microscopy images of the regrown diamond at the grain boundary, highlighting the constituents as – a) non-metallic bonding agent, b) regrown diamond and c) plastically deformed diamond[46]. 197

Figure 5.71 – EBSD maps depicting the maps performed around the closed cracks in specimen with 4 µm microstructure (a), and the 12 µm microstructure (b). As highlighted by the images, it is difficult to extract useful information from these maps. 198

Figure 5.72 - EBSD maps depicting the maps performed around the closed cracks in specimen with 30 µm microstructure (a), and the 30-4 µm microstructure (b). The maps indicate the grain orientation remains nominally the same after the crack splits the crystal. The maps further highlight both trans and intergranular crack propagation. .199

Figure 6.1 – Plot depicting the stress intensity plotted against the crosshead displacement during an experiment in a 4 µm PCD specimen, highlighting the elevated stress intensity associated with establishment of the stable crack front from a notch and a plateau region characterising the toughness of the material. 206

Figure 6.2 – Plot depicting the relationship between the fracture toughness and the measured grain size of the four grades of PCD materials tested. 208

Figure 6.3 - Plot depicting the relationship between the fracture toughness and the cobalt content of the four grades of PCD materials tested. 210

Figure 6.4 - Plot depicting the relationship between the fracture toughness and the diamond phase contiguity of the four grades of PCD materials tested. In the four PCD grades analysed, contiguity increases with

increasing grain sizes and decreases with increasing cobalt content. 210

Figure 6.5 – Fractograph depicting the pre-cracked region in the 30 µm specimen after the load was removed, highlighting the presence of the process zone around the main crack wake. 214

Figure 6.6 – Collage depicting the fracture surface of the four specimens of the four grades tested, highlighting the difference in the appearance of the tortuosity/relief of the fracture surface. 215

Figure 6.7 – SEM micrograph depicting the shape of crack front developed during the double torsion experiment in the 0.5 mm PCD specimen. 215

Figure 6.8 – Optical micrograph depicting the surface of a leached PCD specimen, highlighting the natural surface texture (dark grey) and the additional paint speckles (white globules). For illustration purposes, depicts the same image at the end of the experiment with the crack having fully traversed the field of view from the notch, left to right. 217

Figure 6.9 – Optical micrograph depicting the same field of view as Figure 6.8 after the crack was propagated fully across the field of view and can be considered “wide open”. It is evident that the crack is difficult to identify. 217

Figure 6.10 – Illustration collage depicting a miniature DT specimen (top left) experiencing crack propagation. The surface of the specimen has a speckle pattern (bottom left). The J-integral is evaluated around the crack tip for deformation field determined by DIC. The image in the bottom right corner depicts the MATLAB implementation of the contour integral. 218

Figure 6.11 – Collage depicting the correlation between the applied load and the stress intensity level determined by DIC and Jman techniques. It is important to note that the optical approach correctly identifies critical stress intensity levels in the starter wedge at what is nominally half the load associated with the critical stress intensity as characterised by the classical DT equations. (The global sidebar applies to all three images as the strain range is fixed in the individual plots). 219

List of tables

Page

Table 2.1 – Key mechanical properties for single crystal, Type I diamond[8,35]. 12

Table 2.2 – Range of mechanical and physical properties for PCD's with various starter particle sizes [20]. 13

Table 3.1 - Properties of a range of cobalt matrix PCDs reproduced from Lammer [20]. 63

Table 3.2 – Fracture toughness results obtained by McNamara for the two grades in leached and un-leached conditions. 68

Table 4.1 – Key mechanical properties of PMMA. 89

Table 4.2 – Starter particle sizes and Young's modulus properties of the material grades supplied. 90

Table 4.3 – Table summarizing the result of the ten tests employed to evaluate the consistency of the data generated employing the miniature DT rig. 109

Table 5.1 – Specimen cobalt content as determined employing image analysis software applied to five separate BSD SEM images. 138

Table 5.2 – Specimen diamond particle size measured from the actual microstructure. 141

Table 5.3 – Microstructural contiguity of the diamond phase in the four specimen types employed. 143

Table 5.4 – Fracture toughness, K_{IC}, data for the four grades of PCD, obtained during the in-situ SEM DT propagation experiments. 145

Table 5.5 – Fracture surface cobalt content. 193

List of abbreviations and symbols

Abbreviations

AGG	Abnormal Grain growth
BSD	Backscatter Detector
CN	Chevron Notch
CNBDS	Centre Notched Brazilian Disc Specimen
CT	Compact Tension
CVD	Chemical Vapour Deposition
EBSD	Electron Backscatter Detection
EDS	Energy Dispersive Spectrometry
ESPI	Electronic Speckle Pattern Interferometry
DCB	Double Cantilever Beam
DCT	Disc-shaped Compact Tension
DIC	Digital Image Correlation
DT	Double Torsion
EDM	Electron Discharge Machining
EPFM	Elastic Plastic Fracture Mechanics
FCC	Face Centred Cubic
FIB	Focused Ion Beam
FPZ	Fracture Process Zone
HPHT	High Pressure High Temperature
HRTEM	High Resolution Transmission Electron Microscopy
LEFM	Linear Elastic Fracture Mechanics
PCD	Polycrystalline Diamond
PDC	Polycrystalline Diamond Compact
PMMA	Polymethyl Methacrylate
PTU	Parallel Trigger Unit
RMRD	Residual Metal Removal Depth
SEM	Scanning Electron Microscope
SENB	Single Edge Notch Bend

SIF	Stress Intensity Factor
TRS	Transverse Rapture Strength
WOB	Weight on Bit
YAG	Yttrium Aluminium Garnet
ZNSSD	Zero Normalized Sum of Square Differences

Symbols

a	Nominal crack length
dA	Small area increment
dP	Small load increment
dW_S	Small work increment
P	Applied load/Force
E	Young's modulus
E'	Equivalent elastic modulus for plane stress or plane strain condition
ν	Poisson's ratio
W_s	Work of fracture
B	Specimen width/Valid specimen thickness
σ	Stress
G	Shear strain energy
R	Crack resistance
K	Stress intensity factor
Y	Dimensionless crack shape factor
U	Internal energy
U_{el}	Elastic energy component
U_{pl}	Plastic energy component
J, J_R	J-Integral
W	Work
θ	Angle of rotation
w_m	Torque arm width
T	Applied torque

I_p	Polar moment of inertia
C	Compliance relationship
d	Double torsion specimen thickness
$\psi(t,W)$	Thickness correction factor
L	Length
f	Original image
g	Deformed image

1 Introduction

In contrast to the limitations associated with the standard test geometries employed in the determination of the fracture mechanics properties in polycrystalline diamond (PCD), it is proposed that the double torsion methodology can enable slow, controllable crack propagation in PCD while facilitating observation of the fracture process. To this purpose the current research project was initiated in September 2012 as a collaboration between the University of Cape Town and Element 6 (Pty) Ltd. Element 6 kindly provided the PCD specimens and the financial aid required to undertake such a research project. Further collaboration with the University of Stellenbosch and Nelson Mandela Metropolitan University have aimed at expanding the pool of experimental expertise in the fields of optical strain analysis and high resolution imaging required for the analysis of controlled fracture in this complex material.

1.1 Background

This thesis concerns an investigation of the fracture mechanics properties and crack propagation behaviour and mechanisms in polycrystalline diamond compact (PDC) materials. While PCD does occur in nature, most industrial compacts are produced from grits of synthetic diamond [1–3]. In its simplest form, polycrystalline diamond can be described as material consisting of a large number of randomly orientated diamond particles, Figure 1.1. The method for the synthesis of first synthetic diamond grits was developed independently at two different laboratories in 1953 and 1954 [4],[5]. The synthetic diamond generation process, while taxing on the equipment employed, was repeatable and enabled production of large quantities of diamond grits for industrial applications. These newly developed synthetic grits were freshly grown and were not subject to the crushing process circumventing the disadvantages associated with the damage sustained by natural diamond grits during the crushing process [6].

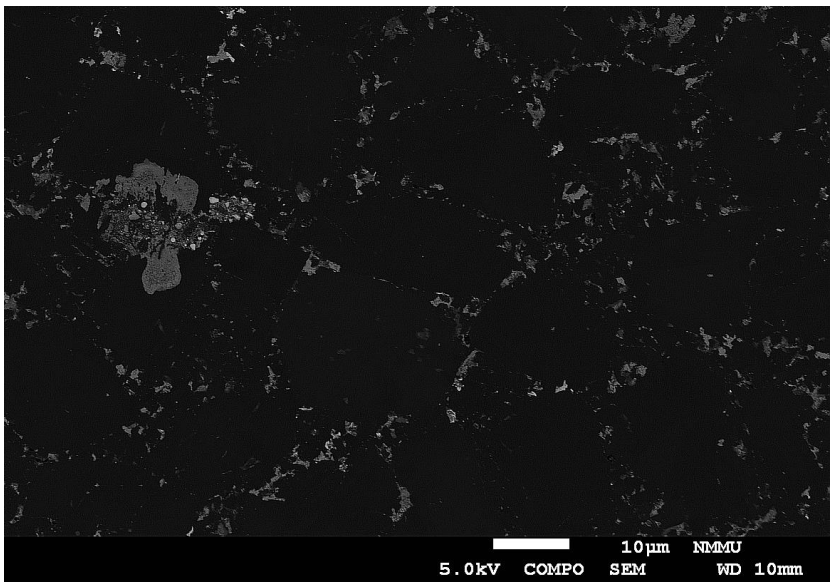

Figure 1.1 – Backscatter electron micrograph depicting a typical microstructure of polycrystalline diamond (PCD) material.

The advent of the method for synthetic diamond grit production resulted in the growth in the number of machining process applications. Critically, in 1972-3 it enabled the development of the procedure for production of the polycrystalline diamond compact (PDC) tools of various geometries through the high pressure high temperature (HPHT) process where diamond-to-diamond bonding could be achieved [4,7]. In this process the particles of diamond are initially compacted under high pressure and are then exposed to the HPHT process in the presence of a metal catalyst, typically cobalt, nickel or iron, to produce a high strength composite compact. A typical example of such PDC technology is the so called "button" cutter insert employed in the tooling of oil and gas and geothermal drill string bits, Figure 1.2.

Figure 1.2 –Photograph depicting a PDC "button" cutter, highlighting the thin wafer of PCD sintered onto a support body of tungsten carbide-cobalt WC/Co.

While natural diamond has very high stiffness (1050 GPa) and hardness properties (57-104 GPa), it also displays a significant level of anisotropy of these properties as a function of impurities and the crystallographic lattice orientation with respect the applied mechanical loading [4]. Therefore, while very expensive, **natural diamond** tool applications had to be planned carefully in terms of the preferential wear/failure orientation of the diamond tool body. On the other hand, PDC tool bodies generated by the high pressure, high temperature (HPHT) process, comprising randomly orientated diamond grits which were nominally fused together in the presence of a binder metal, realised a material with isotropic properties. The properties of such HPHT produced compacts approached the hardness, stiffness, strength and heat transfer properties of natural diamond [8].

The ability to produce diamond compact tools of desirable shapes and sizes, while minimizing the anisotropy disadvantages, lead to significant increase in the industrial use of PCD as a tool material [9]. Improvements in the HPHT techniques resulted in better and better PDC materials and the PDC based tools found their uses in a diversity of applications such as oil and gas drilling, geothermal drilling, high speed machining, excavation equipment as well as wear resistant sliding bearing contact interface materials to name but a few [10–12].

The application diversity of PDC based tools has led to the need to develop a fundamental understanding of the material properties which would maximise the performance of this already outstanding new material. One such property is the resistance of the PCD material to the propagation of cracks, better characterised by its “fracture toughness”. While the strength and hardness of the PCD material is some of the highest among all known materials, its fracture toughness properties are comparatively low (6.9-9.1 MPa√m), typically higher but similar to those of advanced ceramics (3-6 MPa√m) [13]. Such combination of properties results in a material with extreme strength and abrasion resistance properties, but which is quite susceptible to fracture, which manifests in chipping, gross cracking and other brittle failure damage mechanisms leading to the reduced performance of the PDC based tools [11,14]. Improvement of the fracture toughness properties of the PCD material would significantly improve its performance in most applications where loading characteristics promote cracking. More specifically, PCD materials with more predictable cracking behaviour such as cracking along preferential paths could provide “self-sharpening” properties, as gross fracture and spalling would be prevented. Such improvements would provide a significant advantage in situations where tool replacement is a time and cost intensive process.

This brief introductory overview reveals that improved understanding of the crack development and improved fracture toughness properties would be extremely advantageous to the industrial applications of PCD based materials. However, fracture mechanics based properties and crack growth are extremely difficult to study in PCD materials due to the extreme stiffness and strength of the material. Established conventional fracture mechanics and fatigue based methodologies and geometries are for the most part inapplicable to PCD due to the inherent lack of a gap between the threshold fracture toughness and the critical fracture toughness of the material. Simply, this means that once incipient crack propagation is achieved, the additional load required for complete failure of the specimen is very small as the stress intensity level is already rapidly rising due to the crack extension in typically crack length dependant fracture mechanics geometries [8],[15–18]. This makes studies of crack propagation phenomena as a function of make-up/microstructure very difficult. In-situ observation of the fracture process is possible but has historically required high speed image capture techniques [8]. The properties identified at such high propagation speeds may differ from those obtained in the regime near the threshold crack development process reported by multiple sources [19–22].

Further complications associated with fracture mechanics studies in PCD exist but, at this stage, are retained for discussion in the more appropriate chapters of this document.

Based on the discussion presented it is evident that in order to improve the fracture properties of PCD materials, improved methodologies are required to facilitate the investigation of various parameters affecting the fracture toughness and crack propagation properties in PCD. While a number of techniques have been developed for the characterisation of performance of PDC bits (PCD wafers attached to tungsten carbide – cobalt substrate, WC/Co) successful studies in controlled crack propagation and fracture mechanics parameter characterisation in free standing PCD material are limited [16,22,23]. This project aims to make a contribution to the methodologies and understanding in the fracture mechanisms, crack propagation behaviour and fracture properties in PCD. This, as shown later in this thesis, is facilitated by a technique that allows for slow, controlled crack propagation while enabling 'in-situ" microscope observation of the fracture process.

1.2 Structural integrity of polycrystalline diamond compact

Industrial applications such as oil and gas exploration and geothermal drilling are some of the largest consumers of PDC cutters. The high demand formed by these industries has driven the development of the PDC technologies and has driven how the structural integrity of the PCD material on the top surface of the PDC cutter is assessed. A significant number of the integrity assessment approaches is based around the PDC cutter as a component and not free standing PCD material itself. Examples of such tests are the lathe turning tests, where PDC cutters are used to machine a block of corundum and parameters such as bit wear and rate of material removal are assessed [12,22,24]. Another example involves repeated application of impact loading against the diamond table of a PDC cutter [23]. This is achieved by impacting the cutter against an anvil made from hard material such as PCD or WC/Co. Such impact loading, depending on the magnitude of the load, results in fatigue damage and subsequent spalling of the diamond table, delamination of the diamond table from the WC/Co cutter body as well as damage to the WC/Co body itself.

These tests are very useful to the cutter consumer, as they directly evaluate the performance of the various cutter types and the test results are immediately representative of cutter performance. However, these cutter based tests do not provide much information about the mechanisms of PCD material failure nor are they easily observable in-situ, as only the end result of cutter damage and the associated loads are evaluated. Nonetheless, these tests are likely to remain the industry standard for ultimate cutter performance assessment as the results are easily interpreted in terms of economics of the drilling operation.

While cutter performance is important, a more fundamental understanding of the PCD material properties and damage mechanisms need to be researched and developed in order to facilitate further improvements in the sintered diamond compact material performance. To this end, classical fracture mechanics approaches have been applied to free standing PCD material samples to determine the fracture properties of the material. Geometries such as compact tension, three-point bending, diametral compression and double cantilever beam have been investigated by various researchers (the details of these test geometries and associated procedures will be described in further detail in Chapter 3) [15,16,18,20]. While these tests are, to a degree, able to quantify the fracture toughness of PCD, all of them highlight one common trend which is the fact that it is extremely difficult to investigate the fracture processes and properties in PCD. As already briefly mentioned, the extreme stiffness and tensile strength coupled with low fracture toughness, have, to date, made controlled crack propagation extremely difficult [8].

It is proposed that the difficulties mentioned can be overcome by employing the double torsion (DT) test. The elegance of this geometry lies in the fact that once crack initiation is achieved, the test geometry is nominally crack length independent [25–28]. This characteristic enables slow, **controlled** crack propagation to occur in very brittle materials. The technique has been successfully applied to fracture mechanism investigations in brittle materials ranging from cement mortar, polymethyl methacrylate (PMMA), ceramics, glasses and graphite [23,24]. Double torsion has been attempted in PCD with promising results [29].

1.3 Aims of the project

The aim of this project is to improve the understanding of fracture mechanisms, crack propagation behaviour and fracture properties of PCD with the specific

objectives described in Section 3.3. The current body of knowledge provides an understanding of the general mechanical properties of PCD material enabling the selection of appropriate materials for specific application. However, the fundamental understanding of the underlying fracture processes needs to be developed further to enable the design of improved grades of PCD materials.

Such understanding can be achieved by employing the DT test geometry. Successful application of this technique to PCD will enable slow and controlled crack propagation which is observable in-situ. In turn this will enable the investigation of the effects of starter grain size, binder content and crystallographic orientation on the crack development behaviour and fracture properties. In-situ observation of the process will provide qualitative insight into the crack propagation process which should contribute to the knowledge required for the design of tougher PCD materials or manipulation of the crack path along preferred orientations. Attempts to apply optical strain measurement techniques are also made in this research project with the aim of evaluating the potential for non-contact strain measurement in this very low strain to failure material as this would pave the way for future scale independent fracture property determination in PCD materials. Observation of the fractographic features formed at known stress intensity levels will further aid the understanding of the fracture process.

1.4 Thesis document layout

It was considered appropriate to include a brief overview highlighting the layout of the thesis document. The chapters, while consecutive, are essentially self-contained.

In Chapter 2 the reader is introduced to the relevant background information relating to the production of PCD and its key mechanical properties. Tool applications employing this material are presented as this is considered pertinent due to the effect these had on the integrity investigation approaches employed in industry. The chapter further details the fracture mechanics concepts considered pertinent to this research project and fully details the double torsion methodology. Further experimental techniques employed in optical strain analysis and crystallographic orientation mapping are presented.

Previous studies on the fatigue and fracture properties of PCD are presented in Chapter 3. These include the various test methodologies which have been

employed. The overview of these methodologies provides the basis for the understanding of the experimental difficulties and as well as successes experienced in the fracture mechanics based studies of PCD. The chapter also highlights the relative lack of published research in the field, believed to be the result of the highly competitive nature of the PCD material market. A discussion is presented highlighting the current level of understanding into the problem of PCD fracture behaviour which leads to the identification of the areas where improved understanding may be developed and as such forms the basis for the formulation of the key aims and objectives of this research project. The chapter is concluded with the identification of the key aims and objectives which can build on the existing body of knowledge.

Chapter 4 details the experimental methodology employed. The development of the miniature double torsion rig for the use in-situ inside the specimen chamber of a scanning electron microscope (SEM) is detailed first, as it forms the core of the experimental methodology employed. Following on, the additional experimental technique of fracture mechanics parameter measurements by digital image correlation is presented. The methodology employed in the mapping of the surface grain orientation is discussed. Finally, the chapter is concluded with an evaluation of the experimental techniques developed.

The fracture mechanics parameters obtained through the developed experimental methodology are detailed in Chapter 5. The results are divided into two categories, separating those obtained by the established double torsion theoretical equations and the ones obtained by a novel **optical** J-integral extraction method called JMAN. Fractographic observations recorded in-situ during the performed experiments are presented and discussed. The fractographic features of the crack faces captured after failure of the specimens are presented for the various grades of the PCD material.

Chapter 6 presents a discussion of the findings of the research project undertaken. The fracture toughness results are discussed in the context of sample starter diamond grain sizes, grain orientation effects and binder content. The effects of specimen starter notches and thickness are discussed in the context of the double torsion technique. A discussion evaluating the success of the application of the double torsion technique and optical J-integral extraction methods is presented. Experimental observations of fracture mechanics testing in PCD are discussed.

Final recommendations and conclusions are drawn in Chapter 7.

2 Literature review of PCD and testing in brittle materials

This chapter is aimed at providing general information on PCD, its key properties and applications. Methodologies employed in the performance evaluation of the PCD material are discussed. The background theory related to the key fracture mechanics aspects necessary to explain the methodology employed in this research project are also presented. These are followed by the discussion of some of the techniques and specimen geometries employed in the fracture toughness and crack propagation studies in brittle materials. The DT technique is introduced, highlighting its capabilities which make it so useful in the fracture mechanics testing of brittle materials. This is followed by the introduction of two further techniques, namely digital image correlation (DIC) and electron back scatter diffraction (EBSD). These two techniques are employed in an attempt to further the insight into the micromechanisms of fracture in PCD materials under investigation. DIC enables optical full field displacement mapping over the specimen surface, which can provide additional information about the cracking process further to that obtained from classical DT formulations. Also, the deformation field data can be differentiated to obtain information about the surface strain evolution during the onset of fracture. EBSD provides a technique to map the crystallographic orientation of the individual diamond grains making up the PCD material. Information about individual grain orientation in the crack path can provide information about the orientation effects individual grains may have on the crack path in a nominally isotropic polycrystalline material such as PCD. The chapter is concluded by a summary discussion of the techniques presented and properties and is followed by Chapter 3 which details previously published research utilizing some of the tools discussed in this chapter, as well as others, to the analysis of the fracture behaviour and properties in PCD materials.

2.1 Development of synthetic diamond

The first synthetic diamonds were produced in 1953 at the General Swedish Swedish Electric Company, ASEA (Allmana Svenska Elektriska Aktiebolaget) based in Västerås, Sweden [30,31]. However, the methodology and its initial discovery and development were kept secret. The Swedish apparatus design was proposed by Baltzar von Platen, the inventor of the portable gas flame powered refrigerator [32]. While his proposed HPHT apparatus was not the one to yield reproducible results, and he had left the team prior to true success in repeatedly producing synthetic diamond, his methodology provided the underlying basis for future successful HPHT experiments. The first commercially confirmed and published diamond synthesis experiment was performed by H. Tracey Hall and his colleagues from the General Electric company, USA in 1954 [33]. Apparently, no less controversy had surrounded the General Electric "Project Superpressure" process as two scientists; Herbert Strong and H. Tracey Hall, collaborating with Francis Bundy and Robert H. Wentorf, were both able to produce synthetic diamond [30]. However, the experiment designed by Herbert Strong was not easily repeatable which was a key requirement for patenting, leading to the historical claim by H. Tracy Hall to be the first academically published scientist to be recognised as the author of the first successfully repeatable synthetic diamond generation experimental process. The findings of their research were published in the scientific journal "Nature" [24].

These early discoveries and developments enabled the production of diamond grits of various sizes [4]. Such grits are widely used in a number of industries to impart abrasion resistance to various machining and polishing tools. While the production of synthetic diamond grits was a major scientific breakthrough, the industrial impact in drilling, tunnel boring and road scarifying did not occur until a methodology to sinter the diamond grits into a larger body employing a HPHT sintering process was proposed by General Electric company in 1970 [4,5,30]. This historical milestone led to the development of the PDC bit technologies which are still widely used today. The graph depicted in Figure 2.1 provides an example of the rapid gains PDC based drill equipment has made in the oil and gas industry for the period spanning 1980 – 2004, over the traditional WC based Tricone drill bit equipment [9].

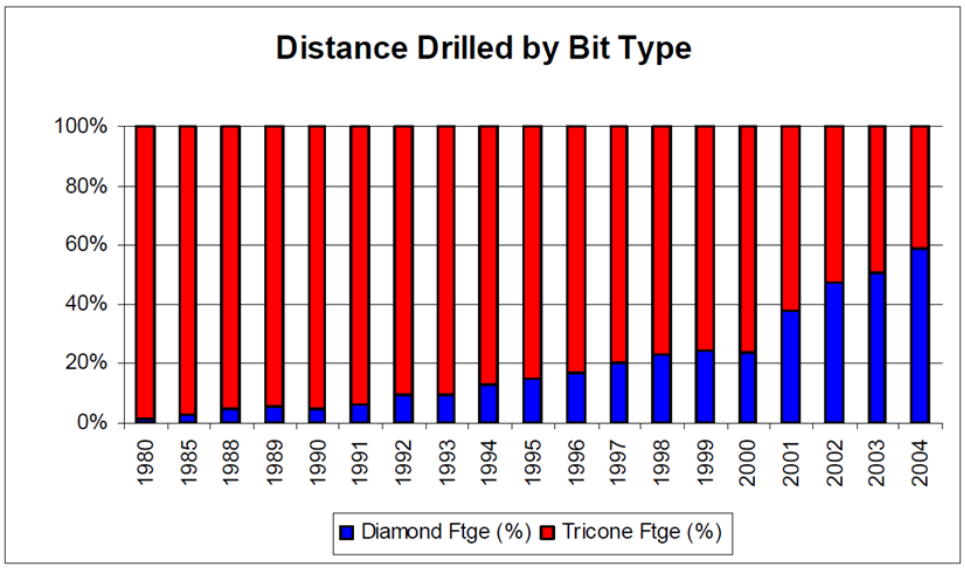

Figure 2.1 – Plot depicting the percentage of total footage drilled, breakdown in accordance with the respective brill bit types [9].

2.1.1 PCD material key properties

PCD is produced by sintering individual diamond crystals into a single body at temperatures in the range of 1500-2000 °C and pressures between 50 000-100 000 bar, typically in the presence of a catalyst required to improve the rate of reaction [32,33]. The pressure and temperature conditions for diamond synthesis and sintering are depicted on the simplified diamond-graphite equilibrium diagram depicted in Figure 2.2 [36]. The key mechanical properties for single crystal diamond employed in the production of PCD are presented in Table 2.1 below [7,8]. Additional information on the synthesis stages and production of thermally stable, leached PCD is provided in Appendix C.

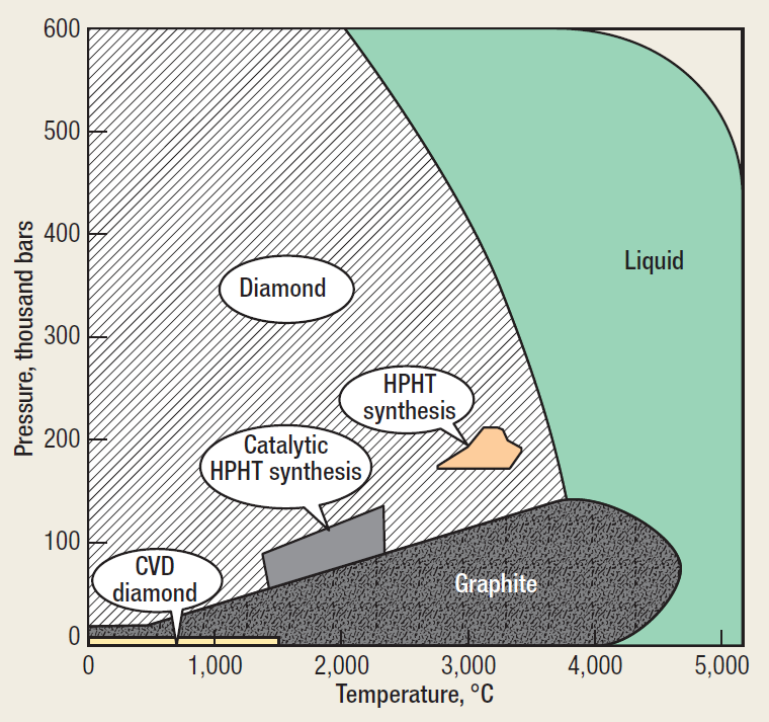

Figure 2.2 – The diamond graphite equilibrium diagram[36].

Single crystal diamond properties – Type-I Diamonds	
Hardness	57-104 GPa
Young's modulus	1050 GPa
Poisson's ratio (isotropic)	0.07
Fracture toughness (K_{IC})	5 MPa√m
Thermal conductivity	600-1000 $Wm^{-1}K^{-1}$
Slip system	{111}<110>

Table 2.1 – Key mechanical properties for single crystal, Type I diamond[8,35].

PCD composites can be produced from natural and synthetic starter powders. Most natural diamonds (about 98 %) are described as Type Ia and the synthetic diamonds are described as Type Ib diamonds. While the mechanical properties

of these two variants are nominally identical, they are differentiated by the nitrogen abundance and its distribution within the crystal lattice [37].

The key advantage of the PCD material is the random orientation of the diamond particles within the body of the material which leads to nominally isotropic properties when considered on the macroscale [18,20,24]. Such isotropy has significant toughness advantages over the anisotropic properties of single diamond crystals where preferential cleavage occurs along the weaker (111) planes. The individual diamond crystals within the bulk PCD retain their preferential cleavage planes but due to random orientation result in the impedance of crack propagation. The particle size of the starter diamond powder has a significant effect on the mechanical properties of PCD. The most recent and comprehensive studies into the properties of PCD have been published by Lammer and Field [8,20]. A summary of these properties is presented in Table 2.2 for PCD's with starter diamond particle sizes ranging from 2-150 µm. The methodologies of obtaining these parameters as well as the effect various particle sizes have on the mechanical properties will be addressed in Section 3.1.1.

Polycrystalline diamond compact properties (2-150 µm grades)	
Transverse rupture strength	300-1540 MPa
Tensile strength	440-1550 MPa
Fracture toughness	6.9-9.1 MPa√m
Poisson's ratio	0.070-0.086
Density	3.43-4.24 kg/m^3
Young's modulus	750-950 GPa
Shear modulus	350-440 GPa
Bulk modulus	290-370 GPa

Table 2.2 – Range of mechanical and physical properties for PCD's with various starter particle sizes [20].

Sintered diamond compacts have some of the best abrasion resistance properties of all man made materials which enables their successful use in the various applications such as oil and gas drilling, geothermal drilling, machining and road surface scarifying [6,10,11,14]. However, combined with the extreme abrasion resistance and hardness is the less favourable fracture toughness property which makes PCD materials brittle and therefore susceptible to damage by crack propagation [7,8,15].

2.1.2 PDC insert performance evaluation methods

The widespread use of PCD in various drilling applications has affected the development of the techniques employed in the evaluation of the PCD materials. This statement is based on the overview of the techniques employed to evaluate the wear and damage resistance of PDC inserts [34,36,37]. Most industry methods currently employed in the analysis of PCD material do not analyse the so called free standing PCD but rather analyse the PDC insert [12]. This is the logical route for industry to follow as the developed assessment techniques characterise the performance of the insert as a whole, evaluating the performance of the PCD surface layer as well as the quality of the attachment of this layer to the tungsten-carbide cobalt base.

Among the techniques employed are impact testing, indentation testing accompanied by acoustic emission logging, abrasive rock cutting tests (vertical turret lathe and granite log machining) and a number of variations of these [22, 24,34,38,39]. Non-destructive techniques such as visual, microscopic and ultrasonic scanning are used to assess the cutter integrity and table to substrate bond quality [42]. These techniques enable the manufacturer to assess the relative volume/mass loss of the cutter table, compare resistance to chipping and spalling and investigate the efficacy of diamond table and substrate interface [43].

All of the abovementioned methods, while providing very useful industrial assessment tools, provide a comparative/grading methodology and serve the purpose of optimised tool selection, relative performance assessment and investigation of the typical mode of failure related to specific environments. The clients who employ PDC insert based tooling provide further feedback to the manufacturers. One such example is the “dull-grading system”, which feeds back

the degree of drill bit damage as a function of drilling application parameters [44].

All of the abovementioned techniques have provided a high level of empirical understanding of the performance of the various grades of PCD in a diverse range of drilling and machining applications. It is widely accepted that fine grained grades of PCD possess good wear resistance and sharp edge retention but have low fracture resistance. Conversely, coarse grained grades are better at tolerating higher impact conditions. All grades of PCD suffer significant thermal degradation by graphitisation mechanisms at temperatures exceeding 750 °C [45]. Graphitisation, a process of decomposition of metastable diamond phase at atmospheric pressures into graphite, is exacerbated by the presence of residual catalytic metals employed during the HPHT synthesis process [46]. Therefore, removal of such residual catalytic phase greatly assists thermal stability and improves performance of the PCD material.

2.1.3 Summary

The overview presented highlights the extreme nature of PCD properties in terms of its hardness, strength and high thermal conductivity. However, accompanying these favourable properties is relatively low fracture toughness. This combination of properties tends to affect negatively the performance of the PCD based tools which tend to spall or develop cracks under service loads. However, the most widespread techniques in industry do not provide for ease of observation and study of the failure mechanisms in PCD materials. Therefore it is believed that further technologies and tools need to be developed to facilitate the study of free standing PCD materials. In the following section, an introduction to fracture mechanics is provided in order to introduce the reader to the background theory associated with the tools proposed for the study of PCD in the further sections of this dissertation.

2.2 Fracture mechanics and its applicability to brittle materials

Fracture mechanics is an established discipline involving the analysis of the potential for a material containing a flaw to undergo failure by fracture

mechanisms due to an applied load. Simply, fracture mechanics can be summed up as the discipline of solid mechanics enabling characterisation of stress singularities within a body. Typically, such singularities cannot be analysed by the classical approaches of mechanics of solids.

Fracture mechanics enables the study of crack propagation within a material. The inherent lack of plasticity within the PCD materials lends it to analysis by elastic fracture mechanics approaches as most fundamental derivations are based on assumptions of linear elastic material properties. Although many fracture mechanics techniques and methodologies have since been developed for the analysis of materials with significant levels of plasticity at the crack tip, their energy balance requirements enable analysis of very brittle materials, where the plasticity term approaches negligible levels.

The following sections present aspects key to the fracture mechanics techniques used elsewhere within this thesis. Among others these are topics such as the energy methods, the concept of stress intensity, modes of fracture and in more detail, the crack length independent testing methodology of crack propagation with a brittle material called double torsion. Fundamental fracture mechanics theory, derivations and application examples can be found in the established works of Anderson [47], Broek [48], Suresh [49], and Knott [50] among others.

2.2.1 Linear elastic fracture mechanics (LEFM) energy principle

The central hypothesis of fracture mechanics is the Griffiths energy criterion, proposed in the early 1920s [51]. Consider a large plate made of an elastic material which contains a crack of dimensions 2a, as depicted in Figure 2.3. Griffiths postulated that, in order for crack extension to occur, sufficient potential energy must be available in the plate system to overcome the resistance to the formation of new crack faces i.e. to overcome the surface energy of the material.

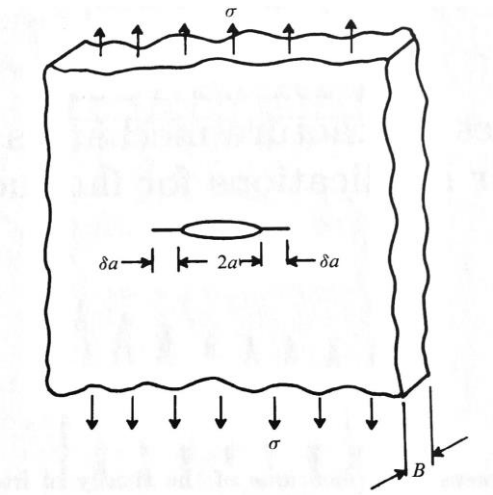

Figure 2.3 – A large loaded plate of an elastic material containing a crack-like defect of width 2a [49].

Using the example in Figure 2.3, the energy balance for an incremental increase in the crack area, *dA*, under equilibrium conditions can be expressed as,

$$\frac{dU}{dA} = \frac{dP}{dA} + \frac{dW_s}{dA} = 0, \tag{2.1}$$

or, the change in the available potential energy must equal the energy expanded for the formation of new crack surfaces, which can be expressed as

$$-\frac{dP}{dA} = \frac{dW_s}{dA}. \tag{2.2}$$

where, *U* is the total system energy which must remain constant for equilibrium, *P* is the potential energy supplied by the internal strain energy and external forces and, W_S is the work required to create new surfaces.

The potential energy of the system due to incremental crack extension in the same plate system can also be expressed, employing the stress analysis reported by Inglis [52], as follows

$$P = P_0 - \frac{\pi\sigma^2 a^2 B}{E'}. \tag{2.3}$$

where, P_0 is the energy state before crack extension, B is the plate thickness and for plane strain and plane stress, respectively,

$$E' = \frac{E}{1-\nu^2} \quad \text{for plane strain}$$

$$\text{and} \quad E' = E \text{ for plane stress.}$$

where E is Young's modulus and ν is Poisson's ratio. Therefore, the incremental potential energy change term can be expressed as

$$-\frac{dP}{dA} = \frac{\pi\sigma^2 a}{E}. \tag{2.4}$$

Since the formation of a crack requires formation of two crack surfaces per crack tip resulting in four new crack surfaces for symmetric crack extension in the system depicted in Figure 2.3, the surface energy of the crack can be described by

$$W_S = 4aB\gamma_s, \tag{2.5}$$

where γ_s is the surface free energy of the material. The incremental energy change associated with formation of an incremental crack area dA can then be expressed as

$$\frac{dW_s}{dA} = 2\gamma_s. \tag{2.6}$$

Combining Equation (2.4) and Equation (2.6), the critical stress for fracture initiation can be described as

$$\sigma = \sqrt{\frac{2E'\gamma_s}{\pi a}}. \tag{2.7}$$

The above model by Griffith considers ideal purely elastic conditions at the crack tip which seldom occur in reality. Irwin [53] and Orowan [54] proposed a

modification to the expression shown in Equation (2.7) by adding a term which describes the plastic energy dissipation term,

$$\sigma = \sqrt{\frac{2E'(\gamma_s + \gamma_p)}{\pi a}}. \tag{2.8}$$

where γ_P is the plastic work per unit area. This modification has enabled the extension of the idealised Griffith formulation to materials which exhibit limited crack tip plasticity. It is worth noting that the elastic and plastic components described in Equation (2.8) are not easily differentiated in practice [53], [54].

2.2.2 Crack face displacement modes during fracture

Three distinct fracture modes, with respect to the relative movement of the newly formed crack faces due to the applied load direction, are employed in the characterisation of the fracture processes. The three geometries are depicted in Figure 2.4.

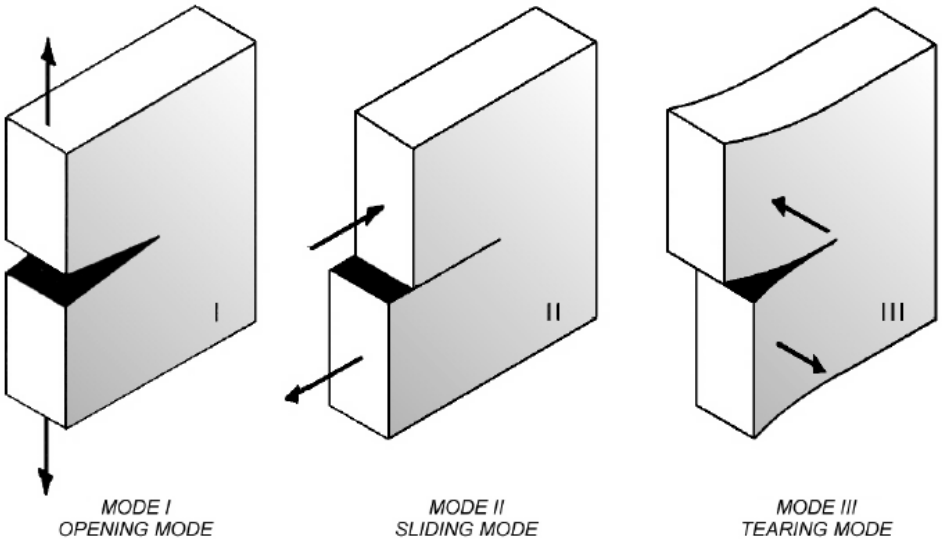

Figure 2.4 – The three modes of crack development under the application of the various loading geometries [55].

Each of three modes has its own energy requirement to cause crack propagation and thus each of the three modes have to be considered and characterised in order to fully describe the fracture process in any given material.

Mode I crack development (tensile opening mode) occurs by the displacement of the crack faces normal to the crack plane. Conversely, the crack plane is normal to the applied load direction which is typically considered the least energy intensive mode of crack development due to the minimised shear stress components. Hence, cracks often tend to orientate themselves in such a manner as to minimise the energy of fracture and hence they enable the mode I cracking mechanism. In mode II (in-plane sliding shear mode) crack face displacement occurs co-planar with the crack plane and the crack front is driven by the shear stress components associated with the loading geometry. Mode III (anti-plane shear/tearing mode) occurs due to out of plane shear loading and the crack faces are sheared parallel to the crack front [45,47]. Generally for metals the load required to cause fracture is lowest in Mode I and highest in Mode III.

2.2.3 **Strain energy release rate *G***

Having introduced the key energy principles and crack face displacement modes, it is worth describing the meaning of the model described by Equation (2.7). By rearranging, we obtain equation,

$$\frac{\pi\sigma^2 a}{E} = 2\gamma_e. \tag{2.9}$$

where γ_e is the equivalent elastic work term of surface energy. The left hand side of the equation is a function of applied stress level and has been termed as the energy release rate, *G.* The term represents the elastic energy release per unit of crack surface extension. The right hand side of the equation represents the increase in the energy level, or fracture resistance, associated with the formation of new free surfaces and is termed the fracture energy criterion, *R.* Therefore, for unstable crack development to occur, the energy release rate, *G,* must exceed the fracture resistance level equivalent to *R.* Following from Equation (2.9), and postulating that the material has some critical level of energy release rate, G_c, which can be sustained, these criteria can be employed to describe the fracture characteristics of a material as

$$\frac{\pi\sigma^2 a}{E} \geq \frac{\pi\sigma_c^2 a}{E} = \mathrm{G_c} = \mathrm{R}. \tag{2.10}$$

The critical value of the energy release rate, G_c, can be determined experimentally by determining the critical stress level, σ_c, at which a plate with a crack of a known dimensions undergoes fracture.

2.2.4 Strain energy release rate during Mode I crack extension

The energy balance described by Equation (2.10) can be applied to a wide variety of crack geometries as it simply provides a means of expressing the energy changes associated with crack extension. In the context of experimental work it is important to note that strain energy release term, *G,* includes energy contributions from the specimen as well as the experimental loading mechanism.

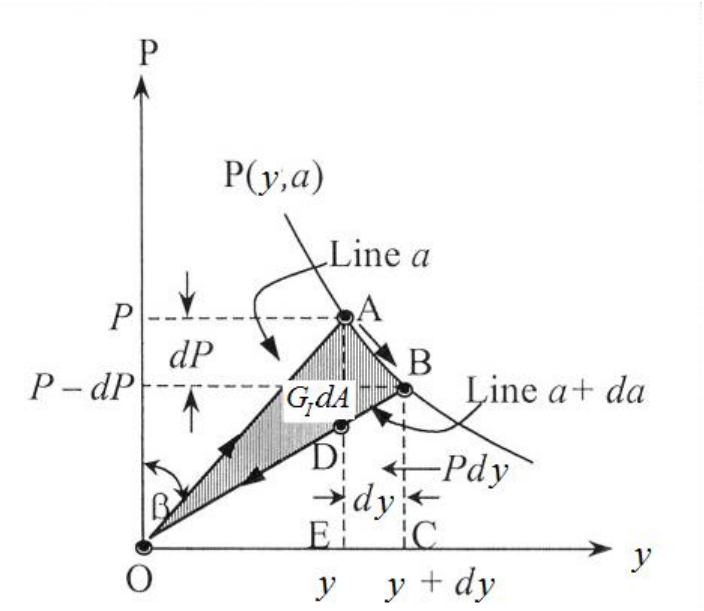

Figure 2.5 – A load vs. displacement plot describing the system energy during Mode I incremental crack extension *da* [47].

Consider a system depicted in Figure 2.5 which describes the changes which occur during linear Mode I incremental crack extension. The total stored energy due to the applied tension loading can be determined by the area under the

load-displacement curve. *G* can be found by energy lost during the fracture process

$$G_I = \frac{1}{2}\left(P\frac{dy}{dA} - y\frac{dP}{dA}\right). \tag{2.11}$$

In Mode I fracture, it is convenient to evaluate *G* in terms of the compliance (inverse of stiffness) *C* of the sample. Compliance is defined as the displacement *y* of the force application region divided by the applied load *P.* Therefore, the strain energy release rate during the incremental crack extension is independent of loading configuration and can be used to determine *G* through measuring compliance as a function of crack length [54,55] (the term "rate" in this instance is not a time dependant quantity but rather a quantity associated with an incremental crack extension *da*). The relationship between crack extension area and the resultant compliance can then be expressed for load controlled and displacement controlled systems as follows,

$$G_{I,y} = \frac{1}{2}\left(P^2\frac{dC}{dA}\right) \tag{2.12}$$

$$G_{I,P} = \frac{1}{2}\left(\frac{y^2}{C^2}\frac{dC}{dA}\right) \tag{2.13}$$

where $G_{I,y}$ denotes a constant displacement assumption and $G_{I,P}$ denotes a constant load assumption. The subscript G_I highlights the Mode I loading assumption employed. A powerful feature of the diagram depicted in Figure 2.5 is its ability to graphically describe the energy terms associated with the fracture process. For instance:

- *OA* = Initial loading line
- *AB* = Unloading line, where the load *P* dropped to *P-dP*, and similarly *y* changed to *y+dy.* Consequently, the crack area changed from *A* to *A+dA*

This leads to the graphical description of the key energy terms:

- Area *OAE* = Stored energy at fracture = *Py/2*
- Area *OBC* = Stored energy after fracture = (*P-dP)(y+dy)/2*

- Area *ABCE* = Work done = *Pdy* (for the case of load control)
- Area *OAB* = *OAE+ABCE-OBC* = Release of elastic energy = *GdA*

2.2.5 **Stress Intensity Factor (*SIF, K*)**

The Stress Intensity Factor (SIF) is another methodology which can be employed to characterise whether a crack will propagate under a given combination of flaw geometry, applied stress and material toughness properties. Stress intensity factor solutions aim to characterise accurately the stress state at the tip of the crack and determine whether the local conditions under the action of remote loading, will lead to incremental extension in the singularity dominated zone.

Under the assumption of homogeneous, linear elastic material each mode of loading produces the 1/√r singularity at the crack tip. Under mode I loading the stress intensity factor at the crack tip is described by

$$K_I = \lim_{r \to 0} \left[\sigma \sqrt{2\pi r}\right], \tag{2.14}$$

Where, σ is the remote tensile stress and r is the distance from the crack tip to the position within the stress field surrounding the crack tip. The shape of the stress field is affected by the geometry of the cracked body. The widely applied form of the expression in Equation (2.14), based on the proportionality between the crack tip and remote stresses, is defined by

$$K_I = Y \sigma_r \sqrt{\pi a} \tag{2.15}$$

where, *Y* is the geometrical shape factor accounting for the specific solution of the stress intensity field and, σ_r is the remotely applied stress. The maximum level of stress intensity which can be sustained by a material due to a given combination of applied stress and crack size is termed as critical stress intensity level, K_{Ic} (Mode I fracture toughness), and it characterises the fracture toughness of the material for the crack opening mode employed. The expression described by Equation (2.15) is employed in a multitude of geometries by selecting the correct geometrical correction factor from a diverse body of solutions available.

2.2.6 Elastic Plastic Fracture Mechanics (EPFM) considerations in brittle materials

Although the current research project involves one of the most brittle materials and plasticity is highly unlikely in its common form, it is considered important to touch on the aspects of the elastic-plastic fracture mechanics principles. The reason for this is the fact that the linear elastic fracture mechanics approach assumes that all the energy is absorbed by the formation of the new crack surfaces of the primary (only) crack. However, there exists a potential for the brittle material to have a Fracture Process Zone (FPZ), a small region surrounding the primary crack where the energy is dissipated by the formation of smaller, secondary microcracks. Such secondary cracking or FPZ phenomena would manifest themselves as an error in the calculation of the energy associated with formation of the primary crack alone.

In order to account for the potential FPZ phenomena, the energy balance discussed in Section 2.2.1 can be written as

$$\frac{\mathrm{d}U}{\mathrm{d}a} = \frac{d}{dA}(U_{el} + U_{pl}). \tag{2.16}$$

where, U_{el}, is the energy component associated with the formation of the new crack surfaces and, U_{pl}, is the component associated with the energy consumed by plastic deformation or in this particular instance, by the secondary microcrack development in the FPZ. As described in Section 2.2.3, the linear elastic energy balance is considered as the equivalence of the fracture energy release rate, *G,* and the crack resistance parameter, *R.* A similar energy term describing the criteria for potential for fracture exists in elastic plastic fracture mechanics and is denoted by the *J-integral* (defined in Section 2.2.7). Although associated with the elastic plastic fracture mechanics, the J-integral has both elastic and plastic components, and the equation describing the onset of crack extension can be written as

$$J_{el} + J_{pl} \geq J_c. \tag{2.17}$$

where the sum of the elastic and plastic components, J_{el}, and, J_{pl}, respectively, must exceed the critical level of J_c. Although no significant plasticity or large fracture process zone are expected during the crack propagation in PCD, the

energy balance described by the equation will be satisfied with plasticity term tending to zero and the elastic term approaching the critical level at the onset of fracture.

2.2.7 **The J contour integral**

In 1968, Rice presented the path-independent contour integral evaluating the energy release rate in a body of non-linear elastic or elastic plastic material containing a crack[58]. Considering the diagram depicted in Figure 2.6(a) (compare this diagram to the one depicted in Figure 2.5), the energy release rate is highlighted as the shaded area enclosed by the loading and unloading paths during crack extension.

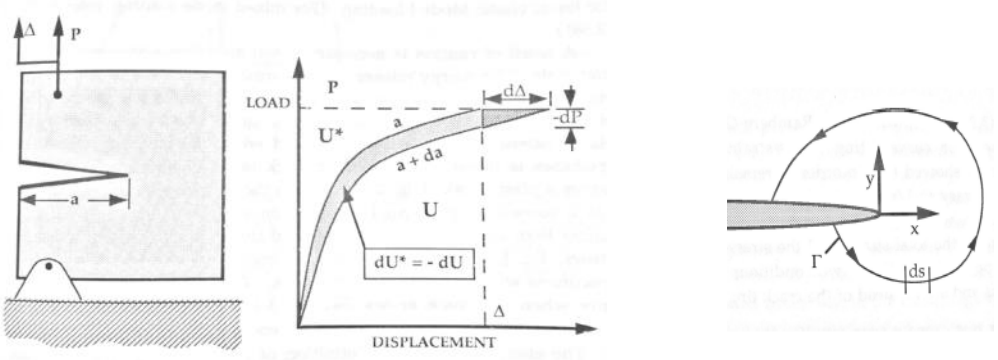

(a) (b)

Figure 2.6 – (a) – diagram describing the energy release rate in a non-linear elastic material with an advancing crack, (b) – an arbitrary contour around the crack tip.

Rice showed that by evaluating the integral in the counter clockwise direction around an arbitrary path (*Γ*), a path starting and terminating at the bottom and top crack faces respectively, Figure 2.6(b), the energy associated with fracture could be evaluated. In indicial notation the *J-integral* is written as

$$J = \int_{\Gamma} \left(W n_x - n_i \sigma_{ij} \frac{\delta u_{ij}}{\delta x} \right) \delta s, \tag{2.18}$$

where σ_{ij} and u_{ij} are stress and displacement components in indicial notation, δs is an arc increment along the integration path *Γ*, and n_i is a unit vector normal to the integration contour path. The term *W* describes the strain energy density defined as

$$W = \int_0^{\varepsilon_{ij}} \sigma_{ij} d\varepsilon_{ij.} \tag{2.19}$$

where σ_{ij} and ε_{ij} are the stress and strain tensors respectively.

The J-integral evaluates the rate of change of the potential energy with respect to the crack advance in a non-linear elastic solid or it can be thought of as the rate of energy flow into the crack tip. For linear or non-linear elastic homogeneous materials, the J-integral is path independent. Therefore, evaluating the J-integral at a remote contour and one near the crack tip can relate the conditions at the crack tip to the parameters describing the load applied to the system.

The complete derivation and proof for the path independence of *J-integral* are available in the works of Rice [58] and Anderson[47].

2.2.8 **Equivalence of fracture mechanics parameters**

On the condition that the fracture processes occur within the domain of linear elastic fracture mechanics i.e. with little plasticity and fracture process zone development, the fracture criteria can be related, for the condition of plane strain, by the following equation

$$G = J_{el} = \frac{K_I^2(1-\nu^2)}{E}. \tag{2.20}$$

The above expression must be employed with care as any significant plasticity or significant fracture process zone development would invalidate the described equivalence. In such instance, the parameter best quantifying the fracture process should be selected. Where SIF is selected, it can be related to the strain energy release rate *G,* through the following relationship

$$K_I = \sqrt{E'G} \tag{2.21}$$

where *E'* is the Young's modulus related to the shear modulus μ and the Poisson's ratio *v* of the material by $\mu = E'/2(1+v)$ and where $E' = E/(1-v^2)$ for plane strain and $E' = E$ for plane stress.

2.2.9 **Standard test geometries**

The aim of this section is to introduce some of the geometries commonly used in the fracture mechanics parameters characterisation of brittle materials. There are a number of standard as well as non-standard approaches available, with all of them having their own merits.

The common geometries and the general stress intensity solutions employed are – i) three point bend test, Figure 2.7, ii) compact tension test, Figure 2.8, iii) double cantilever beam, Figure 2.9, and iv) diametral compression (Brazilian disc), Figure 2.10.

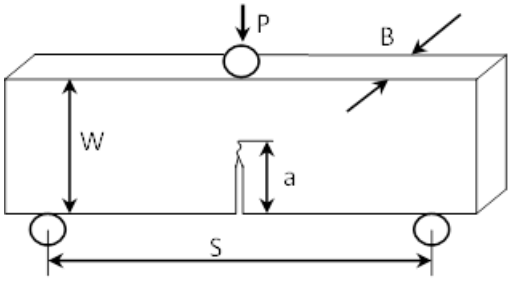

$$K_I = \frac{PS}{BW^{\frac{3}{2}}} \cdot f\left(\frac{a}{W}\right)$$

Figure 2.7 – Three-point bend specimen geometry (SENB)[55]

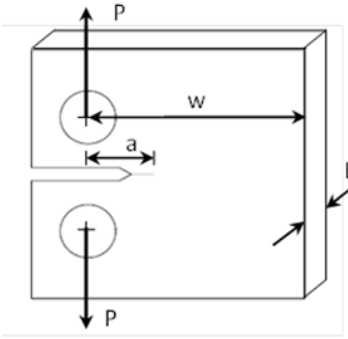

$$K_I = \frac{P}{BW^{\frac{1}{2}}} \cdot f\left(\frac{a}{W}\right)$$

Figure 2.8 – Compact tension specimen (CT)[55]

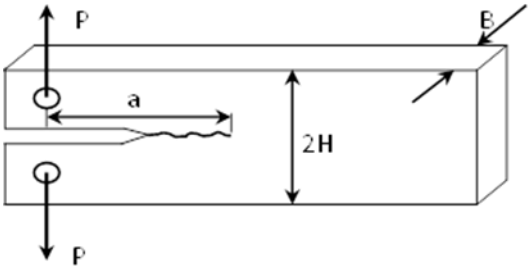

$$K_I = 2\sqrt{3}\frac{Pa}{Bh^{\frac{3}{2}}}$$ Plane stress

$$K_I = \frac{2\sqrt{3}}{\sqrt{(1-\nu^2)}} \cdot \frac{Pa}{Bh^{\frac{3}{2}}}$$ Plane strain

Figure 2.9 – Double cantilever beam specimen (DCB)[55]

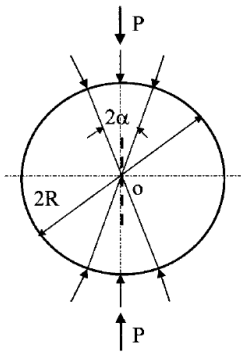

$$K_I = \frac{P\sqrt{\lambda}Y}{t\sqrt{\pi R}}$$

Where P – compressive load, λ = a/R, t - disc thickness
R – disc radius and

$$Y = \frac{1.01227}{\sqrt{1-\lambda}}(1 - 0.60387\lambda + 1.67239\lambda^2 - 1.16988\lambda^3)$$

Figure 2.10 – Centre notched diametral compression specimen otherwise known as centre notched Brazilian disc specimen (CNBDS)[21].

The four test geometries shown provide a reliable means of determination of the fracture toughness of brittle materials. However, in very brittle materials, they do not provide a robust means of controlling the crack growth process after initiation. This is due to the fact that the stress intensity equations all contain the crack length term, *a*, which affects the stress intensity level in the specimen

as the crack propagates. As the crack extends, the energy balance becomes difficult to maintain and complete fracture of the specimens occurs.

A further test geometry, called the chevron notched (CN) compact tension, Figure 2.11, proposed by L.M. Barker in 1977 and standardised in ASTM E1304 [57,58]. The specimen is a modified version of the compact tension specimen where a notch is machined in such a manner as to enable controllable crack growth initiation which proceeds into a region of increasing cross-section with increasing crack length (shaded region between dimensions a_0 and a in Figure 2.11). The controllable crack initiation is achieved by obtaining a region of high stress intensity K_I for a small applied load P. Crack initiation is stabilized by the stress intensity reduction due to the increasing specimen cross-section which accompanies crack extension.

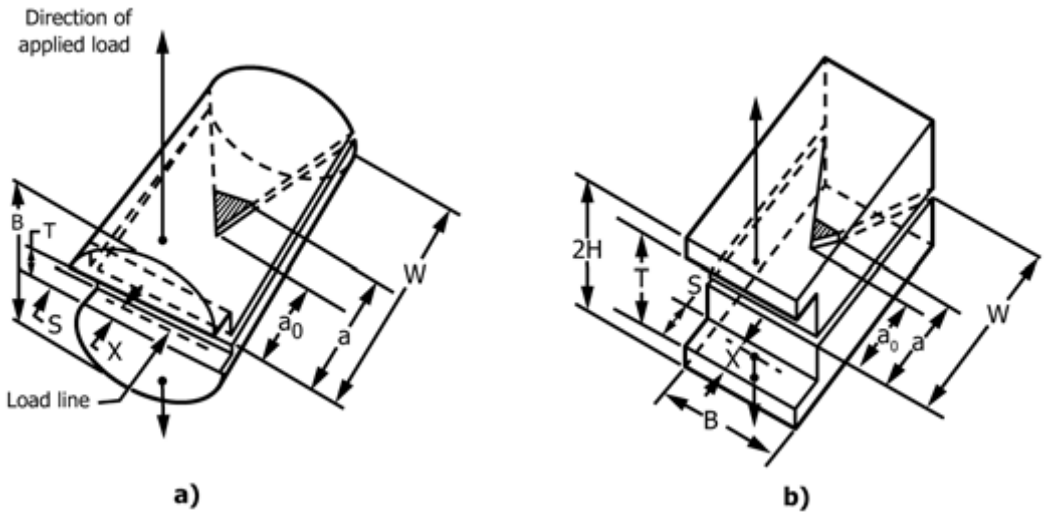

Figure 2.11 – Schematic diagrams of the – a) short rod specimen and b) short bar specimens.

While the specimen overcomes some of the shortcomings of the more standard geometries it also has disadvantages. One of these disadvantages is the fact that these specimens require more complex machining in order to obtain accurate geometry[61]. The second disadvantage is the fact that the crack tip is recessed into the notch of the specimen and is not easily available for observation[57].

The geometries presented are just some of those available in the testing of a wide variety of brittle and quasi-brittle materials. Combined with high quality

industrial testing equipment which enables refined control of test parameters such as load and cross-head displacement, good results can be achieved. However, when custom built, miniature equipment (lacking the characteristic stiffness of the large machines) is considered, the discussed geometries can be difficult to employ successfully, particularly in the study of slow, controlled crack growth. In an attempt to address the shortcomings discussed, a technique named DT is presented in the following section.

2.3 The double torsion technique

The current section provides an overview of the DT geometry and presents the underlying formulation which enables the analysis of the fracture mechanics parameters of a given material employing the technique. While a detailed derivation of the DT principle is provided, the reader is further referred to the literature for any further detail. The phenomenon of the stress intensity level being **independent** of the crack length is highlighted. Finally, research examples employing the technique in the analysis of brittle material properties are provided. The section is concluded with examples of successful fracture process observation where experiments were performed in-situ using various optical and electron imaging systems.

2.3.1 Double torsion geometry and formulation

The DT configuration is now a well-established fracture toughness parameter characterization and measuring technique. Originally proposed by Outwater et. al.[62] and Kies and Clarke [63], the technique has been analysed by a number of researchers such as Fuller and Pletka [64], [65], Evans [28], Trantina [66], Tait et. al. [26] and most recently by Becker et. al. [25] among others. The key feature of this configuration is the fact that the stress intensity K_I is nominally **independent** of the crack length, a for at least the middle one third to half of the specimen length. The loading geometry comprises two joined elastic torsion beams endeavouring to rotate in opposite directions, resulting in a tensile stress field at the upper junction of the un-cracked ligament adjoining the two beams, Figure 2.12. As the crack propagates, the beam system becomes more compliant and stores more strain energy, but the torsional load in the ligament immediately ahead of the crack front remains effectively constant. As a consequence, due to

the torsional load remaining constant, the stress intensity is basically constant with respect to crack length. This is a **unique** feature among different testing techniques and makes the DT system particularly powerful.

The mathematical derivation describing the fundamental principles of the DT technique, which enable the quantification of the energy release rate (as a function of crack extension and not time) is presented below. Considering the two halves of the specimen as torsion bars with polar moments of inertia I_P and shear modulus μ subjected to a torsional moment T (with their width significantly larger than their thickness), Evans [28] described the angle of twist as

$$\theta = \frac{y}{W_m} = \frac{Ta}{I_P \mu} \tag{2.22}$$

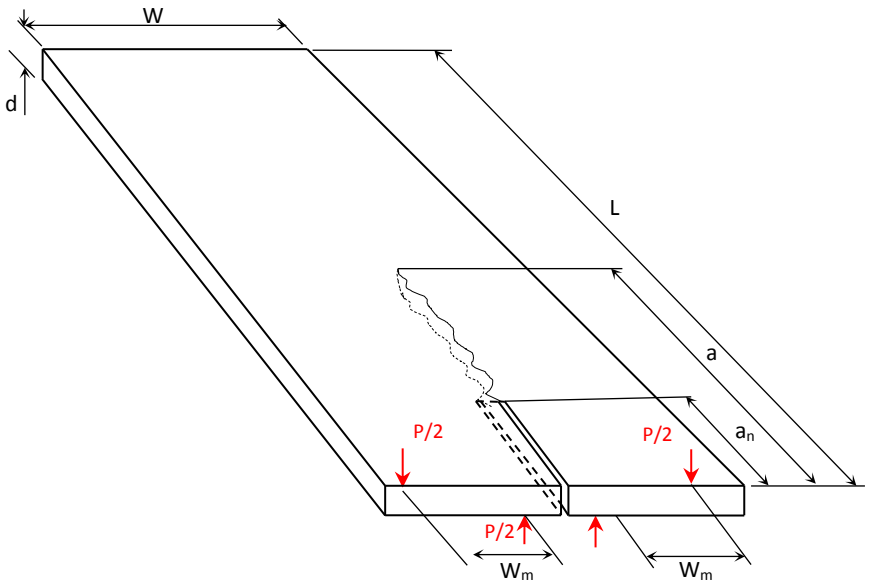

Figure 2.12 – Schematic representation of the DT specimen and the associated loading geometry.

where the torque term on each can be rewritten in terms of the DT loading geometry as

$$T = \frac{P}{2} W_m \tag{2.23}$$

In the analysis of Outwater [62] the polar moment of inertia I_P is given, ignoring terms which approach zero as specimen width significantly exceeds its thickness, as

$$I_P = \frac{W d^3}{6} \tag{2.24}$$

Combining Equations (2.22), (2.23) and (2.24), an expression for the theoretical compliance as a function of crack length (subscript *A* and *E* typically used for analytical and experimental compliance terms respectively) of the double torsion specimen can be rewritten as

$$C_A(a) = \frac{y}{P} \approx \left(\frac{3 W_m^2}{W d^3 \mu} \right) a \tag{2.25}$$

It is worth noting that this relationship is typically linear.

The Mode I SIF for the DT specimen can be calculated by employing the fracture mechanics analysis of the elastic strain energy release rate presented in Section 2.2.4. Employing the energy release rate relationship for a displacement controlled system established in Equation (2.12) and assuming that the crack front shape is independent of crack length for incremental area extension to remain consistent, the strain energy release rate is written as

$$G_P = \frac{P^2}{2} \frac{dC}{dA} = \frac{P^2}{2d} \frac{dC}{da} \tag{2.26}$$

note that the term $dA = d \cdot da$. Differentiating Equation (2.25) with respect to crack length *a* and substituting into Equation (2.26), an expression for strain energy release rate can be written as

$$G_P(a) = \frac{3 P^2 W_m^2}{2 W d^4 \mu} \tag{2.27}$$

Employing the relationship between K_I and G provided in Equation (2.21), the expression for the SIF can be written as

$$K_I(P) = P\sqrt{\frac{3W_m^2}{Wd^4(1-\upsilon)}} \tag{2.28}$$

for the case of plane strain and

$$K_I(P) = P\sqrt{\frac{3W_m^2(1+\nu)}{Wd^4}} \tag{2.29}$$

for the case of plane stress. A commonly employed modification of Equation (2.28) (plane strain) involves the geometrical effects correction, where

$$K_I(P) = PW_m\sqrt{\frac{3}{d^4W(1-\nu)\psi(t,W)}}. \tag{2.30}$$

and $\psi(t,W)$ is the specimen geometry correction factor,

$$\psi(t,W) = 1 - 0.6302\tau + 1.20\tau e^{\frac{-\pi}{\tau}}. \tag{2.31}$$

where $\tau = 2d/W$. The validity of this equation has been experimentally tested and shown to be reliable[67].

At this point it is worth noting the most important property of the DT geometry in the fact that the expression for the stress intensity does not contain a crack length term *a.* Williams and Evans verified the expression experimentally, obtaining good agreement except for small discrepancies near the start and end of the crack path within the specimen [28]. This leads to two very important properties of this technique. Firstly, one does not need to know the exact crack length in order to extract the stress intensity parameter for the material (this aspect of the DT technique is discussed in further detail in Section 2.3.2). This is especially useful in materials where crack tip position observation is difficult or impossible. Examples would be opaque materials, materials with rough surface texture as well as very stiff and brittle materials which exhibit very little crack opening displacement. The second advantage afforded by the crack length independence is the ability to propagate cracks controllably in brittle materials.

Such increased control over the crack extension process is the result of the fact that crack extension does not alter the loading geometry such as would be the case in a compact tension specimen for example.

Finally, in small specimen configurations the applied loads required to generate crack initiation and propagation are of low magnitude meaning that compact equipment can be designed. This, in contrast with commonly employed laboratory fatigue machines, provides another key advantage as a compact double torsion test rig provides flexibility when interfacing the test rig with microscopic and other auxiliary observation as well as the data capture systems.

2.3.2 **Crack length independence**

It has been highlighted that one of the most useful characteristics of the double torsion technique is the independence of the stress intensity from crack length. However, caution must be exercised when applying this assumption experimentally. Many researchers have shown that the crack independence assumption does not hold for the first and last quarter of the specimen length[61,65,66]. Fuller and Pletka [65] performed a comprehensive experimental analysis of this observation obtaining the results of stress intensity versus crack length depicted in Figure 2.13. The plotted data implies the validity limit for stable stress intensity lies between $0.18<a/L<0.78$. A similar limit was obtained independently by Trantina [66], who performed an elastic finite element analysis of a specimen with a length-to-width ratio of $L/W = 3$.

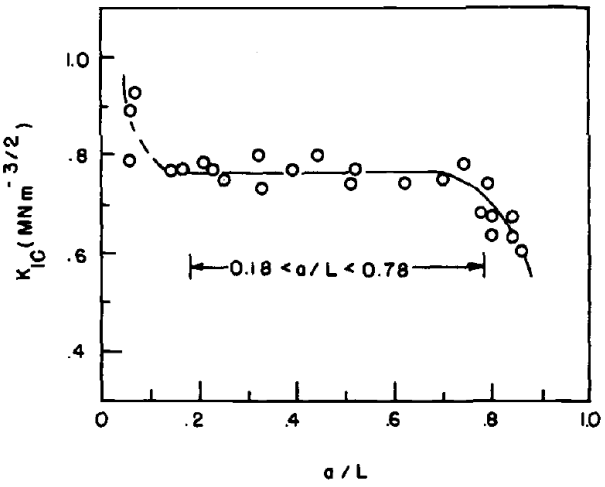

Figure 2.13 – Plot depicting the critical stress intensity, K_{IC}, as a function of the crack length normalised by the specimen length[65].

A similar analysis was undertaken by Shetty and Virkar [69], who investigated the same phenomenon but in specimens with length-to-width ratio of *L/W = 2.* Their results revealed a more restrictive condition for constant stress intensity in the range of *0.275L<a<0.675L*. Based on these results it was observed that the specimen with a higher length-to-width ratio had a larger region where the crack independence condition held [69].

2.3.3 **Specimen thickness effects**

With regard to standard fracture mechanics geometries, there exists a concept of valid thickness. The valid thickness parameter determines the minimum thickness the specimen should possess in order to obtain the fracture toughness property of the material in the plane strain failure mode. Increased deformation and plasticity associated with the plane stress mode tend to result in elevated fracture toughness results which can lead to non-conservative material fracture toughness properties. The expression for valid thickness is written as,

$$B \geq 2.5\left(\frac{K_{IC}}{\sigma_y}\right)^2 \tag{2.32}$$

where B is minimum specimen thickness required, K_{IC} is the material critical stress intensity (fracture toughness) and σ_y is the material yield strength. The concept is represented graphically in Figure 2.14.

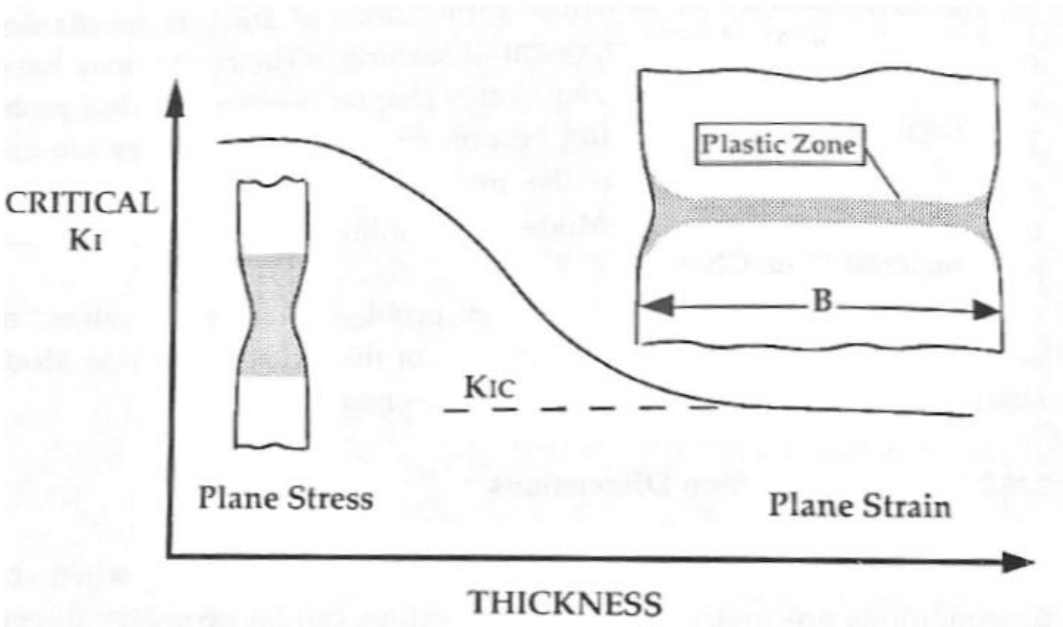

Figure 2.14 – Graphical representation of the valid thickness concept.

It has been shown by a number of researchers, and indeed by those who have proposed the double torsion technique, that the valid thickness condition as expressed in Equation (2.32) is overly restrictive when brittle materials are studied[25,52,62]. Outwater et. al. have performed extensive testing in samples of 2124-T851 aluminium, where plasticity would be expected to be higher than in glasses and ceramics, yet achieved good agreement between the results obtained by double torsion and double cantilever beam techniques[62]. Therefore, given the brittle nature of PCD, the valid thickness requirement is readily met. However, satisfying the requirement set out by Equation (2.32) ensures that the experimental data obtained is accurate and consistent with plane strain and provides an appropriate measure of conservatism.

2.3.4 **Crack path effects**

One of the underlying assumptions in the development of the double torsion technique is the fact that the specimen consists of two equal, elastic beams in torsion[59,60]. In practice this is not always the case as the crack can deviate from the ideal centreline path due to effects of misalignment as well as specimen microstructure[25,67]. The deviation of the crack from the centreline

results in the reduction of the stress intensity level required for continued crack extension, because the lever arm loading changes.

Salem et. al studied the effect of crack misalignment on the effective stress intensity level for propagation and plotted a diagram highlighting the effect of crack deviation from centre line, Figure 2.15. (Note that the y-axis scale is enhanced and is remote from zero, depicting an exaggerated effect the misalignment introduces).

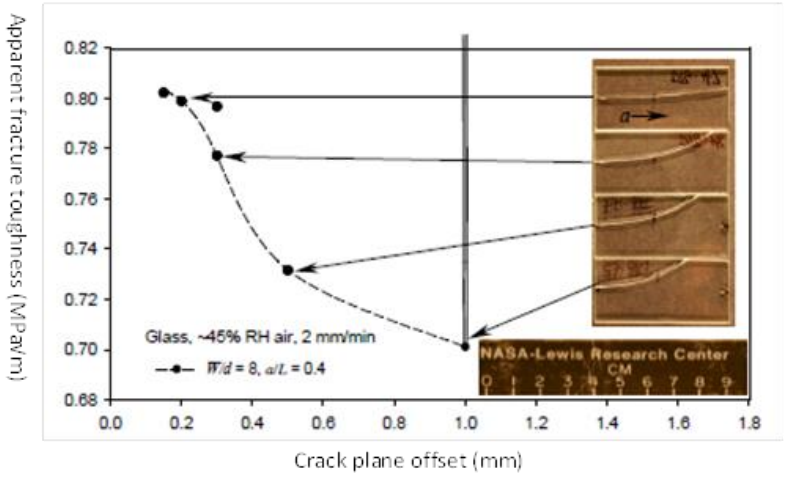

Figure 2.15 – Plot depicting the effect of the crack plane misalignment on the apparent critical stress intensity level obtained.

Becker et. al. have also evaluated these effects employing both finite element methods and experimental techniques[25]. The analyses revealed that the effects of the crack path deviation from the centreline can be considered negligible if such deviation does not exceed the value of *W/8*[57].

2.3.5 In-situ microscope studies employing double torsion

The double torsion loading geometry provides an opportunity to design equipment which can be used in a manner which facilitates the study of the fracture process “in-situ” microscopes or other observation methods. This is in part due to the fact that the specimen geometry is quite simple and the loading points only obscure the initiation region of the specimen, before the notch, which enables the observation of the full crack path. It is worth noting that most

researchers, who employed standard tensile machine type equipment for load actuation, developed rigs which resulted in the tensile face being on the bottom of the specimen. While it does not affect the test procedure as the technique is nominally crack length independent, the tensile face fracture process cannot be readily observed. Consequently most “in-situ” DT loading rigs designed for simultaneous propagating crack observation have the tensile surface on the upper face of the DT specimen as highlighted by the researchers whose work is presented below.

These researchers such as Tait [71], Vekinis [72], Rosie [73], [74] and most recently Becker [57] among others, realised the importance of not only extracting the fracture properties and crack growth velocities for the material in question, but also studying the fracture mechanism phenomena by observing the tensile face in the region of the crack tip. Such observation enables the researcher to study the fracture process in-situ by employing techniques such as optical microscopy, scanning electron microscopy (SEM), electronic speckle pattern interferometry (ESPI) and digital image correlation (DIC).

The miniature rigs employed for the in-situ SEM studies by Tait [71] and Rosie [74] are shown in Figure 2.16. In both instances the top face of the specimen is the tensile face. Tait was able to observe the cracking mechanisms in cement mortar and pure hardened cement paste, identifying mechanisms such as crack branching, crack discontinuities and micro-cracking process zone surrounding the main crack. The micrographs depicting these features are depicted in Figure 2.17 and Figure 2.18. Similar observations were made by Rosie [74] when observing the fracture process in nuclear grade graphite in “in-situ” SEM studies. An example of crack path discontinuity followed by local closure is presented in Figure 2.19. Such observations provide the information necessary to understand the various toughening mechanisms in a material. Once understood, these can provide a way to develop a tougher material by introducing more of such toughening features.

In his investigation of the fracture processes in nuclear graphite Becker [57] employed ESPI techniques to observe the fracture process in a custom built rig which was fitted to a standard tensile testing machine, Figure 2.20. The results of such experiments are shown in Figure 2.21 where secondary microcracking is evident. Further to the ESPI approach, DIC was employed to characterise the fracture process, Figure 2.22. The results were consistent with those of ESPI, providing evidence of a secondary microcracking as well as revealing that the

secondary microcracks did not completely shut down in the wake of the main propagating crack.

As shown in this section, the DT methodology is well suited to slow, controllable crack propagation studies in brittle materials. The crack length independence is a powerful feature of this technique which enables testing of additional parameters once the main crack is in the constant stress intensity crack length region. The geometry of the test further enables relatively easy observation of the fracture process, which makes the technique particularly useful in applications where one seeks additional techniques to interpret and/or quantify the fracture process. Techniques such as ESPI and DIC have been shown to be useful in this regard. The following section provides the background information relating to the DIC technique as it forms a part of the experimental approach employed in this project.

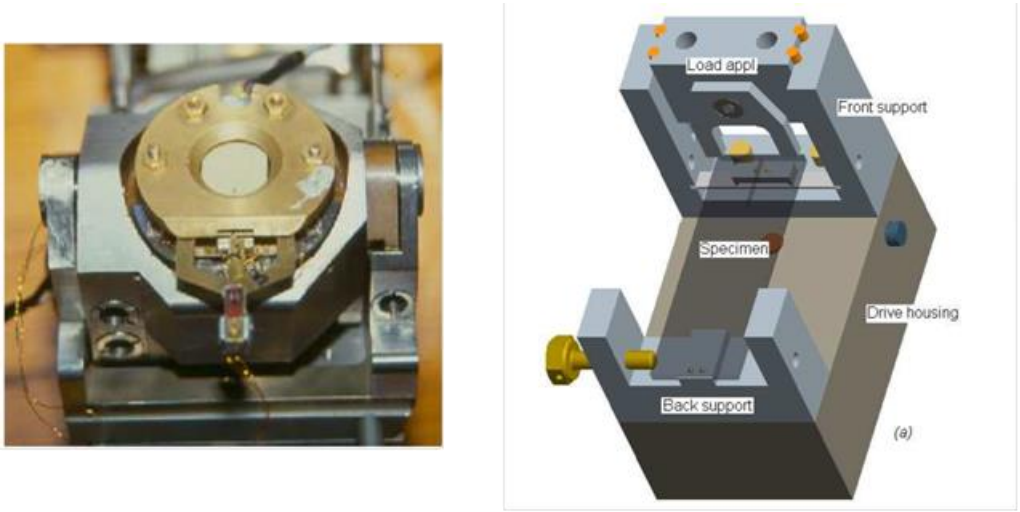

Figure 2.16 – Examples of purpose built equipment for in-situ SEM double torsion studies which are locatable in the specimen chamber of an SEM and used for fracture testing in cement mortar, polymethyl methacrylate (PMMA) and nuclear graphite – (a) Tait and Garrett [71], (b) Tait and Rosie [74].

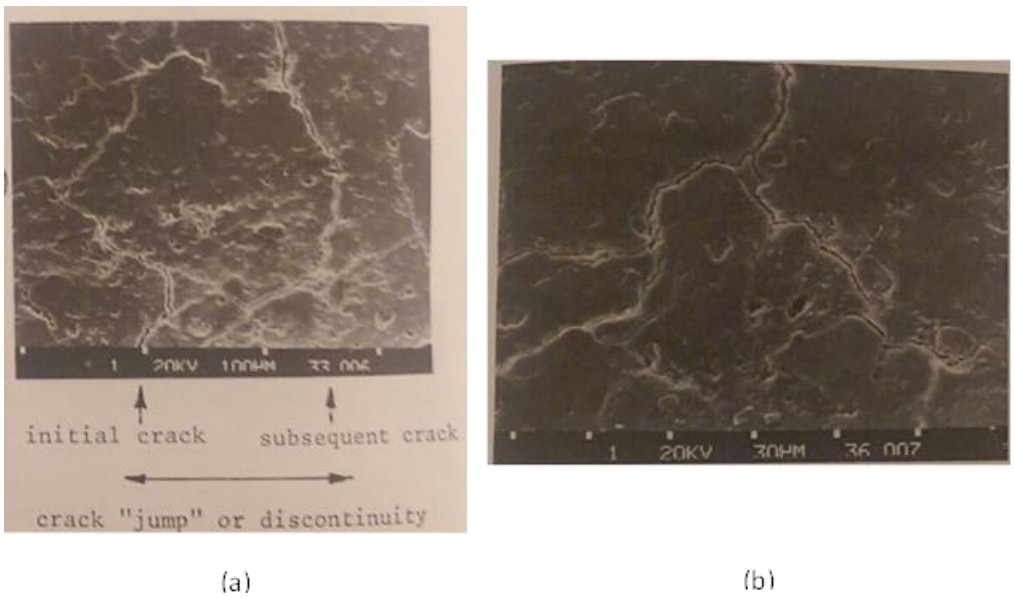

Figure 2.17 - Micrographs reproduced from Tait [71] depicting crack paths in concrete double torsion specimens which were controllably fractured in-situ in the SEM. (a) Highlights a crack path which had shut down due to a discontinuous "crack jump" and (b) depicts an example of crack branching.

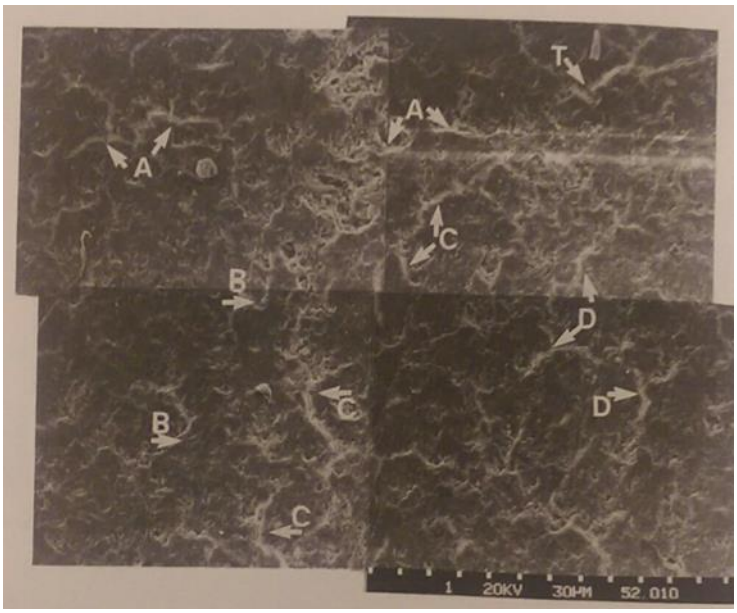

Figure 2.18 – Micrograph reproduced from Tait [71] depicting crack paths in concrete double torsion specimens which were controllably fractured in-situ in the SEM. The main crack propagated from the top right (T-tip). Significant "process zone" microcracking was observed preceding the crack as highlighted by letters A-D.

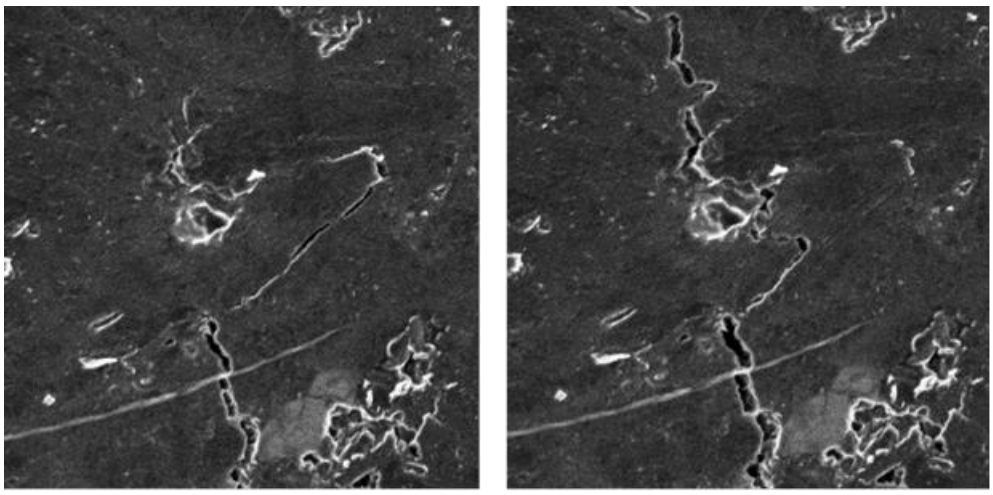

(a) (b)

Figure 2.19 – Micrographs reproduced from Rosie [74] depicting a crack propagating (bottom to top) in a miniature DT specimen of nuclear graphite. The initial crack path which initiates a particle pull out (a) is changed as the crack develops, causing the particle to fracture (b) as the new path becomes preferential in terms of energy required.

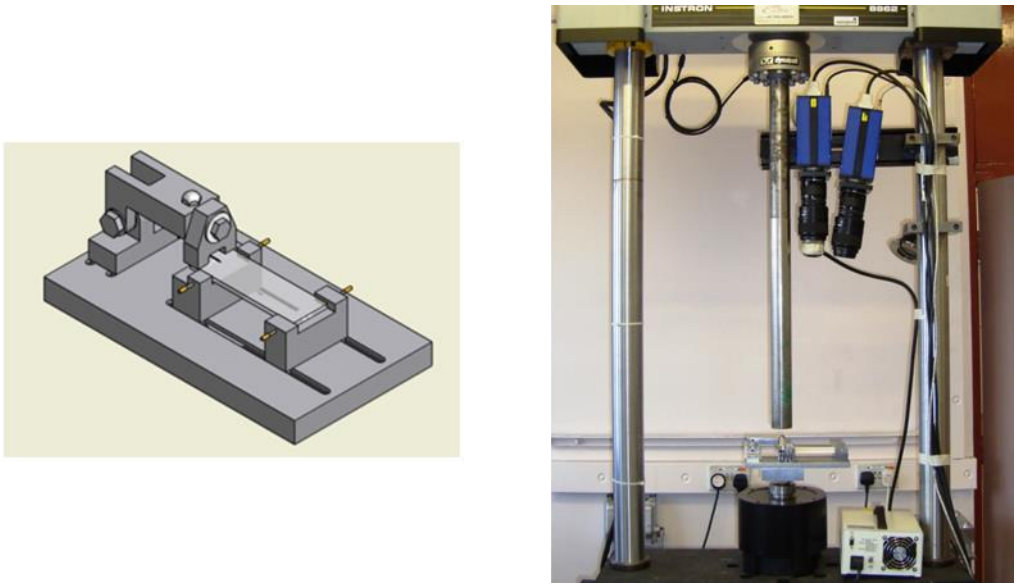

Figure 2.20 – Test rig employed by Becker et. al. for in-situ DIC investigation into the fracture mechanisms in nuclear graphite [57].

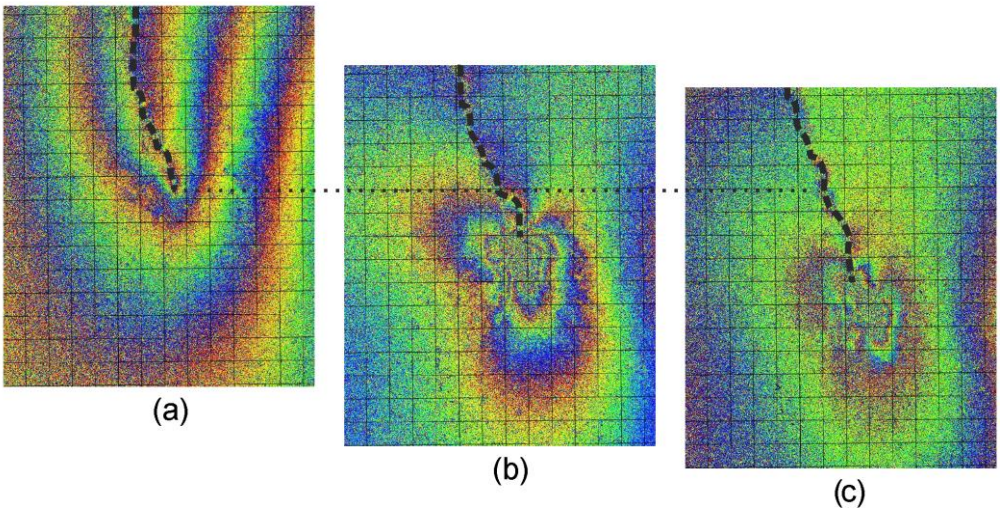

Figure 2.21 – Images depicting the results capturing the fracture process zone by ESPI techniques, Becker [57]. The three images depicting three stages of crack propagation associated with three discrete events being (a) crack arrest at a pore, (b) crack branching and (c) crack bridging. The general size of the ESPI fringes provides an indication of the fracture process zone (FPZ) around the crack tip.

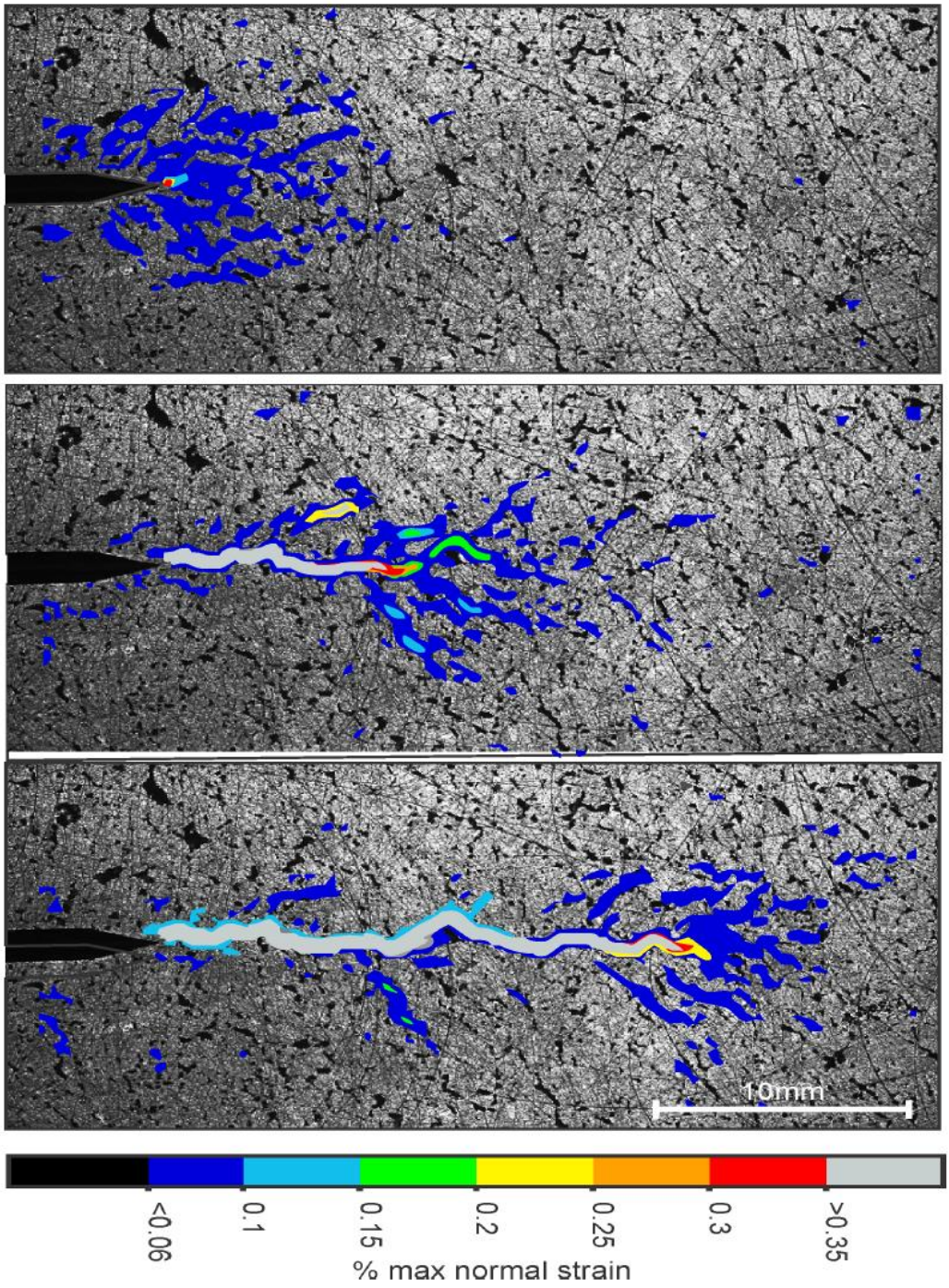

Figure 2.22 – Maximum normal strain mapping during crack propagation in nuclear graphite, employing DIC, reproduced from Becker [57]. The strain level of 0.35% was considered as the threshold for the formation of a microcrack. As can be seen, significant microcracking occurs ahead of the crack tip but partially closes up with passage of crack tip strain field. Some of the damage is permanent as microcrack closure in the crack wake is incomplete.

2.4 Digital image correlation

2.4.1 Introduction

Digital Image Correlation (DIC) is a technique which enables extraction of the full field surface deformation from digital images of the specimen surface undergoing deformation [72,73]. In its simplest form DIC can be described as comparison of images taken before the deformation of the specimen to those taken during or after the loading process. In order to achieve this matching of the similar images before and after loading (and cracking), a speckle pattern has to be applied to the surface of the specimen to be tested. The images can be captured by a single camera, 2D-DIC or by two cameras simultaneously which results in a stereovision approach enabling 3D-DIC and hence characterisation of the out-of-plane motion of the sample [77]. While 3D-DIC is an obviously desirable configuration, it is not always practical or possible to apply, and 2D-DIC can be employed. However, when employing the 2D-DIC approach, the out of plane displacements cannot be accounted for by the system. If the observed specimen surface moves away from the initial imaging plane, the specimen will appear to have undergone bulk shrinkage. An opposite effect occurs when the specimen moves towards the imaging apparatus. Such out-of-plane motion can be accounted for when the displacements are known but can affect the accuracy of the results obtained if the surface deformation occurs with parts of the surface moving by unknown amounts. However, when expected out-of-plane displacements are negligible, good results can be obtained. Examples of applications where only 2D observation of the deformation process is possible are optical or scanning electron microscopy, where a single image is formed.

The following section provides an overview of the theory underlying the digital image correlation technique and presents the novel approach to J-integral extraction from optical deformation measurements.

2.4.2 Background theory

As discussed in the introduction, DIC is a technique by which displacements and displacement gradients can be determined by comparing digitally acquired images. The 12-bit image typically employed in DIC analyses is comprised of pixels with varying levels of grey intensity (12-bit greyscale image has intensity range of 0-4096, with 0 = Black and 4096 = White). Simply, DIC is the process of comparing subsets of intensity values, to obtain subset matching. Therefore every image is subdivided into a mesh of individual subsets, Figure 2.23.

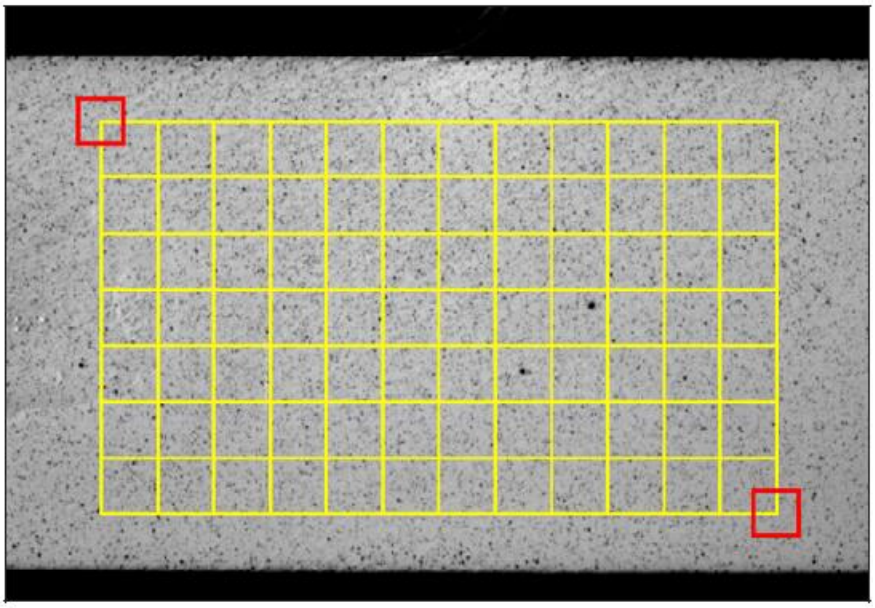

Figure 2.23 – A figure depicting an example of a region of interest which has been meshed into small subsets (the blocks of the yellow grid)

The subset size is selected in such a manner as to have a sufficient number of unique speckle features and is typically described as having the size of *(2M+1)x(2M+1)* pixels, centred around a point $P(x_0,y_0)$. When the specimen, and hence the speckle pattern, is deformed, the individual subset deformations are typically small and the vector displacement leading to the new subset position can be determined for the small subset. An example of small subset displacement with some deformation is depicted in Figure 2.24.

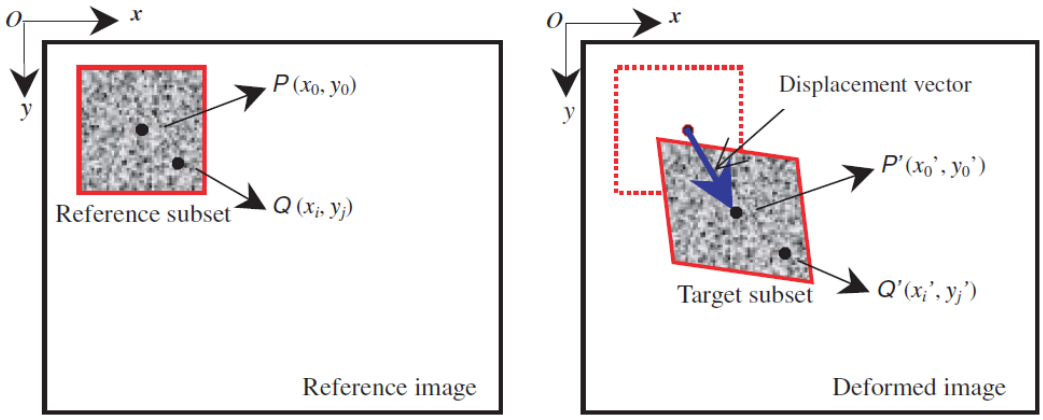

Figure 2.24 – An illustration of a reference image subset (left) and a deformed image subset (right) where some displacement and deformation of the subset has occurred.

In order to determine the position of the subset after deformation and also map any deformations which the subset may have undergone, shape functions are employed. Referring to Figure 2.24, the new positions of the point $Q(x_i,y_j)$ can be determined by using the polynomial shape functions. In this example a first order polynomial is employed to describe the new positions of

$$x_i' = x_0 + u + u_x\Delta x + u_y\Delta y \tag{2.33}$$

$$y_i' = y_0 + v + v_x\Delta x + v_y\Delta y \tag{2.34}$$

in the above equations, the $(i,j = -M:M)$, u and v are the x and y displacement components of the subset centre point $P(x_0,y_0)$, $\Delta x = x_o - x_i$, $\Delta y = y_0 - y_i$ and u_x, u_y, v_x *and* v_y are the first order displacement gradients of the reference subset.

The zero normalized sum of square differences (ZNSSD) correlation approach, described by the equation below, is employed

$$C_{ZNSSD} = \sum_{i=-M}^{M}\sum_{j=-M}^{M}\left[\frac{f(x_i,y_j) - f_m}{\Delta f} - \frac{g(x_i',y_j') - g_m}{\Delta g}\right] \tag{2.35}$$

where

$$f_m = \frac{1}{(2M+1)^2} \sum_{i=-M}^{M} \sum_{j=-M}^{M} f(x_i, y_j) \tag{2.36}$$

$$g_m = \frac{1}{(2M+1)^2} \sum_{i=-M}^{M} \sum_{j=-M}^{M} g(x_i', y_j') \tag{2.37}$$

and

$$\Delta f = \sqrt{\sum_{i=-M}^{M} \sum_{j=-M}^{M} [f(x_i, y_j) - f_m]^2} \tag{2.38}$$

$$\Delta g = \sqrt{\sum_{i=-M}^{M} \sum_{j=-M}^{M} [g(x_i', y_j') - g_m]^2} \tag{2.39}$$

Where *g* and *f* are deformed and undeformed images respectively.

The displacements of all points within the subset can be determined. It is worth noting that while a two dimensional example was employed to illustrate the basic principle of subset mapping, the ZNSSD correlation algorithm is especially useful in 3D systems as it is able to compensate for the differences in lighting intensity which often result from using two cameras which capture two slightly different lighting intensities[74,75].

Having obtained all the displacement vectors for all subsets, a vector map of the displacement field can be obtained as depicted in Figure 2.25. The full field displacement data can be processed to further extract information such as surface strain components and much more.

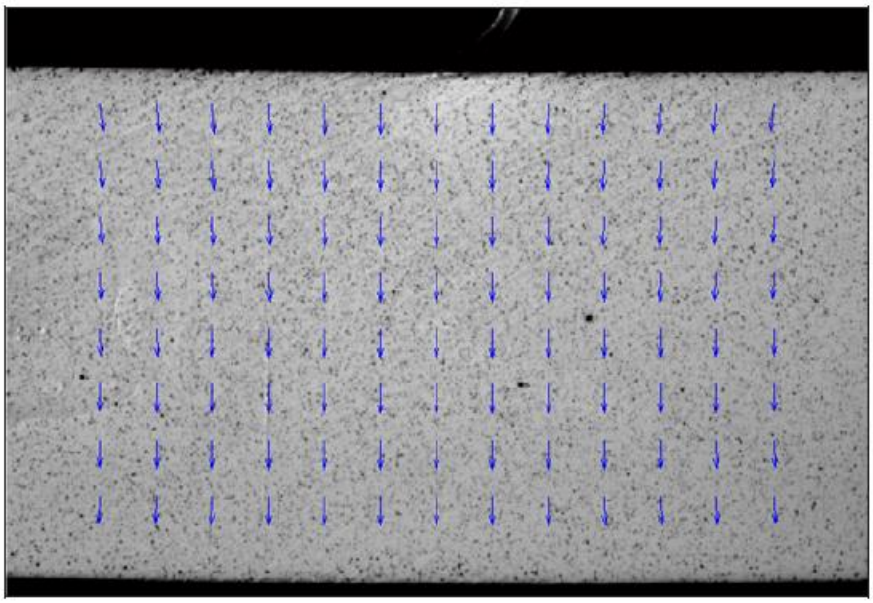

Figure 2.25 – An illustration of the displacement field obtained from calculating the displacements of each individual subset.

2.4.3 Speckle pattern analysis and accuracy estimates

As mentioned earlier, DIC requires a method to discriminate between pixels of random level of grey value intensity. Because the intensity property of a pixel is not a unique value in the context of a full image, neighbouring values have to be taken into consideration in order to develop unique signature regions known as subsets. The average displacement of pixels in such a subset can then be attributed to the centre of the subset to infer displacement/deformation in the global image. During the analysis, the subset window is stepped along the x and y coordinates of the global image by a user defined amount of pixels, typically overlapping the subsets to obtain a higher number of unique signature regions. Subset uniqueness can only be achieved if the speckle pattern features within it are non-repetitive, isotropic and have sufficient contrast[76,77]. For this reason, random speckle spray patterns are essential in digital image correlation experiments.

A further consideration in speckle pattern and subset size selection is related to the relative size of the speckle features to the chosen subset size. In order to achieve good accuracy, a sufficient number of discrete features have to exist within a chosen subset to determine accurately the average displacement and deformation Figure 2.26. This phenomenon has been studied by Lecompte et.

al.[81] with the results revealing, as may well be expected, the strong dependence of subset size and speckle size influence on accuracy of digital image correlation solution for displacements, Figure 2.27 and Figure 2.28, [81]. As shown in the figures, the speckle pattern plays an important role when the scale of the test specimen is considered. DIC is a scale independent technique, meaning that the field of view can be fitted to the region of interest in order to maximise the use of the camera sensor resolution potential. However, with that, the speckle pattern must also be refined in order to retain sufficient unique features within the decreasing subset size.

Therefore in order to obtain good levels of correlation, the speckle pattern and subset sizes have to be carefully optimised in such a way as to extract the maximum information about the surface deformation. The tools available to perform the evaluation of the speckle pattern quality as well as the subset selection process are discussed in more detail in Chapter 4.

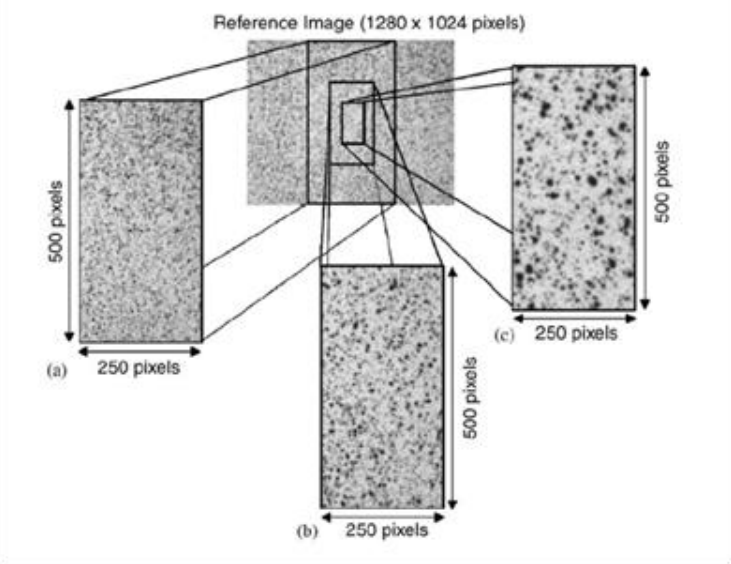

Figure 2.26 - Pictured are three levels of speckle sizing, generated by selecting various digress of magnification of the same physical pattern, scaling over equivalent pixel domain. These three levels of speckle size were compared to study the influence of speckle size on homogeneous and heterogeneous strain fields. Results depicted in Figure 2.27 and Figure 2.28.

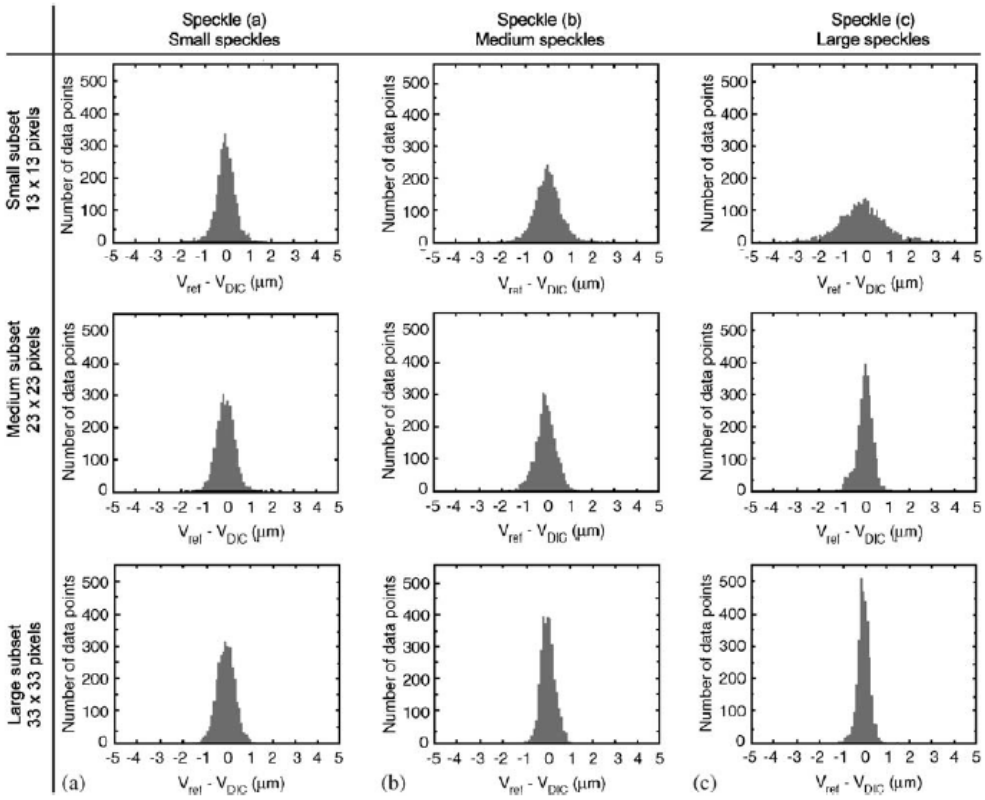

Figure 2.27 - Plot collage depicting the relative influence of speckle size (horizontal axis) and subset size (vertical axis), on the accuracy of DIC identification of a theoretically imposed uniaxial strain. It is evident that in general small speckle and larger subsets are useful for increased accuracy. The plot further highlights that in general, larger subsets improve global accuracy but would lose local resolution [81].

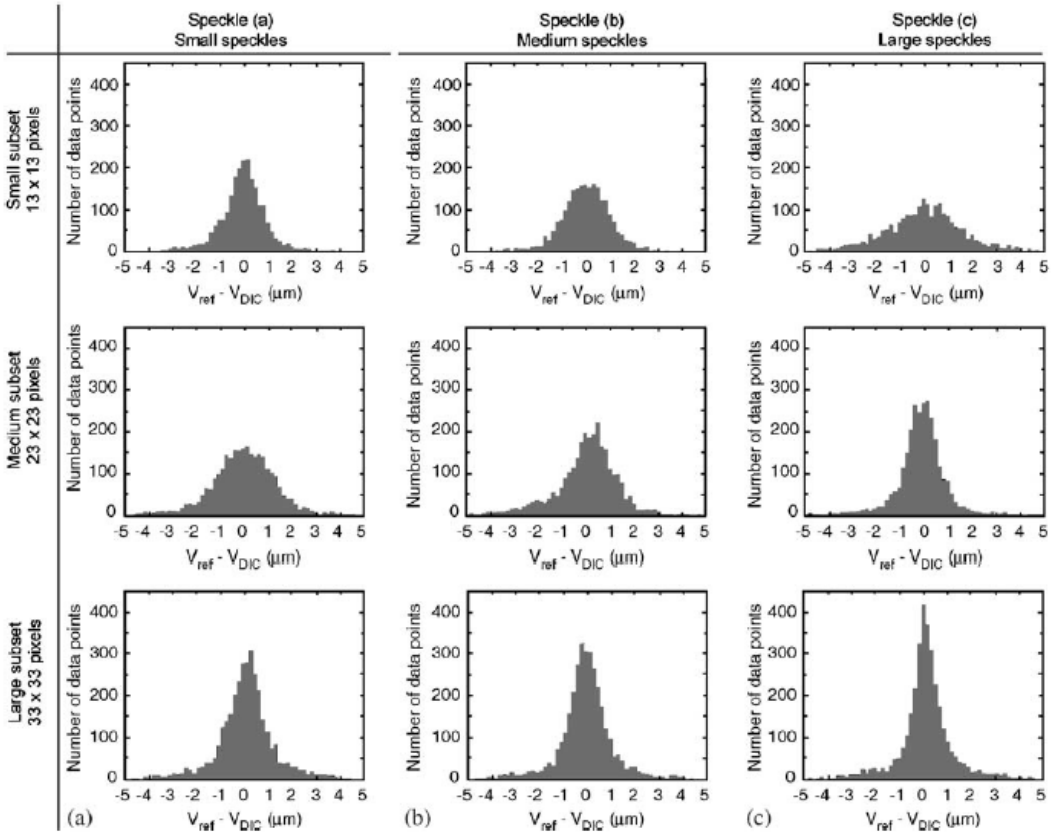

Figure 2.28 - Plot collage depicting the relative influence of speckle size (horizontal axis) and subset size (vertical axis), on the accuracy of DIC identification of a theoretically imposed heterogeneous strain. It is evident how complex strain fields require good speckle patterns[81].

2.4.4 **Extracting material properties from DIC**

Employing the full field displacement data provided by the DIC technique, Becker proposed that this vector field can be discretised into a finite element domain [55,79]. That is, the known displacements of a given subset are imposed onto the nodal displacements of a finite element mesh of matching parameters. Thus, each element is assigned an experimentally measured displacement at the boundary condition. The elastic stresses and strains can then be extrapolated at the integration points for each element following the conventional elastic finite element procedure. Plane stress conditions are employed in the analysis as digital image correlation derived deformations are representative of the specimen surface behaviour.

The classic finite element boundary problem applies where the displacement field u in conventional Cartesian coordinates (x1,x2) of a body is related to the applied force F by the body stiffness matrix S:

$$\{F\} = [S]\{u\} \tag{2.40}$$

To calculate the J-integral from the displacement field, elastic strain and stresses at each integration point are calculated (employing the displacement field obtained from DIC data). The strain matrix at every coordinate is given by

$$\{\varepsilon\} = [B]\{u\} \tag{2.41}$$

where B is the strain-displacement matrix formed by the differentiation of the interpolate shape functions and mapping from the local domain to the global domain. Similarly, the stress matrix is calculated by

$$\{\sigma\} = [D]\{\varepsilon\} \tag{2.42}$$

where, D defines the stress-strain relations according to Hooke's law for the linear elastic materials. Rice introduced the J-integral as a path independent contour integral that quantified the rate of change in potential energy, with respect to crack length, within a region of material that contained a singularity [47]. The standard formulation of the J-integral, neglecting the kinetic energy and body forces, for a crack lying in x1 axis is

$$J = \int_{\Gamma} \left(\bar{W} n_1 - \sigma_{ij} n_i \frac{\partial u_i}{\partial x_1} \right) ds \tag{2.43}$$

where, Γ is an arbitrary contour path around the crack tip, n is the unit normal vector to the contour at an arc increment ds, u is the displacement field and W is the strain energy density represented as

$$\bar{W} = \int_0^{\varepsilon_{ij}} \sigma_{ij} d\varepsilon_{ij} \tag{2.44}$$

For an elastic field the relationship between J-integral and the stress intensity factor, assuming pure Mode I loading, can be expressed employing Equation (2.21).

Because line integration is not accurate and is mathematically complex, Li, Shih and Needleman[77], introduced an equivalent expression in terms of the volume integral using the divergence theorem. This volume integral can be converted into an area integral for two dimensional problems and a crack lying in x1

$$J = \int_{A1} \left(\sigma_{ij} \frac{\partial u_i}{\partial x_1} - \bar{W} \delta_{1j} \right) \frac{\partial q_1}{\partial x_j} dA \tag{2.45}$$

where A is an area surrounded by two arbitrary contours encompassing the crack tip, *q* is a smooth function that ranges from *0* on the outer contour to *1* on the inner contour and δ is the Kronecker delta. The formulation of the J-integral can be evaluated in the finite element model by dividing the area A into rings of elements

$$J = \sum_{\text{elements in } A_1} \sum_{p=1}^{GP} \left[\left(\sigma_{ij} \frac{\partial u_i}{\partial x_1} - \bar{W} \delta_{ij} \right) \frac{\partial q_1}{\partial x_j} \det \left(\frac{\partial x_k}{\partial \eta_k} \right) \right]_p \omega_p \tag{2.46}$$

where *p* denotes the integration points (depending on element selection), η is the local coordinate, ω_p is the weight associated with each Gaussian integration point *p* for the total number of integration points per element (GP). If the displacements of a matrix of point around a crack are known along with the material properties, the J-integral can be calculated. Based on the theory presented, a MATLAB code has been developed which, when a displacement field of known points as a function of load and material properties such as Young's modulus and Poison's ratio are known, allows the computation of the J-integral – the energy required for crack propagation[57].

The described technique can be a very powerful tool in extracting material properties. In multiple situations it is not possible to measure the deformation behaviour of the material by techniques such as strain gauging or those similar to it. Of particular interest is the ability to characterise material behaviour on microscopic level. Where optical or scanning electron imaging is employed to obtain images of very small regions, the material properties of these regions can be extracted.

2.5 Electron backscatter diffraction (EBSD)

2.5.1 Introduction to EBSD

EBSD is a useful tool in the characterisation of the grain structure, orientation, size distribution and grain boundary properties of polycrystalline materials [83]. The general system components as well as sample orientation during a typical EBSD mapping experiment are shown in Figure 2.29. The sample is almost always orientated at 70 degrees to the mounting stage which results in a beam impingement angle of 20 degrees. The electron beam strikes the specimen resulting in a range of electrons which scatter out of the interaction volume where crystallographic planes result in the diffraction of the electron paths. A phosphor screen is placed at a distance of approximately 25 mm from the sample being mapped and receives the scattered electrons. The electrons result in luminescence of the phosphor screen and this luminescence is captured by the CCD detector placed behind the phosphor screen. The luminescence patterns created by the scattered electrons are called Kikuchi bands, Figure 2.30, and it is these bands that provide the crystallographic orientation of grains in the specimen. In order to determine the grain orientation, the system is provided with information about the expected phases which will be encountered and it then compares the obtained Kikuchi patterns to the ideal patterns of the known crystal structure.

Modern automated EBSD mapping systems can operate at high speeds up to 100 samples per second, generating information maps about the grain size, crystallographic orientation and even state of strain of the specimen surface.

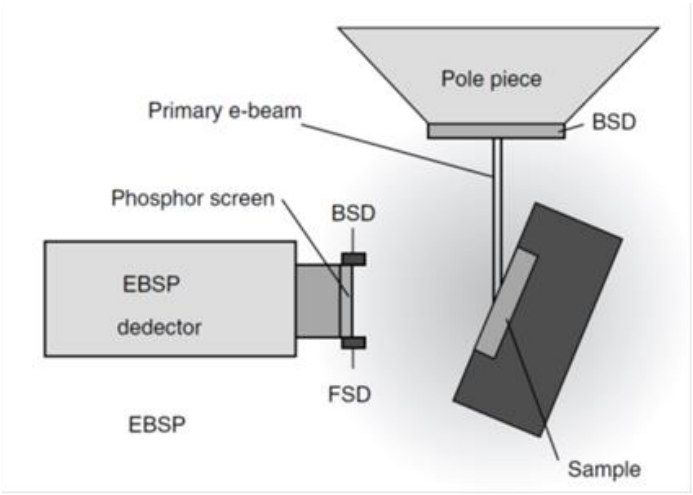

Figure 2.29 - Schematic depicting a typical sample orientation and the general system components associated with EBSD mapping [83].

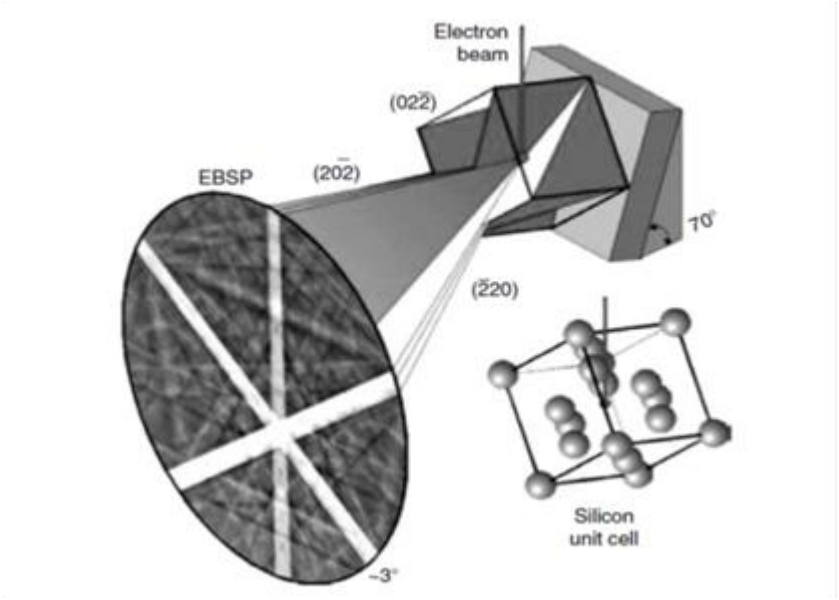

Figure 2.30 - Schematic depicting the electron beam interaction with the crystallographic plane of the sample and the resulting Kikuchi bands forming due to the scattered electron luminescence of the phosphor screen [83].

2.5.2 The unit cell and Miller indices

In order to employ the EBSD technique to characterise the crystallographic orientation of individual grains in a polycrystalline material, Miller indices are employed. In order to illustrate the principle a simple cubic unit cell is depicted in Figure 2.31. A unit cell is the smallest group of atoms which possesses the overall symmetry of the larger crystal [84]. The entire crystal lattice can then be built up by repeating the unit cell in three dimensions. It can be thought of as a small building block. When a number of these identical blocks are used, a structure can be created. In order to describe a crystallographic plane, the following convention is used to generate the indices. The coordinates at which the plane intercepts the axis are recorded. Reciprocals of these coordinates are calculated. The fractions are then simplified by employing a common multiplier in order to obtain the same ratio but in an integer form [80,81].

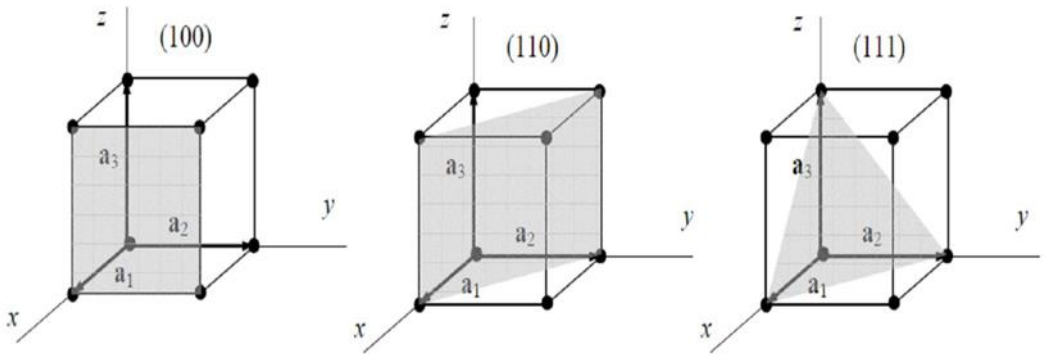

Figure 2.31 – An illustration of a simple square unit cell of atoms with superimposed examples of the Miller indices describing the shaded planes[84].

When an EBSD scan is performed, information is obtained about the orientation of the grain in terms of its rotation with respect to the three principal axes otherwise referred to as the Euler angles of the crystal. However, such description is almost impossible to visualise and, to aid visual interpretation of the data, a colour can be assigned to the key crystallographic planes. Such graphical approaches are much easier to interpret as highlighted by the example in Figure 2.32.

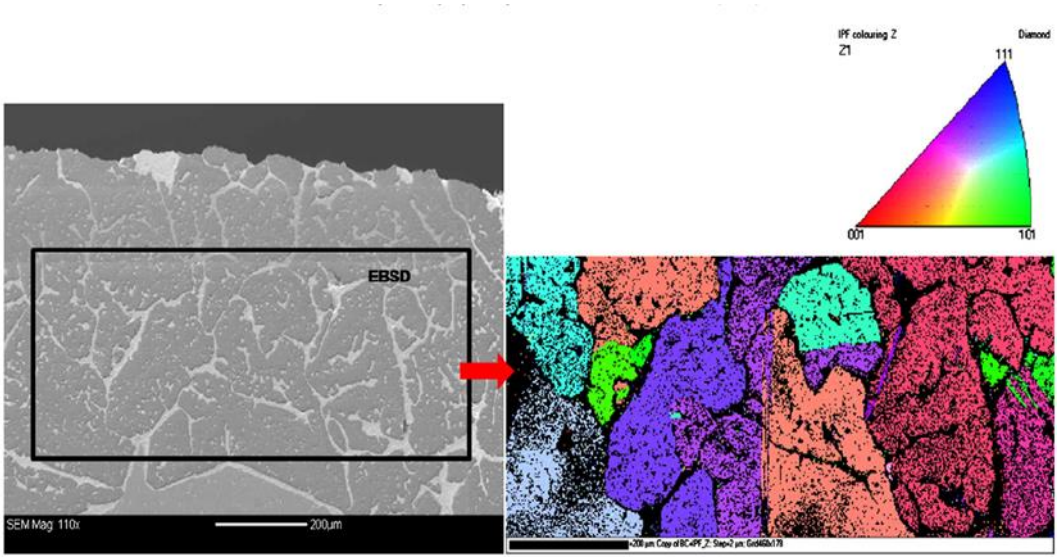

Figure 2.32 – An example of an EBSD scan of a region of abnormal diamond crystal growth where the inverse pole figure visualisation approached is employed to differentiate the orientation of different crystals [86].

2.5.3 EBSD analysis of polycrystalline diamond (PCD)

Polycrystalline diamond compacts produced by sintering of randomly orientated starter powders are considered to be isotropic at the macroscopic level [7,20]. However, at a microscopic level, the orientation of a single anisotropic crystal can have a localised effect on the behaviour of the material. Therefore, knowing the crystallographic orientation can help explain the localised behaviour of the material.

EBSD investigations of the crystallographic plane orientation effect on the wear performance of PCD have been studied by El-Dasher et. al. and have revealed a clear difference in the resistance of the (111) crystallographic plane to abrasive wear compared to all other orientations [87]. McKie et. al [86] and Shin et. al. [84,85] have studied the abnormal grain growth effect (AGG) in the HPHT sintered fine grain PCD grades by employing EBSD techniques in order to investigate the effect of the high and low grain boundary angles on the abnormal growth of large crystals from fine grained starter powders. Further, EBSD techniques have been used to map the orientation and study its effects in the etching resistance of polished polycrystalline diamond films [90].

When investigating the grain orientation of cobalt catalysed HPHT sintered diamond compact, EBSD mapping is often not sufficient as the cobalt phase has the same face centred cubic (FCC) structure as that of diamond [91]. Therefore, the analysis has to be aided by energy dispersive spectrometry (EDS) in order to obtain confidence in the distinction between the two very similar phases [92].

The information about the crystallographic orientation of individual grains making up the material can provide an explanation as to why the cracks propagate in a certain manner. Figure 2.33 provides an example where the crack path is related to the orientation of the individual grains. The example highlights that the reason for the crack path deviation can be explained by studying the orientation of the adjacent crystals. The observed change in the crack path was caused by the preferential orientation an adjacent grain in terms of the energy required to cause cleavage [93].

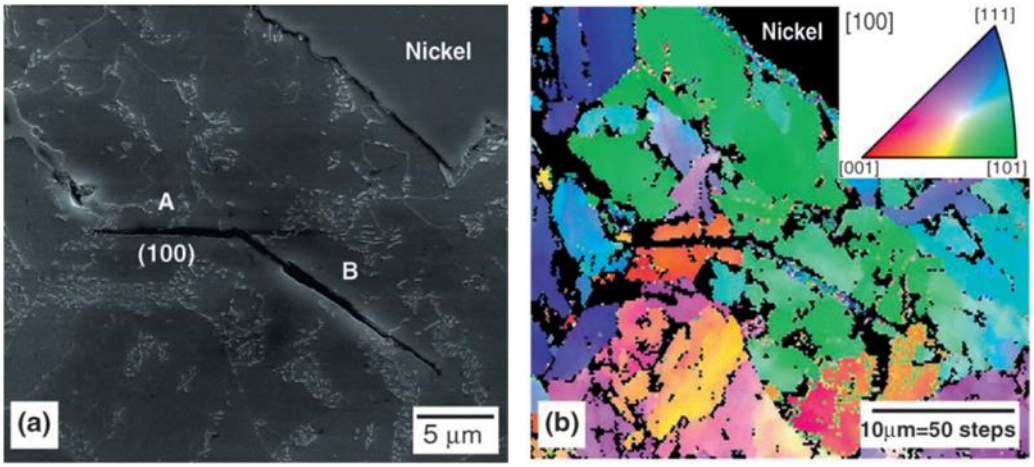

Figure 2.33 – An example of crack propagation related to the crystallographic orientation of the individual grains – (a) an SEM micrograph depicting a sudden change in the direction of the crack and (b) highlighting that a high angle grain boundary resulted in the crack path deviation into a crystal which is preferentially orientated in terms of the energy required for cleavage[93].

2.6 **Summary**

The current chapter has provided an overview of the key aspects related to the current research project. PCD has been introduced as the material of interest and the properties important to the mechanical performance of PCD have been highlighted. PCD possesses outstanding hardness and a very high stiffness modulus. It also possesses a good level of toughness, however when compared

with the extreme level of hardness and stiffness, toughness of PCD materials can be a limiting factor in a number of applications as the material develops cracks leading to spalling and/or more catastrophic damage. Therefore, understanding of the mechanisms of crack propagation in PCD needs to be improved. This can be achieved by employing the techniques developed in the field of fracture mechanics. Fundamental principles of fracture mechanics have been presented in the chapter followed by the various techniques and test geometries which can be employed in the study of brittle materials. It has been highlighted that all geometries except that of the DT tend to be unstable due to the rising stress intensity factor with crack extension. The DT technique alone provides a unique loading geometry where the stress intensity factor is nominally constant during the crack propagation process. This makes the DT configuration the most suitable approach to follow in the study of extremely brittle materials such as PCD. The DT technique has further advantages in that the specimens are relatively simple to machine. It is important that the fracture process zone in the DT configuration is unobstructed during crack propagation in order to investigate the mechanisms associated with crack extension. Therefore, further to the material toughness data obtained through the DT loading data, the fracture process can be observed by employing various microscopy techniques as well as techniques such as DIC, through which material properties can be obtained in a non-contact manner. EBSD orientation mapping of the individual surface grains provides a further method of development of an understanding of how individual crystals may affect the performance of the nominally isotropic polycrystalline material.

The following chapter examines previous studies in the field of fatigue and fracture as applied to the polycrystalline diamond material and highlights the areas where the current research project aims to aid the understanding of the fracture process in free standing PCD.

3 Previous studies in PCD damage mechanisms

The following chapter presents studies which have previously been undertaken in characterising the fatigue and fracture properties of PCD materials. At this point it is worth noting the scarce nature of published research pertaining specifically to the fracture mechanics based characterisation of free standing PCD materials. Such scarcity can be highlighted by the fact that one of the most respected texts on properties of synthetic and natural diamond by Field [37] contains only four pages on the mechanical properties of PCD materials. The trend can be further observed when studying the reference matter of more recent academic work, where works by Lammer [20], Lin, Cooper and Hood [29], and Dunn and Lee [22] remain the core texts with little new research having been published where fundamental fracture mechanics techniques have been employed in the study of the fracture behaviour of PCD.

The work published by Lammer [20] formed the foundation of the current understanding of the mechanical properties of PCD materials at room temperature. Material properties such as strength, fracture toughness and elastic constants were determined. Lammer identified that the strength properties of PCD materials increased with decreasing grain size. However, fracture toughness properties appeared to reach a maximum of about 9MPa√m in the grain size range of 10-30µm. It was further noted that the fracture mechanisms were brittle and transgranular. Post fracture SEM microscopy revealed grains with slipping bands. This observation could not be directly related to the fracture process as similar slippage mechanisms can occur during the HPHT production processes of the PCD material [94].

Drory [15] and Achilles [19] investigated the fracture properties of CVD and PCD diamond composites employing disc-shaped compact tension (DCT) specimens. Both research programmes experienced difficulties with controllable propagation of the cracks. Drory identified a fracture toughness of 6.3 MPa√m [15]. The work of Achilles appeared more successful in identifying the initiation stress intensity level at 8.1 MPa√m and a stress intensity of 10.1 MPa√m was consistent with the onset of fast fracture.

Tze-Pin Lin, Cooper and Hood [29] and Davies and Field [95] performed DT fracture experiments on PCD and CVD diamond respectively. The results obtained in PCD revealed elevated fracture toughness levels of 13-14 MPa√m. The authors noted that while the microstructures of the tested materials were significantly different, 5-15 µm vs 10-30 µm vs 20-50 µm, the measured fracture toughness results were within 1MPa√m for the five specimens tested. The authors concluded that the grain size distribution was too small to identify clear differences in the fracture toughness properties of the tested materials [29]. In their SEM investigations the authors noted crack deflection along the diamond grains as a potential toughening mechanism. A "jumping" crack propagation mechanism was described and attributed to either inhomogeneity in the microstructure or presence of cobalt pools leading to crack retardation. Davies and Field calibrated their double torsion experiments employing alumina plates followed by testing CVD material. The authors described the CVD material as mechanical and di-electric grades and obtained average fracture toughness measurements of 8.5 and 8.3 MPa√m. The results obtained in the optical grade CVD were more consistent varying by 0.4 MPa√m versus 1.0 MPa√m determined in the mechanical grade [95].

The relative dearth of fracture mechanics based research into PCD can perhaps be attributed to the following causes. The cost of producing PCD specimens of various standard geometries is very high and machining of intricate geometries can be difficult. Therefore, research is only possible with the involvement of a PCD manufacturer. The extreme stiffness and strength of the PCD compacts also results in little data which can be extracted from tests beyond simple crack initiation in conventionally loaded specimens in tension or bending. PCD material manufacturers employ testing methodologies most suited to the evaluation of the PDC cutter products as a unit (PCD table and WC-Co body) and not the freestanding PCD material itself. Lastly, it is believed that in-house fracture studies may well have been undertaken but the findings are not readily published in order to retain the intellectual property and market place advantage.

3.1 Fracture and fatigue studies in PCD

3.1.1 Fracture toughness and mechanical properties of PCD

Following early research by Roberts [96] and Giggl [97], the most extensive research attempt into the understanding of the mechanical properties of PCD was undertaken by Lammer in 1988 [20]. This test programme involved a total of 408 samples of which 32 were dedicated to fracture toughness testing by means of diametral compression of a centre notched disk (Refer to Section 2.2.9 for the geometry and the expression for the stress intensity). The specimens were produced by the introduction of a 2 mm notch into a 4 mm disk specimens which were 0.8 mm thick (d/t ratio of 5). A pulsed yttrium-aluminium-garnet (YAG) laser was employed. The results obtained are reproduced in the table shown in Table 3.1. The results revealed that the typical fracture toughness of PCD material was in the approximate range of 6.9-9.1 MPa√m. The mode of fracture was typically transgranular [20].

An observation was made that transverse rupture strength (TRS) and fracture toughness depend on the grain size of the material tested. The TRS behaviour indicated that the strength of the material increased with the decrease in grain size, as often seen in ceramics. A plot depicting the relationship between TRS and grainsize is provided in Figure 3.1. Similarly, a relationship between the fracture toughness and grainsize is depicted in Figure 3.2, highlighting the fact that fracture toughness appears to attain its maximum levels in PCD with starter powder size in the region of 12-30 µm.

Lammer [20] proposed that the grain size dependence follows the mechanisms proposed for other ceramics by Rice [98], whereby the apparent toughness of the material depends on the ratio between pre-existing flaws of some length, *c*, existing in the material and the grain size, *d*. In cases where the ratio *c/d* was less than unity, single grain toughness would be observed during testing. If the ratio was more than unity, polycrystalline toughness is involved [99]. The grain size influence on fracture toughness was similarly explained by a mechanism proposed by Rice, whereby the large difference in the expansion coefficients of the diamond and cobalt creates large interfacial stresses and elastic anisotropy [98].

	Cobalt Matrix PCD supported by tungsten carbide-cobalt				Unsupported cobalt matrix PCD			Unsupported silicon carbide matrix PCD
Property	**A**	**B**	**C**	**D**	**E**	**F**	**G**	**H**
Nominal Grain Size (μm)	2	12	30	125	30	95	150	22
Matrix (cobalt or silicon carbide) content (vol%)	13	11	11	12	5	6	5	19
Density (kg m^{-3})	4.24±0.10	4.12±0.09	4.10±0.11	4.15±0.10	3.77±0.12	3.83±0.06	3.79±0.12	3.43±0.08
Longitudinal speed of sound (ms^{-1})	13360±460	13810±800	13130±660	14370±790	15520±165	15400±240	15910±160	16570±150
Transverse speed of sound (ms^{-1})	---	---	---	---	10520±140	10450±190	10820±170	11150±180
Transverse rupture strength (MPa)	1550	1260	1190	440	1090	520	390	1040
Tensile strength (MPa)	---	---	---	---	1540±210	300±140	340±75	525±275
Compressive strength (MPa)	---	---	---	---	4700±1200	2500±900	2000±600	4200±1300
Fracture toughness ($MNms^{-3/2}$)	6.9±0.4	8.8±0.5	8.9±0.4	7.5±0.8	9.1±0.4	7.5±0.2	7.0±0.6	6.9±0.4
Poisson's ratio	0.07	0.07	0.07	0.07	0.075	0.07	0.073	0.086
Young's modulus (GPa)	750	775	810	850	900	900	950	925
Shear modulus (GPa)	350	360	380	400	420	420	440	425
Bulk modulus (GPa)	290	300	310	330	350	350	370	370

Table 3.1 - Properties of a range of cobalt matrix PCDs reproduced from Lammer [20].

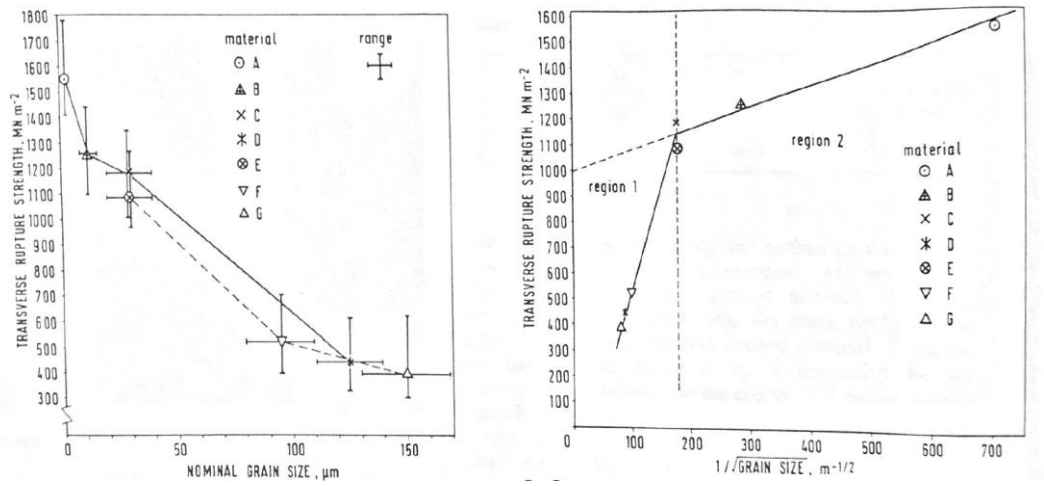

Figure 3.1 – Plots depicting the transverse rupture strength vs. grain size dependence in PCD.

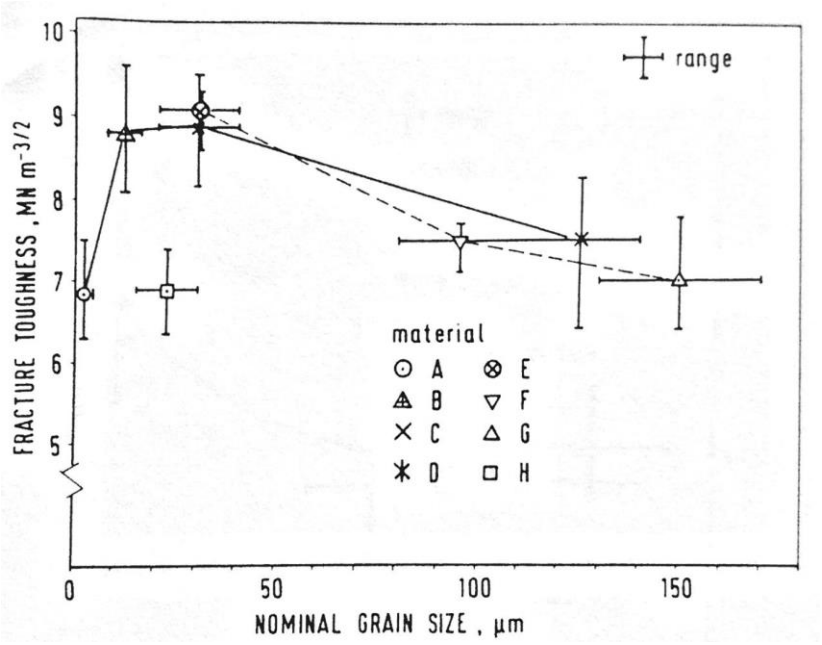

Figure 3.2 – Plot depicting the relationship between fracture toughness and PCD grain size.

3.1.2 Application of standard FM geometries to PCD

Compact tension

Disk-shaped compact tension (DCT) geometry specimens were employed by Drory et. al. [15] and Achilles et. al. [19] in an attempt to evaluate the fatigue and fracture parameters of chemically vapour deposited (CVD) and polycrystalline (PCD) diamond compacts respectively. The specimen geometry employed by Drory was a 25 mm diameter standard disk-shaped specimen with a laser cut starter notch (the exact dimensions were not reported). However, the geometry employed by Achilles is depicted in Figure 3.3. The disks employed were 19 mm in diameter and a chevron starter notch was attempted by both EDM and laser machining techniques. The deflection of the EDM wire proved to be an unreliable technique to reproduce the symmetry required by starting geometry and therefore specimens notched by laser techniques were significantly more reliable in terms of the repeatability of the performed tests.

Both experimental programmes were attempted in accordance with the ASTM E399 standard[100]. The attempt by Drory to initiate a sharp fatigue crack, required by the procedure, was not successful and catastrophic failure of the specimens occurred. The applied load level at fracture was therefore employed to calculate the fracture toughness of the CVD material. The two tests performed resulted in fracture toughness levels of 5.3 MPa√m and 7.3 MPa√m (average of 6.3 MPa√m as described by the authors).

In the Achilles test programme [19], initiation and propagation of cracks was described as successful. While the EDM machined specimens yielded poor results, the YAG laser machined specimens subjected to fatigue loading in the constant stress intensity mode achieved initiation and propagation. The plot depicting an example of the results obtained is depicted in Figure 3.4. The crack lengths achieved at failure were quite small, of the order of 1mm. The average of ten tests revealed that the stress intensity level at crack initiation was 8.1 MPa√m and 10.1 MPa√m at final fracture. The fracture toughness determined by the compact tension approach was in fair agreement with the 9.1±0.59 MPa√m control fracture toughness for the test material, obtained by diametral compression techniques[19].

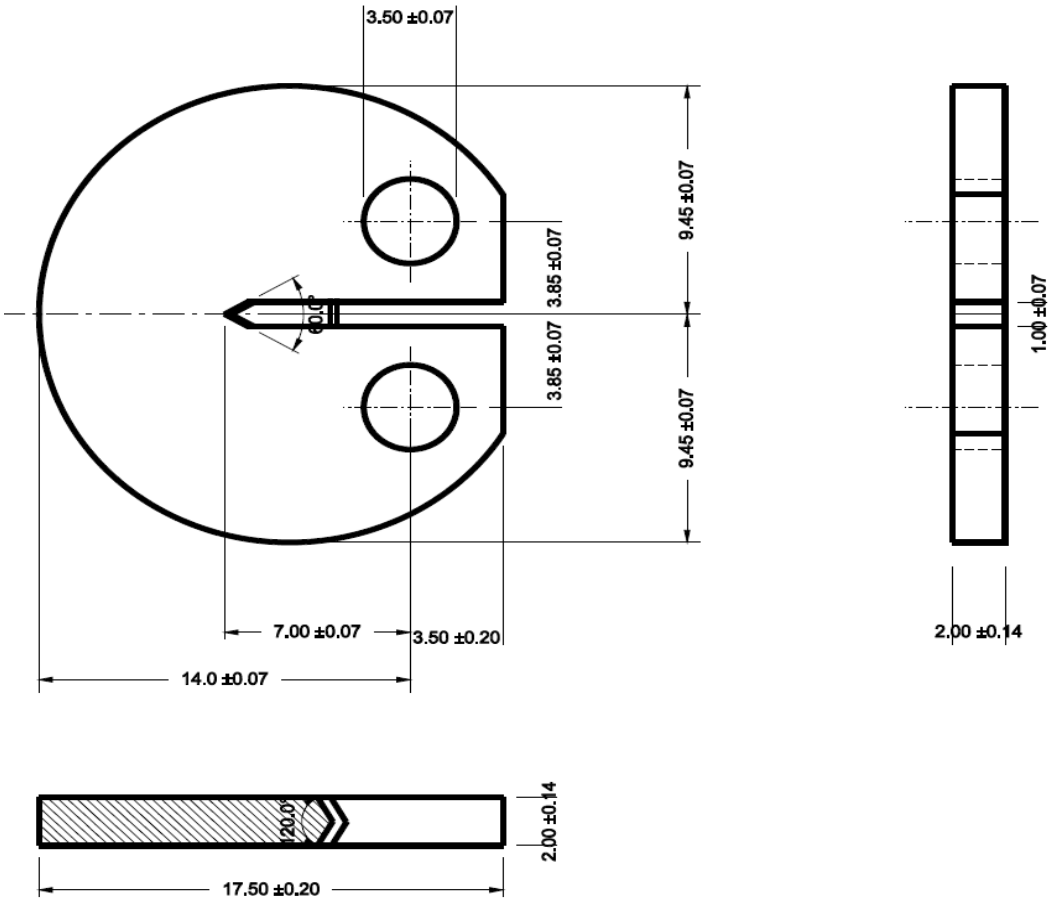

Figure 3.3 – Disk shaped compact tension specimen geometry employed by Achilles[19].

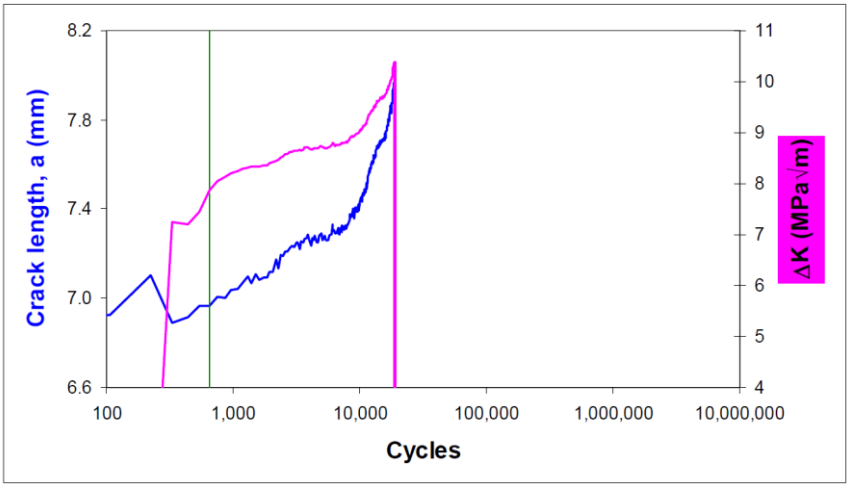

Figure 3.4 – Example of the crack initiation and growth by fatigue mechanisms[19].

Three point bending

McNamara [16] and Morrell [17] studied the fracture properties of various grades of PCD employing the three-point bend geometry. Morrell employed both the single edge V-notched bend (SEVNB) specimens as well as a chevron notch bend (CNB) specimen, Figure 3.5. The PCD grades studied by McNamara were the 4 µm and 30 µm starter particle sizes with additional testing of specimens of the same particle size but additional leaching of the cobalt metallic phase. Morrell did not disclose the specific grade of the PCD studied and only referred to it as “one particular product”.

McNamara and Morrell followed the method described by ISO 23146 (BS EN 15732)[101]. However, departures had to be made from the standard in terms of the overall specimen geometries being smaller and the “pre-cracks” being introduced as relatively blunt notches.

The results obtained by Morrell revealed a fracture toughness of 9.9 MPa√m for the SEVNB specimen tests and a range of 8.0-9.5 MPa√m for the chevron notched specimen. Morrell also performed high temperature tests at 500 °C and 700 °C. Keeping in mind the potential lack of loading equipment stiffness at high temperature and low applied load levels, the fracture toughness results obtained for the two temperatures were in the range of 8.7-10.2 MPa√m and 8.5-9.9M Pa√m respectively [17].

No clear evidence of fatigue could be obtained by methods employed by Morrell. Application of 2 000 000 cycles to SEVNB specimens at a load level which was 90% of load required to cause catastrophic fracture did not lead to crack propagation. No significant reduction in the load required for fast fracture was observed in the specimens which had undergone the described fatigue loading. Elevated temperature testing (580 °C) of chevron notched specimens also did not reveal evidence of fatigue [17].

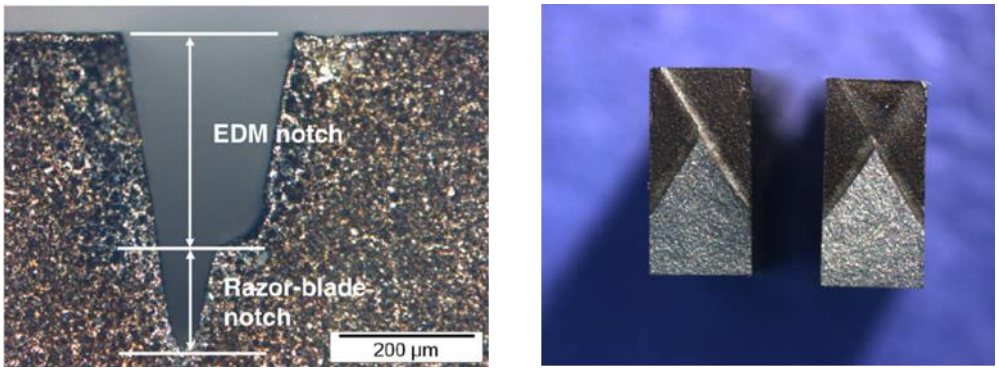

Figure 3.5 – Photographs depicting the SEVNB notch geometry (left) and the CNB notch cross-sectional geometry after fracture (right).

The results of the experimental work performed by McNamara revealed clear differences in the performance of the 4 µm and 30 µm material grades. The results were adjusted for the finite notch diameter employing the concept of a material microstructural parameter - *characteristic length,* R_c[102]. The data summarizing the results obtained is presented in Table 3.2.

Fracture toughness results obtained by McNamara[16]	
PCD30A	9.55 MPa√m
PCD30B	9.53 MPa√m
PCD30C	8.52 MPa√m
PCD4A	8.49 MPa√m
PCD30B (leached)	7.31 MPa√m
PCD30C (leached)	6.48 MPa√m
PCD4A (leached)	5.68 MPa√m

Table 3.2 – Fracture toughness results obtained by McNamara for the two grades in leached and un-leached conditions.

Furthermore, McNamara presented results which highlight the effects of the notch root radius (NRR) diameter and the effect of the residual metal removal depth, plotted in Figure 3.6 and Figure 3.7, respectively.

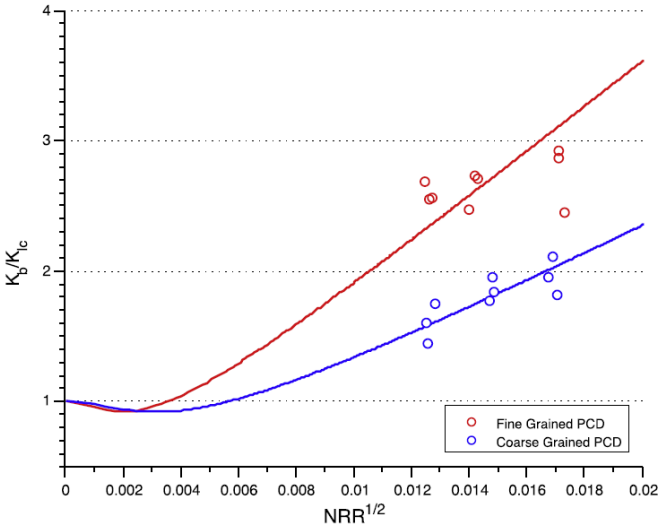

Figure 3.6 – Normalised fracture toughness results highlighting the sensitivity of the PCD material measurement to the notch root radius dimension[16].

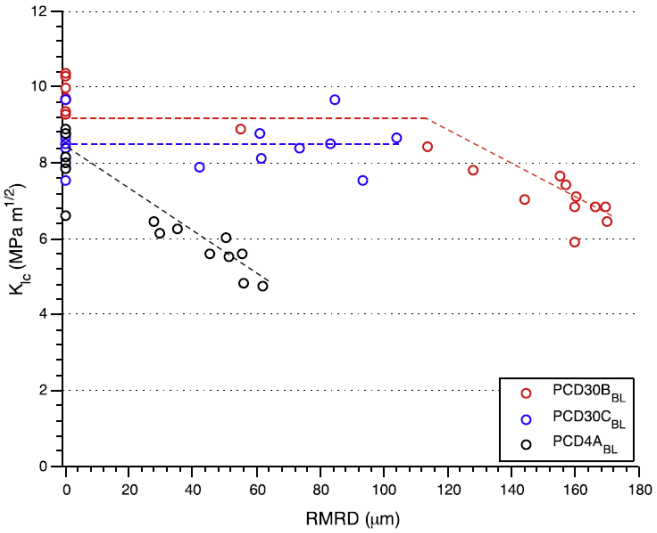

Figure 3.7 – Effect of the residual metal removal depth (RMRD) on the fracture toughness result obtained[16].

Diametral compression (Brazilian disc)

Further to the extensive use of the diametral compression geometry by Lammer [20], Miess and Rai [18] employed the methodology to investigate the effect the microstructure has on the fracture toughness properties in PCD. In the experimental programme undertaken by Miess and Rai, a total of 11 batches of 10 specimens each of microstructural composition ranging from 2 µm to 140 µm diamond starter grain size were tested (a total of 110 specimens). The results obtained are reproduced in Figure 3.8. The trend observed in the experimental programme was similar to the one observed by Lammer [20], where toughness increased rapidly with increasing grain size up to about 30 µm after which a less pronounced size effect was observed.

It is evident that the diametral compression technique is suitable for the purpose of fracture toughness characterisation of PCD materials in a repeatable manner.

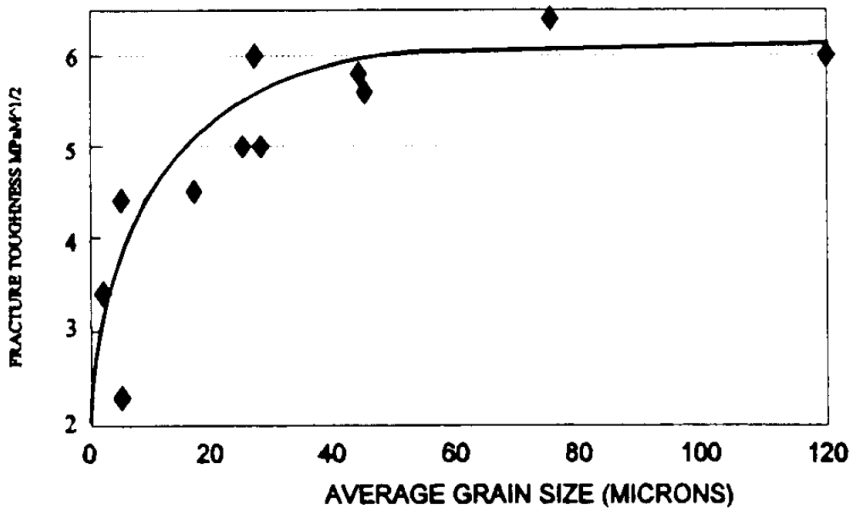

Figure 3.8 – PCD fracture toughness as a function of starter particle grain size (each point represents an average of 10 fracture toughness measurements) [18].

3.1.3 Fatigue testing of PCD employing custom methodologies

The widespread use of the PCD based cutters in the oil and gas industry has led to the development of custom methodologies aimed at assessing the fatigue

performance of the PCD layer attached to the working surface of the PDC cutter. Two examples of such systems are described in the work of Dunn and Lee [22] and Kanyanta et. al. [23].

Dunn and Lee developed a rig which enabled the simulation of the cyclic application of the weight on bit (WOB) scenario experienced in the field during rock drilling. The schematic representation of the rig is depicted in Figure 3.9.

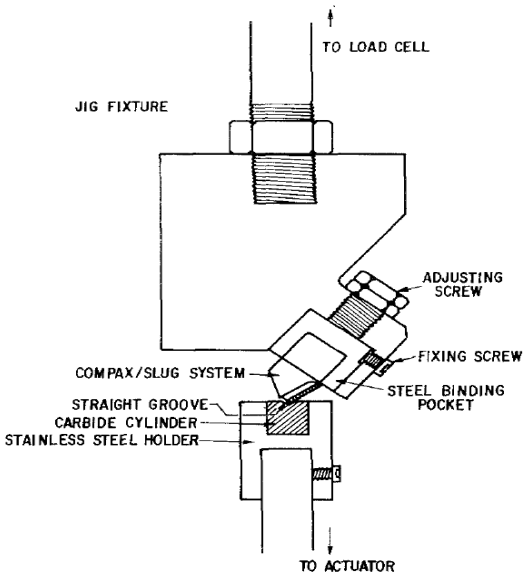

Figure 3.9 – Schematic view of the fixture developed for the cyclic compression loading of PDC cutters [22].

The PDC cutter was pressed into a carbide cylinder at a rake angle which aimed to reproduce the contact angle the bit experiences during real rock cutting. The negative rake on the cutter was therefore set to 15° which led to a resultant geometry of "force-on-bit" angle of 40°, Figure 3.10. The bits were cyclically loaded at a range of loads in order to develop an S-N type diagram for the fatigue life of the cutters, Figure 3.11. Failure typically manifested through edge chipping of the PDC diamond table, as it tends to do in the field, at which point the tests were arrested and the fractographic features of the failure region inspected. The system described provides a useful tool in the characterisation of the fatigue performance of the PDC cutters.

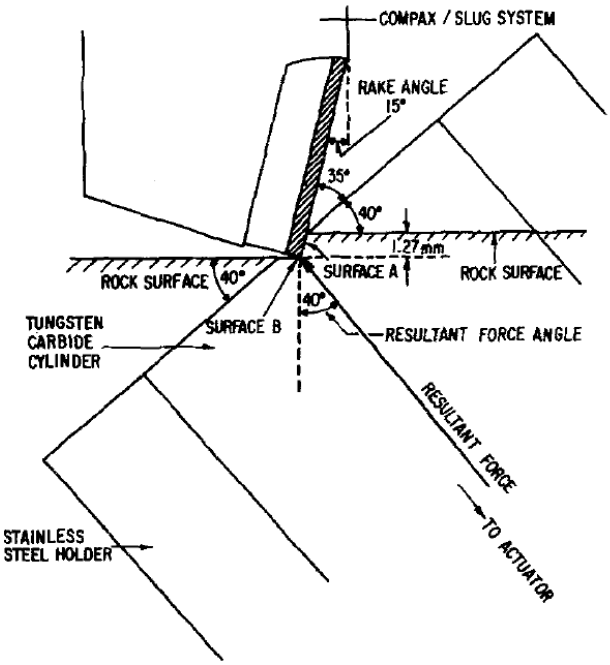

Figure 3.10 – The contact geometry between the PDC cutter and the tungsten carbide cylinder[22].

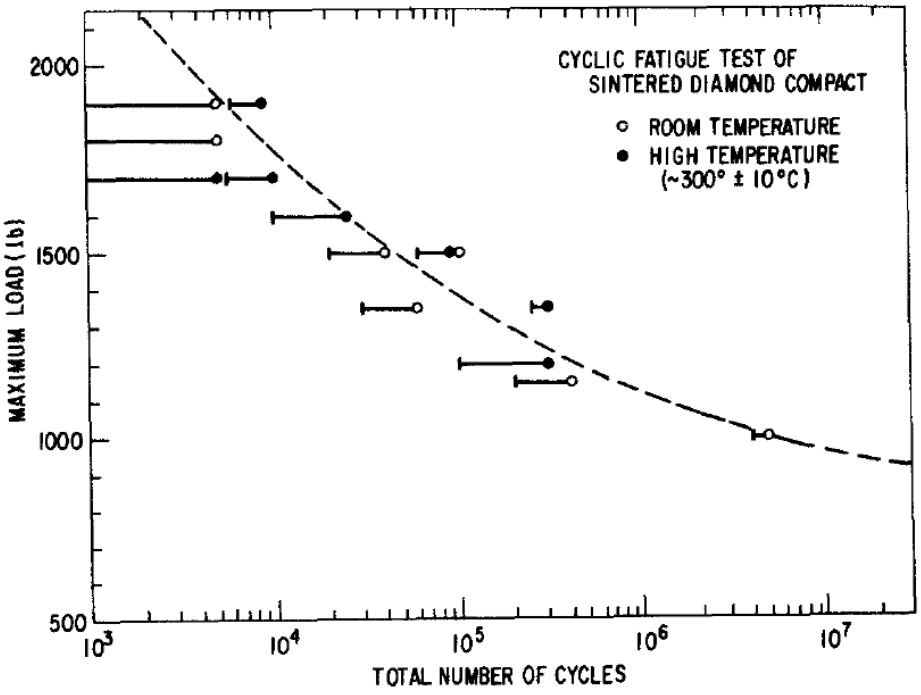

Figure 3.11 – Plot depicting the maximum load versus the number of cycles leading to failure[22].

Kanyanta et. al. [23] aimed at developing a similar testing methodology but with a larger emphasis on the impact component associated with severe downhole conditions during oil and gas well drilling. The test rig developed is depicted in Figure 3.12. The cutters were assigned three levels of damage, namely i) first visible surface crack (FVSC), ii) crack growth through polycrystalline layer (CG-PCD) and iii) catastrophic failure (CF). Employing this grading system, the cutters were subjected to repeated impact up to a maximum of 5000 cycles. The result of such testing was another S-N type plot characterising the impact fatigue life of the PDC cutters, Figure 3.13.

Similar to the cyclic compression testing system developed by Dunn and Lee [22], the system developed by Kanyanta et. al. [23] provides a means of characterising the performance of the PDC cutters under cyclic impact loads.

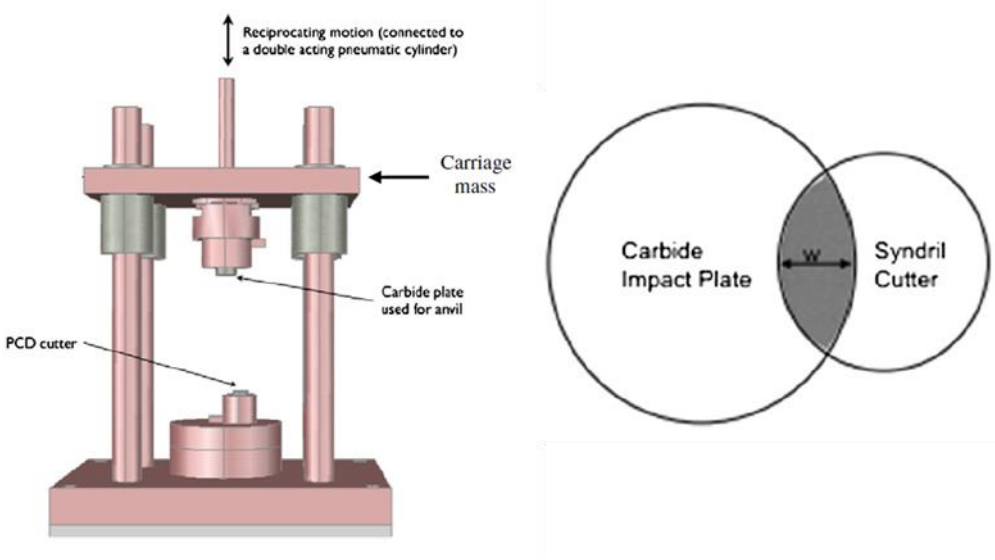

Figure 3.12 – Test rig developed by Kanyanta et. al. [23] to investigate the impact fatigue lives of PDC cutters (left) and the geometry of the impact zone between the carbide anvil and the Syndril cutter (right).

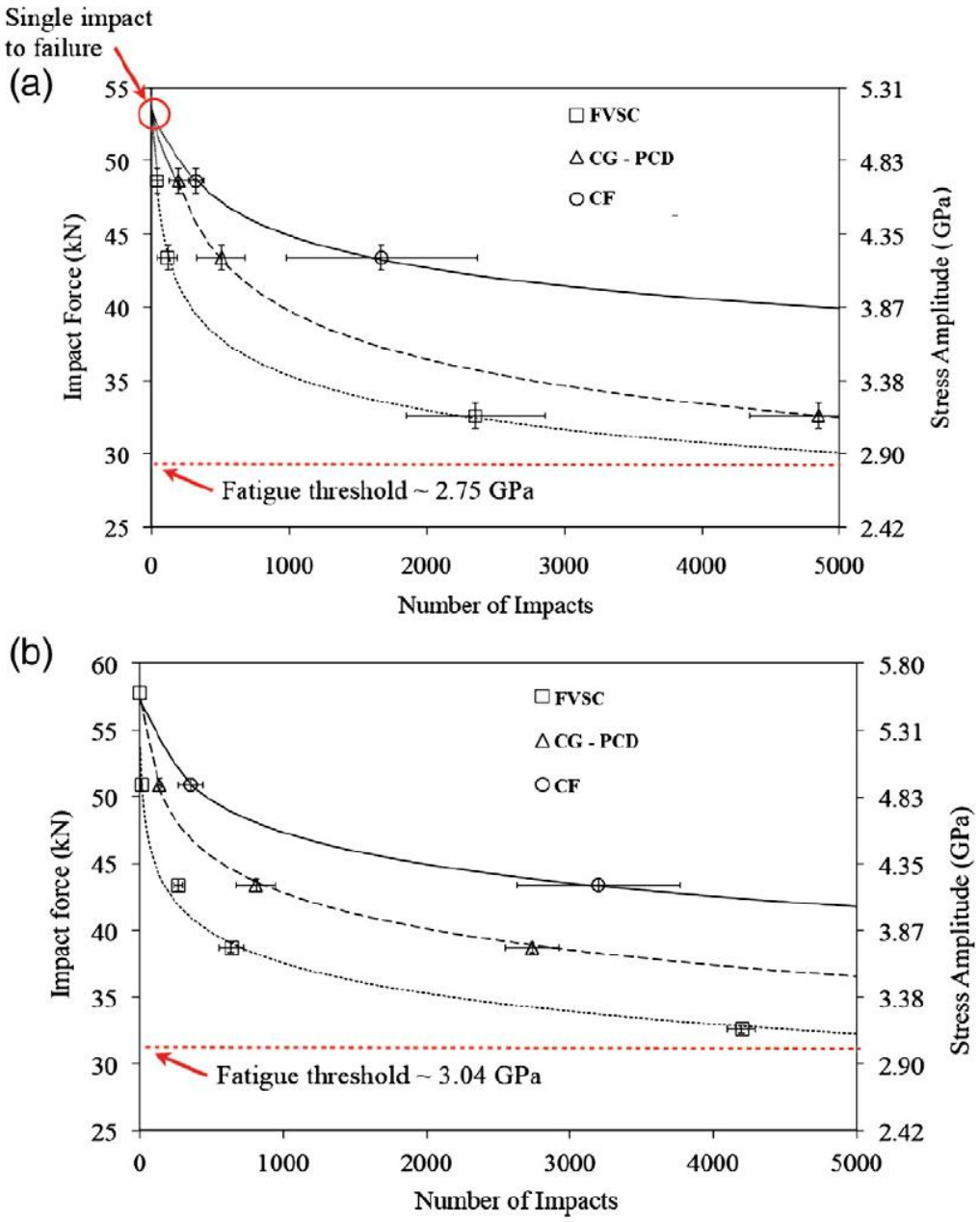

Figure 3.13 – Cyclic impact S-N fatigue life curves developed for two different cutters of undisclosed composition[23].

3.1.4 **Indentation techniques**

Indentation techniques have been used by a number of authors in the analysis of the fracture properties of single crystals of natural and synthetic diamonds [7,21,99,100]. Attempts at characterising the fracture properties of polycrystalline diamond have also been made. Further to the compact tension

studies presented earlier in this chapter, Drory [15] attempted to characterise the fracture toughness of the polycrystalline CVD diamond by means of Vickers indentation[15]. The schematic geometry of the Vickers indentation test as well as an example of the cracks emanating from such an indent in CVD diamond are depicted in Figure 3.14. The fracture toughness for the material can be calculated by employing the following expression

$$K_C = \xi \left(\frac{E}{H}\right)^{\frac{1}{2}} \left(\frac{P}{c^{\frac{3}{2}}}\right) \tag{3.1}$$

where *P* - is the applied load, *c* - is the mean length of the crack emanating from the indent corners, *E* and *H* – are the Young's modulus and hardness respectively. The *ξ (=0.016±0.004)* parameter is an empirical factor determined for a wide variety of engineering ceramics, required to correlate the indentation fracture toughness to the fracture toughness levels determined by other methods[15].

Employing the indentation technique, the polycrystalline CVD fracture toughness was measured to be 5.6 MPa√m in a material where disk-shaped compact tension fracture toughness measurements revealed a toughness level of 7.3 MPa√m [15]. The significant variation in the results was attributed to the uncertainties associated with empirical nature of the correction factor *ξ* employed in the fracture toughness determination.

The indentation techniques can also be employed with a round indenter to generate cone cracks in the polycrystalline diamond material. While this does not directly quantify the fracture mechanics properties, it provides a technique to study microstructural damage response to a known loading history[40]. It is worth noting that indentation techniques characterise the properties of a small volume of a material and can be affected by the size and shape of the indenter employed[7].

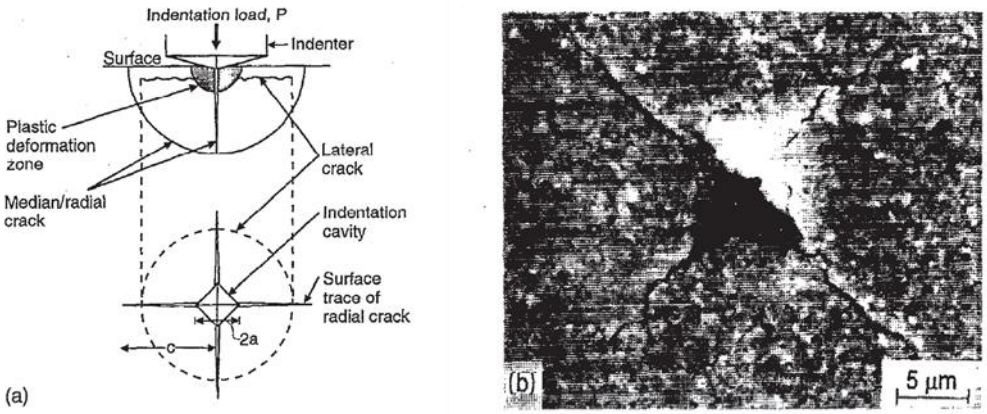

Figure 3.14 – (a) Schematic representation of the key elements required to determine fracture toughness from the Vickers indentation test, (b) cracks emanating from the corners of a Vickers indent in polycrystalline CVD diamond [15].

3.1.5 **Double torsion**

The double torsion technique has been employed by Lin et. al. [29] and Davies and Field [91,101] to study the fracture mechanics parameters of PCD and CVD diamond materials respectively. In both experimental programmes the double torsion specimens were notched along the centre line in order to constrain the crack. It is noteworthy that the specimen geometry employed by Davies and Field had a length to width ratio of 1.38 while those used by Lin et. al. had the length to width ratio of 2. More recent research suggests that significantly improved performance can be obtained with DT specimens of length/width ratio of 3:1 [25,67,71] as used in this thesis. Lin et. al. employed calibration specimens of standard glass microscope slides and 99.5 % pure alumina in the development of their experimental procedure. These samples had the dimensional ratio of 3:1 and with the length and width dimensions being 75 mm to 25 mm respectively. Furthermore, the loading geometry employed by Lin et. al. resulted in the tensile face of the specimen being on the bottom which did not facilitate easy observation of the cracking process. The schematic representations of the two loading geometries are depicted in Figure 3.15.

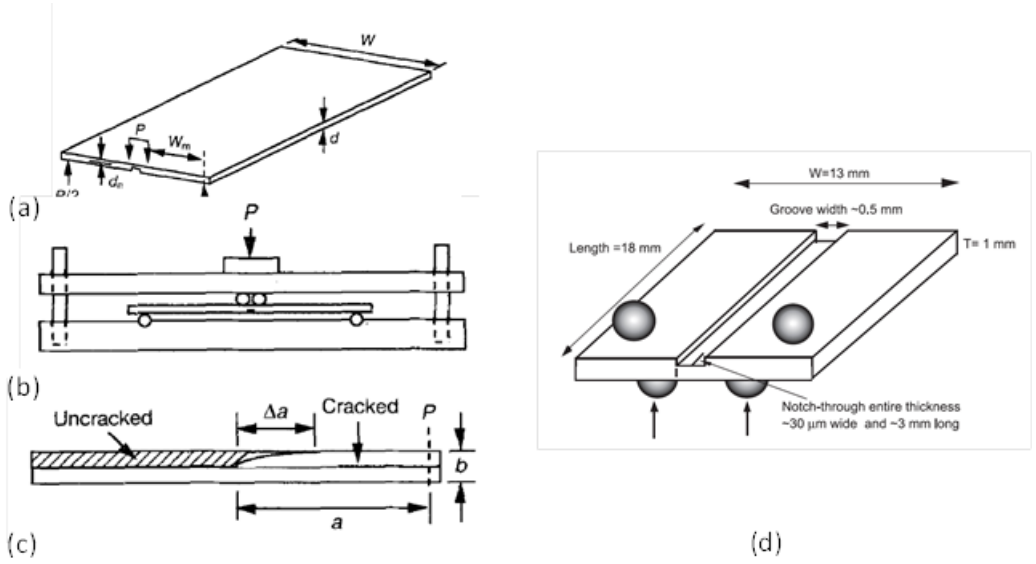

Figure 3.15 – The illustration on the left (a-c), show the specimen geometry, loading geometry as well as the schematic of the crack front in the Lin et. al. experiments while (d) shows the experimental arrangement of the Davies and Field experiments[29,91].

The results obtained by Lin et. al., for microstructurally different grades of PCD material, ranged between 13-14.3 MPa√m for a series of ten tests. The grain size of the PCD material varied significantly between specimens with a diamond grain size range of 5-15 µm and 20-50 µm. The authors concluded that the range of grain sizes used in the test programme were not significantly different to result in significantly different fracture toughness properties. Comparing the results obtained to those from the work of Lammer [20], the authors observed that the fracture toughness values were elevated but in the correct magnitude sequence. Furthermore, good repeatability was achieved[29].

Prior to initiating the fracture experiments in diamond, Davies and Field [91, 101] performed tests on identical geometry specimens of alumina. The results of these tests were compared to published results for alumina and good agreement was achieved (3.6±0.4 MPa√m by double torsion vs. 3.7±0.2 MPa√m obtained from literature). Having achieved the necessary level of confidence, two types of CVD diamond materials were tested, namely i) mechanical and ii) di-electric grades. The fracture toughness measurements obtained were 8.5±1 MPa√m for the mechanical grade and 8.3±0.4 MPa√m for the di-electric grades. These were in good agreement with published values for CVD diamond. The slightly higher toughness of the mechanical grade was caused by a higher

number of flaws and imperfections believed to be resulting in crack deflection[95].

Both Lin et. al. and Davies and Field reported experimental difficulties. Having exercised great care in specimen alignment and rig fabrication, it was nonetheless difficult to control the crack path and the cracks tended to deviate from the centre grooves. Davies and Field experienced catastrophic failure of three of the ten specimens at high loads. This indicated that controllable initiation of a sharp crack through the notch region did not occur and the specimens failed at the load level associated with notch toughness [95].

3.2 Discussion of the current understanding of fatigue and fracture in PCD

The information highlighted in the previous sections of the current chapter revealed that, while limited, successful attempts at characterising fracture toughness of PCD materials have been undertaken. While there exist differences between the values of fracture toughness determined by the different methodologies, a typical toughness range of 5-10 MPa√m appears to be the general consensus for PCD materials with starter particle sizes ranging from 2-40 µm [20,29,91]. It is worth noting that subsequent to the work of Lammer [20] on PCD grades with starter particle sizes exceeding the 30-40 µm range, no similar work has been reported. This is believed to be related to two factors. The first is the fact that the fracture toughness ceases to increase with increasing starter particle grain size at particle sizes in order of 30-40 µm and hence these grades are not desirable. The second is believed to be related to the cost of producing starter particles of large sizes. Therefore it appears that the current practical grades of PCD have starter particle grain sizes ranging between 4-30 µm and combinations thereof [16,23,29].

There appears to be a general consensus in published research with regard to the difficulties associated with fracture toughness and crack propagation mechanism studies in PCD materials. The stress intensity level required for crack initiation is similar to the critical stress intensity level which leads to rapid propagation. Because of this property, it is very difficult to obtain the so called sub-critical crack propagation in PCD. The studies performed by Achilles [19], on compact tension specimens of PCD, revealed that controllable initiation depended strongly on the degree of sharpness and geometrical accuracy of the

starter notches. Furthermore, observations were made that the local diamond particle size effects could significantly affect the crack propagation process resulting in crack deflection and arrest. It was proposed that the more ductile cobalt ligaments in the wake of the crack may shield the crack tip from the full range of the applied stress cycle and cause R-curve type behaviour, where the material toughness appears to increase with increasing crack length.

In their DT experiments in PCD Tze-Pin Lin, Cooper and Hood [29] experienced difficulties maintaining centralized cracks. They reported that the crack path was affected by the accuracy of the specimen machining as well as the inhomogeneous microstructure of the material. Although a centring groove was employed by these researchers, the cracks deflected outside the groove leading to premature specimen failure. Similarly, Field and Davies [105] experienced problems with the cracks initiating outside the starter notches despite the notches being only 30 µm wide and 3 mm in length.

In light of the difficulties associated with the experimental fracture work in PCD materials, little micromechanistic observations have been presented in the reviewed studies. Observation of trans and intergranular fracture mechanisms are typically made with evidence of crack propagation being affected by the twinning dislocations within the diamond crystals [18,38]. A hypothesis describing the behaviour of two part ceramics containing pre-existing flaws has been proposed to describe the behaviour of the PCD material [20,95]. In his work with a diverse range of diamond grain sizes, Lammer [20] correlated a region of peak fracture toughness to correspond with the PCD grain size range of 10-30 µm. It is suggested that beyond this grain size range single large crystal transgranular fracture is the strength controlling parameter. In case of the finer grain sizes and increased cobalt content, the failure mechanisms are assumed to be controlled by microplastic flow activity or dislocation flow activity which leads to initiation. For the fine grained PCD materials, grain size less than 30 µm, Lammer[20] achieved correlation between the transverse rupture strength and grain size in PCD in a manner consistent with the Hall-Petch strength relationship.

Techniques such as the three-point bend test, diametral compression and compact tension have been shown to be capable of toughness property quantification but these do not provide the ability to propagate a crack in a slow, controllable manner while facilitating the observation of the fracture process. Such observation may provide valuable information in terms of the fracture

process and extend the understanding of the damage mechanisms in PCD. Also, in-situ observation of the fracture process may enable new stress-intensity quantification techniques and development of new specimens. It is believed that development of a new miniature specimen for stress intensity studies in PCD may expand the field of knowledge of PCD damage mechanisms by making the material more accessible through the use of standard manufacturer geometries.

3.3 Aims and objectives of this thesis

This chapter discusses previous published research on crack growth and fracture toughness in PCD materials and their dependence on testing methodologies. While the general objectives of the proposed research effort have been presented in Chapter 1, the following objectives summary presents a more detailed overview of the proposed work in the context of the existing methodologies discussed in the previous section. Further to the core aspect of the double torsion approach to fracture mechanics properties investigation in PCD, additional techniques are to be attempted and are discussed.

3.3.1 Introduction

The current research project was initiated between the University of Cape Town and Element 6 (Pty) Ltd., in an attempt to improve the understanding of the fracture processes in PCD. The research material presented in the literature review and the previous work applied to PCD, highlights the important common thread that, among other difficulties, – slow, controllable crack propagation in PCD is very difficult. Techniques necessary to compare the fracture toughness of various grades of PCD have been developed. While absolute result accuracy may depend on the test geometries employed, in general, good tools are available to compare various PCD grades, especially so, when applied specifically to the performance evaluation of PDC cutters and, indeed the same techniques were used in the DT testing of all grades, so the results may be regarded as truly comparable. However, it is believed that in order to further the understanding of the fracture processes associated with the various grades of PCD, a technique for controllable crack initiation and propagation in PCD materials is required.

In the light of the presented information, it is believed that the DT technique provides a reliable testing methodology that meets the requirements for stable crack initiation and propagation for the evaluation of fracture related properties in PCD. Development of a stable, controlled crack propagation methodology

would enable fine incremental advance which could in turn enable observation of the effects of the various microstructural features on the crack development process in PCD. Furthermore, the double torsion geometry facilitates the development of equipment which can be used in existing servo-hydraulic fatigue laboratory equipment as well as development of custom loading fixtures which can improve the portability of the test rig to enable in-situ SEM observation by various imaging techniques such as light microscopy, electron microscopy and digital image correlation. Critically, with successful implementation of the proposed techniques, it would become possible to develop cost effective equipment for in-situ studies in PCD fracture mechanisms.

3.3.2 **Objectives**

The key objectives of this research project can be separated into three main groups, namely, i) development of the miniature DT rig which could be operated in-situ in the SEM, ii) characterisation of the fracture mechanics properties of four grades of PCD material of varying, known composition, iii) qualitative observation of the micromechanical cracking processes and microstructural features affecting them and iv) attempt to quantify simultaneously the fracture toughness parameters by using a novel non-contact optical approach employing DIC and JMAN MATLAB routines. These three fundamental objectives are described in the following three sections with further detail being provided about the more specific objectives.

3.3.2.1 The miniature DT rig for in-situ fracture studies

Review of the previous fracture property studies performed in PCD identified slow, controllable crack propagation in PCD as very difficult. Therefore the first objective of this project was to develop a double torsion rig which would enable desirable slow, **controlled** crack propagation. The elegance of the technique has been discussed in Section 2.3 and promising attempts at application to PCD have been presented in Section 3.1.5. Therefore, it is believed that the advantages associated with the DT test geometry can be combined with a miniature approach to not only enable slow, controlled crack propagation but also facilitate observation by various microscopy techniques in-situ.

The key requirements important to successful development of a miniature DT rig are itemised below:

- Stable crack initiation and propagation

- Use of “compact” specimens
- Mobility facilitating in-situ experiments in various environments (Optical and SEM microscopy, DIC)
- The rig controls need to be simple and intuitive
- A balance between stiffness and sensitivity
- Simplicity of the design
- Low cost and simple production

A miniature double torsion test rig satisfying the requirements would be designed and tested employing specimens machined from PMMA in order to validate the design as well as develop the experimental techniques and confidence. Subsequently, having developed these tools, experimental work would be undertaken in the available PCD samples.

3.3.2.2 Fracture property extraction and cracking mechanism observation

Having developed the experimental tools capable of propagating cracks in PCD controllably, it is envisaged that the fracture toughness parameters for the PCD grades available can be extracted employing the classical DT formulation as well as a non-contact J-integral extraction approach named JMAN. It is believed that in-situ observation of the fracture process can provide understanding of the fracture processes in the various grades of PCD. Qualitative observation of the fracture process as a function of composition and microstructural features may enable the design of future functionally graded types of PCD, where crack propagation can be managed and apparent fracture toughness of the PCD material increased.

The non-contact, optical J-integral extraction, if successful, will enable future fracture studies in specimens of non-standard geometries as well as experiments at high temperatures or tailored environments of interest. The technique also enables observation of any secondary damage mechanisms which may accompany the primary fracture zone. The ability to study non-standard geometries would significantly simplify the procurement of PCD specimens for further studies of various parameters of interest. Also, success in optical

methods would relax the constraints associated with the rig requirements for PCD testing as aspects such as load sensitivity and stiffness could be relaxed.

3.3.2.3 Grain orientation effects and fractography

To further the understanding of the microstructural effects on the fracture resistance and crack propagation mechanisms, EBSD mapping of the surface diamond particles is proposed. Although such mapping will only reveal the influence of the surface grains 4-30 µm in size, in a 500 µm thick specimen, the information may provide a first step in understanding the influence of the crystallographic orientation of individual diamond particles. Such understanding, while difficult to implement, could enable tailored microstructures to be placed in the path considered to be most damaging in order to achieve propagation in the least damaging manner and in effect slow down cracking and increase toughness.

Upon completion of destructive testing, the fracture surfaces of the available PCD grades will be analysed employing SEM in order to correlate the features associated with known stress intensity levels associated with slow crack propagation. Fractographic analysis, beyond a simple observation of the fracture surface produced by the propagating crack, may provide insight into how the failure process occurred. Therefore, it is believed that there is a potential that fractographic features will provide further information needed to improve the understanding of the fracture mechanisms in PCD materials.

3.4 **Summary**

In light of the commonly reported difficulties and expenses associated with the testing of PCD materials, it is believed that the current research project can provide a new methodology in understanding the micro-mechanisms of crack propagation in PCD. In-situ observation of a controlled crack propagation process achieved by the double torsion technique may provide the information required to develop the understanding of how various material properties and microstructural features impact the fracture toughness properties of this advanced material. Such controlled cracking has to date been difficult due to the requirement of very sharp notch root radius effects, testing machine stiffness and stored strain energy effects and the cost of producing samples of standard geometries employed for fracture mechanics studies.

Therefore, the aim of this research work can be summarized as an attempt to slow down and control the crack propagation process in the extremely stiff and brittle PCD materials in order to subject such fracture process to observation, quantification and interpretation. Achieving this will provide a platform for a number of further investigations into the properties of PCD as well as provide the tool for evaluation of the efficacy of any **functionally designed** PCD material grades.

The following chapter details the experimental methodology employed to fulfil the proposed research project objectives.

4 Experimental methodology

The previous chapter has detailed the motivation for the development of an approach to enable slow, controlled crack propagation in the extremely brittle PCD materials in order to investigate their fracture toughness properties, observe the fracture process and attempt to correlate these to the sample make-up as well as diamond particle orientation. The fracture surfaces obtained under slow, controlled conditions are also documented in order to generate data about the PCD fracture surface appearance as a function of make-up and stress intensity during the fracture process.

Specifically this chapter details the rig development process in the context of its applicability to testing of stiff and brittle polycrystalline diamond material. Rig loading geometry, control and test parameter logging resolution capabilities are discussed. The specimen geometry, composition as well as microstructural properties such as grain size and inter-grain contiguity are discussed. Results of the validation tests performed in polymethyl methacrylate (PMMA) are presented. Early results obtained from the attempts to propagate cracks in polycrystalline diamond (PCD) are presented to show the applicability of the miniature DT rig.

The chapter continues with the details about the digital image correlation (DIC) approach employed to extract full field deformation data by the non-contact optical measurement technique called DIC, followed by the methodology of applying the JMAN approach to extract fracture mechanics parameters from the full field deformation data. The fracture toughness results obtained by the established double torsion equations approach are compared with those obtained by employing DIC and the JMAN routine.

Following the fracture mechanics parameter characterisation techniques, the chapter describes the methodology employed in an attempt to relate the fracture process observations to the surface diamond particle orientation by means of electron back scatter diffraction (EBSD) techniques. The strategy

employed in pre-mapping of the potential region of crack propagation as well as post-mapping of the features of interest after the crack has been established, are discussed. Upon completion of destructive double torsion tests, the fracture surfaces are documented in order to correlate the surface appearance and morphology to the specimen make-up and test loading parameters.

Finally the chapter concludes with the discussion of the global methodology developed for characterisation of fracture mechanics parameters of stiff, brittle materials.

4.1 Experimental procedure overview

The experimental component of the current research project can be divided into two discrete phases – i) development of the miniature DT rig and ii) the testing programme in polycrystalline diamond in-situ SEM and DIC with additional EBSD mapping. It is believed that such separation will aid the explanation of key experimental techniques as well as the methodology designed to maximise the data extracted from the limited number of polycrystalline diamond specimens.

The development of the experimental methodology with the aim of achieving controlled, stable and observable crack propagation in the extremely stiff and brittle material that is polycrystalline diamond was initiated with the evaluation of the available experimental solutions. Such evaluation revealed what existing components could be applied to the current research work and which areas would require modification and improvement to achieve the current goals. In particular, the existing double torsion rig, available within the research group, was microscope specific and could not be used in other SEM microscopes, the load path components were insufficiently stiff for controlled propagation in PCD and logging of experimental load-displacement parameters needed to be introduced. Upon completion of the identified modifications, the system was tested employing PMMA specimens as this material is cheap and is often used in fracture mechanics studies due to its brittle, isotropic fracture properties [25,26,102]. Once satisfactory performance was achieved in PMMA, attempts were made to evaluate the toughness of, and achieve controlled propagation in, PCD. These experiments were concurrently used to develop the experimental techniques necessary to apply the DIC system to the observation of the fracture process. Finally, an experimental approach was developed where slow, controllable crack propagation in PCD could be observed in-situ SEM while obtaining DT fracture toughness data and where necessary data could be

extracted simultaneously by DT equations and DIC optical techniques. The full field deformation data was processed employing the JMAN method whereby J-integral values could be extracted from the displacement data around the crack tip [57].

Furthermore, attempts were made to map the diamond-cobalt system grain orientation by EBSD techniques before and after cracks were initiated, in an attempt to investigate the dependence of the fracture path on grain orientation. Although the developed experimental approach proved to be robust in initiating and controllably propagating cracks in PCD, this was not known at the time of the EBSD mapping strategy development and thus pre-mapping of large areas ahead of the starter notch was undertaken. The pre-mapping would provide information regarding the grain orientation in the crack path even if controlled crack propagation could not be achieved.

The second phase of the experimental programme involved the development of the testing sequence which would facilitate the extraction of the most data from the limited sample numbers available. Although the sample make-up range was diverse, the number of samples was limited. Therefore, it was proposed that cracks would be grown in-situ in the SEM and if propagation was controllable, the cracks would be arrested before complete specimen failure. The sample would then be removed from the SEM in order to perform EBSD mapping of areas immediately adjacent to the crack path to further investigate any regions where the crack path had been affected by local surface grain orientation. Upon completion of the mapping process, a speckle pattern would be applied and final crack extension until final fracture of the specimen would be characterized by DIC techniques. Upon completion of the fracture parameter extraction experiments, the fracture surface resulting from crack initiation at a known stress intensity level would be recorded using the SEM.

The following sections of this chapter provide further detail into the individual steps of the described methodology.

4.2 Test specimens

During the course of the experimental programme, polymethyl methacrylate (PMMA) and polycrystalline diamond (PCD) specimens were employed. All specimens had a consistent length and width of 45x15 mm respectively, however, the thickness of the specimens was selected in such a manner is to

obtain similar load levels at fracture in both PMMA (2 mm) thick and PCD (0.5 mm) thick. The PMMA specimens were employed to develop the experimental confidence before proceeding to fracture experiments in PCD as the number of the PCD samples was limited. Once it was felt that a sufficient level of experimental confidence was achieved and successful application of additional techniques such as DIC was practiced, the experimental focus shifted to PCD. The two specimen material types are discussed separately in the following subsections for the purposes of clarity.

4.2.1.1 Polymethyl methacrylate (PMMA) specimens

The miniature DT specimens were laser machined from a 2 mm thick sheet of non-toughened Evonix PMMA manufactured to ISO 7823-2 standard. The general specimen dimensions are highlighted in Figure 4.1. The properties of PMMA are presented in Table 4.1. These specimens have a fracture toughness in the range between 0.8-1.6 MPa√m. The load corresponding to these fracture toughness levels, calculated employing Equations (2.30)and (2.31), is in the range between 30-60 N [25,70,103]. The specimens were employed to develop the experimental confidence and assess the performance of the various miniature DT rig design modifications.

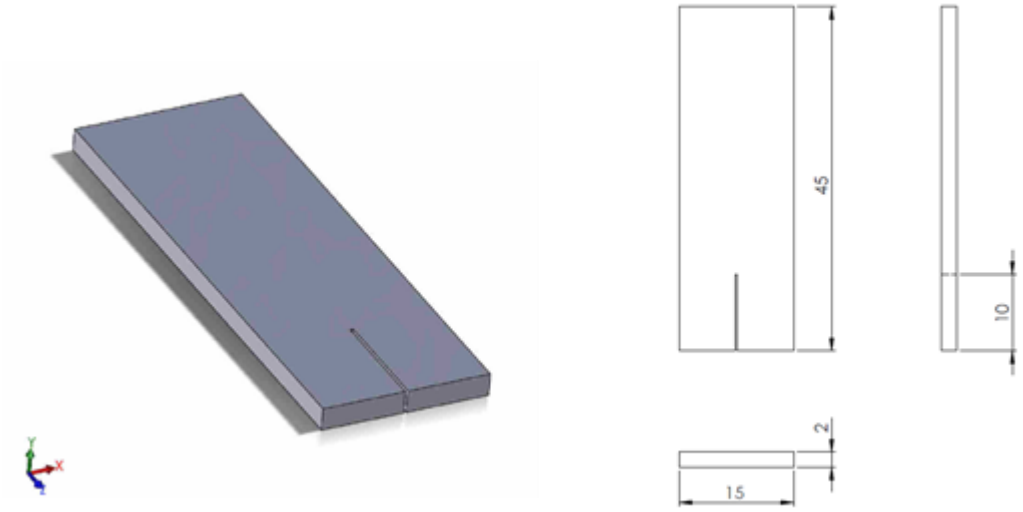

Figure 4.1 - Sketch depicting the PMMA specimen, highlighting the general dimensions of the specimen.

Mechanical properties of PMMA	
Tensile strength	75 MPa
Fracture toughness	0.8-1.6 MPa√m
Poisson's ratio	0.40
Density	$1.18x10^3$ kg/m^3
Young's modulus	2.5 GPa
Shear modulus	0.8 GPa

Table 4.1 – Key mechanical properties of PMMA.

4.2.2 Polycrystalline diamond (PCD) specimens

The polycrystalline diamond specimens were produced by Element 6. Specimen geometry as depicted in Figure 4.2. Five different PCD materials, each having a specific starter particle size, were supplied. These particle sizes are presented in Table 4.2. The specific grades were i) Grade 4 µm (2), ii) Grade 12 µm (2), iii) Grade 30 µm (2), iv) Combination Grade: 4 and 30 µm mix, 10 and 90% respectively (2) and v) industrial quad-modal grade designated as CTM 502. Table 4.2 further details the Young's modulus properties for the different grades. These values were obtained both from literature as well as directly from Element 6. The starter particle size of the industrial CTM502 grade was not known but for the fact that it is a partially leached, quad-modal grade (meaning four sizes of starter diamond powder are used).

Specimens one to four were polished by Element 6, employing the diamond impregnated lapping platen technology to a "mirror finish" in order to aid the observation of the fracture process in-situ in the SEM. The specimen surface roughness is also detailed in Table 4.2. While the samples do appear polished, observation of these under the SEM microscope reveals surface imperfections. This appears to be caused by the relative hardness difference between the

diamond and softer cobalt binder phase and the resulting surface damage due to pull-out.

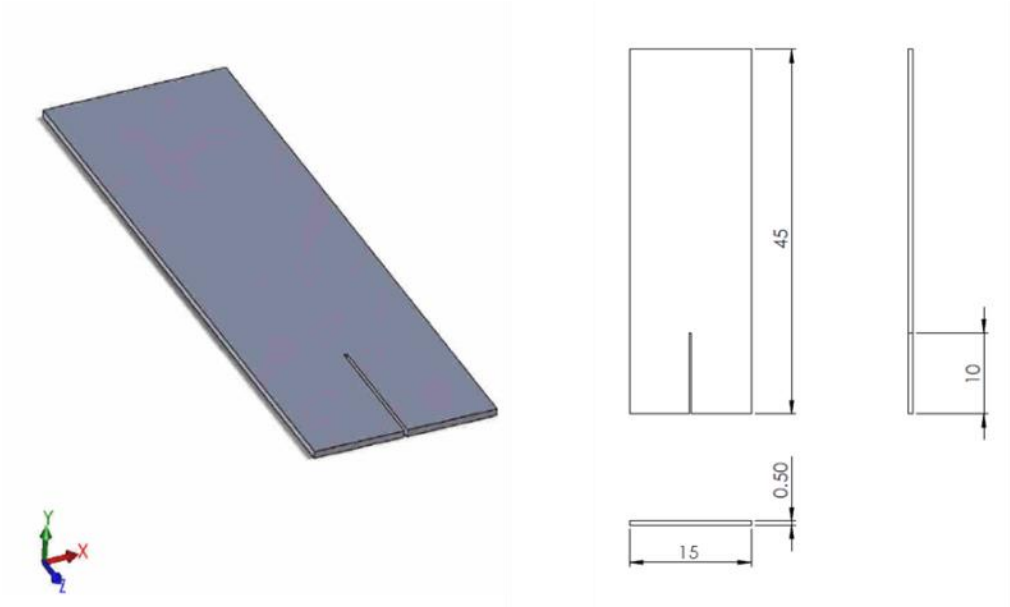

Figure 4.2 – Drawing depicting the geometry of the PCD specimens.

PCD specimen composition and Young's modulus		
Designation	**Starter particle size**	**Young's modulus (GPa)**
Grade 4	4 µm	980
Grade 12	12 µm	880
Grade 30	30 µm	1040
Grade 4/30	4 (10%) and 30 (90%)	unknown
CTM 502	unknown	unknown

Table 4.2 – Starter particle sizes and Young's modulus properties of the material grades supplied.

4.3 Miniature Double Torsion Methodology

The decision to employ the miniature double torsion approach is based on the fundamental properties of the loading geometry, the objective of studying extremely brittle material as well as the possibility of producing polycrystalline diamond samples with the required geometry. All three of the abovementioned parameters play an equally important role in defining the direction of the experimental programme in that, double torsion geometry is, nominally, independent of crack length, making it applicable to studies of very brittle and hence unstable crack systems. The miniature geometry proposed further enables two key requirements to be satisfied, namely the ability to fit into the chamber of an SEM microscope or be observed under a light microscope and employ specimen geometry that is sufficiently small to remain feasible for production from polycrystalline diamond substrate discs of 80 mm diameter – the largest diameter currently in production by the material supply partner. The following subsections detail the specific design requirements identified, the developed solutions and the resulting miniature double torsion loading system which enables experimental testing of the PCD material in an attempt to satisfy the objectives set out.

4.3.1 Overview of the design requirements

The key design requirements can be grouped into three general subgroups, namely – i) controllable crack propagation, ii) miniature rig dimensions and iii) test data recording.

The primary requirement, and indeed the core objective of the research project, is to obtain slow, controllable crack propagation in extremely stiff and brittle polycrystalline diamond material. Controlled propagation can only be obtained by a high level of control and incremental resolution of the loading crosshead and sufficient component stiffness which prevents strain energy storage which becomes available to the crack during the dynamic extension phase. Minimal misalignment and free play are required in order to ensure load application geometry repeatability. Upon crack extension, the loading mechanism must not supply additional energy input to the crack in the dynamic state i.e.it is to remain in the state which had resulted in the controlled initiation of the crack extension.

The rig dimensions need to be sufficiently small to enable experimental work inside the chamber of a typical scanning electron microscope as well as on the stage of a stereo light microscope. Position of the specimen in the rig must be such that it presents the specimen to observation from above (typical operating mode for SEM and stereo microscopes). Rig components must not protrude significantly above the specimens as this affects the capability of using the optimum working distance in the scanning electron microscope. Further to the requirement of the rig being compact, it is desirable that the rig installation is simple, to save time and prevent any modifications to the SEM.

4.3.2 **Design constraints**

The main design constraints were imposed by the geometry of the SEM LEO S1450vp microscope chamber and the need to actuate the rig internally while recording the load displacement data externally. The primary spatial constraint was imposed in the space between the sample to be tested and the electron microscope detector situated above it as depicted in Figure 4.3.

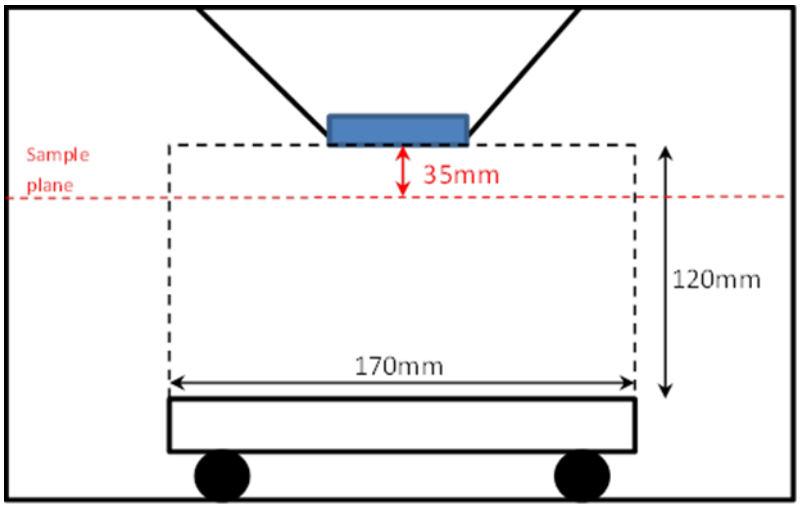

Figure 4.3- No part of the rig could protrude more than 25mm above the plane of the sample as such protrusions could impact the SEM column/detector during the panning process and cause damage to the microscope.

The LEO S1450vp microscope does not have manual controls enabled by the vacuum sealed rotary actuators which were common on older microscope units.

Therefore the rig and its motor would have to be situated internally, further reducing the available space and necessitating motor signal input through the available 15-pin D-SUB door connectors. Similarly, the wiring for the capture of the load-displacement data would be routed via the existing SEM connectors.

The stiff and brittle nature of polycrystalline diamond composites dictated the need for a high degree of control of the cross-head displacement as well as the system response to the onset of crack propagation. The susceptibility of the material to fast, uncontrollable fracture further required minimization of strain energy storage in the load sensing components such as the load cells as well as cross-head components in the load path.

Lastly, as no prognosis could be made as to the degree of the success of the application of the miniature in-situ DT methodology to slow, controlled crack propagation in PCD, the design had the potential to be iterative and therefore high cost and complex components were avoided.

4.3.3 **Existing miniature double torsion rig**

The successful application of the double torsion technique in the current project stems from a significant body of research which has preceded the current project. Prior experimental approaches, sample geometries and critical experimental parameters have been identified by researchers such as Prof. R. B. Tait [71], Dr. T.H. Becker [25] and most recently Ms. K. Rosie [70,71]. This section provides an overview of the experimental rig capabilities obtained during a research project investigating the applicability of the double torsion technique to the fracture process characterisation in nuclear graphite and its modification for the application in the fracture studies of PCD.

4.3.3.1 System overview

The miniature double torsion rig developed for in-situ SEM fracture parameter studies in nuclear graphite is depicted in, Figure 4.4 and Figure 4.5. The system consists of a stepper motor which provides drive to the 1:400 worm gear reduction gearbox which in turn transforms the rotational motion into the vertical linear travel of the cross-head via the two M3 threaded rod posts connected to the cross-head. In order to achieve 1 mm of vertical cross-head travel, 800 revolutions of the stepper motor are required as the M3 thread has a thread pitch of 0.5 mm. The stepper motor can be advanced continuously or incrementally, enabling rotational speeds in the range of 0-100 rpm or at 7.5

degree increments. The combined effect of the 1:400 gearbox reduction and the 7.5 degree incremental advance of the stepper motor, allows minimum vertical movement increments of 26 nm. Such cross-head displacement control is highly advantageous in the context of brittle material testing where displacement to fracture can be considered very small, especially so in miniature specimens. A further advantage of the worm drive gearbox is the self-locking capacity which prevents any cross-head displacement during crack extension.

Spatial constraints associated with the need to perform in-situ SEM experimentation led to the decision of creating a custom load bridge solution as such approach allows for implementation of the load application geometry, bearing balls in this particular case, into the structure of the load bridge, Figure 4.6.

The early rig design was developed to work in-situ in the Leo S440 microscope which was an older machine with manual rotary manipulators in the chamber door. Therefore, the drive to the miniature rig could be applied externally via the vacuum sealed rotary manipulators. Such configuration had advantages in that the motor could be affixed externally saving space inside the chamber, motor rotation could be easily observed and recorded to determine cross-head displacement and motor drive current did not result in electro-magnetic interference with the beam of the scanning electron microscope, Figure 4.7.

As a whole the miniature double torsion rig solution developed for the Leo S400 microscope was an elegant solution providing a means of testing materials such as Perspex and nuclear graphite. The control and fine incremental cross-head advance enabled by the high reduction worm gearbox was the key advantage of the specific design approach. Therefore, it was felt that the core design solution would be an appropriate starting point for the development of the experimental programme aiming at controlled crack propagation in PCD. However, a number of design parameters would have to be altered/improved in order to enable fracture work in the very stiff and brittle material that is PCD.

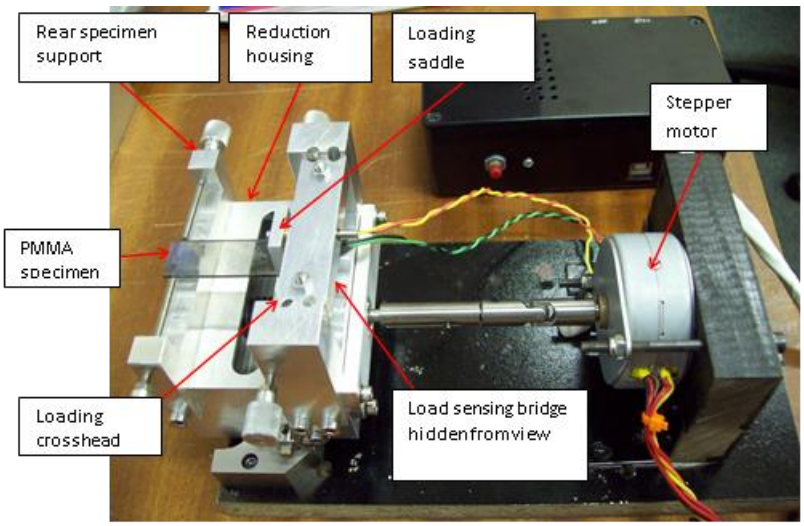

Figure 4.4 - Photograph depicting the general layout of the miniature double torsion rig employed in the nuclear graphite research project. The key components are labelled.

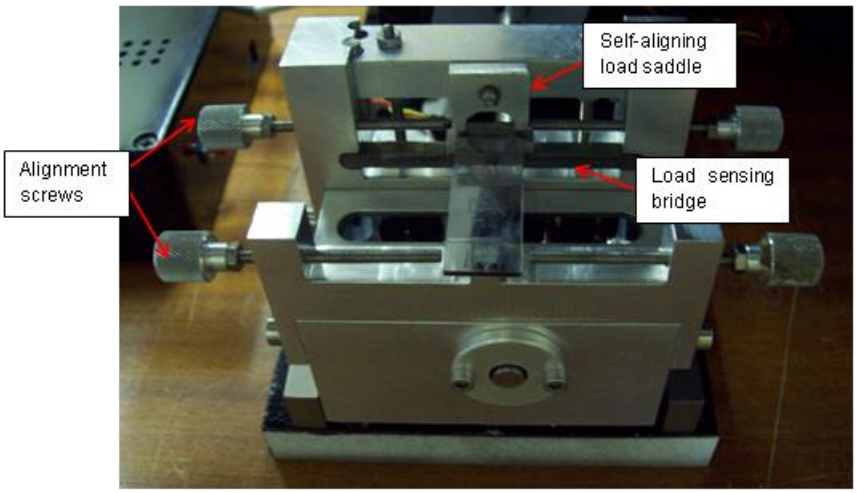

Figure 4.5 - Photograph depicting the general layout of the miniature double torsion rig employed in the nuclear graphite research project, highlighting the loading geometry employed.

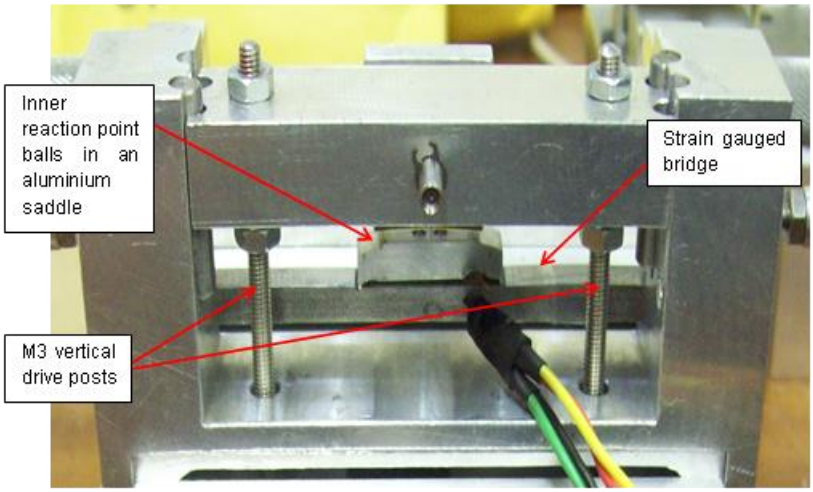

Figure 4.6 - Photograph depicting the layout of the load sensing bridge geometry, highlighting the composite approach where a half bridge strain gauge setup is applied to the load sensing beam and an aluminium saddle is employed to “float” the inner reaction balls over the upper gauge.

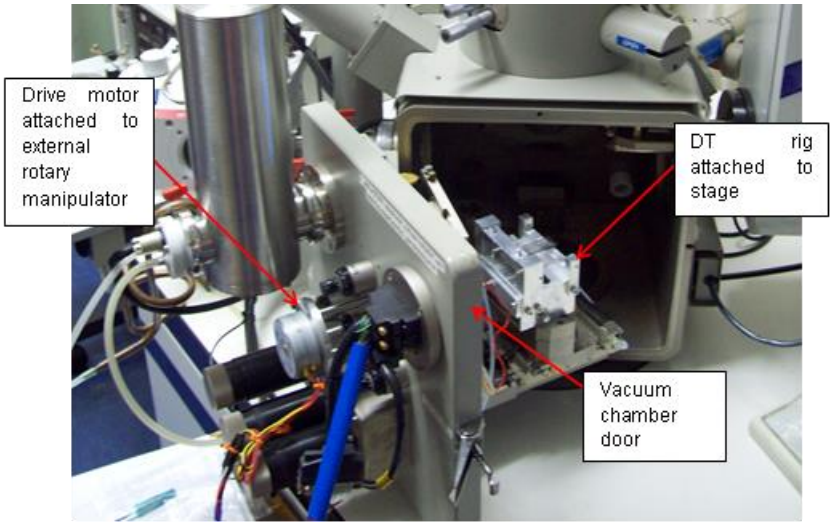

Figure 4.7 - Photograph depicting the miniature DT rig as installed in the Leo S400 SEM, highlighting the internal rig position and the external motor drive application via a rotary manipulator.

4.3.4 Evaluation of the existing double torsion rig

Having identified the key capabilities of the existing double torsion rig developed for nuclear graphite studies an attempt was made to propagate cracks in polycrystalline diamond specimens. Two initial experiments were undertaken to

i) investigate whether it was possible to propagate a crack in PCD employing the rig, ii) whether crack propagation could be observed in-situ in the SEM.

4.3.4.1 Initial attempts to achieve propagation

The initial experiments revealed that indeed the experimental approach being pursued was successful in initiating a crack in an industrial CTM 502 grade of polycrystalline diamond, Figure 4.8. However, an immediate observation was made that the cracking process is very difficult to observe due to very small rotation of the specimen arms which in turn produces very little crack opening displacement. The crack became clearly visible when its length was in the region of 15mm. This finding indicated that crack path observation by optical stereo microscopy would be challenging and that SEM observation, as initially intended in the scope of research, would be necessary to observe the fracture process. The second preliminary experiment was carried out in-situ in the SEM and was again successful in initiating and propagating the crack, Figure 4.9, however, the specimen fractured completely soon after the crack was established. This indicated that the load bridge components released additional stored strain energy resulting in instability in the extension of the crack and the resulting uncontrolled specimen failure. The experiment further indicated that a means of accurately logging of the cross-head displacement, directly in-line with loading saddle would be beneficial to prevent any errors associated with clearances between the gear train and the cross-head components.

The findings of the preliminary experiments performed revealed that it was indeed possible to propagate cracks in PCD, however, a number of areas were identified as needing improvement in order to increase the level of control as well as the quality of the experimental parameter data obtainable.

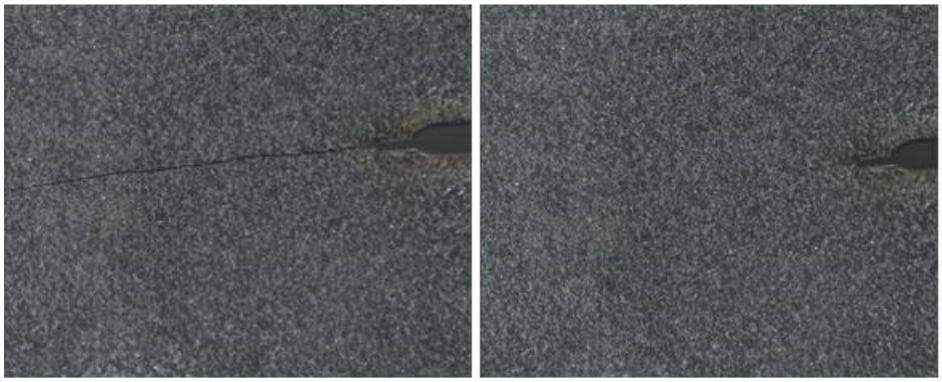

(a) (b)

Figure 4.8 – Optical micrograph (a) depicting the wide open crack at the tip of the starter notch after propagation has been achieved through approximately 50% of the sample length. The degree of closure and lack of any discernible features after load removal are highlighted in micrograph (b). This highlights the difficulty in the tracking of the crack.

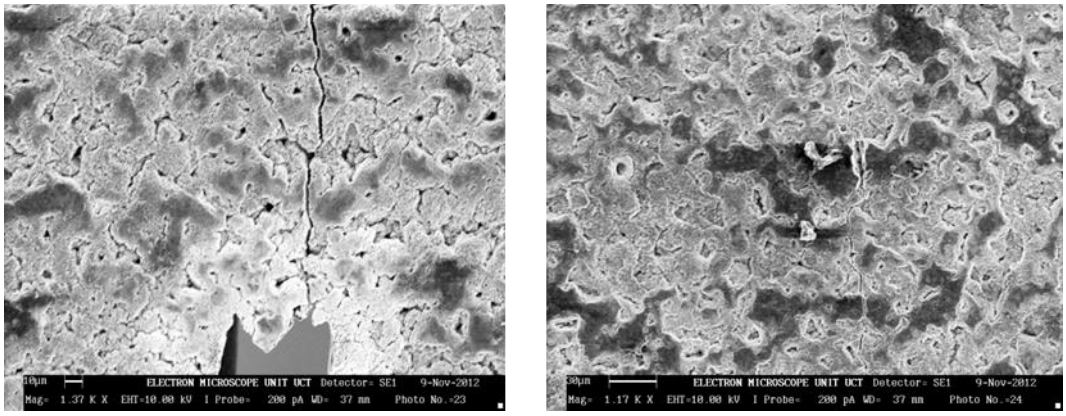

Figure 4.9 – SEM micrographs highlighting the initiation region (left) and the propagation region (right) in the first in-situ SEM PCD experiment.

4.3.5 **Miniature rig development for PCD applications**

Key areas of modification were identified to improve the rig performance with a view to its application to controlled crack propagation in the extremely stiff and brittle polycrystalline diamond materials. The key modifications which were identified were – i) ease of use in different SEM microscopes, ii) on-board actuation, iii) development of a stiffer load bridge and iv) improvement of the cross-head displacement logging. The four areas of modification are presented

in an order which best describes the chronological order of development as well as the identification of each modification need.

4.3.5.1 Applicability to different SEM microscopes

During the initial experimental phase of evaluation of the applicability of the existing equipment to controllable initiation and propagation of cracks in PCD, the Leo S400 SEM experienced a component failure which rendered the microscope repair unfeasible. Due to the rig design solutions incorporating the specific features of the Leo S400 microscope, no further experiments could be performed until such time that the rig could be re-designed to be employed in the new, different SEM microscope. Such failure demonstrated that to prevent similar problems in future, the experimental approach should be transferable between various microscopes and thus should not rely on technological features specific to one particular microscope. This led to the decision to integrate the drive motor with the step down gearbox body and locate both components on a buffer base which could have multiple attachment holes patterned for installation onto the XY-stage of any typical SEM microscopes. The resulting solution concept is depicted in, Figure 4.10. The final design resulted in the following improvements:

- The double torsion rig became independent of SEM employed.
- Motor torque reaction path was retained with the rig body.
- The rig could be installed and removed in a matter of minutes.
- The same solid buffer base can be attached to a table top for observation by **optical** microscopes and DIC equipment.

Figure 4.10 - Photograph depicting the in-situ DT rig, highlighting the new actuation approach (left), where the motor is placed “on-board” the rig to prevent the need for complex cardan shaft arrangements and expensive rotary throughput development. The native Z-axis stage adjustment and “stage touching” alarms have been removed from the SEM to facilitate optimized working distances.

4.3.5.2 Load bridge stiffness and sensitivity

Initial double torsion experiments in PCD have revealed that rig stiffness and hence the potential to store and release strain energy, are critical to control crack propagation in PCD. Therefore, stiffness is ultimately sought in the load path. However, stiffness is obtained at the cost of load sensing circuit sensitivity and thus a careful balance needs to be maintained in order to resolve sufficiently small load changes while not allowing significant uncontrolled crack propagation due to high bridge compliance. Evaluation of the available load cell technologies revealed that many miniature load cells do not provide a stiffness advantage versus a currently employed beam strategy. Miniature load cell bridges are produced from brass materials, which have a lower modulus than steel, providing increased sensitivity in the range of 0-100 N which results in increased load path compliance. In cases where stiffness is sufficient, geometrical constraints remain, and use of existing load cell solutions requires gearbox modifications. Therefore, the load sensing system was changed to

employ stiffer beams, which would allow 0.5 N incremental resolution of loads up to the maximum level of 100 N.

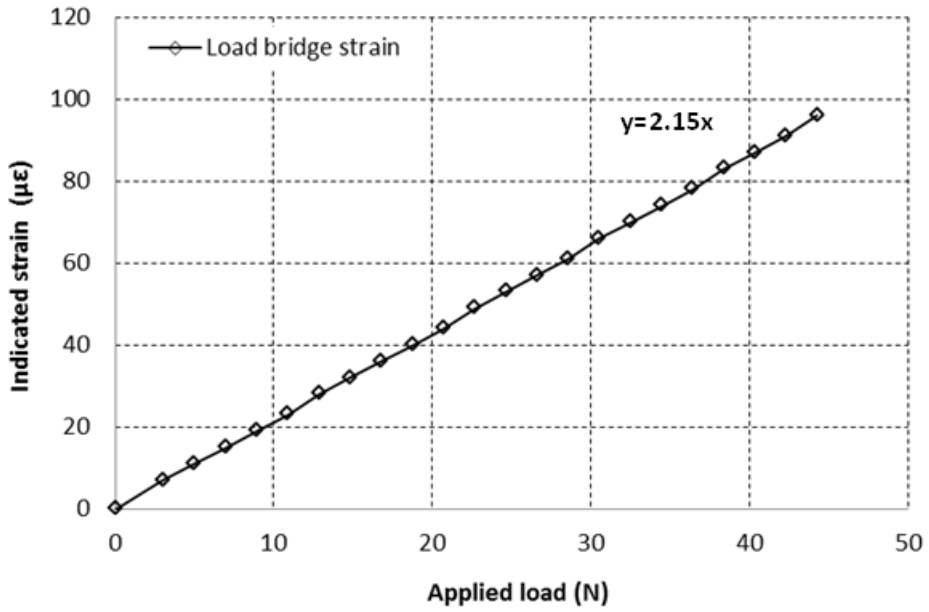

Figure 4.11 – Plot depicting the load bridge calibration data, highlighting the linear behaviour.

4.3.5.3 Cross-head position logging

The height constraints associated with the microscope chamber dimensions and requirement to not have anything protruding significantly above the specimen plane, resulted in the need to develop a means of accurately obtaining cross-head displacement data without the use of an LVDT. Typical LVDT dimensions prevent their installation on the rig during in-situ work as the working distance for best beam focus is in order of 35 mm. Therefore, a clip gauge analogy was employed, where a slender flat beam measuring 40x12x0.8 mm, was instrumented with a strain gauge bridge and calibrated to obtain an in-situ cross-head displacement sensor, Figure 4.12. The design enabled reliable measurement of the vertical cross-head displacement with an incremental resolution 1.7 µm.

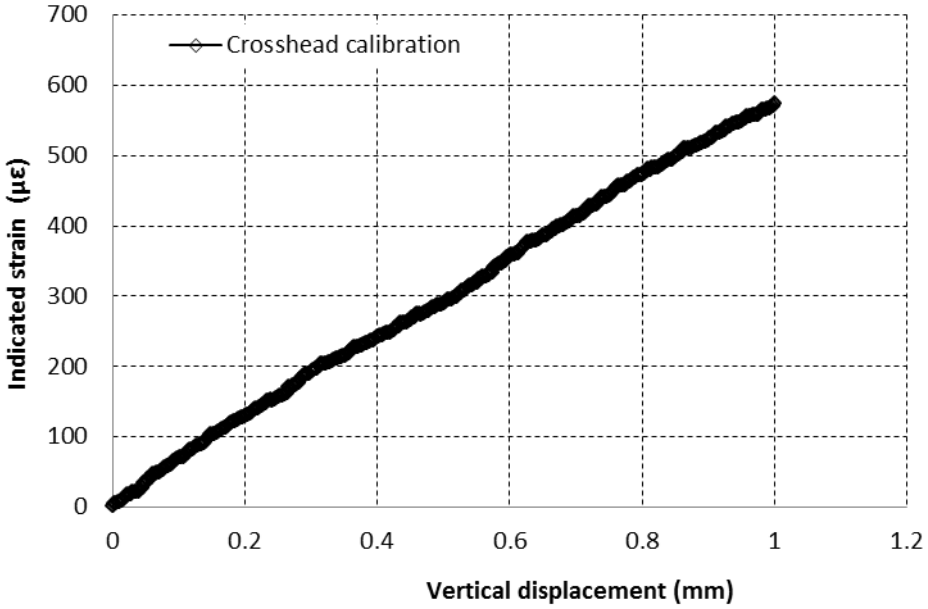

Figure 4.12 - Chart plotting an example of the calibration data for the cross-head displacement gauge, highlighting the linearity and resolution of the displacement gauge.

4.3.5.4 Connectivity and data logging

Employing the new rig methodology, the control of the rig as well as the signal data from the cross-head displacement and the load sensing bridge were channelled through the 15 pin D-SUB connectors of the SEM microscope. Because it is often useful to perform testing in a light microscope (or other observation means), the three electronic elements, namely the cross-head displacement, load sensing bridge and the motor were equipped with quick connectors which enable connectivity in the SEM or the use of the rig elsewhere simply employing its adapter base.

The load sensing and cross-head displacement bridges were excited and logged by means of a Vishay Micro-Measurements P3 unit which provided ease of use but more importantly robust filtering and lack of drift. The data depicted in Figure 4.13 highlights the low level of system noise and drift. The noise level did not exceed the 0.5 N (≈1 μStrain) resolution level provided by the P3 strain indictor while a total system drift over a period of one hour, without temperature compensation, did not exceed a level of 1 N.

While development and evaluation of high speed strain logging systems was attempted and two systems were tested, the noise effects associated with electron microscope equipment as well as ambient noise sources have made these systems less desirable at the current phase of the research project where the methodology was to be tested rather than refined.

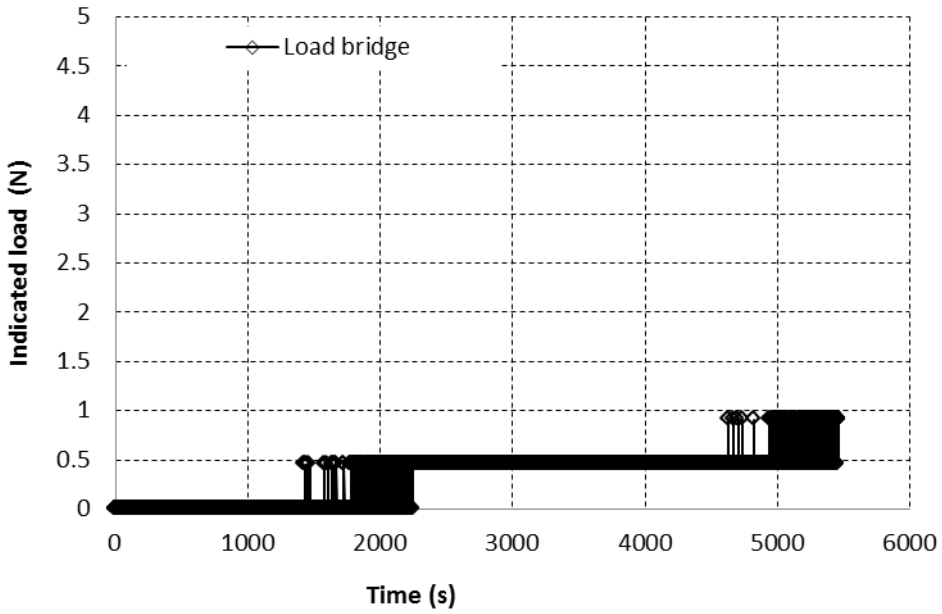

Figure 4.13 – Plot highlighting the noise and drift performance of the load measuring system.

4.3.5.5 Load bridge compliance correction

Due to the non-standard geometry of the EDM machined bridge, as depicted in Figure 4.14, a theoretical solution could not be easily obtained in the region of the strain gauge transducer. Therefore, the bridge deflection was measured during the calibration process, employing a dial indicator, to obtain the deflection under load. The results obtained during such calibration are plotted in Figure 4.15. It can be seen from the plot that the data does not look perfectly linear while it is expected that the bridge will have a linear response at low load levels. The non-linearity experienced is believed to be caused by the in-sufficient accuracy of a dial gauge in measuring individual deflection steps. However, the average load-deflection coefficient obtained by performing a linear fit to the data is believed to be a reliable method of obtaining the bridge stiffness coefficient of 2.54 MN/m.

Due to the stiffness, and the resultant small deflections of the miniature DT specimens, the experimental displacement data has to be corrected to account for the abovementioned bridge compliance effects.

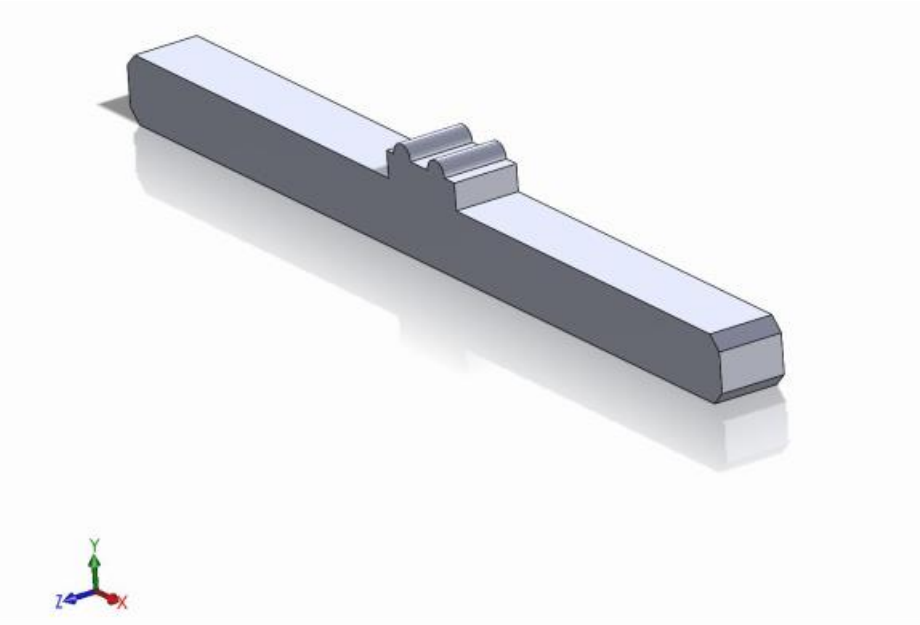

Figure 4.14 - EDM machined load bridge geometry, highlighting the fact that the bridge load- deflection coefficient cannot be easily calculated employing theoretical calculations.

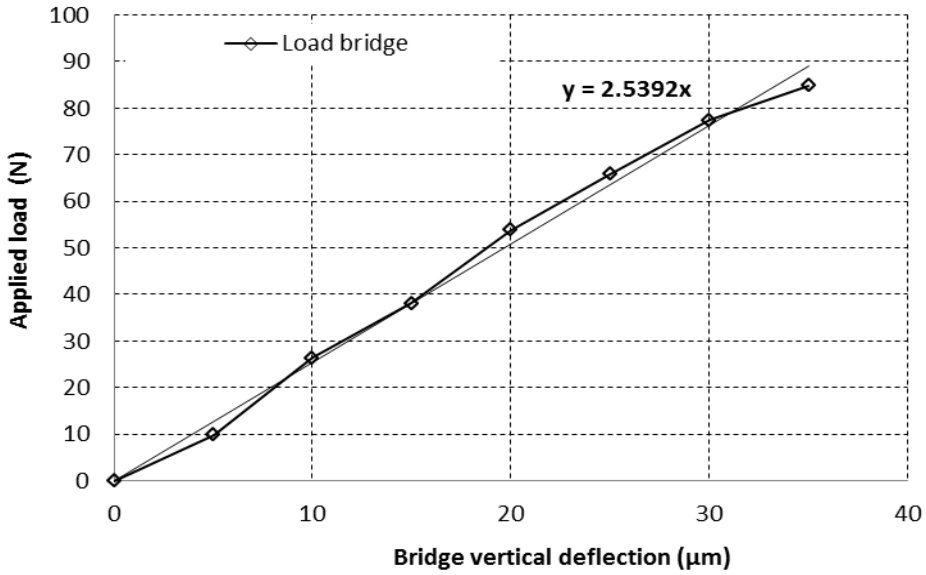

Figure 4.15 – Plot depicting the vertical bridge deflection under load.

4.3.5.6 Summary of rig modification and resulting capabilities

Having presented the key modifications individually in the preceding sections, a summary of the rig modification process as well as the resulting capabilities are summarised below.

One of the most important changes to the rig and the whole experimental approach as a whole has been the facilitation of rig use in various SEM microscopes. This has been achieved by incorporating the drive motor into the rig gearbox housing and actuating the rig externally by electronic signals only. Such modification has two key advantages, i) the rig system can be easily adapted to another SEM microscope by machining a mounting hole pattern consistent with new microscope's X-Y-stage and ii) because the motor is situated internally, electrical connectors through the microscope door, as opposed mechanical drive components, is all that is required for rig actuation. Furthermore, attachment of the drive motor to the gearbox enables reaction of the motor torques within the rig body, preventing the need for specific fixation of the rig, simplifying the use of the rig when observed on the benchtop by stereomicroscopes or digital image correlation camera systems.

Modification of the load bridge stiffness has resulted in the reduction of the strain energy storage which was detrimental to the controlled propagation of cracks in brittle materials due to additional, uncontrollable energy release during crack extension. Modification of the load transfer contacts from point (balls) to line contact (cylinders) in the saddle and load bridge (top, outer and bottom, centre contacts respectively) has improved the success rate of centred crack propagation along the specimen length. This is believed to be the result of improved accuracy of the component fabricated by electron discharge machining as well as fewer loose parts making up the system.

A new cross-head displacement logging methodology was developed to detect cross-head movement directly above the saddle centreline, minimizing the potential errors associated with employing the motor revolution monitoring approach which is susceptible to errors associated with the clearances and deflections of the components in the load path.

Finally, improved data logging was enabled by employing a dedicated Vishay Micromeasurements P3 strain gauge amplifier and indicator unit which incorporates very good levels of noise protection and filtering. The system also showed very good levels of drift consistency which were considered important in

the context of in-situ SEM tests which lasted up to three hours per specimen. Signal noise levels during experiments were identified to be within 1-2 µm which equals to a force range of 0.5-1 N and a total system drift per hour was within 1-2 N.

Overall, the concomitant effect of the effected modifications significantly improved the performance of the system and better enabled the experimental attempts of studying the very stiff and brittle polycrystalline diamond material.

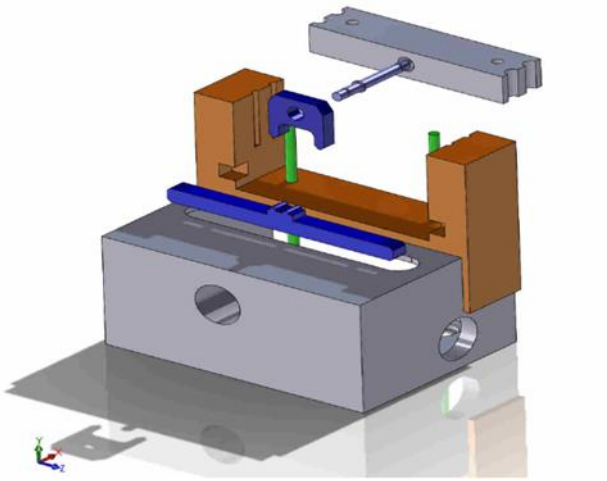

Figure 4.16 – Exploded CAD view of the miniature rig.

4.4 Evaluation of the miniature DT rig

The modified rig was first tested employing the PMMA specimens to investigate the overall system performance such as motor actuation, data and displacement logging. Upon successful completion of these tests, the PCD samples were used. The results detailing the findings of the tests performed in the two material types are presented in the two following subsections.

4.4.1 Testing in polymethyl methacrylate (PMMA)

The figure below displays a typical load displacement curve obtained during the testing of PMMA material, Figure 4.17. Employing the equations presented in Section 2.3.1. of this document, the stress intensity corresponding to the applied load can be calculated and is plotted in Figure 4.18.

Due to the limited number of PCD specimens available, PMMA specimens were also employed in the evaluation of the consistency of the results obtained when employing the newly developed rig. Results from a series of ten tests undertaken in 2 mm thick PMMA specimens are plotted on the same chart depicted in Figure 4.19. The specimens were machined from a single sheet of 2 mm PMMA in order to eliminate any potential differences in the properties of the PMMA. The statistical analysis of the results presented in Table 4.3 revealed a good degree of consistency in the results indicating that the rig produces repeatable experimental data. The standard mean error for the series of the experiments was calculated to be 0.017 MPa√m with the standard deviation being equal to 0.051 MPa√m.

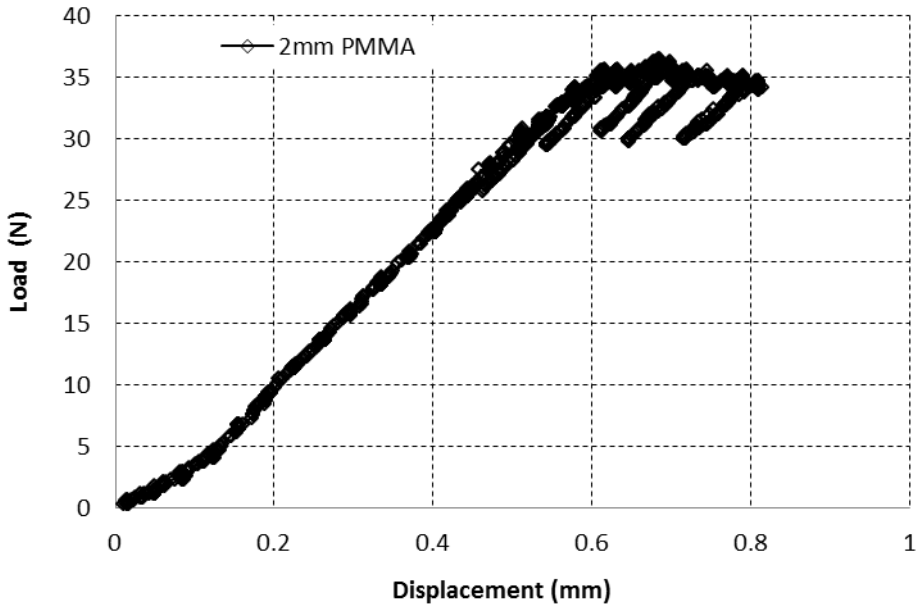

Figure 4.17 – Plot depicting the load displacement data obtained during a fracture test of a 2 mm PMMA miniature DT specimen.

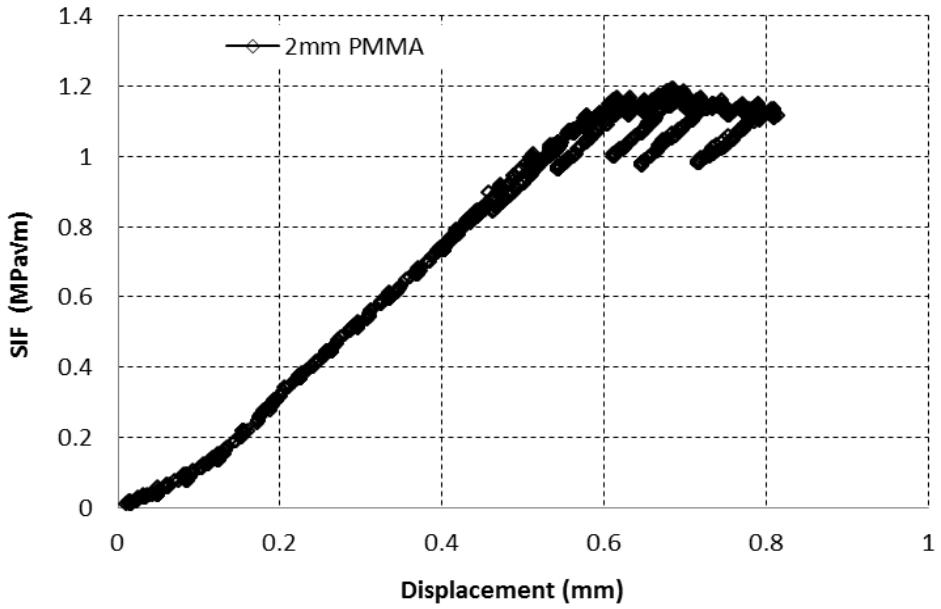

Figure 4.18 – Plot depicting the stress intensity values calculated from the load displacement data presented in Figure 4.17.

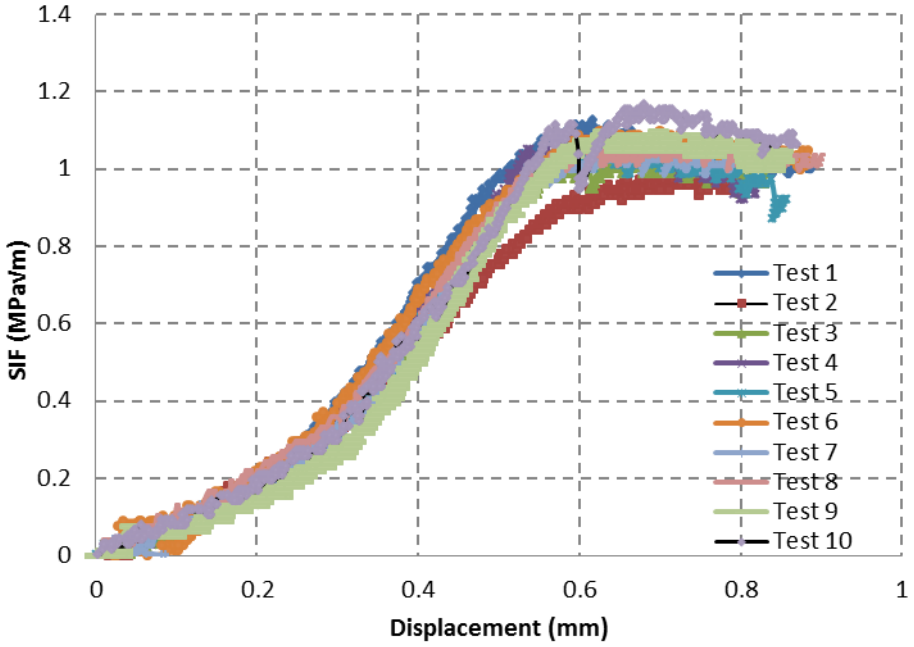

Figure 4.19 – Plot depicting the SIF results of ten crack propagation experiments in 2 mm PMMA material.

2mm PMMA Specimen No.	Fracture toughness (MPa√m)
1	0.996
2	0.983
3	0.970
4	0.932
5	0.890
6	1.020
7	1.008
8	1.021
9	1.047
10	1.059
Average Toughness (MPa√m)	**0.993**
Standard Deviation (S)	**0.051**
Standard Mean Error (Sxbar)	**0.017**

Table 4.3 – Table summarizing the result of the ten tests employed to evaluate the consistency of the data generated employing the miniature DT rig.

4.4.2 Testing in polycrystalline diamond (PCD)

Initial testing of a PCD specimen revealed that the miniature rig was capable of controllably initiating and controllably propagating a crack. The results of a validation test carried out in a CTM502 industrial, quad-modal PCD grade, Figure 4.20, revealed that the rig stiffness was sufficient to overcome the notch toughness effect associated with notch geometry and then consistently propagate the crack into the constant stress intensity region.

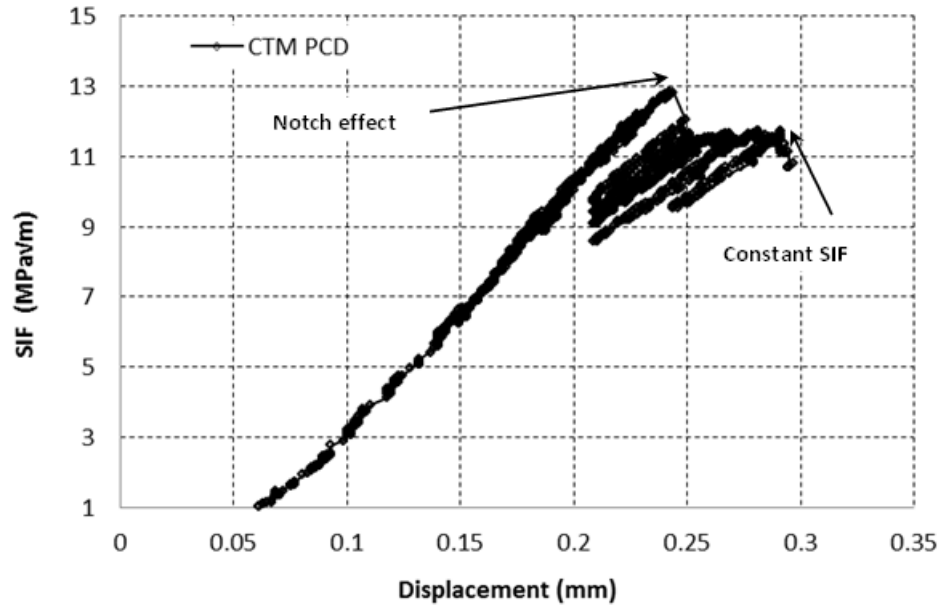

Figure 4.20 – Plot depicting the SIF-displacement data for a test carried out in CTM502 PCD, highlighting the notch toughness effect (red arrow) as well as controllable propagation in the constant stress intensity region.

4.5 In-situ SEM fracture process observation

A key objective of this project was to enable in-situ SEM observation of the fracture process. The miniature DT rig was installed inside the Leo 1450VP microscope and cracks were controllably initiated, grown and then shut down in all available grades of PCD samples.

4.5.1 Overview of the experimental procedure

The components involved in the in-situ SEM testing are depicted in Figure 4.21. The experimental programme entailed the initiation and propagation of cracks in all grades of the PCD material supplied. Each test was initiated by inserting a specimen in the rig while the rig was outside the microscope. The specimens were manually aligned with respect to the loading points of the miniature DT rig employing an engineer's square, accurate to 16 µm over a length of 150 mm and an offset square of similar accuracy. A preload of 0.5 N was applied to prevent specimen movement. The rig was then inserted into the microscope and fastened to the microscope stage. Having performed all the requisite SEM start-up procedures, such as pumping to achieve vacuum and aligning the beam via

gun parameters, an initial image of the starter notch root radius would be obtained in each case, Figure 4.22. Once an image of acceptable quality was obtained, the fracture initiation process was undertaken by advancing the miniature DT rig loading mechanism in steps of 0.5 N or less. The rig was stopped after each step, for purposes of crack increment control as well as to minimise any electromagnetic interference experienced by the microscope beam. A micrograph was captured for every such step and a further load advance was performed. Once crack initiation was observed, Figure 4.23, the crack was propagated across the screen at which point the view was panned to track the tip of the crack.

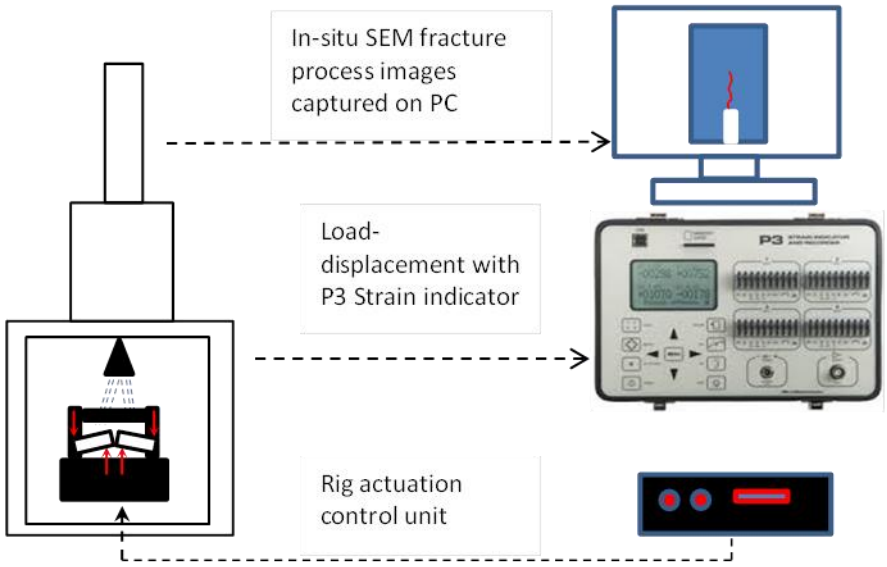

Figure 4.21 – Layout of the components employed during the in-situ SEM miniature double torsion fracture experiments.

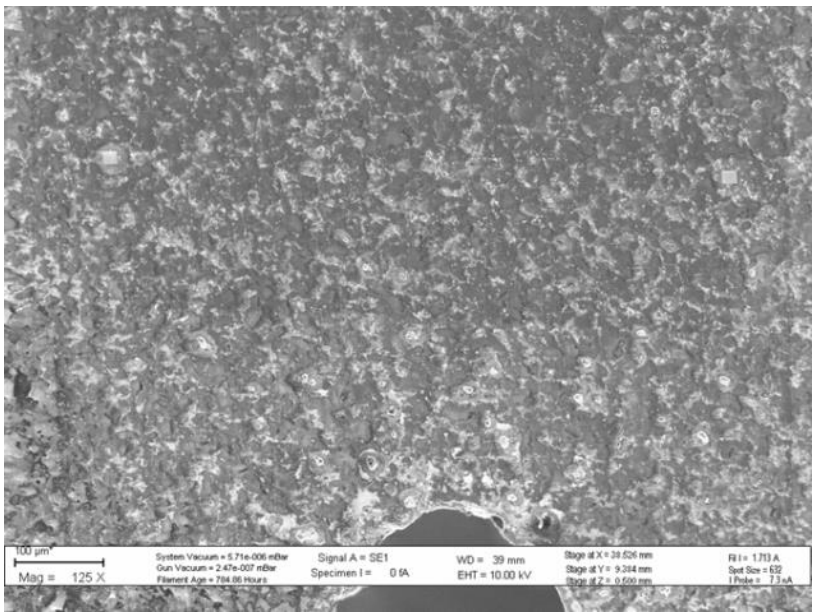

Figure 4.22 – Micrograph depicting the root of the starter notch prior to the initiation of loading.

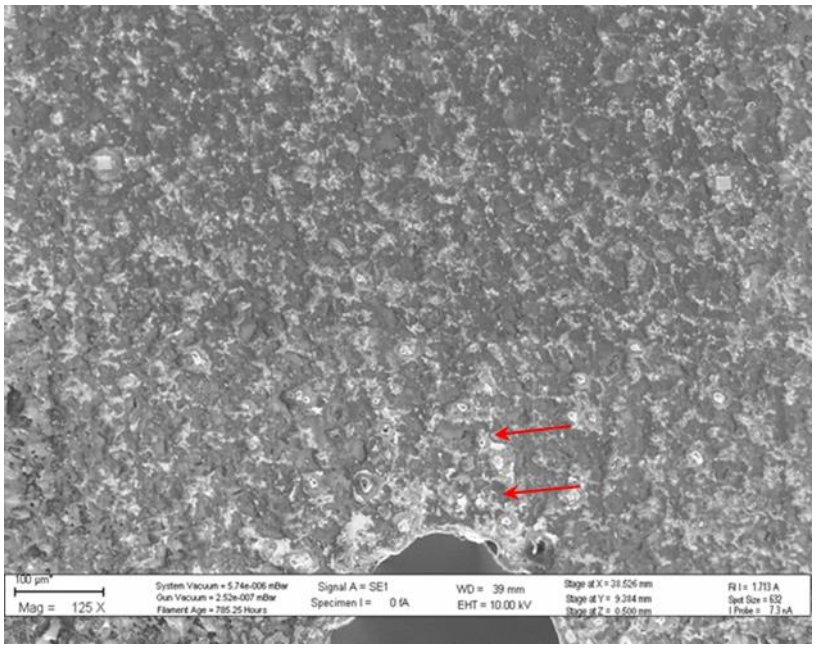

Figure 4.23 – Micrograph depicting the initiation of the crack. Note the arrows as the crack is difficult to observe.

4.5.2 Fracture phenomena observation

Various propagation phenomena can be observed when capturing the crack propagation process in-situ SEM. Phenomena such as crack tip deflection, crack jumping and formation of bridging artefacts can all be observed when the crack front is observed as it develops. Some of these features are lost when inspecting an already formed fracture surface of a broken specimen. It is believed that therein lays the additional value of performing the crack propagation experiments in-situ. An example is shown in Figure 4.24, where the crack front advanced into a grain causing fracture along what appears to be a preferential cleavage plane (red arrow). However, at the edge of the grain, there is a tougher region associated with a cobalt binder pool (bright constituent in the micrograph). This feature causes the crack to terminate (at least on the surface of the specimen) and proceed along a path of lower fracture resistance. Once gross fracture occurs, such features are no longer easily distinguishable.

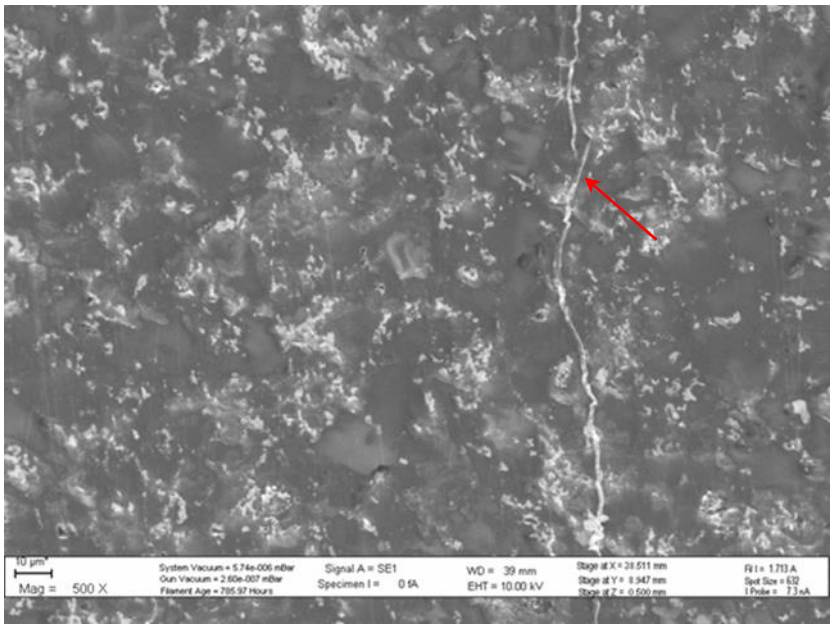

Figure 4.24 – Micrograph depicting a crack deflection feature caused by microstructural features in 30 µm PCD specimen.

4.6 Full field deformation methods

In an attempt to extract further information regarding the mechanisms of specimen deformation as well as the underlying fracture processes, a full field deformation method, namely DIC, was employed. The following section

describes the DIC system employed in the current project followed by the application of a new experimental technique called JMAN, which enables the extraction of the fracture toughness parameter from the deformation data obtained by DIC [57].

4.6.1 Digital image correlation approach

The photograph depicting the camera system and the diagram describing the components are depicted in Figure 4.25 and Figure 4.26, respectively. The digital image correlation system employed in the current project was a commercial system supplied by La Vision, employing the Da Vis 8.3 software package. The system consisted of a stereo vision camera tripod with two E-Lite 5 megapixel full CCD chip cameras and LED lighting driven by La Vision parallel trigger unit (PTU) in order to synchronise the cameras and the lighting. In order to obtain the magnification and the field of view applicable to the experiment carried out in the 45 x 15 mm miniature DT specimens, Edmunds Optics tele-centric lenses with a fixed focal length of 75 mm were employed. The PTU was used further to synchronise the capture of the image and load-displacement data. This was achieved by providing an analogue signal from Quantum MX440 multipurpose strain gauge amplifier to the analogue-to-digital converter of the PTU unit. The miniature double torsion rig was affixed to a table below the DIC system to prevent any displacement with respect to the camera system.

Similarly to the experiments carried out in-situ in the SEM, the now pre-cracked miniature DT specimens were inserted into the DT rig and pre-loaded to a load level of 0.5 N. The DIC system was set to acquire an image at a frequency of 1 Hz for 1000 seconds, generating a maximum of 1000 images. The number of images to capture was chosen to exceed the count at which the samples typically failed. Once the specimen failed, the image acquisition procedure would be interrupted and data stored for processing.

Figure 4.25 – Photograph depicting the stereo camera rig employed to capture the images for the DIC analysis.

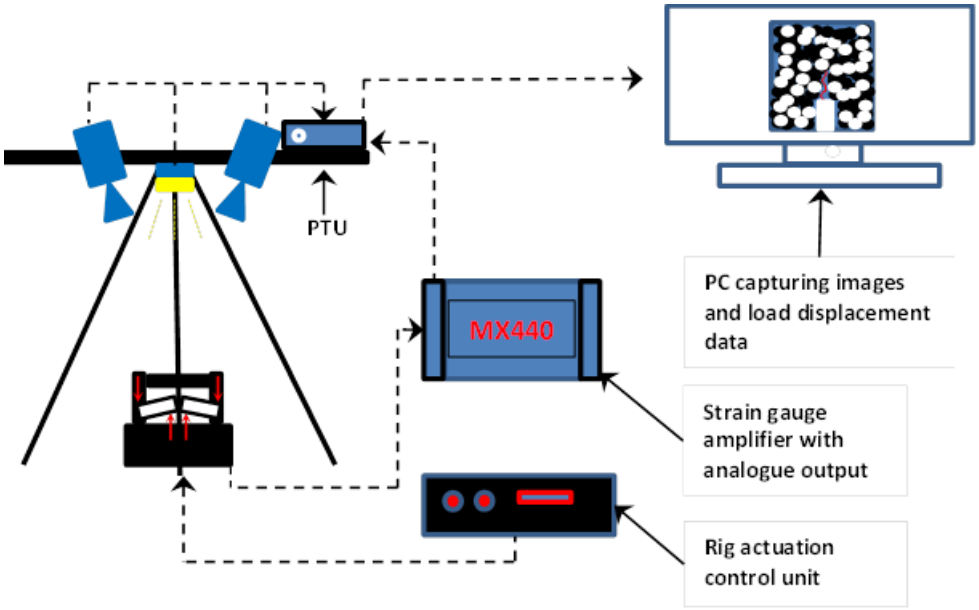

Figure 4.26 – Diagram depicting the components making the in-situ DIC miniature double torsion fracture experiments.

4.6.2 Speckle pattern

In order to enhance image contrast required for accurate subset correlation through DIC, a random speckle pattern was applied to the specimen surface. The paints selected for this purpose were the Matt Black 911079 and Matt White

911069 Plascon Aerolak series spray paint. In the case of the PMMA specimens, the surface of the specimen was initially sprayed with black paint in order to achieve an opaque specimen, followed by the introduction of the white overspray, which provided the desired speckle pattern. The opaque specimen prevented light transmission from the rear of the specimen which can cause errors or complete decorrelation in the DIC process.

All speckle patterns were applied manually using an aerosol can in such a manner as to obtain a uniform distribution of fine unique features which would aid the computation of their displacements, Figure 4.27. By lightly depressing the aerosol nozzle approximately 300 mm away from the specimen surface, a fine mist of paint droplets was created that adhered to the black base coat to form the fine speckle pattern.

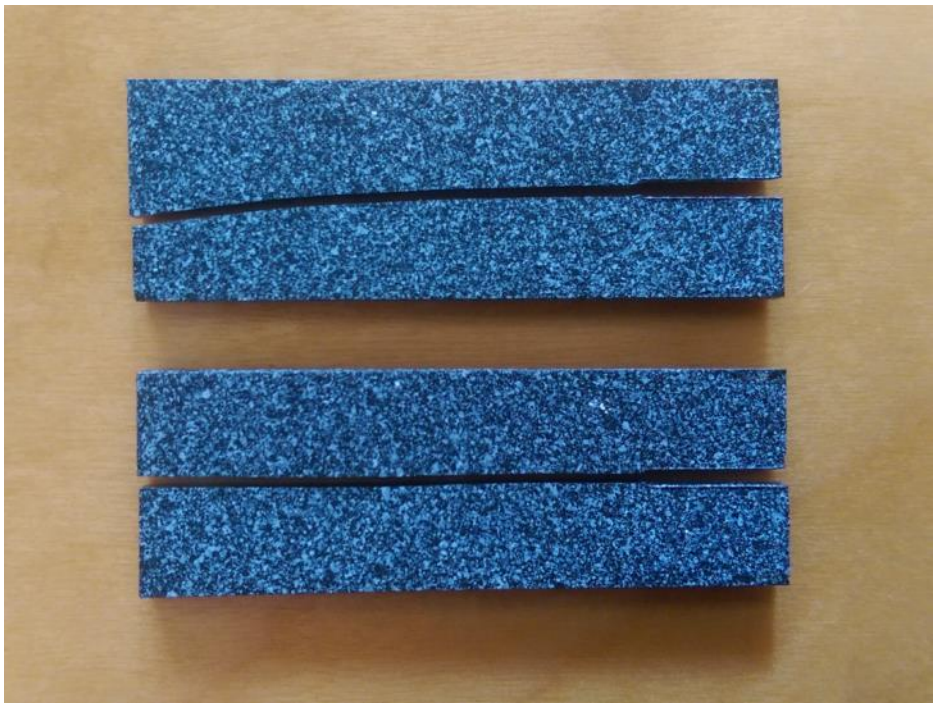

Figure 4.27 – Photograph depicting two PMMA specimens, highlighting the speckle pattern obtained by the described paint spraying method.

4.6.3 System calibration

In order to correlate the acquired image pixel dimensions to real metric dimensions of the features in the image, a relationship between these

dimensions needs to be established. This can be achieved through a camera calibration process which involves extracting a combination of intrinsic and extrinsic parameters based on a simplified camera model [108].

The current work employed the pinhole camera model in the calibration of the 3D-DIC system depicted in Figure 4.25. The pinhole camera model is depicted in Figure 4.28, with the pin hole aperture positions highlighted in the image and correspond to the image centres. It is considered to be an ideal model based on perspective projection which is commonly applied to calibration algorithms [76]. The imaging characteristics of the camera modelled employing this methodology can be described by five parameters. These parameters are i) the pinhole distance *(phd)*, ii) the two-dimensional location of the intersection of the optical axis and the sensor plane, defined as the centre of the image (C_x, C_y), iii) a lens distortion factor, k, and iv) the aspect ratio, λ. These five parameters describe the camera properties and are referred to as *intrinsic* parameters. Further six *extrinsic* camera properties are $\alpha, \beta, \gamma, X_0, Y_0, Z_0$ describe the spatial orientation of the camera system. The eleven parameters are required to map the real world coordinate system to the camera coordinate system[77].

A total of seven coordinate systems are used to describe the location of points in space and in images. The optical centres or pinhole apertures are located at the points $\hat{C}_1$ and $\hat{C}_2$ which are also the origins for the spatial coordinate systems *Xcam1, Ycam1, Zcam1* and *Xcam2, Ycam2, Zcam2* for Camera 1 and Camera 2, respectively. The mapping of the same point in three-dimensional space to the two-dimensional image planes is achieved by relating the cameras to the global coordinate system, *Xsys, Ysys, Zsys* which serves as the bridging coordinate system for the two cameras. The four remaining coordinate systems are used to transform the positions from pixel coordinates in each camera into physical dimensions in the cam1 and cam2 systems. The calibration process determines the position and orientation of the system wide coordinate system with respect to a calibrated grid and determines the location of each of the two cameras with respect to the global coordinate system. The relationship between the camera systems and the global system is determined by initially aligning the camera and global systems followed by re-mapping of the camera positions employing the use of a rotational matrix. The matrix is developed by consecutive rotation of the system coordinate system about i) α about Z*cam,* ii) β about *Xcam* and iii) γ about *Ycam* [77].

The process of calibration involves the determination of six intrinsic camera properties including the *X* and *Y* coordinates Px and Py of the principle point C_0, the focal length f, third-order and fifth-order lens distortion correction coefficients $\kappa 1$ and $\kappa 2$ and the scaling factor λxy that relates the row and column pixel dimensions of the sensor to a metric value [74,105]. Moreover, the 3D translational Tx, Ty, Tz and rotational Rx, Ry, Rz positioning of the cameras relative to the object are the extrinsic parameters. Both types of parameters are obtained by a stereovision-combined calibration technique which employs the use of a two-level precision LaVision 058-2 calibration plate, as shown in Figure 4.28 [79]. For detailed derivation of the rotation matrix, *[R]*, translation vector, *[T]*, refer to Sutton [77].

Following the calibration process, the computed parameters can then be used together with a triangulation approach to calculate the 3D coordinate of a system point that matches the corresponding stereo image locations [78]. Since the model is an idealisation, first-order optics are assumed in which image distortions and other aberrations caused by lens geometry and larger aperture sizes are not fully accounted for [109]. The calibration procedure described is followed by the LaVision Davis 8.3.1 DIC software which was employed to capture and process the DIC data in this project.

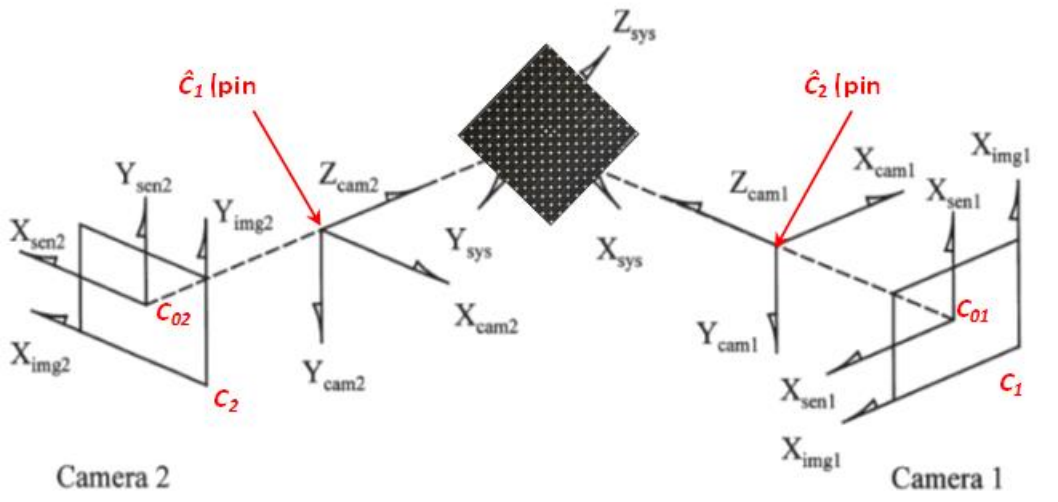

Figure 4.28 – Pinhole camera model described by Sutton [77] for the purposes of calibration of a stereo DIC system.

4.6.4 **Application of JMAN to a theoretical displacement field.**

In order to provide an example of the application of the JMAN methodology to calculate the J-integral, a theoretical displacement field can be plotted. The displacements are calculated by employing the equations formulated in the Williams analysis [45]. The following equations, in cartesian form, are employed to generate the displacement field for an arbitrary stress intensity level of ***K = 1 MPa√m***.

$$U_x = \frac{K_I}{2\mu}\sqrt{\frac{r}{2\pi}}cos\frac{\theta}{2}\left[k - 1 + 2sin^2\left(\frac{\theta}{2}\right)\right] \quad (4.1)$$

$$U_y = \frac{K_I}{2\mu}\sqrt{\frac{r}{2\pi}}sin\frac{\theta}{2}\left[k + 1 - 2cos^2\left(\frac{\theta}{2}\right)\right] \quad (4.2)$$

Where U_x and U_y are displacements in the *x* and *y* directions respectively, *r* and *Θ* are the polar position coordinates with respect to the crack tip, *μ* is the shear modulus of the material and factor *k = 3-4v* and *k = (3-v)/(1+v)* for plane strain and plane stress respectively [45].

Once the theoretical field is plotted, Figure 4.29, the position of the crack tip, and hence the point about which the area contour integration occurs, are selected, Figure 4.30. The JMAN code evaluates the J-integral along the area contour, starting from the crack tip and moving outwards and the results begin to converge once the contour moves away from the tip of the crack, Figure 4.31.

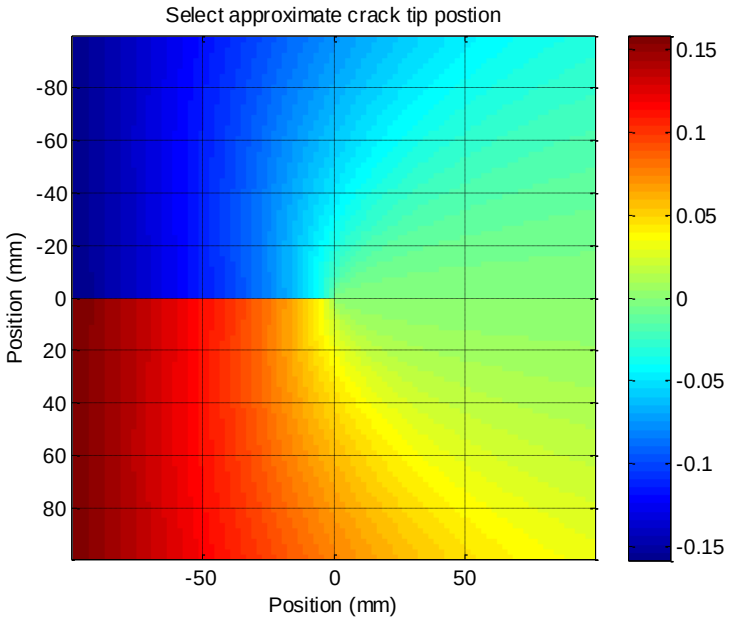

Figure 4.29 – Theoretical displacement field calculated employing the Williams analysis solution for the stress intensity level of 1MPa√m. The position of the crack tip has to be selected from the plotted field (in the theoretical case the position is at the origin of the plot).

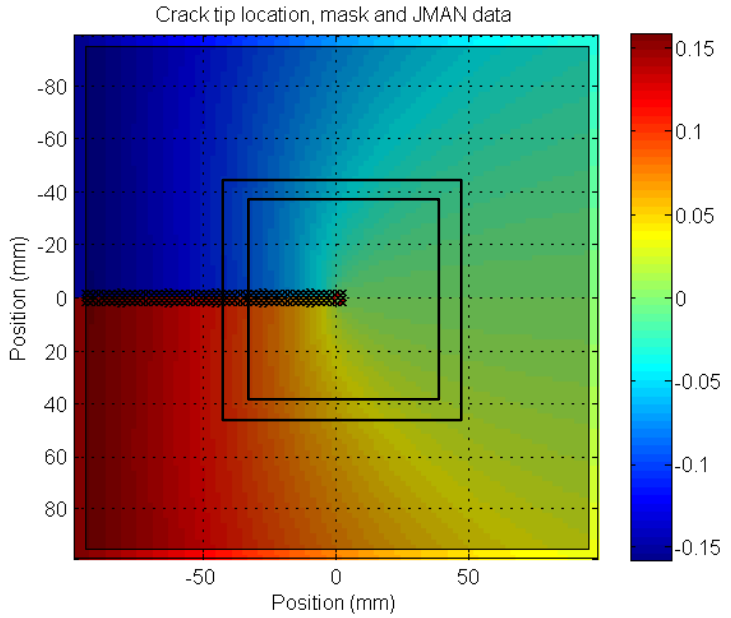

Figure 4.30 – Plot depicting a square integration region (grey square region) applied to the displacement field with elements adjacent to the crack faces masked out to prevent the use of erroneous data associated with the crack. An example of an area integral contour is also shown.

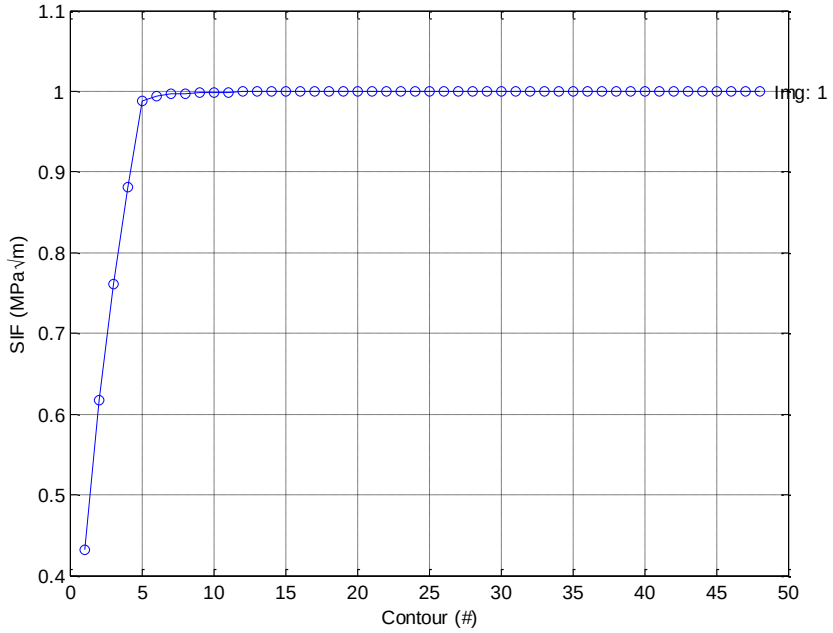

Figure 4.31 – Plot depicting the stress intensity value calculated by the application of the JMAN code to the theoretical displacement field.

4.6.5 Extracting fracture toughness from 2D DIC data employing JMAN

Having developed the miniature double torsion rig for table top operation, experiments were undertaken on samples of PMMA (2 mm thickness) as well as on one sample of CTM grade PCD material (0.5 mm thickness).

Processing the PMMA specimen load-displacement data obtained during propagation of the crack front, depicted in Figure 4.32 and Figure 4.33 revealed maximum load and stress intensity levels at the onset of crack propagation of 35 N and 1.1 MPa√m. This was consistent with the fracture toughness properties of PMMA material. Simultaneously, images of the speckle pattern at the initiating notch were captured and analysed employing DIC techniques. Having obtained the experimental displacements, the data was processed employing the JMAN MATLAB routine, enabling calculation of the stress intensity levels in the material analysed. Figure 4.34 and Figure 4.35 depicts the results of the JMAN routine in terms of the solution convergence plots as well as the area contour employed to calculate the desired parameters.

In a similar manner, the PCD specimen load-displacement data obtained from an experiment on the CTM grade sample was processed employing the double

torsion equations. The results, plotted in Figure 4.36 and Figure 4.37, revealed that the maximum sustained load and associated stress intensity factor in the order of 38 N and14 MPa√m and the region associated with propagation in the constant stress intensity regime was characterised by the load and stress intensity levels of approximately 35 N and 12.5 MPa√m. Processing of the images captured by DIC techniques revealed correlation between the results, Figure 4.38 and Figure 4.39.The high stress intensity value associated with the onset of propagation is the result of the notch toughness phenomenon and is governed by the geometry of the starter notch.

These early results revealed that a sharp laser machined notch is highly beneficial to reduce the disparity between the stress intensity level at the start of propagation and the stress intensity associated with developed crack propagation in the constant stress intensity region. If the difference in the two stress intensity levels is not minimised, typically, sudden and complete specimen fracture occurs due to the strain energy stored in the components of the experimental apparatus. A good degree of agreement was observed between the classical double torsion formulation and the new, optical approach. However, a clear difference of approximately 10 % was observed. It should be borne in mind that the calculated results obtained through both approaches depend strongly on the accurate knowledge of properties such as Young's modulus, Poisson's ratio as well as the shear modulus of the material under investigation. It is therefore considered important that these parameters are well understood, before the experimentally determined data is considered accurate in terms of absolute toughness levels.

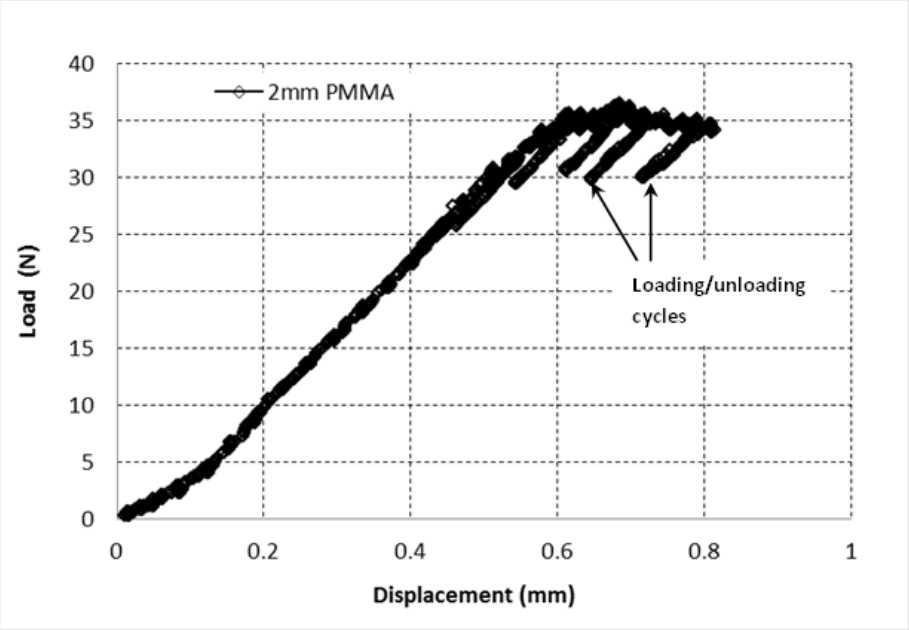

Figure 4.32 - Chart plotting the load-displacement behaviour for the 2 mm PMMA specimen in the DT experiment. It is noteworthy that the sample thickness selection results in a similar critical load level as that for 0.5 mm PCD sample, Figure 4.36. Processing that load data employing the classical DT formulations, the stress intensity results are obtained, plotted in Figure 4.33.

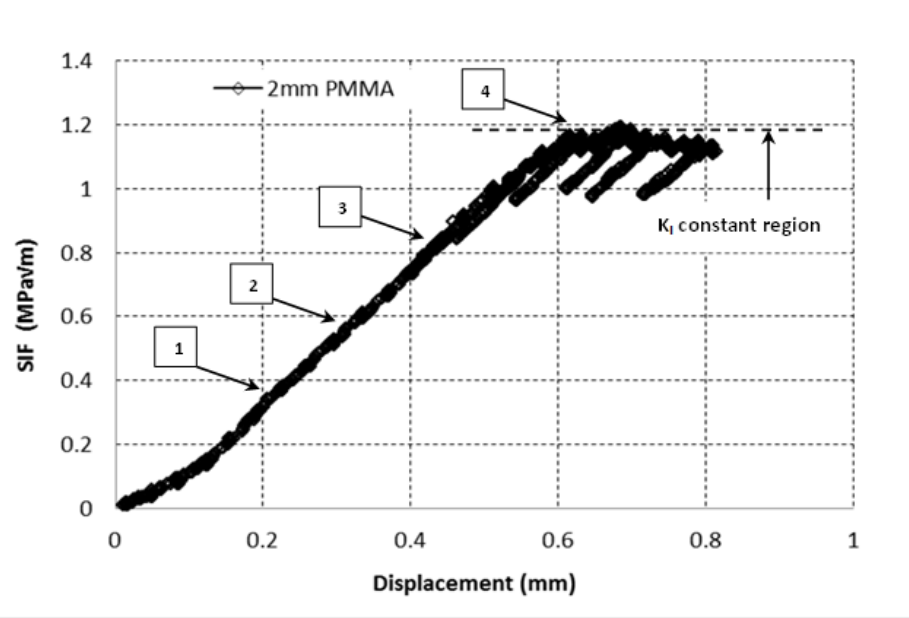

Figure 4.33 - Chart plotting the stress intensity factor for the 2 mm PMMA DT specimen calculated employing classical DT equations. The numbered balloons correlate the positions at which stress intensity was evaluated employing JMAN routine as presented in Figure 4.35.

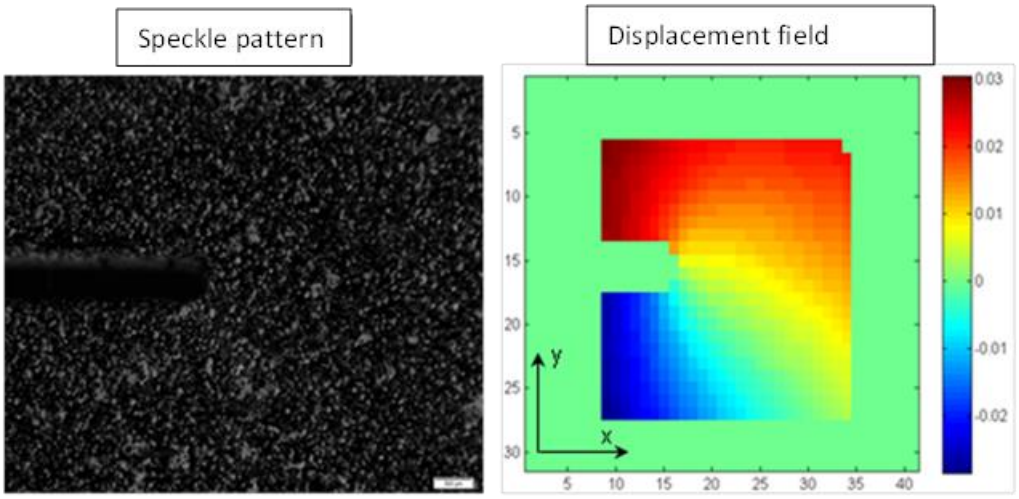

Figure 4.34 - The speckle pattern applied to the otherwise transparent PMMA sample is depicted on the left. Analysing the speckle pattern deformation employing DIC techniques, material displacement field is extracted.

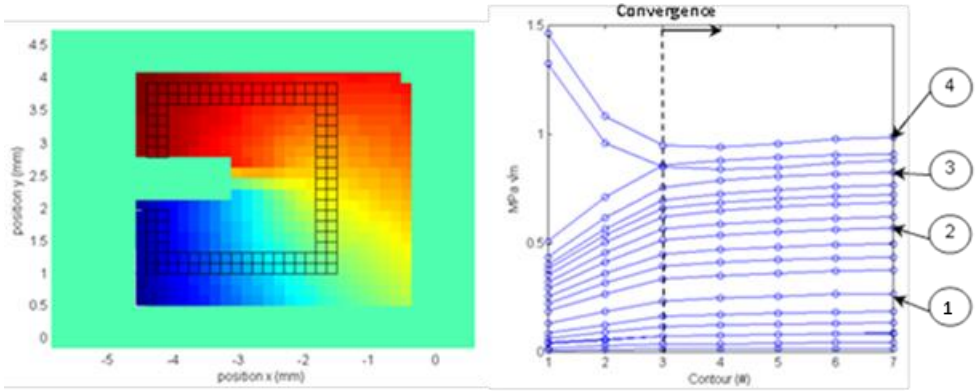

Figure 4.35 - Charts plotting the area contour employed to calculate the stress intensity parameter (left) as well as the plot of the stress intensity solution for each of the seven contours (right, starting at the notch tip and progressing outward). Comparing the results depicted above to those calculated and plotted in Figure 4.33, good level of correlation is revealed.

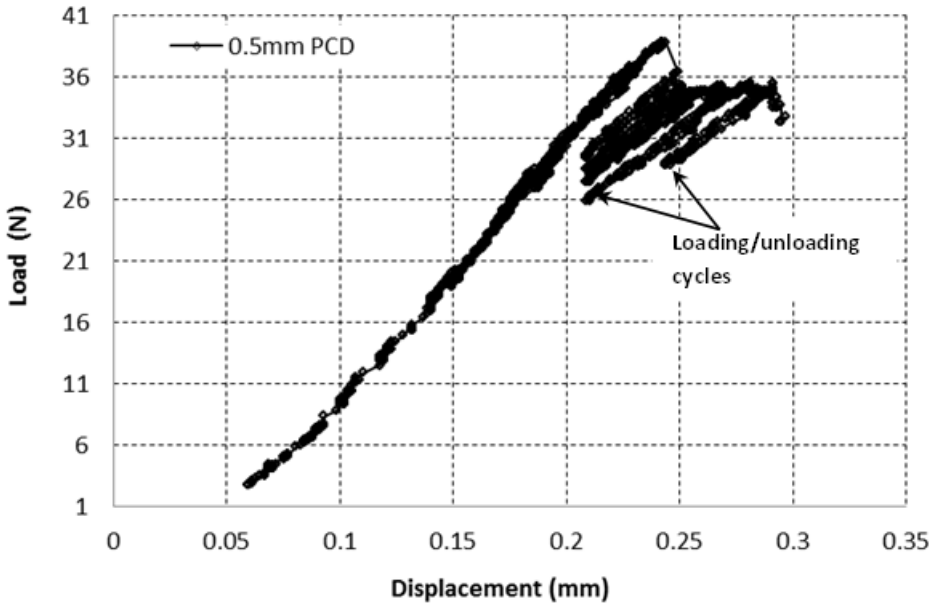

Figure 4.36 - Chart plotting the load-displacement behaviour for the 0.5 mm PCD sample in the DT experiment. Processing the load data employing the classical DT formulations, the stress intensity results are obtained, plotted in Figure 4.37.

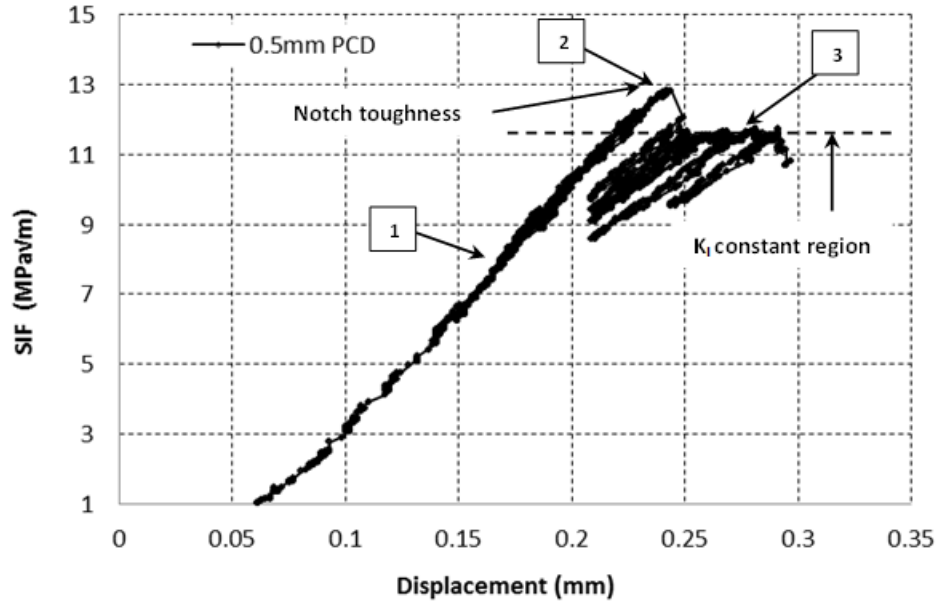

Figure 4.37 - Chart plotting the stress intensity for the 0.5 mm PCD DT specimen as calculated employing classical DT equations.

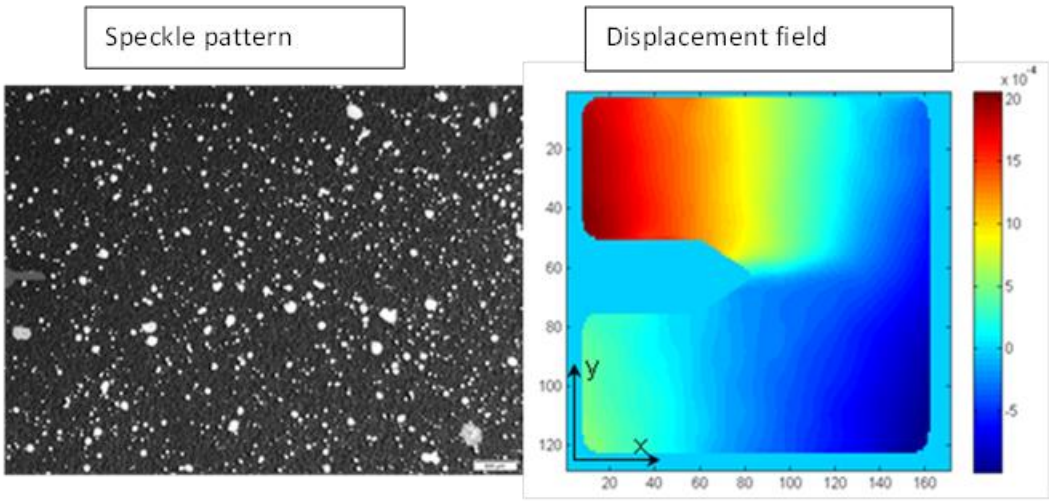

Figure 4.38 - The natural pattern of the PCD sample is depicted on the left (addition of white spray pattern was performed to aid the DIC analysis). Analysing the surface deformation data employing DIC techniques, the displacement field was extracted.

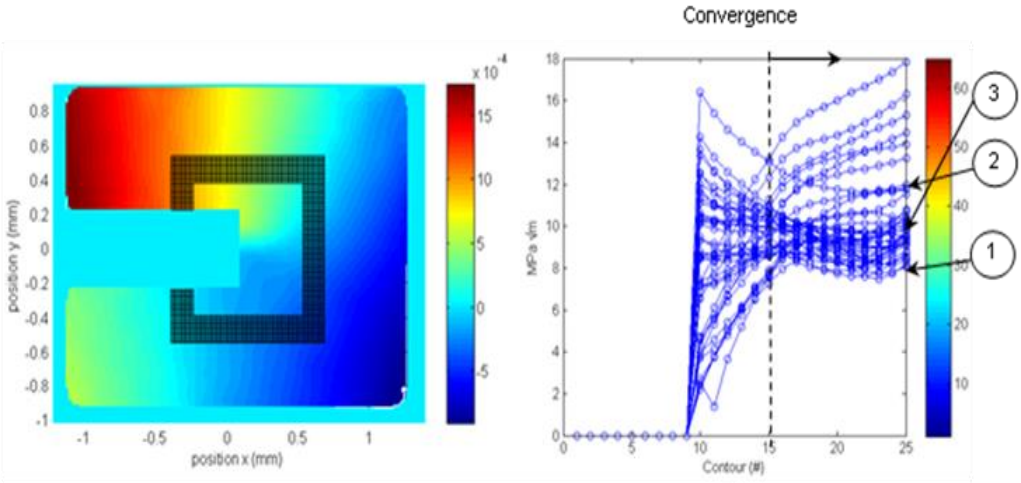

Figure 4.39 - Charts plotting the area contour employed to calculate the stress intensity parameter (left) as well as the plot of the stress intensity solution for each of the 25 contours (right, starting at notch tip and progressing outward). Comparing the results depicted above to those calculated and plotted in Figure 4.35, a good level of correlation is revealed.

4.6.6 Extracting PMMA fracture toughness parameters from 3D DIC data

In order to investigate the degree of consistency between the results obtained via the classical formulations and those obtained by the optical non-contact methodology, both sets of data were recorded simultaneously. The load displacement data is plotted in Figure 4.40. The corresponding stress intensity plot is depicted in Figure 4.41. It is evident from the plots presented that after overcoming a notch toughness effect described by the highest recorded load, the crack enters a stable region described by the nominally constant stress intensity levels of 1.7 MPa√m as highlighted by the arrow in Figure 4.41. It is worth noting that the constant stress intensity region is clearly identifiable in PMMA. In contrast, this region is very small in PCD, due to the extreme stiffness of the material and the resulting small displacements until onset of specimen failure. Each load-displacement data point in the experiment described is accompanied by an image which was acquired simultaneously employing the parallel trigger unit (PTU). Therefore, the surface deformation and crack position can be correlated with the associated load. Examples of images detailing surface deformations are depicted in Figure 4.42. Importing the specimen surface deformation data into MATLAB, allows for the selection of the crack tip position, Figure 4.43, around which the J-integral is then evaluated employing the JMAN methodology. The stress intensity values, assuming a linear elastic material behaviour, are obtained from the J-integral data and are plotted in Figure 4.44. As can be seen from the two stress intensity plots, the critical stress intensity results are in very good agreement at 1.7-1.8 MPa√m. It is noteworthy that the toughness values obtained are significantly higher than those obtained in unpainted PMMA DT specimens as detailed in Section 4.4.1.

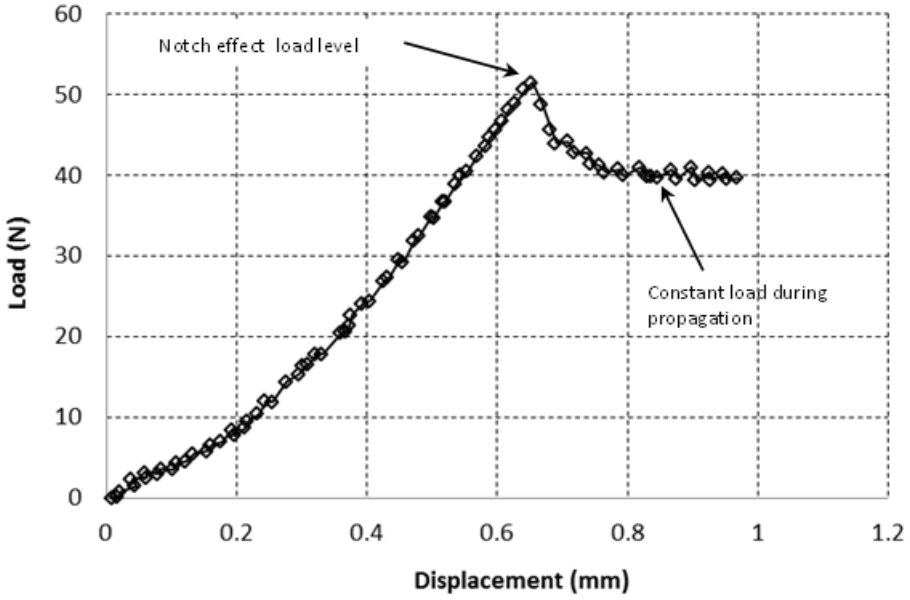

Figure 4.40 – Plot of the load-displacement data for a 2 mm PMMA DT experiment.

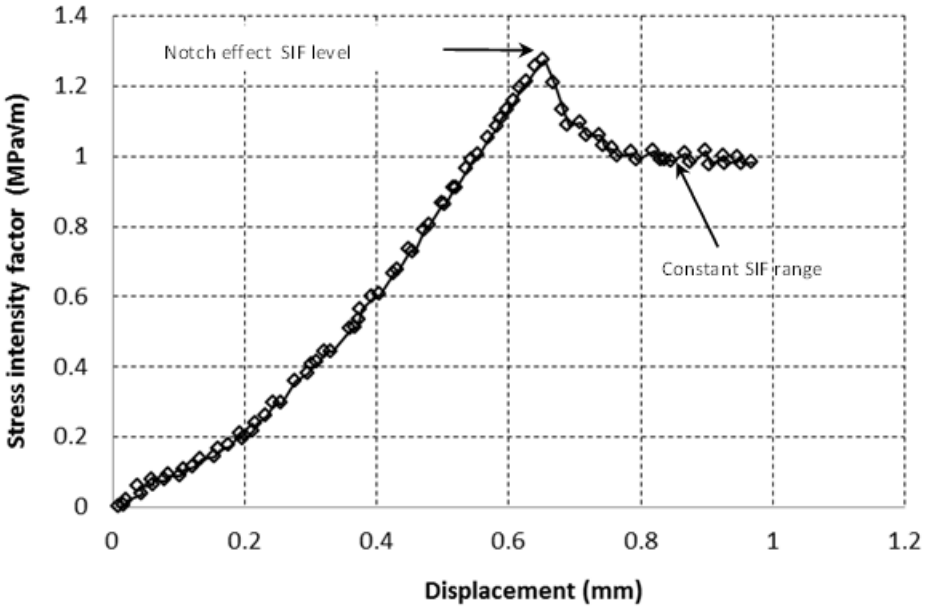

Figure 4.41 – Plot of the stress intensity-displacement data for the 2 mm PMMA DT experiment.

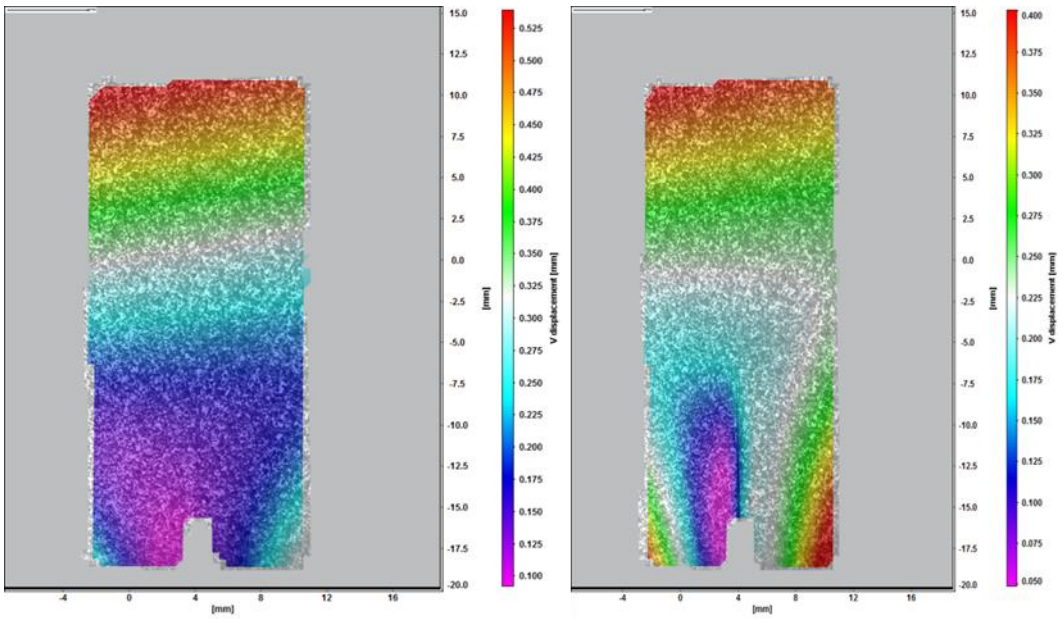

Figure 4.42 – Images depicting the surface deformation of the specimen prior to initiation (left) and once the crack is in the constant stress intensity range (right).

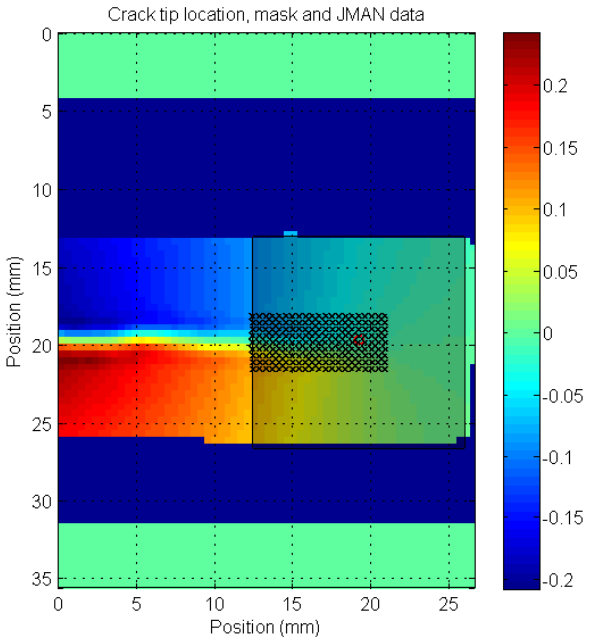

Figure 4.43 – Plot depicting the specimen deformation data as imported into MATLAB, highlighting the crack tip position (red circle), masked noisy data adjacent to the crack faces (crosses) and the field of data (grey area) over which the area J-integral is calculated.

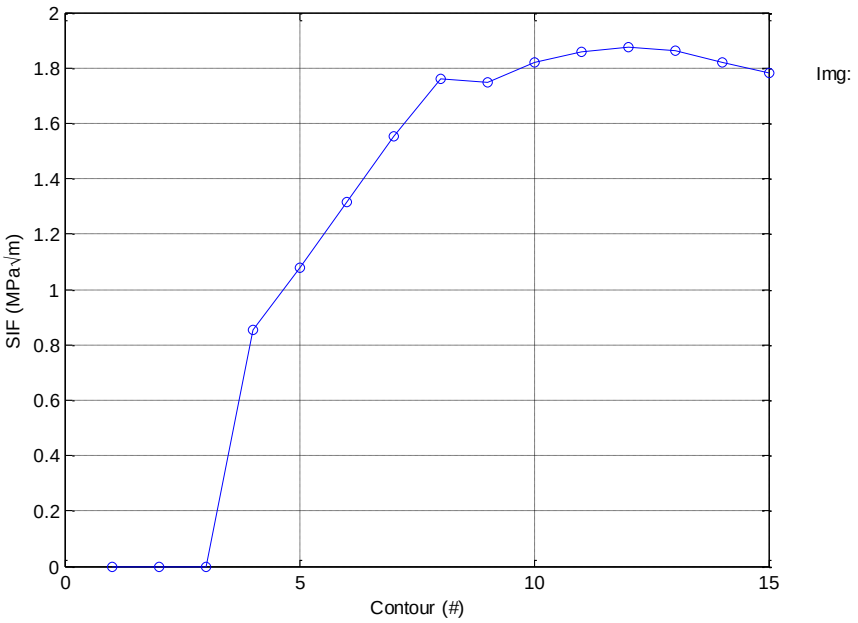

Figure 4.44 – Plot depicting the stress intensity value obtained in the constant stress intensity region by the non-contact optical approach.

4.7 Surface grain orientation mapping by EBSD

Polycrystalline diamond composite materials are produced by sintering starter powders of various diamond grit sizes in the presence of a catalyst/binder. Such process results in essentially random orientation of the diamond particles within the composite. In the context of crack propagation this means that some of the grains in the crack path are either preferentially or otherwise orientated with respect to their weaker cleavage planes. Therefore it became of interest to correlate the surface crack path, which was already observed in-situ SEM, to the orientation of the surface grains. It is postulated that the subsurface grain morphology has a significant effect on appearance of the surface crack path, however, because the crack front does not have a perfectly planar geometry, the immediate sub-surface component of the crack path would be affected by the grain orientation of the immediate surface layer of diamond particles.

Electron backscatter diffraction (EBSD) was employed to obtain interpretation of the crystallographic orientation of the surface grains. The orientation maps obtained were then correlated with the crack paths in order to investigate the effect of the crystallographic orientation properties on the crack path followed.

4.7.1 Surface finish and EBSD mapping

Initial attempts to map the “polished” specimens revealed that the surface finish was not of sufficient quality to enable mapping with a good success rate. The surface finish and an initial EBSD map are depicted in Figure 4.45. The mapped region size is 200x200 µm. The time required to perform such a map is approximately 12 hrs. The resulting indexing rate, a percentage measure of the number of successful attempts versus a total number of positions probed, of 36 % was obtained during the initial attempts. Interpretation of the results was further complicated by the fact that the cobalt binder and diamond particle have a similar face centred cubic crystallographic structure and EBSD mapping alone did not differentiate easily between the two [8], [46]. Therefore, the EBSD mapping would need to be supplemented by energy dispersive spectroscopy (EDS) at every sample point, to differentiate between the diamond and the cobalt binder phase. To perform such mapping efficiently, collaboration was sought with the High Resolution Transmission Electron Microscopy (HRTEM) centre at the Nelson Mandel Metropolitan University in Port Elizabeth. The EBSD system employed was a Nordlys HKL fitted to a JEOL JSM 7001F SEM. The mapping was typically performed at 15 kV. The acquired data was processed employing Aztec and Channel 5 HKL software from Oxford Instruments.

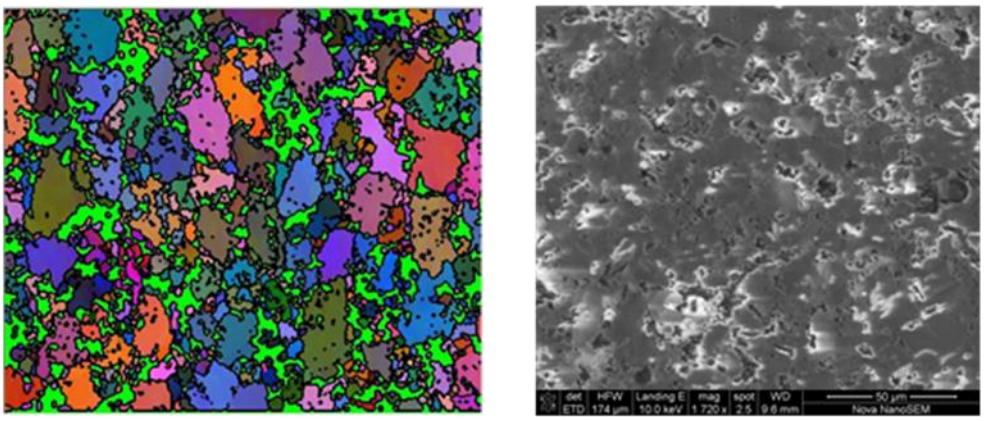

(a) (b)

Figure 4.45 - EBSD plot (a) depicts the results of a scan performed over a smaller region (200x200 µm), highlighting improved resolution of the constituent’s orientation. The surface finish in the region of the map is highlighted in SEM micrograph (b).

4.7.2 **Mapping approach**

Two mapping approaches were employed during the experimental programme. The first approach aimed at pre-mapping a region ahead of the zone of potential crack initiation. This was done to pre-empt the potential for complete and uncontrollable fracture of the specimens. Even if such fracture occurred, the crack would likely pass through the large, pre-mapped region and some information could be obtained. The second approach depended on the success of obtaining controlled crack initiation and propagation and the ability to shut down the crack and unload the specimen. This would then allow mapping of the cracked grains as well as those adjacent to the crack at localised regions which appeared to be of interest. Examples of such regions would be those where the crack had abruptly changed direction or appeared to bypass a particular grain. The schematic depicting the two approaches are depicted in Figure 4.46.

The pre-mapped regions needed to be correlated with the SEM images taken during the in-situ fracture experiments. This would be very difficult because the EBSD mapping is performed at an angle of 70 degrees to the horizontal and the mapped region is then converted into a map which appears normal to the specimen plane [83]. Therefore simple position coordinates or seeking out of microstructural features would not provide the accuracy necessary for consistently mapping the EBSD mapped regions to the secondary electron SEM images obtained during crack propagation experiments. In order to simplify the correlation process and achieve the best results, focused ion beam marks were applied to the corners of the mapped region as well as two addition marks along the side, Figure 4.47. The marks were created using carbon deposition in the FEI Helios NanoLab650 dual beam focused ion beam (FIB) SEM. The deposition was obtained by passing a gas chemistry solution (Naphtalene) over the sample via the gas injection system (GIS). Ga-ions accelerated to 30 keV were used to deposit the carbon with a beam current of 0.79 nA.

An example of an EBSD map performed in a region of interest in a specimen where a crack was controllably propagated and shut down is depicted in Figure 4.48. The EBSD information is further supported by high resolution back scatter detector (BSD) images, which highlight the propagation of the crack with respect to the binder pools, Figure 4.49.

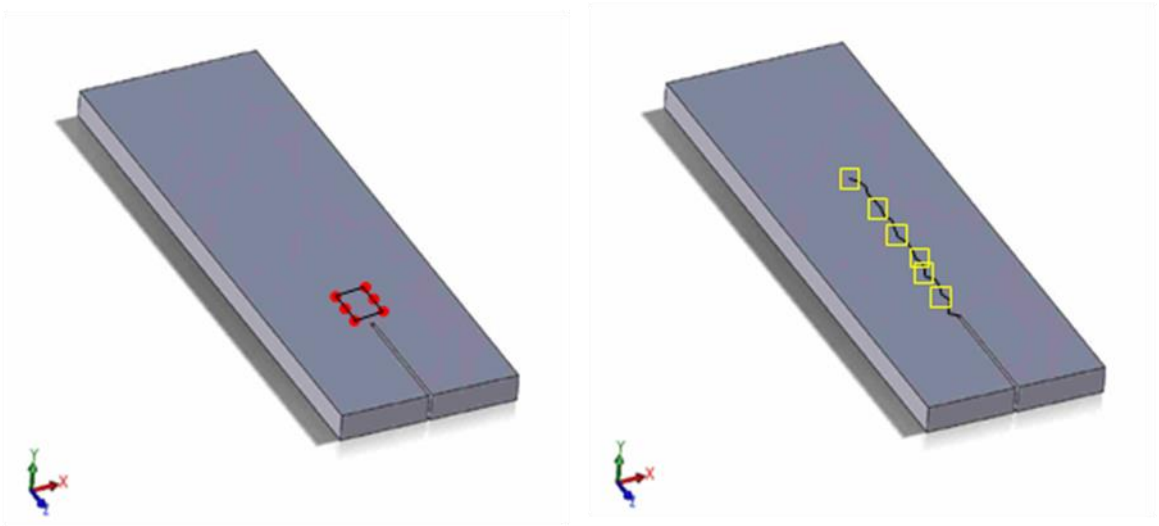

Figure 4.46 - Schematic representation of the two EBSD mapping approaches employed. On the left, a specimen is shown with a region being highlighted for pre-mapping. On the right, a specimen containing an arrested crack is shown, highlighting small regions of interest identified for mapping.

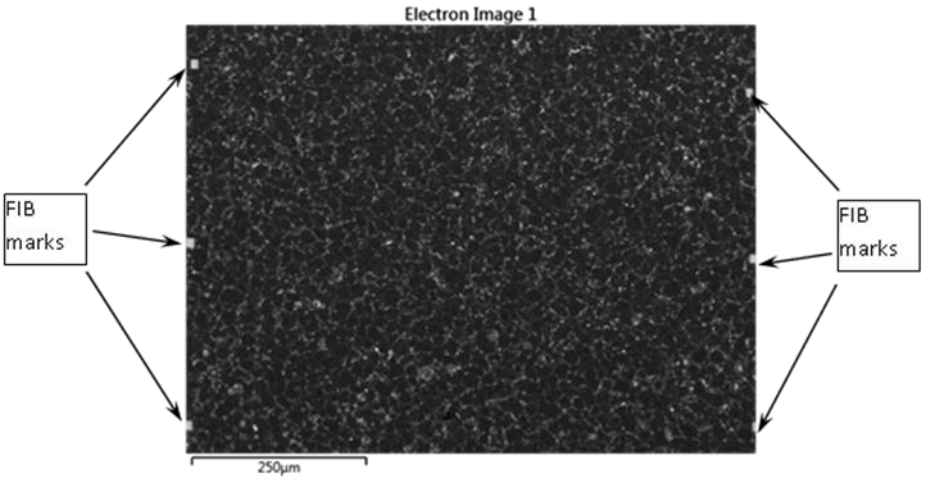

Figure 4.47 - Scanning electron micrograph depicting the region to be mapped, highlighting the focused ion beam (FIB) marks at the perimeter of the region.

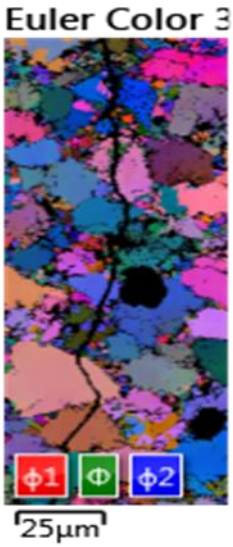

Figure 4.48 – EBSD Euler angle map highlighting the crack path as a function of orientation of the various diamond grains. Crystallographic preference can be observed at the bottom of the map.

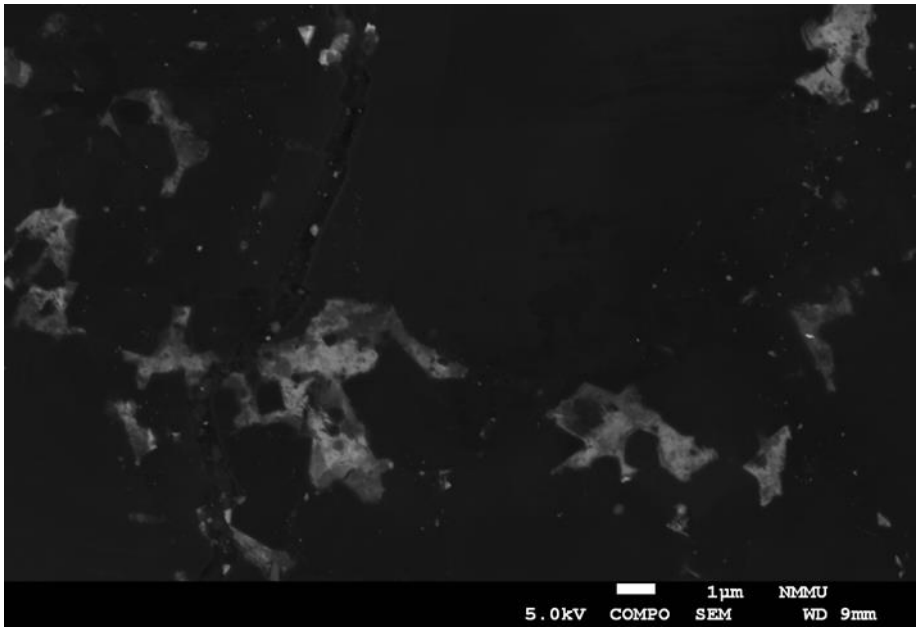

Figure 4.49 - BSD micrograph highlighting the crack path as a function of the diamond particles (dark phase) and the cobalt binder pools (grey phase). The bright speckles are believed to be particles of tungsten residual from the sintering process.

4.8 Summary

The current chapter has outlined the experimental methodology proposed in an attempt to enable slow, controllable crack propagation in the stiff, brittle polycrystalline diamond material of various grades supplied.

The miniature double torsion rig design and modification process has been detailed highlighting, first and foremost, its ability to propagate cracks in a slow and controllable manner in brittle materials such as PMMA and PCD. Analysis of statistically significant number of experiments carried out in PMMA revealed that the developed equipment and procedures produce consistent results with a good degree of repeatability as revealed by the PMMA testing programme. While caution has to be exercised when assuming similar accuracy would carry over to the PCD fracture experiments, it is believed that a solid experimental basis has been established.

The miniature DT rig developed allows for easy transportation and adaptation to different SEM microscopes as well as uncomplicated mounting for observation by other techniques such as optical microscopes and stereo vision camera systems. This facilitates observation and documentation of the fracture process in-situ. Such fracture process observation provides a means for identifying mechanisms which affect the crack propagation process in the material being tested. Furthermore, a methodology to employ digital image correlation to complement the fracture parameter studies has been presented along with a computational technique named JMAN to extract the J-integral and the surface stress intensity parameters by non-contact optical techniques.

An EBSD mapping approach has been presented aimed at observing the effects of individual surface grain orientation on the crack propagation dynamics. One of the properties of PCD is significant diamond-diamond grain intergrowth which makes optical identification of exact grain boundaries difficult. Therefore, EBSD mapping further assists in identifying these individual grains and their sizes to better understand the crack path dependence on microstructure.

Lastly, documentation of the fracture surfaces obtained during slow crack propagation at known stress intensity levels may be of value in understanding of the fracture behaviour of PCD in the laboratory and in the field by comparison of the fractographic features generated during component failure.

5 Results of fracture observations in PCD

The current chapter presents the quantitative results of the experimental programme carried out. PCD specimen properties such as cobalt content, diamond particle size and contiguity, which are believed to have an effect on the fracture toughness and crack propagation mechanisms, are presented first. These specimen material properties are followed by the fracture toughness properties obtained through the classical double torsion testing and equations characterising fracture toughness of the material. These toughness results are further presented as a function of the specimen properties discussed above. This is performed in order to highlight the effects of the various material parameters on the fracture toughness properties.

The classical double torsion approach is followed by the results obtained by employing the non-contact DIC techniques to characterise the maximum SIF experienced by the specimens. The results are compared to those obtained by the classical toughness testing techniques.

The numerical results are followed by the results obtained during the in-situ optical capture of the fracture process and observations made during the crack initiation and propagation process.

5.1 PCD specimen characteristics

5.1.1 Cobalt content

The cobalt content of the specimens was evaluated by employing an optical phase analysis toolbox provided by the Olympus Stream material analysis software [110]. The images for the analyses were captured employing an Oxford Instruments FEI NanoSEM microscope in backscatter detection (BSD) mode at 5 kV accelerating voltage and a working distance (WD) range of 7.0-7.5 mm. For comparison purposes, the 4 µm and 12 µm as well as the 30 µm and 30/4 µm microstructures are presented side-by-side in Figure 5.1 and Figure 5.2. The images highlight clear microstructural differences. The fine grained specimens tend to have less well defined diamond grains with a presence of dispersed cobalt pools. In contrast, the coarse grained specimens have well defined diamond grain features with the cobalt populating the grain boundary regions. The larger diamond grains found in coarse grained specimens are believed to be

responsible for the toughening effect associated with the crack path deflection which they can cause.

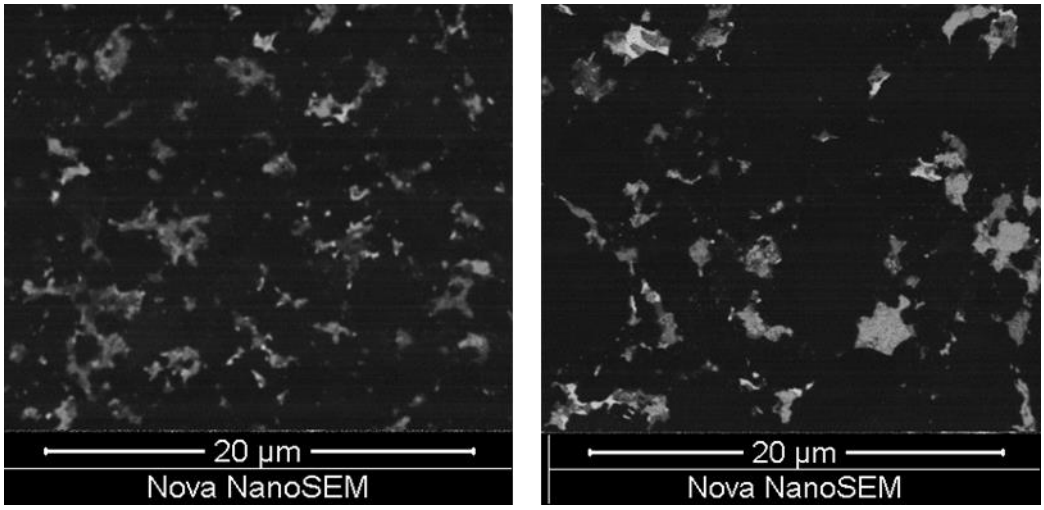

Figure 5.1 – SEM backscatter micrographs depicting the microstructures of the 4 µm PCD material (left) and the 12 µm PCD material (right). The dark phase is diamond while the bright phase is cobalt with small inclusions of tungsten which is characterised by the brightest speckles.

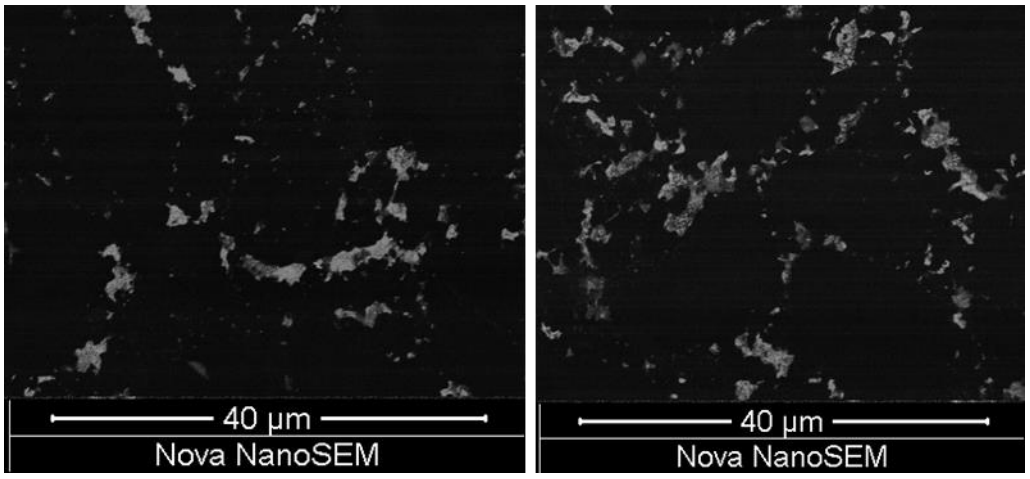

Figure 5.2 - SEM backscatter micrographs depicting the microstructures of the 30 µm PCD material (left) and the 30/4 µm bi-modal PCD material (right). The dark phase is diamond while the bright phase is cobalt with small inclusions of tungsten which is characterised by the brightest speckles.

Thresholding was employed in order to differentiate and quantify the dark diamond phase and the lighter cobalt phase, Figure 5.3 (images depicting the phase analysis of all grades are depicted in Appendix B). The thresholding grey

intensity level was selected as 50 based on visual examination of the images. This intensity level was kept constant for all images as the microscope settings were not altered between images. Therefore, while such thresholding technique may not yield the exact cobalt content of the PCD material, it provides a sound basis for cobalt content comparison in the context of the current investigation. The obtained results, averages for five separate BSD images taken in different specimen locations, are summarized in Table 5.1. The results revealed, as expected from visual observation, that the fine grain materials contained more cobalt than the coarse grain materials. The presence of extra cobalt between the diamond grains is believed to be associated with a lesser degree of diamond-diamond bonding during sintering, leading to lower degree of contiguity.

PCD specimen cobalt content			
Designation	**Starter particle size**	**Young's modulus (GPa)**	**Average cobalt content (%)**
Grade 4	4 μm	980	**11.7**
Grade 12	12 μm	880	**10.3**
Grade 30	30 μm	1040	**7.8**
Grade 4/30	4 (10%) and 30 (90%)	unknown	**5.7**

Table 5.1 – Specimen cobalt content as determined employing image analysis software applied to five separate BSD SEM images.

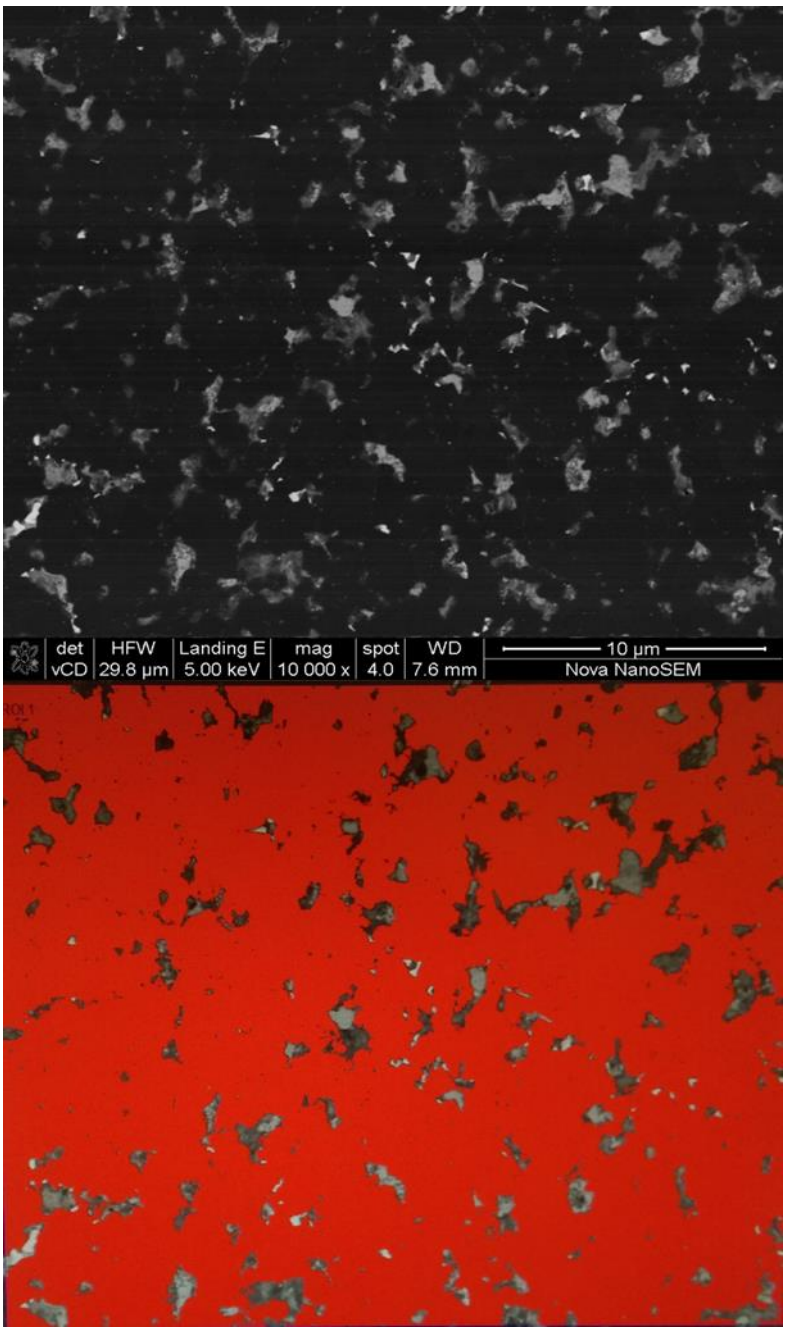

Figure 5.3 - Two phase composition analysis (bottom) of the BSD image (top) of the cobalt phase in a 4µm specimen. All data below the intensity level equal to 50 is considered to be diamond and is highlighted red, the remaining areas are considered to be cobalt.

5.1.2 **Diamond particle grain size**

The four grades of PCD specimens, described by their starter particle grain size, can undergo crushing and grain size change during sintering [111]. In order to measure the actual size of the grains in a two dimensional section of the specimen the equivalent circle diameter (ECD) parameter approach was employed [112]. The ECD parameter does not include a correction to provide a description of three dimensional grain sizes yet it does provide a method of comparing the different microstructures evaluated. The measurements were performed on backscatter detected SEM images of the polished specimens. The images were obtained in five different locations along the specimen surface and the results of the measurements were averaged. An example of a 4 µm microstructure is depicted in Figure 5.4, highlighting the circular measurement markers employed to determine ECD (images employed in the analysis of all other grades are included in Appendix B**)**. Two different levels of magnification, 5000x and 1000x, were employed in the microstructural analyses. This was done to obtain the most suitable magnification to identify the individual grains of different sizes. Higher magnification was employed to analyse the 4 µm and 12 µm specimens while the lower magnification was employed for the coarser, 30µm and 30-4 µm specimens. The average grain sizes measured are reported in Table 5.2. The measurements revealed that the actual two dimensional grain size is significantly smaller than the starter particle size, approximately 61-67 % reduction. The reduction level appears to be consistent for all grades of material. This is expected for the three mono-modal grades. However, it was expected that the bi-modal grade would reveal a different trend as the finer diamond grit is believed to fill in the gaps between the coarse grains and reduce the degree of grain fracturing during the HPHT process.

It is well documented and discussed in section 3.1.1, that grain size has an effect on the mechanical properties of PCD materials. The grain size effect cannot be simply quantified in isolation as it affects a number of processes which lead to the final properties of the material. Grain size affects the binder content, contiguity and acts as the crack deflecting feature in the microstructure. Therefore, it is of interest to analyse the obtained fracture toughness properties with respect to the starter particle as well as the measured grain size.

PCD specimen measured 2D particle size			
Designation	**Starter particle size (µm)**	**Measured particle size (µm)**	**Standard Deviation**
Grade 4	4	2.47	**0.08**
Grade 12	12	7.30	**0.26**
Grade 30	30	20.1	**0.53**
Grade 4/30	4 (10%) and 30 (90%)	20.3	**0.51**

Table 5.2 – Specimen diamond particle size measured from the actual microstructure.

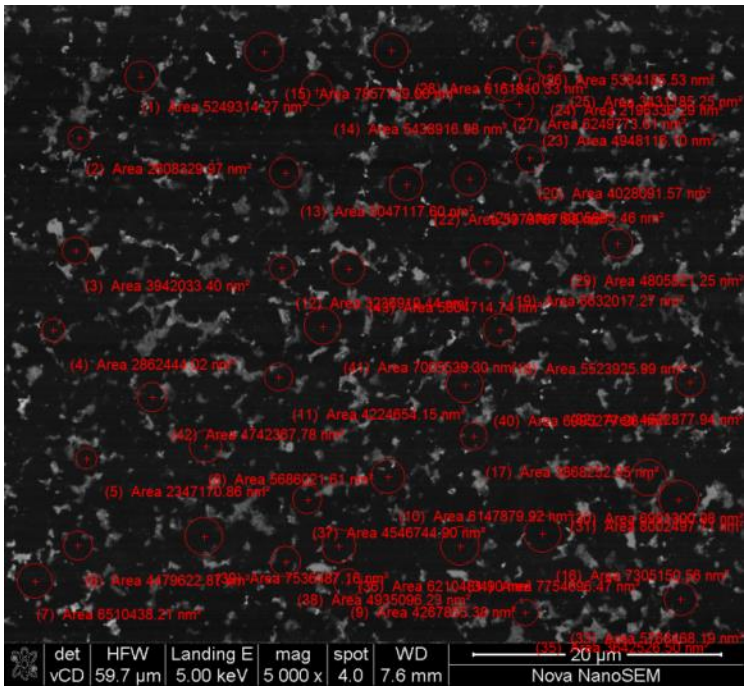

Figure 5.4 – BSD micrograph depicting the microstructure of the 4 µm grade PCD specimen, highlighting the regions where measurements were taken.

5.1.3 **Diamond phase contiguity**

During the HPHT sintering process of the diamond-cobalt system, diamond-diamond intergrowth occurs [24,85,109,110]. In a modern PCD material, the diamond-diamond bonds are strong and abundant enough to retain the strength while the cobalt material is leached out. It is this diamond network which provides the favourable properties observed in the so called thermally stable PCD (TSP) products. The thermal stability of the PCD materials is obtained by removing the secondary cobalt phase. This is performed to prevent the intergranular loading associated with the high thermal expansion coefficient of the cobalt phase. Upon removal of the cobalt phase, the contiguous diamond network is solely responsible for the mechanical properties of the material [11,36]. The level of diamond-diamond contiguity can be characterised through quantitative optical microscopy techniques. Random linear intercepts are taken across the microstructure and the grain boundary neighbours are defined as either diamond-diamond or diamond-cobalt. The degree of contiguity of the diamond phase can then be evaluated employing the following expression,

$$C_D = \frac{2N_{DD}}{2N_{DD} + N_{DC}} \tag{5.1}$$

Where C_D is the diamond phase contiguity, N_{DD} is the number of diamond-diamond interfaces and N_{DC} is the number of diamond-cobalt interfaces [115]. An example of such interface counting is depicted in Figure 5.5 and the results of the performed analyses are presented in Table 5.3 (the images employed for the contiguity analyses of other microstructures are depicted in Appendix B). The results revealed that the contiguity of the diamond phase increased with increase in the grain size. This result is consistent with the fact that the cobalt content is lower in the specimens with increasing grain size (refer to Table 5.1).

The results indicate that the contiguity levels appear to increase as the grain size gets coarser and cobalt content is reduced. The effect of the contiguity level on the fracture toughness properties is discussed in the subsequent sections.

PCD specimen diamond phase contiguity		
Designation	**Starter particle size (μm)**	**Contiguity**
Grade 4	4	52
Grade 12	12	54
Grade 30	30	62
Grade 4/30	4 (10%) and 30 (90%)	66.5

Table 5.3 – Microstructural contiguity of the diamond phase in the four specimen types employed.

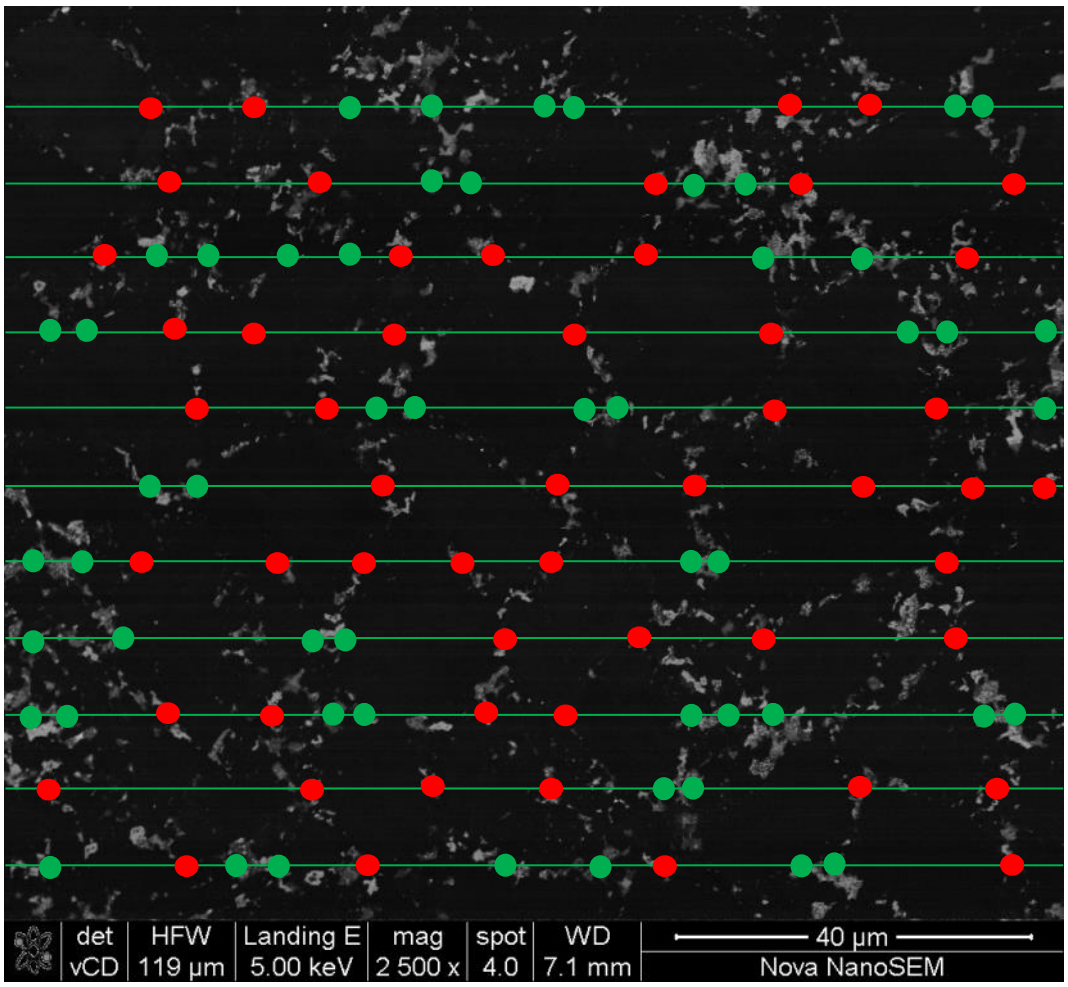

Figure 5.5 – Backscatter micrograph depicting the microstructure of the 30-4 µm PCD specimen, highlighting an example of the line intercepts employed to determine the diamond phase contiguity. Where the boundary contact is diamond-diamond, a red dot is placed, while a green dot is placed at the diamond-cobalt interface.

5.2 Classic DT formulation results

The load-displacement data was recorded during the in-situ SEM experiments. This allowed for the direct calculation of the critical stress intensity and hence the specimen fracture toughness to be determined employing the classical DT formulation, Equation (2.30). The fracture toughness results obtained are presented in Table 5.4. The plots depicting the fracture process, detailing the stress intensity factor (SIF) vs. displacement are presented in Figure 5.6 to Figure 5.9. It is important to highlight that the stress intensity characterising the

fracture toughness does not correspond to the maximum load and stress intensity level depicted in the figures. The maximum loads are associated with the notch toughness effect which precedes the formation of a sharp crack. The fracture toughness of the material is characterised by the stress intensity level obtained after the notch effect is overcome and the crack tip enters the constant stress intensity portion of the DT specimen i.e. approximately the central one third of the length.

The results revealed that the fracture toughness of the PCD material increased with an increase in the grain size of the material. Although only two samples of each grade were available for testing, the results for each of the two specimens of the same grade were consistent with each other.

Fracture toughness, K_{IC}, of the four PCD grades determined by classical DT formulation			
Designation	**Starter particle size (µm)**	**Average fracture toughness (MPa√m)**	**Range (MPa√m)**
Grade 4	4	**8.1**	0.3
Grade 12	12	**9.5**	0.3
Grade 30	30	**10.6**	0.5
Grade 4/30	4 (10%) and 30 (90%)	**11.9**	0.6

Table 5.4 – Fracture toughness, K_{IC}, data for the four grades of PCD, obtained during the in-situ SEM DT propagation experiments.

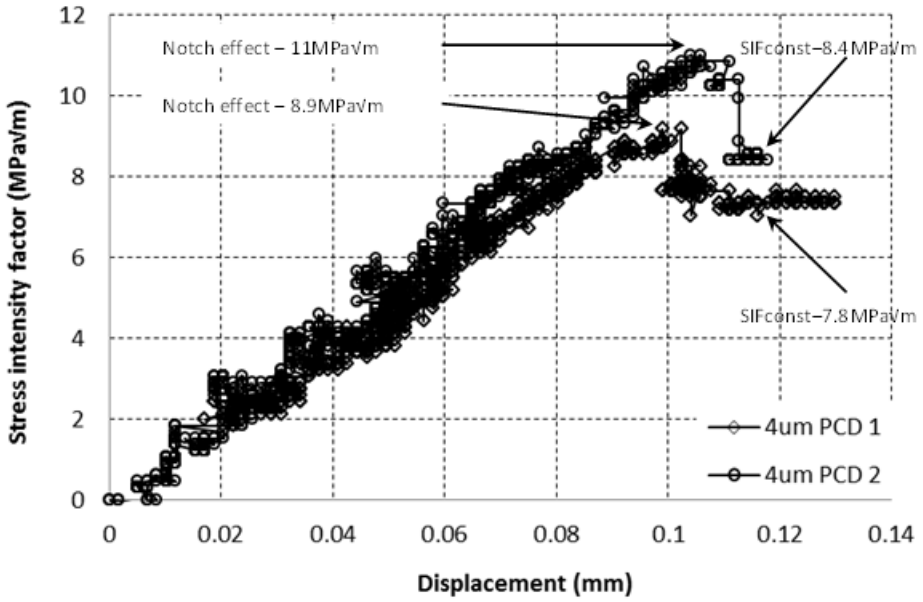

Figure 5.6 – SIF-displacement plot for the 4 µm PCD specimen during the in-situ SEM experiment (raw data).

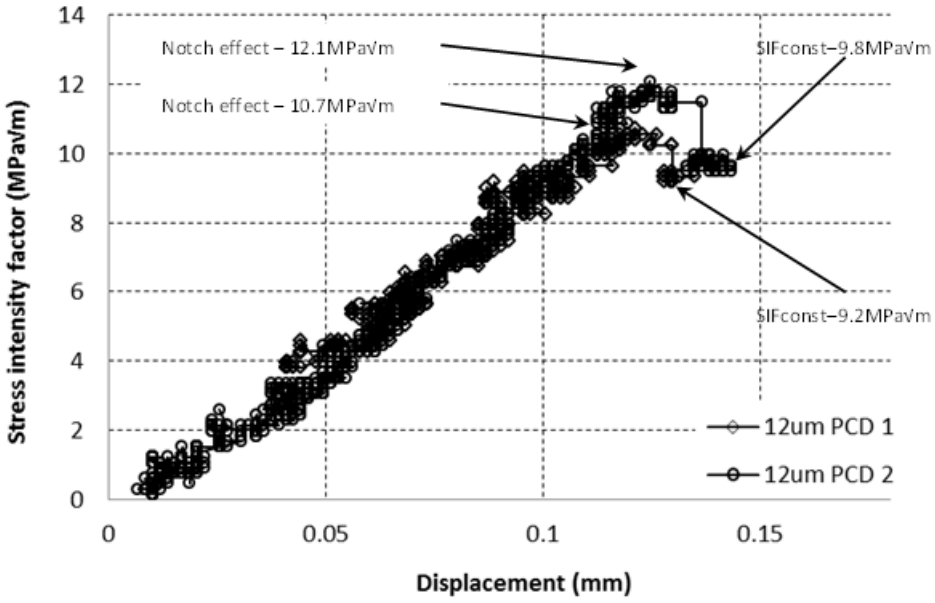

Figure 5.7 - SIF-displacement plot for the 12µm PCD specimen during the in-situ SEM experiment (raw data).

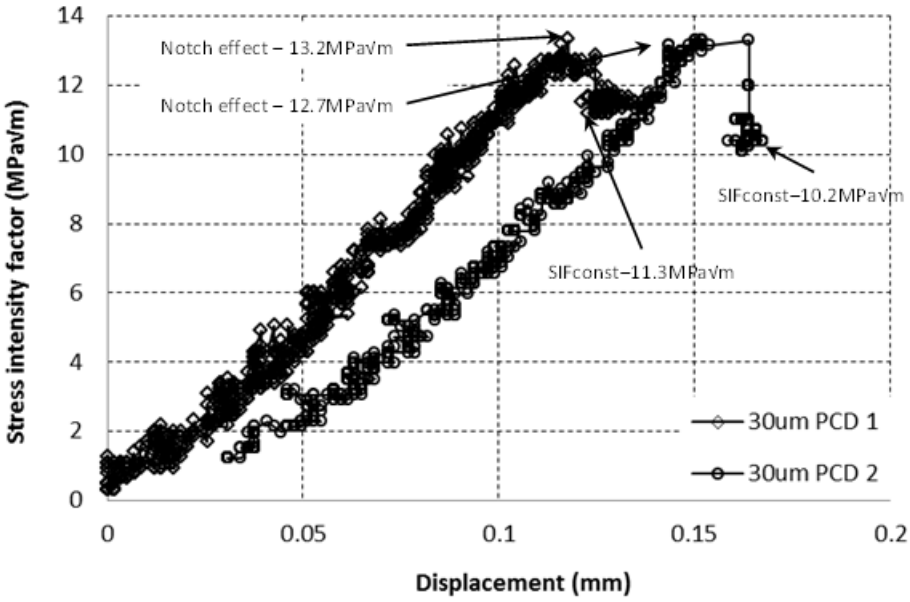

Figure 5.8 - SIF-displacement plot for the 30 µm PCD specimen during the in-situ SEM experiment (raw data).

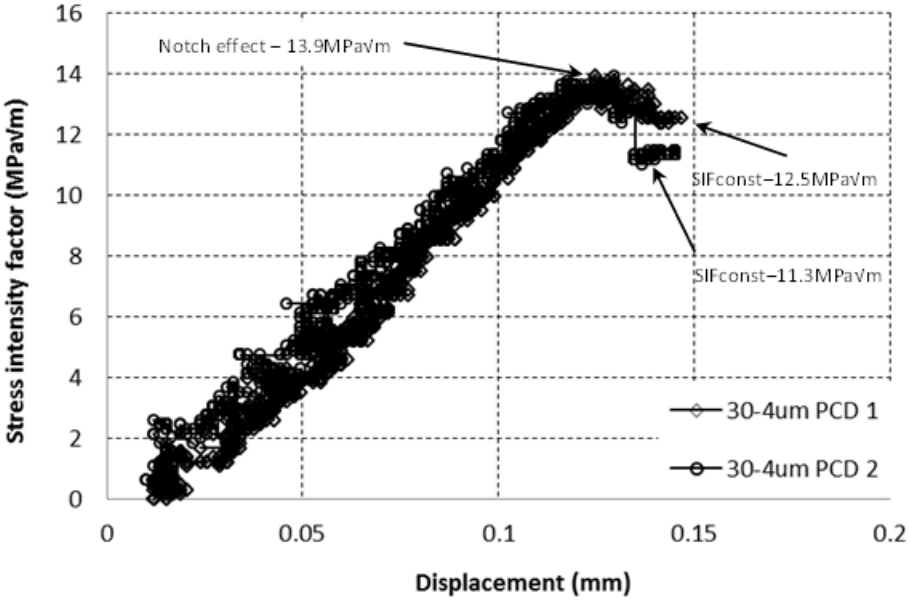

Figure 5.9 - SIF-displacement plot for the 30-4 µm PCD specimen during the in-situ SEM experiment (raw data).

5.3 Extracting fracture toughness parameters employing optical techniques

In addition to the development of the miniature double torsion approach which enabled extraction of the fracture mechanics parameters by employing the classical equations based on the load displacement data, attempts were made to characterise the fracture mechanics parameters via the non-contact optical technique. Double torsion experiments were undertaken in PCD, generating load-displacement data as well as recording the full field deformations of the double torsion specimen upper/tensile surface. The results of these experiments are detailed in the following subsections.

5.3.1 Extracting PCD fracture toughness parameters from 2D and 3D DIC data

In an attempt to extract PCD fracture toughness properties by non-contact optical techniques, the specimens which were pre-cracked in-situ SEM were employed. The speckle pattern was applied by the same method as in the case of PMMA material and the specimens were reloaded in the miniature DT rig in-situ 3D DIC system.

5.3.1.1 Extracting fracture toughness from 2D stereo microscope data

During the development phase of the experimental methodology, a surface leached specimen was available to perform a miniature DT test on. It was thought that the leached surface of the specimen may provide sufficient texture to enable measurement of the surface displacement by DIC techniques. Notwithstanding the specimen's own texture, a number of paint speckles were applied to the surface of the specimen in such a way as to not coat the surface but provide unique features which could be used to resolve the displacement field, Figure 5.10. Simultaneously with the image capture via the Zeiss SZX7 stereo microscope, the load displacement data was recorded during the experiment, Figure 5.11. The images captured were then processed employing the DIC in order to obtain information such as the displacement and strain fields in the miniature DT specimen. An example of the strain field around the developed crack in the region of constant stress intensity is depicted in Figure 5.12. Employing the classical DT formulation and load data from Figure 5.11, the stress intensity in the constant stress intensity region was calculated to be 10.6 MPa√m. Processing the displacement field data with the JMAN algorithm, revealed a stress intensity level of 9.9 MPa√m.

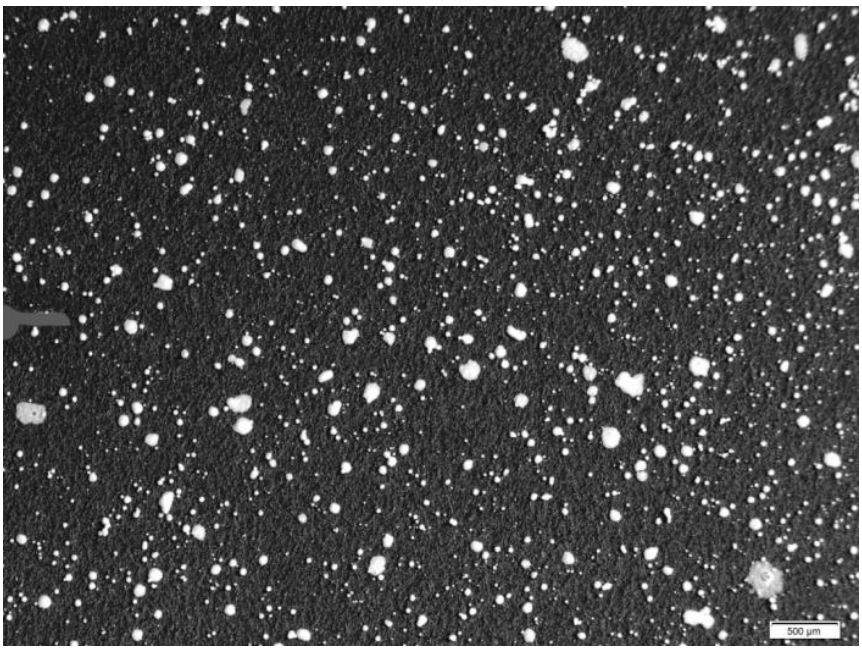

Figure 5.10 – Stereo micrograph depicting the surface of the leached PCD specimen, with an application of white paint speckles aimed at improving the surface contrast.

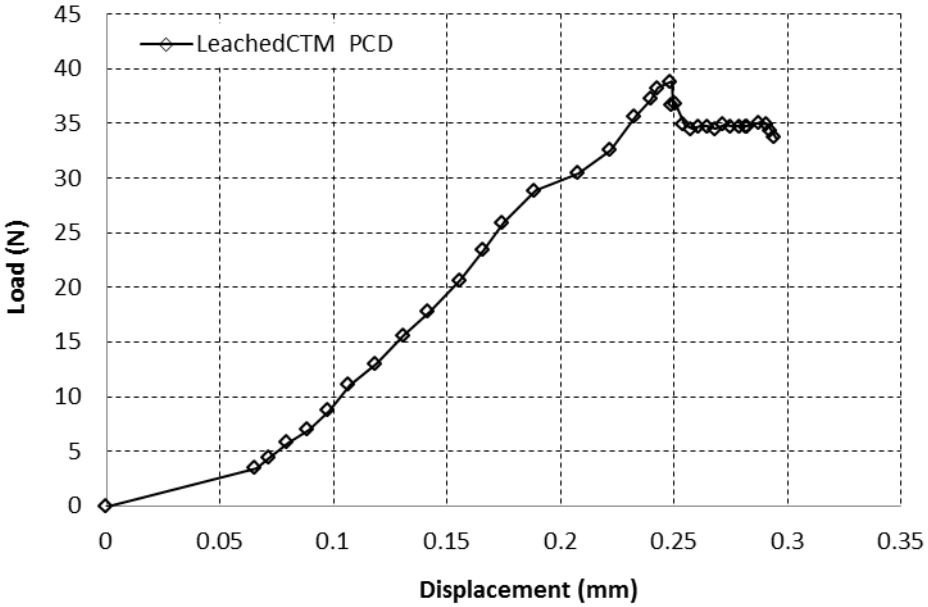

Figure 5.11 – Load displacement data for leached 0.5 mm leached PCD experiment performed in-situ stereomicroscope.

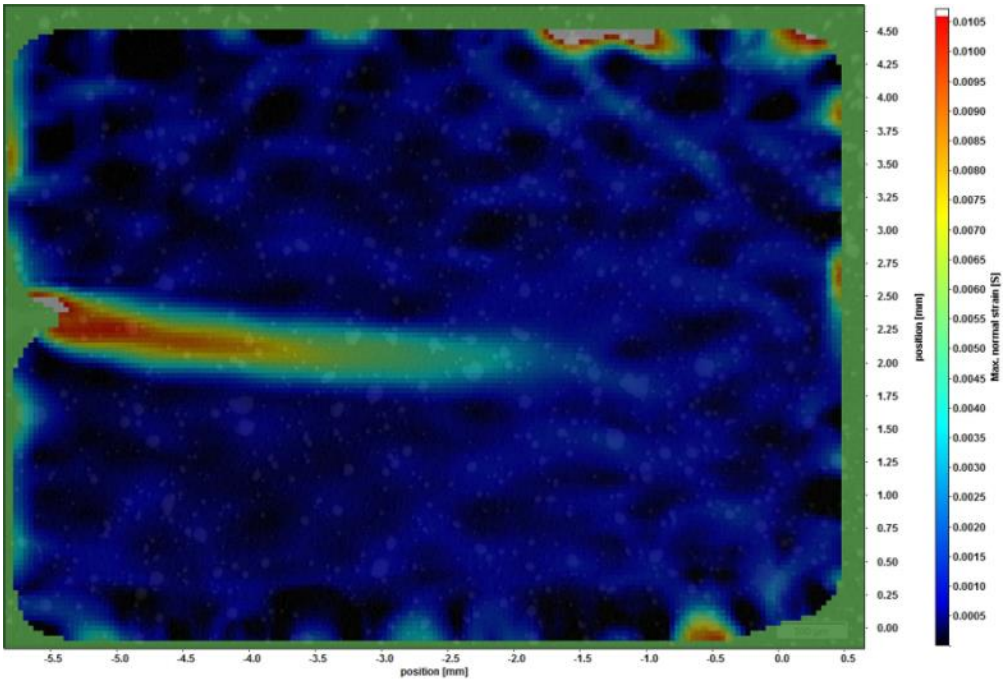

Figure 5.12 – DIC output plot of the maximum normal strain field around the developed crack.

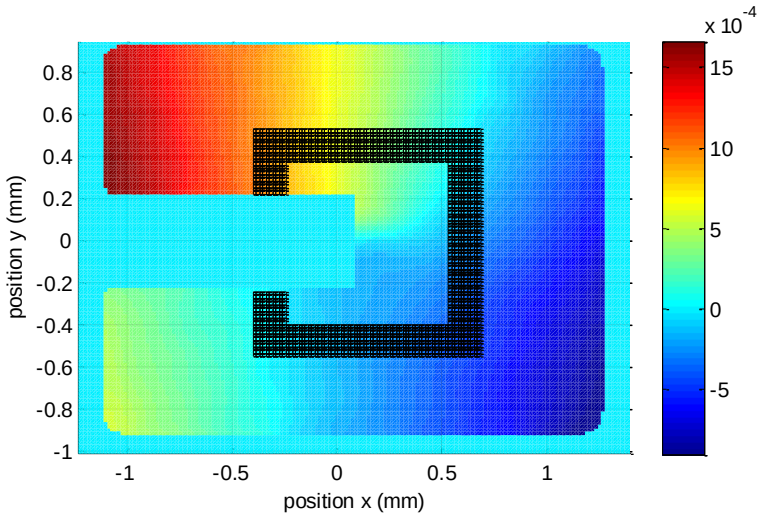

Figure 5.13 – Image depicting the JMAN integration contour superimposed onto the displacement field (vector length) generated by the DIC software.

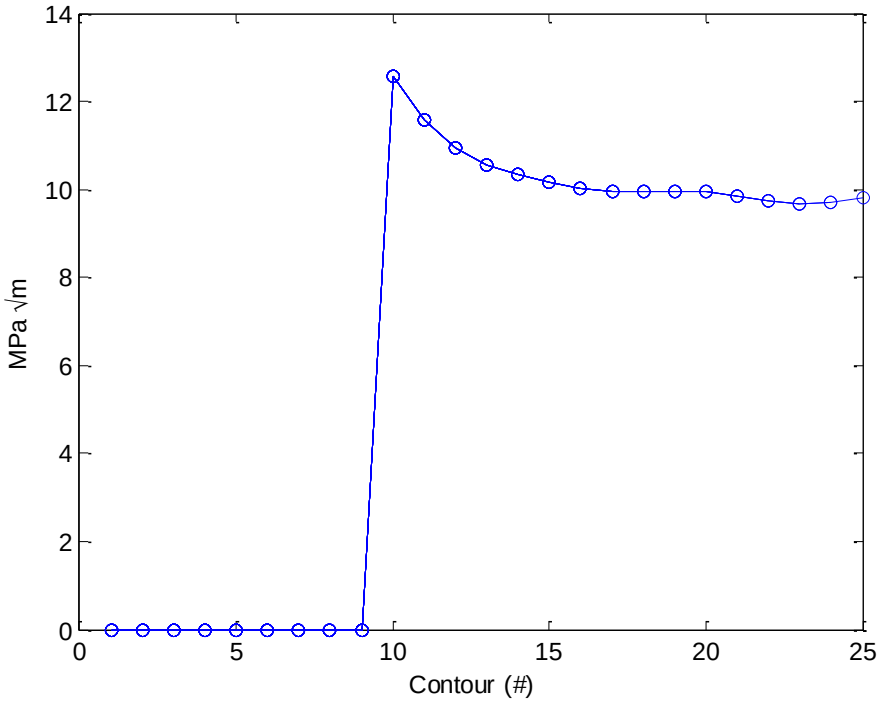

Figure 5.14 – Stress intensity level as evaluated employing the JMAN methodology.

5.3.1.2 Extracting fracture toughness from 3D DIC data

The LaVision 3D DIC system together with JMAN routine were employed in an attempt to extract the fracture toughness parameters from the pre-cracked PCD samples which had, at that stage, undergone pre-cracking in the SEM and were analysed by means of EBSD. A speckle pattern was applied to the specimens as the polished specimens did not have sufficient surface features to enable tracking by DIC algorithms. Due to the fact that the specimens were already pre-cracked, the initial phases of the loading process only rotated the two halves of the DT specimen until the rotation was sufficient to raise the stress intensity to a critical level at the crack tip. It is worth highlighting that the JMAN algorithm is applied at the crack tip. Therefore, until the critical stress intensity level, identified during the in-situ SEM experiments, is reached, no new optical J-integral data could be extracted.

In order to better describe the process, sample images of the displacement fields, selected crack tip positions and the results of the JMAN contour integration are depicted for the 30 µm grade of PCD material tested.

The global displacement field for the 30 µm specimen is depicted in Figure 5.15. It can be seen from the displacement plot that the position of the crack tip is difficult to determine accurately and therefore a subset of the depicted displacement field is extracted and analysed to better determine the position of the crack, Figure 5.16. Once the crack tip position is selected it forms the centre position from which the contours are integrated outwards, generating the plot of stress intensity as a function of the contour number, Figure 5.17.

The fracture toughness results obtained employing the described approach were – i) 7-9 MPa√m for the 4 µm grade, ii) 10-12 MPa√m for the 12 µm grade, iii) 10-14 MPa√m for the 30 µm grade and iv) 12-16 MPa√m for the 30-4 µm. It is evident that the technique is successful in determining the surface SIF in the vicinity of the crack. However, these results have a significant variation when compared to those obtained by employing the classical DT equations and load-displacement data from miniature DT rig. Compared to the consistent results obtained for the PMMA material (described in Section 4.6.6), the results are strongly dependent on number of contours masked around the crack tip. These inconsistencies in the results are affected by two key factors – namely i) extremely high Young's modulus of the material resulting in small strains and ii) masking effect the paint has on the exact position of the crack tip as well as potential strain variation between the PCD/Paint layer interface and the surface of the paint.

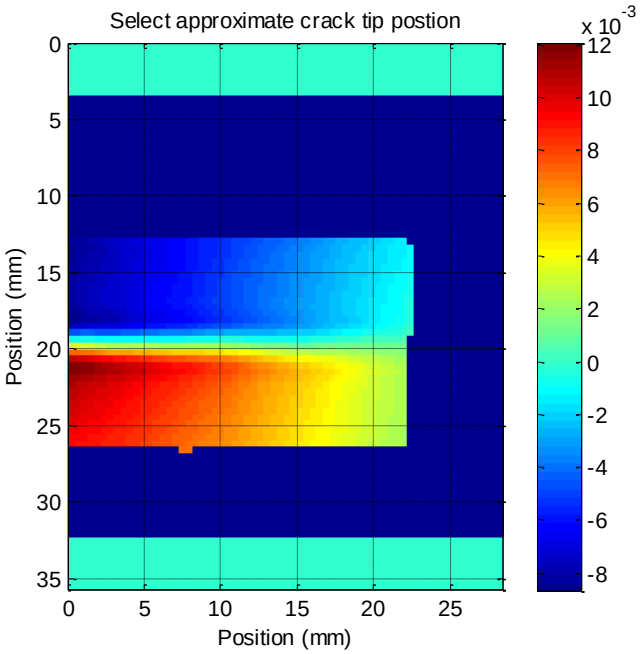

Figure 5.15 – The global displacement field on the speckle painted surface of the DT specimen. The specimen is positioned horizontally with the crack propagating from the left to the right.

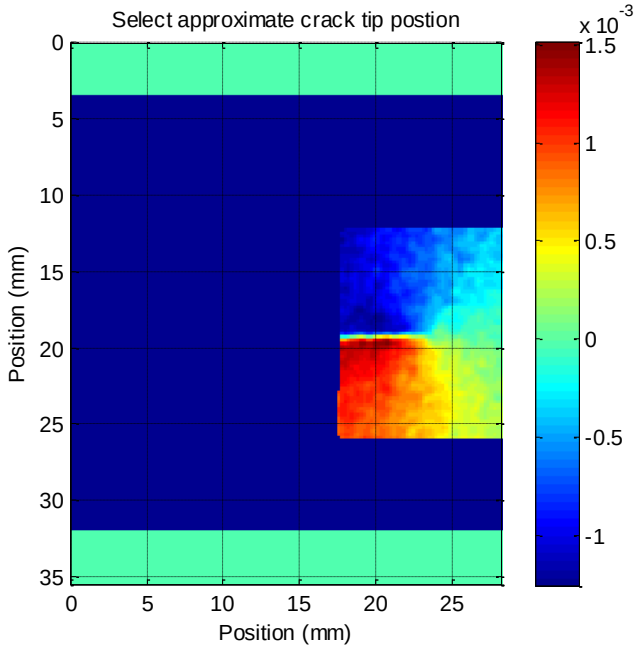

Figure 5.16 – Local displacement field (vector length) around the crack tip, allowing for more accurate selection of the crack tip position.

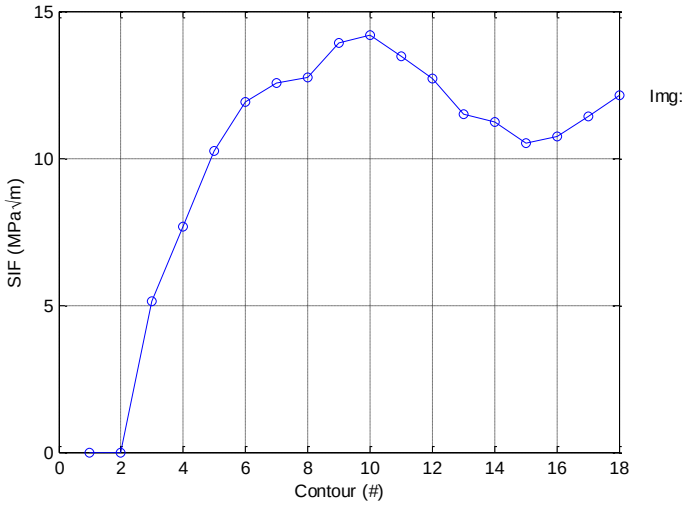

Figure 5.17 – Chart plotting the stress intensity calculated by employing the JMAN routine applied to the displacement field data in Figure 5.16. The SIF data is plotted against the contour number. Note that the first contour SIF values will typically be zero as these data points are masked out to prevent erroneous data around the crack tip where displacements cannot be accurately evaluated by DIC.

5.4 In-situ observation of the fracture process

In order to obtain insight into the fracture process mechanisms, optical and scanning electron microscopy (SEM) are typically used. However, these techniques are typically applied to the fracture surfaces generated by the fracture mechanisms and after the fracture experiments are concluded. The rig and experimental procedure development in the current project aimed at observing the initiation and propagation processes live. With this aim in mind, the miniature DT rig was designed to enable insertion into an SEM microscope while retaining full capacity to carry out a miniature DT experiment. This allowed for the simultaneous generation of DT load-displacement data as well as live observation of the crack propagation. The load-displacement data enabled the characterisation of the material toughness properties while simultaneous observation aimed at obtaining a phenomenological understanding of the crack growth/fracture development process.

The experimental procedure for all grades of PCD specimens was nominally the same. Therefore, the following section outlines the typical factors which were taken into consideration during the experiments and is followed by the

observations made for the different material grades. It is believed that such layout will minimise the potential repetition when describing the experiments in different grades of PCD.

5.4.1 General experimental considerations

The primary concern governing all experiments was the extremely stiff and brittle nature of PCD. Therefore, as previously highlighted in the methodology chapter, regions of potential crack paths immediately after crack initiation at the root of the notch were pre-mapped employing EBSD techniques. These regions were selected a small distance away from the starter notch so as to avoid the damaged PCD material immediately adjacent to the EDM/Laser machined notch. Therefore, at the start of the experiments, the root of the notch was observed until such time as a crack could be clearly identified. Once incremental extension of the crack was achieved, the region pre-mapped by EBSD was obtained within the field of view of the SEM, at a magnification allowing complete observation of all focused ion beam (FIB) marks. The crack was grown through the EBSD region. Once the crack had passed through the EBSD region, the tip was typically centred and the crack was incrementally extended until such time as the region of constant stress intensity could be identified in the load displacement data. If such propagation was to be successful, the specimen would be unloaded, shutting down the crack, to enable post-propagation EBSD investigations as well as SEM imaging of the specimen outside the rig which permitted better working distances which are affected by the rig components extending above the specimen surface plane during live in-situ experiments.

The following section details the observations made in the four grades of PCD employed.

5.4.2 4μm starter particle PCD

5.4.2.1 Notch geometry and initiation

The starter notches of specimen 4μm-1 and specimen 4μm-2 are depicted in Figure 5.18 and Figure 5.19 respectively. The figures highlight the notch geometry which is somewhat irregular and is relatively blunt when compared to a sharp crack. The notch root radius, depending on the feature selected, is in the order of 30-50 μm while the initiating cracks are sharper than one micron. Such a significant geometry difference results in the elevated notch toughness results

detailed in Section 5.2. The irregular notch geometries further result in unpredictability with respect to the position at which crack initiation would occur. Keeping in mind that the SEM images depicted in this section are generated by frame averaging to obtain improved image quality, identification of the moment of crack initiation is non-trivial.

The positions where the cracks initiated in specimens 4µm-1 and 4µm-2 are depicted in Figure 5.20 and Figure 5.21. From the moment of initiation, the cracks were extended to reach the constant stress intensity region characterised by the plateau in the stress intensity data, refer to Section 5.2, Figure 5.6. The observations made during the propagation phase of the experiment are depicted in the following section.

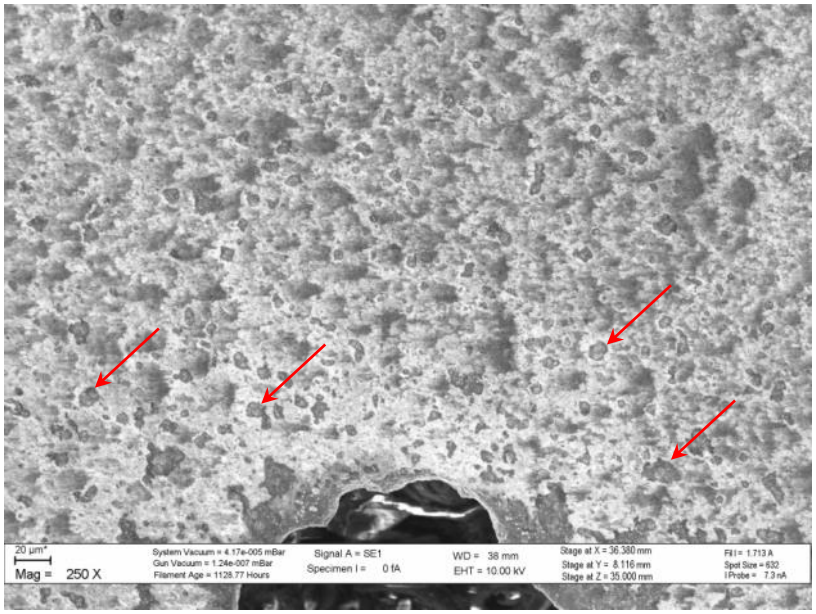

Figure 5.18 – SEM micrograph depicting the starter notch of the 4µm-1 specimen, highlighting its bluntness relative to a sharp crack. Note the pitting/erosion damage adjacent to the root of the starter notch (arrows).

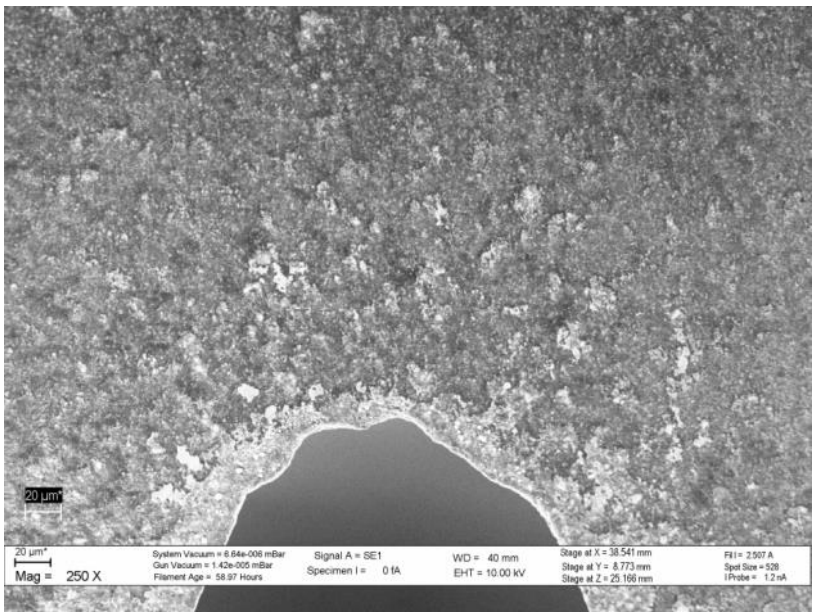

Figure 5.19 – SEM micrograph depicting the starter notch of the 4µm-2 specimen, highlighting an appearance different to that observed in Specimen 1, Figure 5.18.

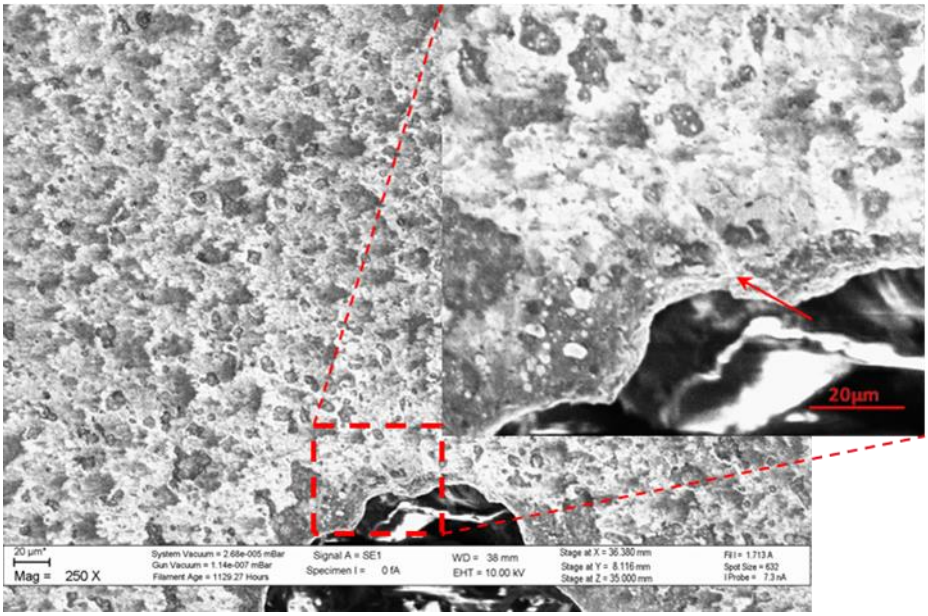

Figure 5.20 – SEM micrograph collage depicting the position of crack initiation in specimen 4µm-1.

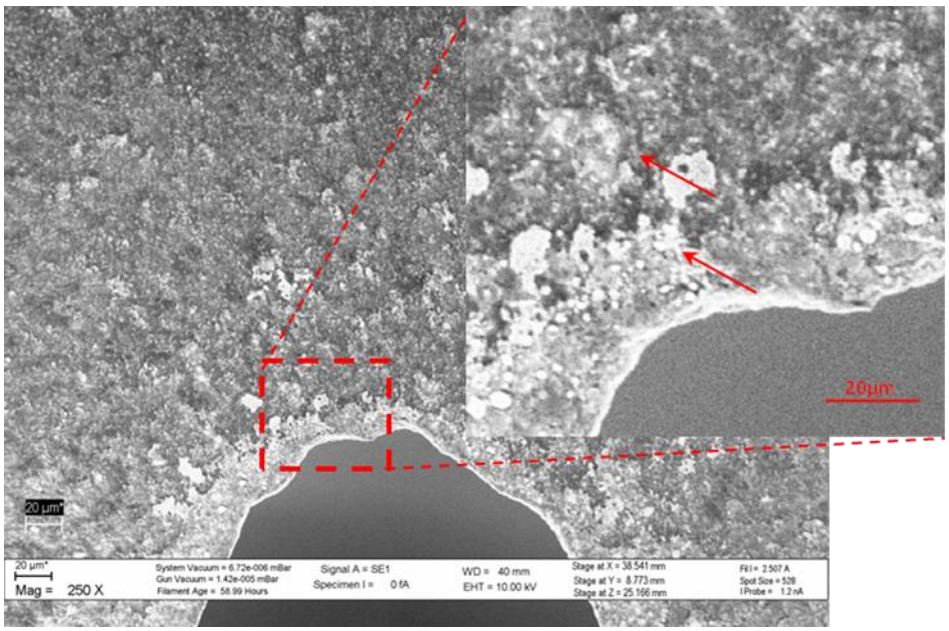

Figure 5.21 - SEM micrograph collage depicting the position of crack initiation in specimen 4µm-2.

5.4.2.2 Crack propagation

The propagation phase of the experiment was aimed at controllably propagating the crack into the constant stress intensity region and shutting the crack down with the aim of later observing the mating crack faces. An example of the developed crack is depicted in Figure 5.22. The image highlights that the crack path is affected by the microstructural features. Further live observation of the propagating crack revealed an instance where the crack "jumped" left, Figure 5.23. The observed feature is the result of the crack path entering a microstructural detail where the localised stress field caused fracture in two adjacent planes and the crack proceeded from the secondary crack face. However, the 4 µm PCD grade is the finest diamond grit grade with the highest binder content, which makes clear identification of various features difficult.

The key aim of the in-situ experiment in the second specimen, 4µm-2, was to propagate the crack through the region pre-mapped by EBSD. This would enable an attempt to correlate the crack path with respect to the orientation of the surface grains. The crack approaching the EBSD mapped region, demarcated by FIB marks is depicted in Figure 5.24. Controlled, incremental propagation

through this region is depicted in Figure 5.25. The crack path and its relation to the EBSD map are discussed in further detail in Section 5.6.

A sample of the crack path is further highlighted in Figure 5.26. The crack path features are similar to those observed in specimen 4µm-1. The levels of tortuosity are consistent and a “jump” ligament can be observed.

Once the region of constant stress intensity could be identified by the lack of change in the loading associated with incremental advance of the crack, the specimens were unloaded.

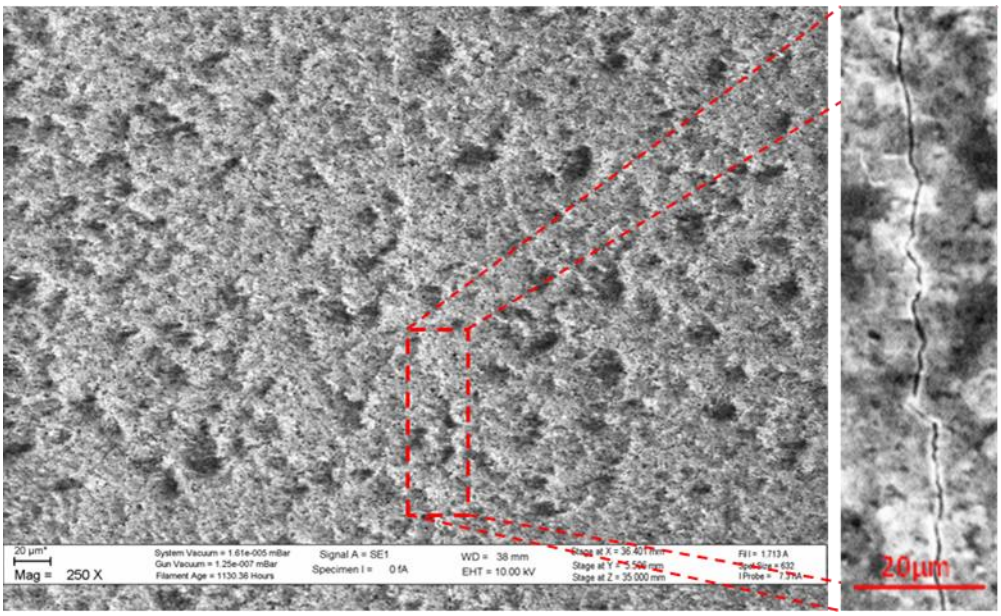

Figure 5.22 – SEM micrograph collage depicting the developed crack in specimen 4µm-1. The insert on the right depicts x2.5 magnification of the region highlighted by the dashed rectangle. The surface breaking portion of the crack plane can be seen deflecting due to the microstructural features.

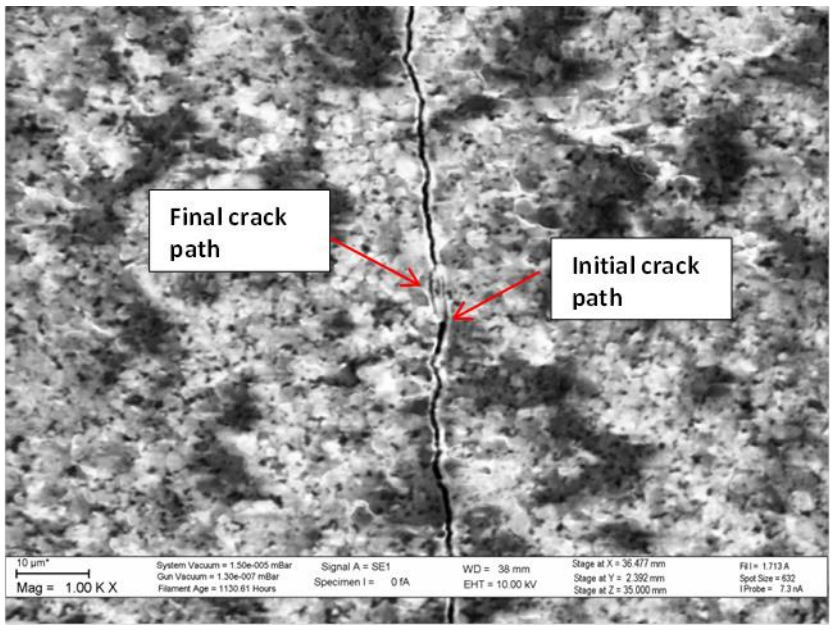

Figure 5.23 – SEM micrograph depicting a broken out ligament of the PCD surface material. The crack initially propagated to the right of the ligament and subsequently, the ligament fractured under the local stresses resulting in the crack jump to the left.

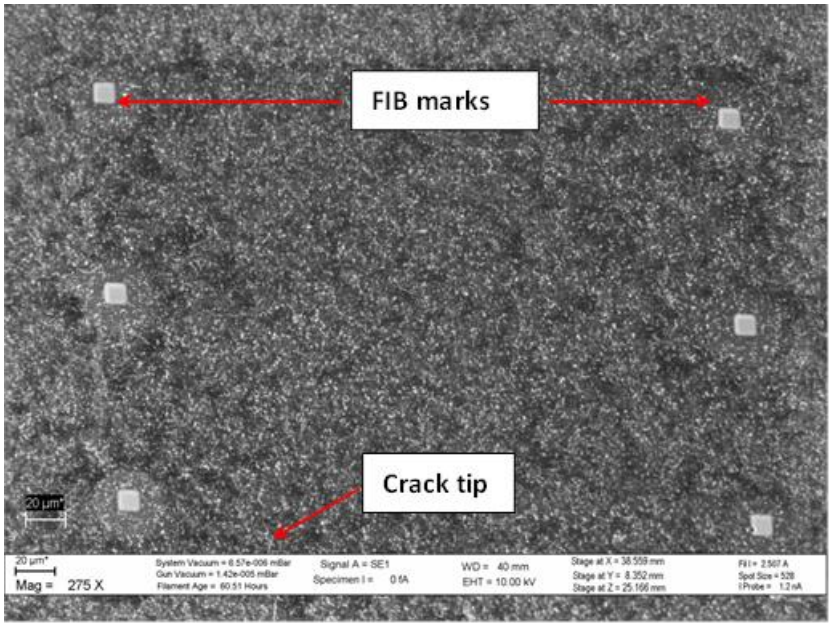

Figure 5.24 – SEM micrograph depicting the EBSD pre-mapped region highlighted by the FIB marks. The crack is entering the region from the bottom, highlighted by the arrow. The propagation of the crack is depicted in Figure 5.25.

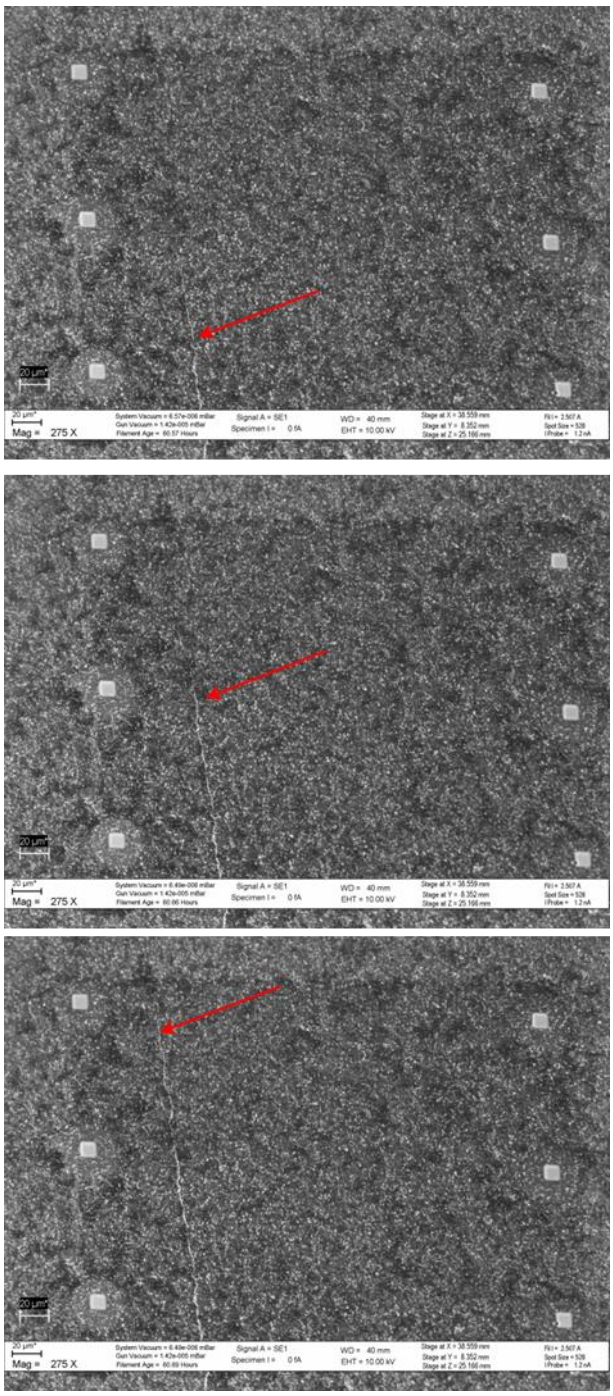

Figure 5.25 – SEM micrograph sequence depicting the crack propagation within the EBSD pre-mapped region.

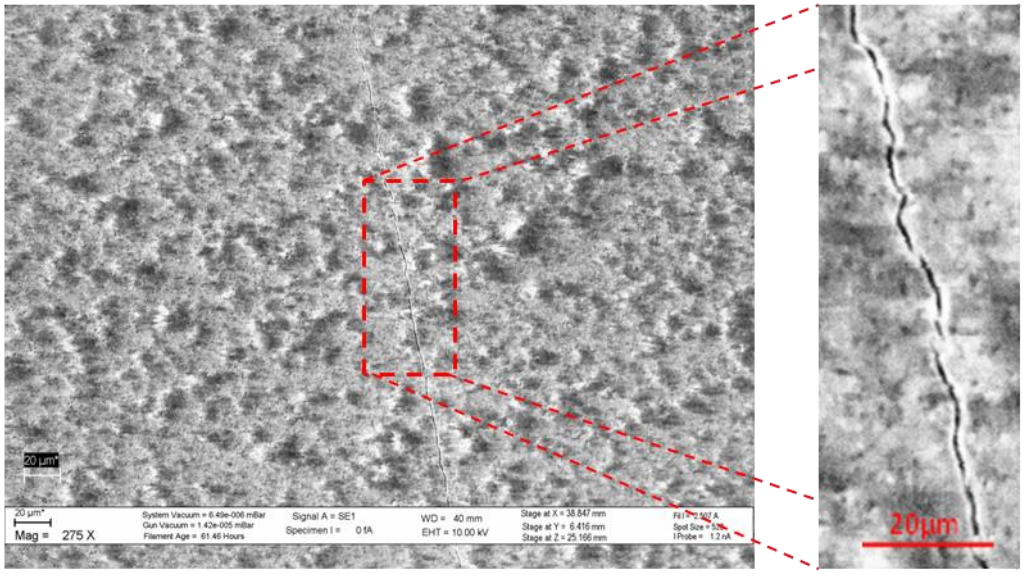

Figure 5.26 – SEM micrograph depicting the surface of specimen 4µm-2, highlighting the crack path (red arrow). The insert on the right depicts a x2.5 magnification of the crack path region highlighted by the dashed rectangle.

5.4.2.3 Inspection of the closed crack

After completion of the in-situ experiments, sample 4µm-1, containing an existing pre-crack, was inserted into the SEM in order to image the crack path at a lower accelerating voltage. The accelerating voltage was reduced from 10 kV to 5 kV in order to reduce the level of charging. This was possible as the working distance to the specimen could be reduced from 38-40 mm to 16 mm as the miniature DT rig was no longer in the chamber.

Inspection of the crack revealed some residual crack opening. The crack initiation region had shut tightly, however, further along the crack, residual opening remained. This is believed to be associated with wedging of the broken ligaments as well as crack wake interference suggesting a degree of secondary damage during crack propagation. These results should be compared to those obtained during the experiment in 30 µm PCD, detailed in section 5.4.4.

Figure 5.27 – SEM micrograph collage displaying a global view of that crack propagation path in the 4µm-1 specimen. The crack remained slightly open after the load was removed.

5.4.3 **12µm starter particle size**

5.4.3.1 Notch geometry and initiation

The starter notches of specimen 12µm-1 and specimen 12µm-2 are depicted in Figure 5.28 and Figure 5.29 respectively. The observed notch geometry was similar to that observed in the 4 µm specimens with fewer irregularities at the root of the notch. The cracks were controllably initiated in both specimens, Figure 5.30 and Figure 5.31. Imaging in specimen 12µm-2 was complicated by significant surface charging which resulted in the need to reduce the accelerating voltage. The accelerating voltage was reduced in increments of 2.5 kV from 10 kV to 2.5 kV in an attempt to obtain an image. At a later stage, the electron emitting filament was identified to have been failing and was subsequently replaced.

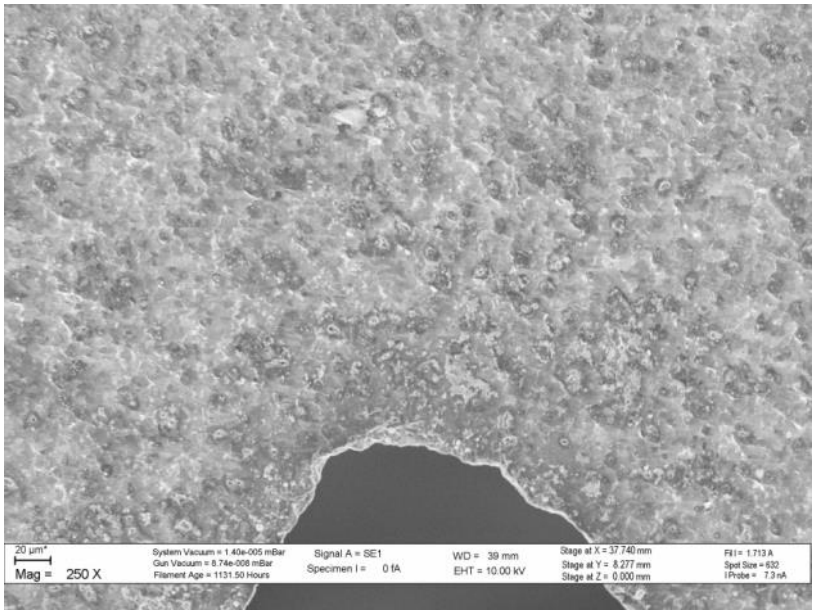

Figure 5.28 - SEM micrograph depicting the starter notch of the 12µm-1 specimen, highlighting its bluntness relative to a sharp crack. Some pitting/erosion, similar to that observed in the 4µm specimens, is evident around the EDM machined notch.

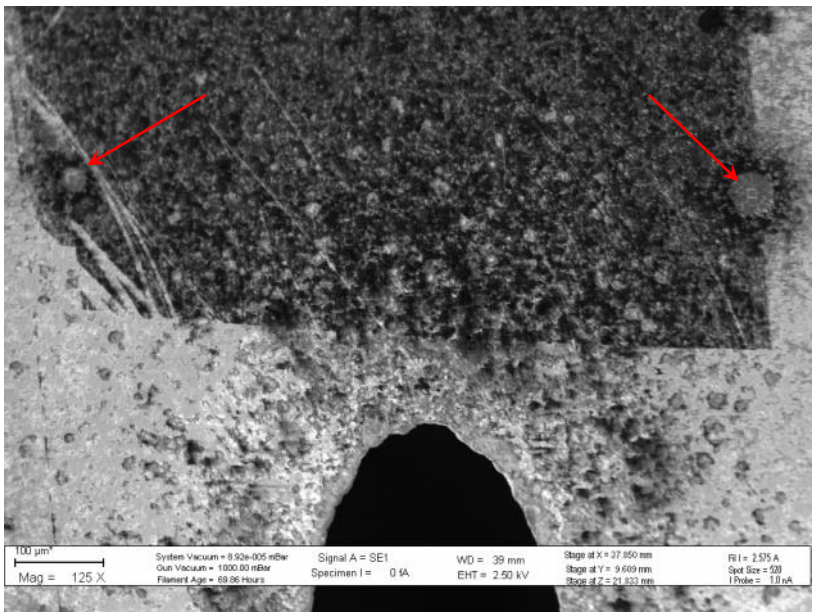

Figure 5.29 - SEM micrograph depicting the starter notch of the 12µm-2 specimen, highlighting an appearance different to that observed in Specimen 1. The specimen experienced significant deposition during the EBSD process which made crack detection difficult. The FIB marks are highlighted by arrows.

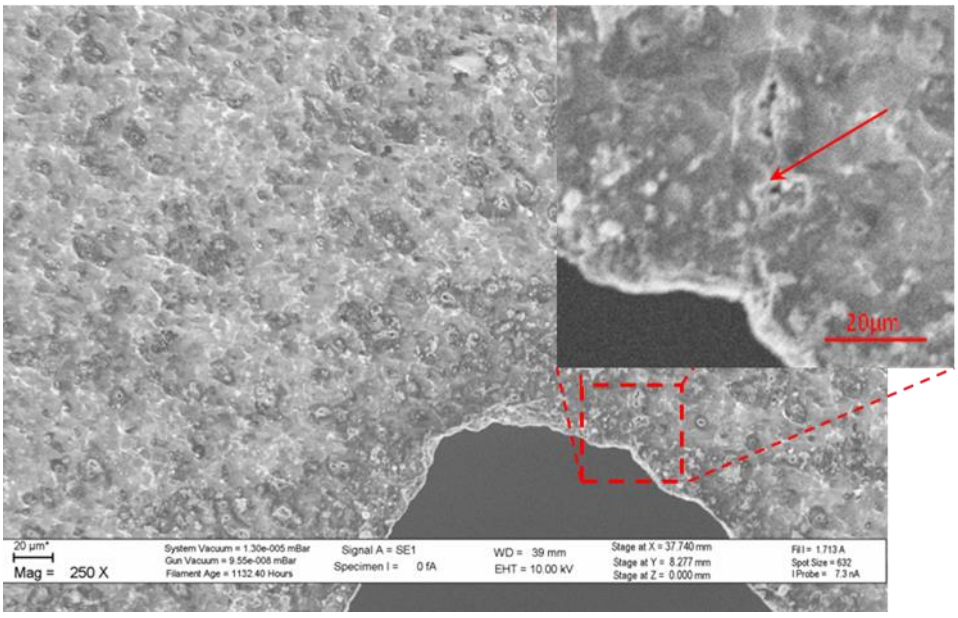

Figure 5.30 – SEM micrograph highlighting the region of crack initiation. The x2.5 magnification inset at the top right corner highlights that initiation coincided with pits believed to be the result of EDM machining process.

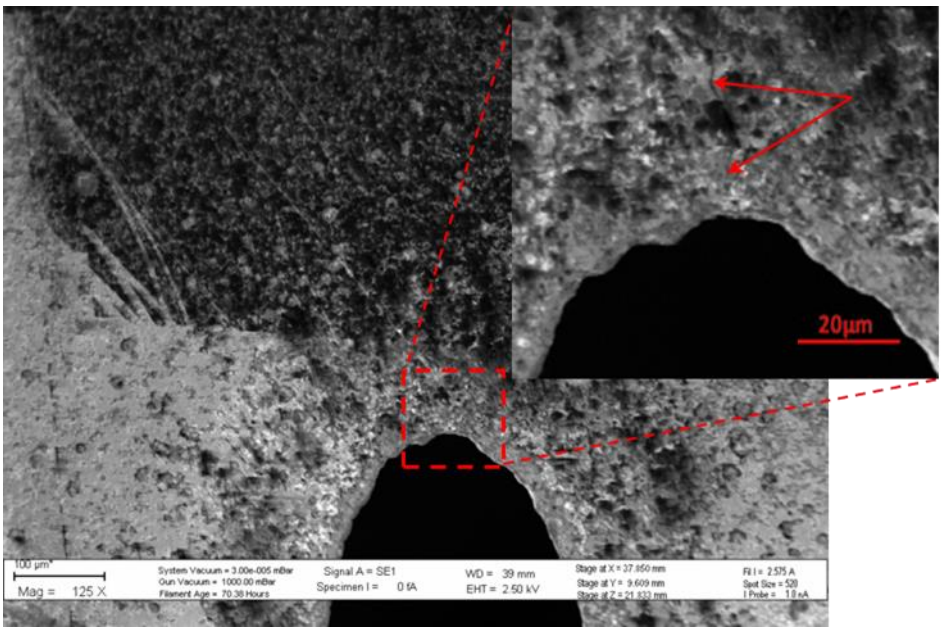

Figure 5.31 – SEM micrograph depicting the initiation notch of specimen 12µm-2. Imaging was complicated by charging the source of which was not well understood as specimens 12µm-1 and 12µm-2 were prepared employing the same procedure. The accelerating voltage had to be reduced to 2.5 kV in order to generate the initiation images.

5.4.3.2 Crack propagation

Due to the difficulties experienced during micrograph acquisition in specimen 12µm-2, only micrographs from specimen 12µm-1, Figure 5.32, are employed to describe the propagation of the crack with respect to the microstructural features of the PCD material. However, a crack was successfully grown through the EBSD pre-mapped region of specimen 12µm-2 and this information could be employed to correlate the propagation path with the EBSD map. Adjusting the contrast and brightness, the image of the crack propagating through the EBSD region is depicted in Figure 5.33.

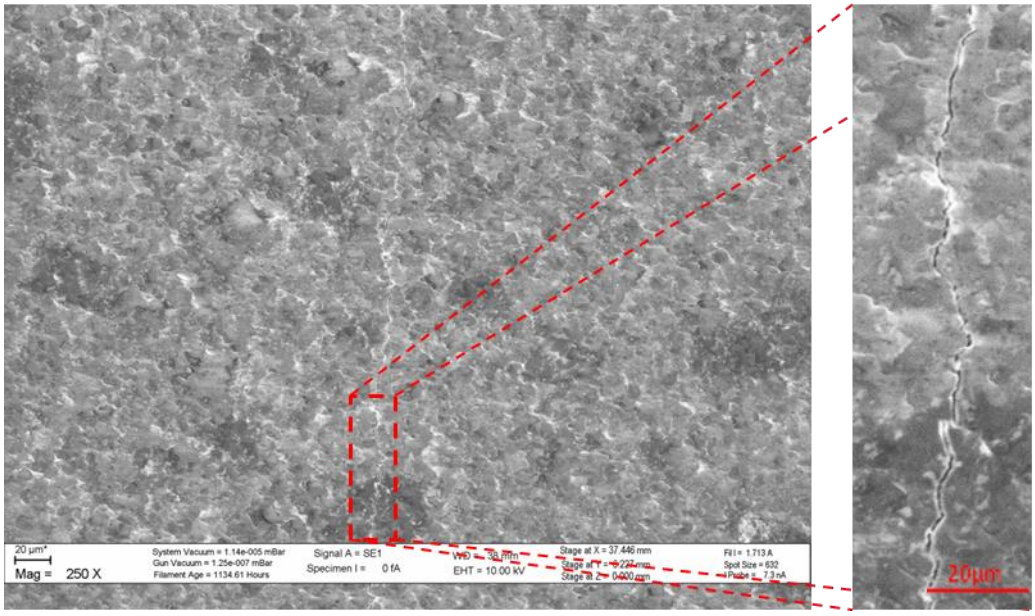

Figure 5.32 – SEM micrograph depicting the crack propagation in specimen 12µm-1. It is believed that the crack deflects along the preferential microstructural features.

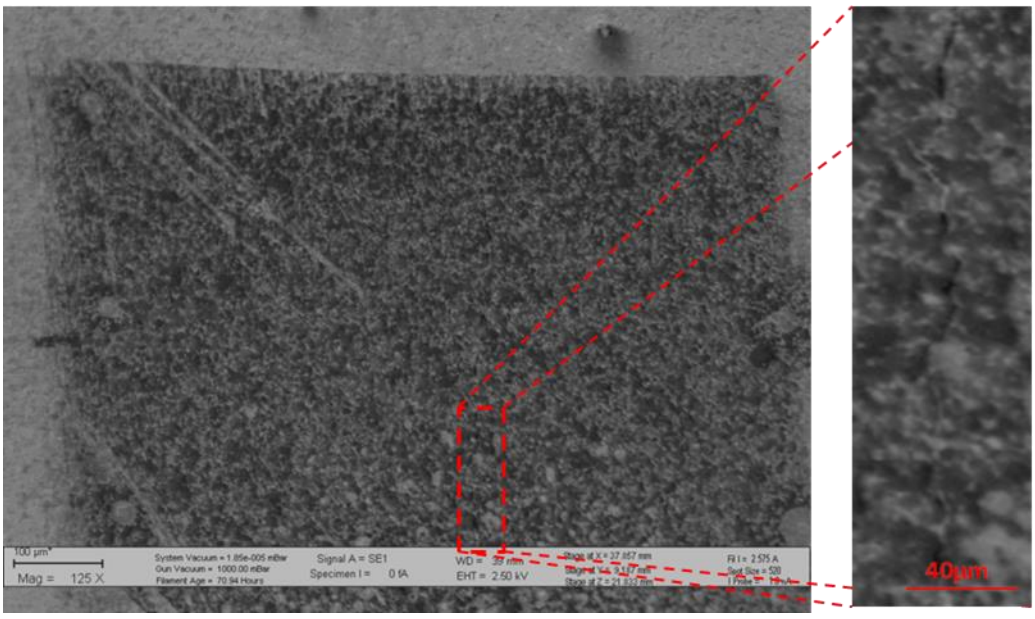

Figure 5.33 – SEM micrograph depicting the crack propagating through the EBSD pre-mapped region of specimen 12µm-2. Due to the difficulties with imaging the magnified view insert is not clear. However, the features resemble those observed in specimen 12µm-1.

5.4.3.3 Inspection of the closed crack

After completion of the in-situ experiments, sample 12µm-1, containing an existing pre-crack, was inserted into the SEM in order to image the crack path at a lower accelerating voltage in a manner similar to that employed in section 5.4.2.3. Accelerating voltage of 5 kV was employed. Inspection of the crack revealed some residual crack opening similar to that observed in the 4 µm specimen, Figure 5.34. These results should be compared to those obtained during the experiment in 30 µm PCD, detailed in the following section, where the crack shut very tightly.

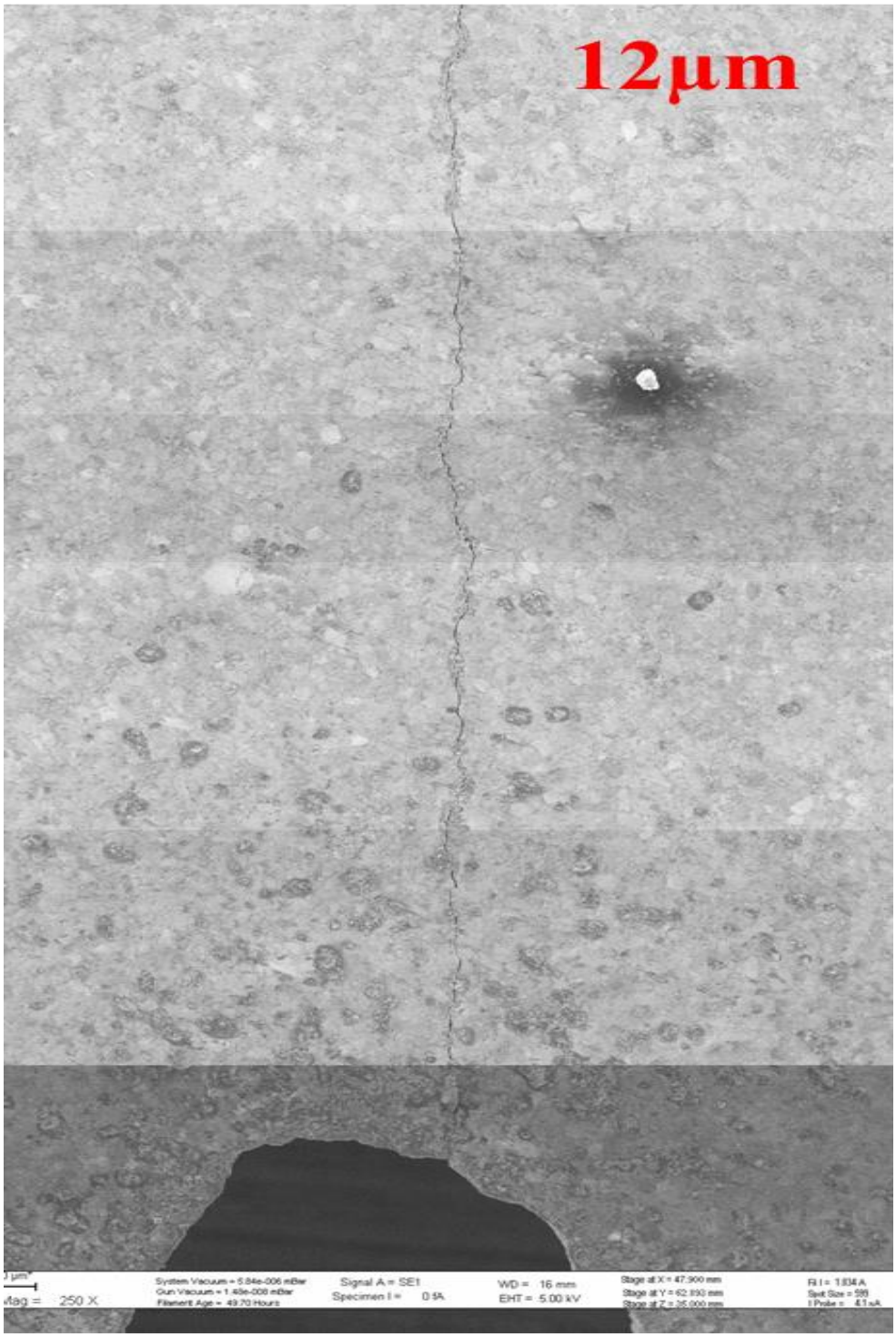

Figure 5.34 – SEM micrograph collage depicting the global view of the crack in the 12µm specimen after unloading of the miniature DT specimen. The crack appears more tortuous than the crack observed in the finer grained 4µm specimen.

5.4.4 **30µm starter particle size**

5.4.4.1 Notch geometry and initiation

The starter notches of specimen 30µm-1 and specimen 30µm-2 are depicted in Figure 5.35 and Figure 5.36 respectively. While different accelerating voltages were employed for the two in-situ experiments, the specimen surface had what appeared as significantly different finishes. Furthermore, the initiation in specimen 30µm-1 was the only instance where the crack initiated away from the centre of the specimen, Figure 5.37. The reason for such misaligned initiation became apparent during the analysis of the fracture surfaces after all specimens were broken. The notch root had a clear geometrical step feature which resulted in the observed initiation misalignment. The information detailing the fractographic feature is detailed in Section 5.5.

Initiation in specimen 30µm-2 was well aligned, Figure 5.38. The crack was propagated controllably into the EBSD pre-mapped region as detailed in the following section.

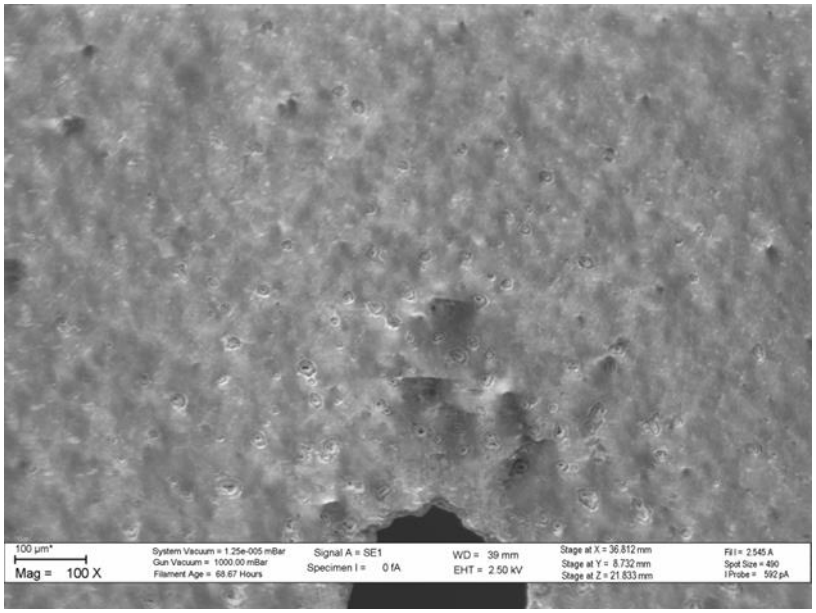

Figure 5.35 - SEM micrograph depicting the starter notch of specimen 30µm-1.

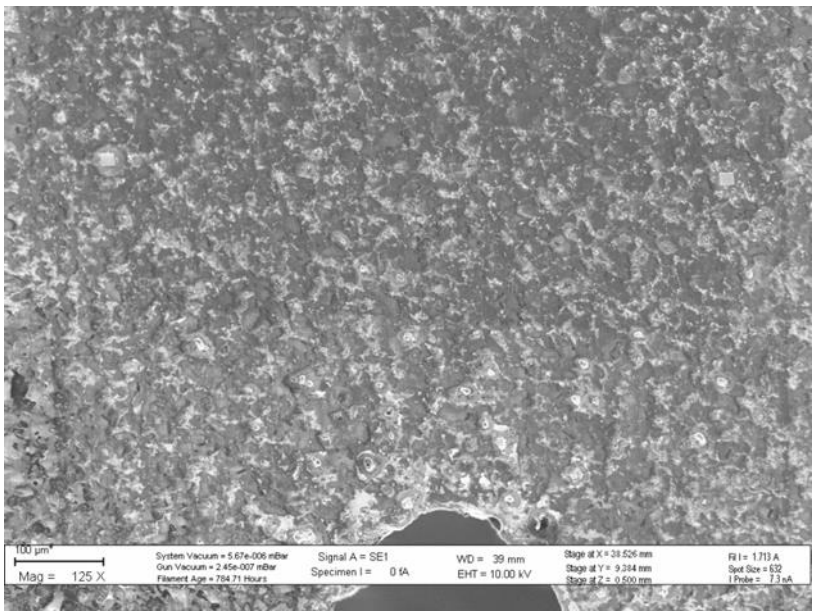

Figure 5.36 – SEM micrograph depicting the starter notch of specimen 30µm-2**.**

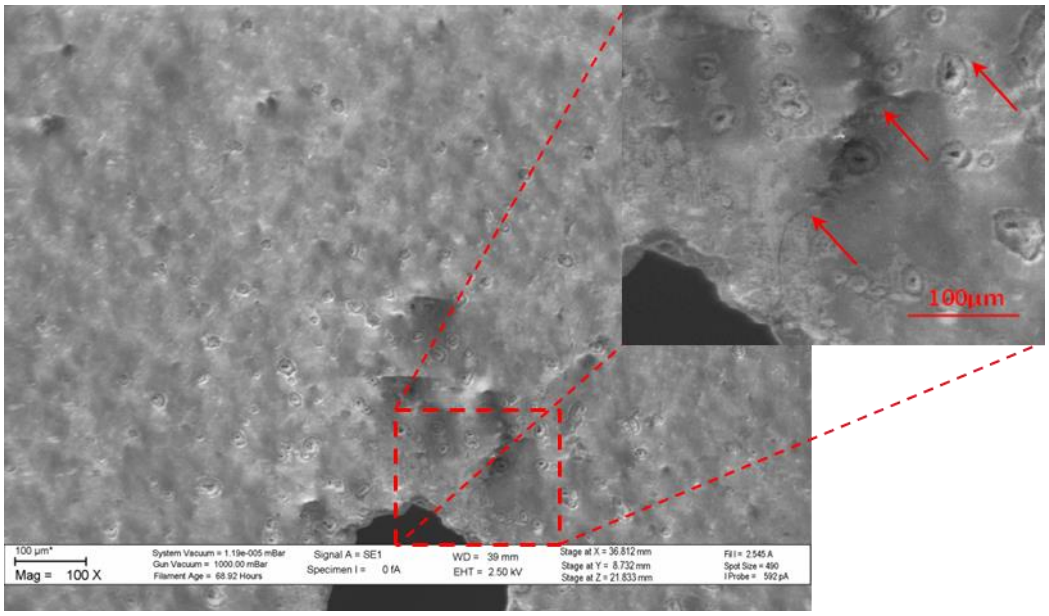

Figure 5.37 – SEM micrograph depicting the initiation observed in specimen 30µm-1. This was the only instance where the crack initiated away from the centre, as highlighted by the x2.5 magnification insert (the crack is highlighted with arrows).

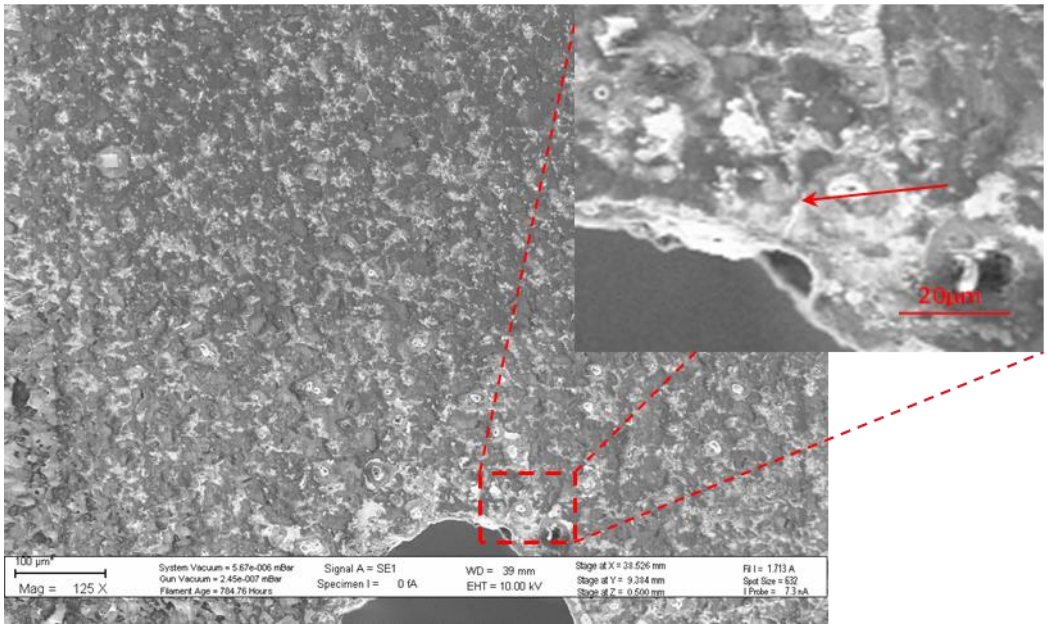

Figure 5.38 – SEM micrograph depicting the crack initiation region in specimen 30µm-2.

5.4.4.2 Crack propagation

As detailed in the previous section, the propagation of the crack in specimen 30µm-1 initiated with a deviation from the centre of the notch, Figure 5.39. Due to this deviation, limited information could be obtained from specimen 30µm-1. However, specimen 30µm-2 initiated correctly and the crack propagated into the EBSD pre-mapped region, Figure 5.40. During observation in the EBSD pre-mapped region, low magnification was employed to frame the FIB marks which demarcate the EBSD region. Once the crack propagated through the pre-mapped region, higher magnification images of the propagation phenomena were obtained, Figure 5.41 and Figure 5.42. These observations revealed crack features associated with the crack front propagation along energetically preferential features. An instance of crack branching was also observed during the experiment, Figure 5.43. Live observation of the crack propagation process in the coarser 30 µm PCD grade revealed more definitive evidence of features such as crack jumping and bridging. These are believed to be the result of the higher energy requirements to circumnavigate the tough diamond grains impeding crack development. The following section further highlights that the 30 µm grade revealed the most tightly closed global crack appearance after unloading.

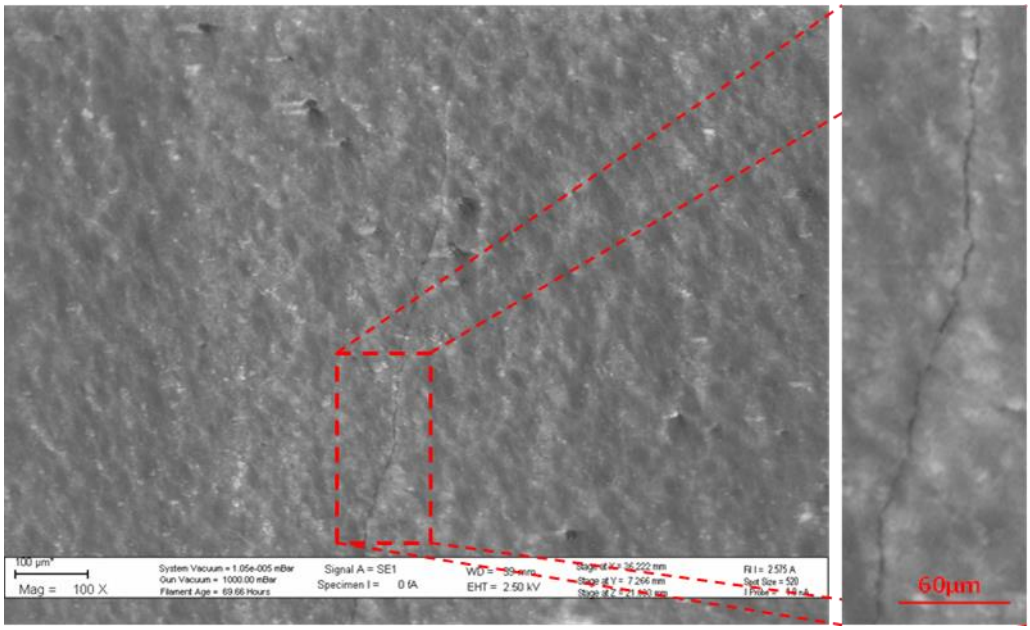

Figure 5.39 – SEM micrograph depicting the propagation of the crack in the 30µm-1, highlighting the fact that the crack is propagating from left to right.

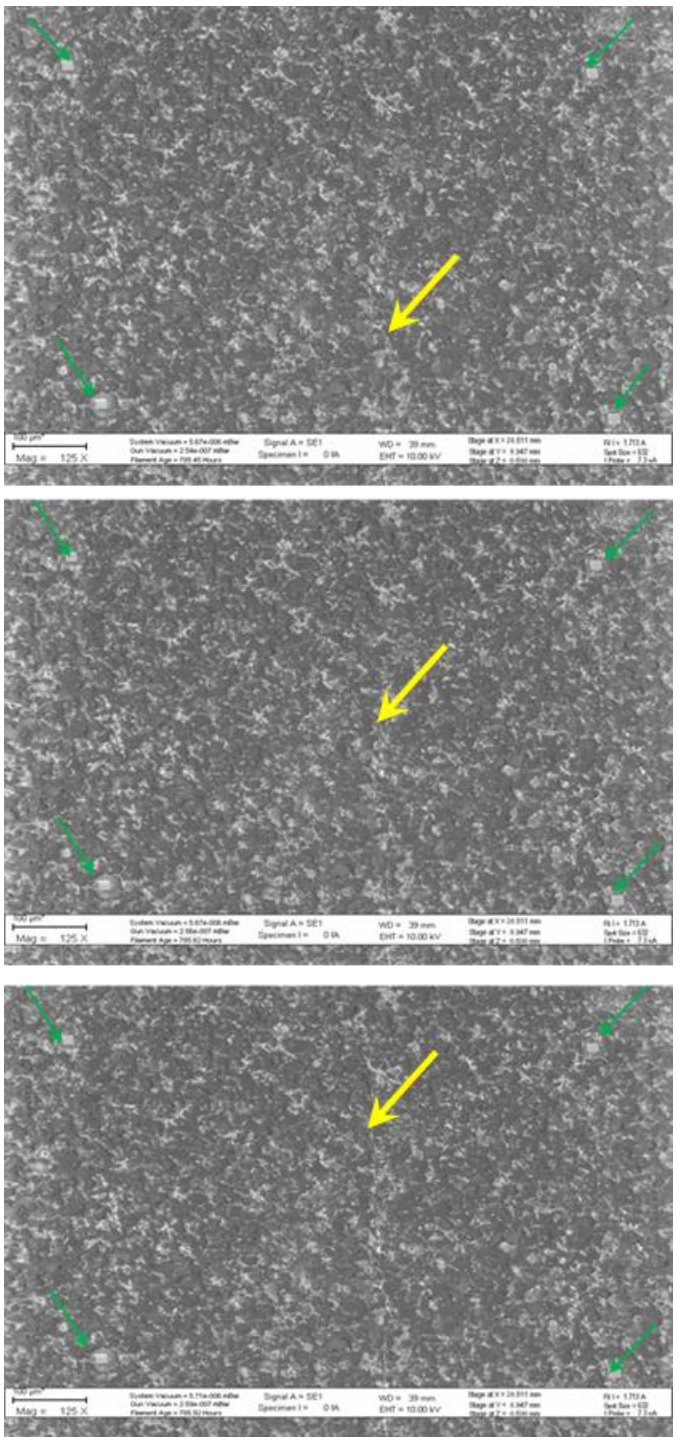

Figure 5.40 – SEM micrograph collage depicting three stages of crack propagation through the EBSD mapped region (green arrows highlight FIB marks and red arrows highlight the crack tip position).

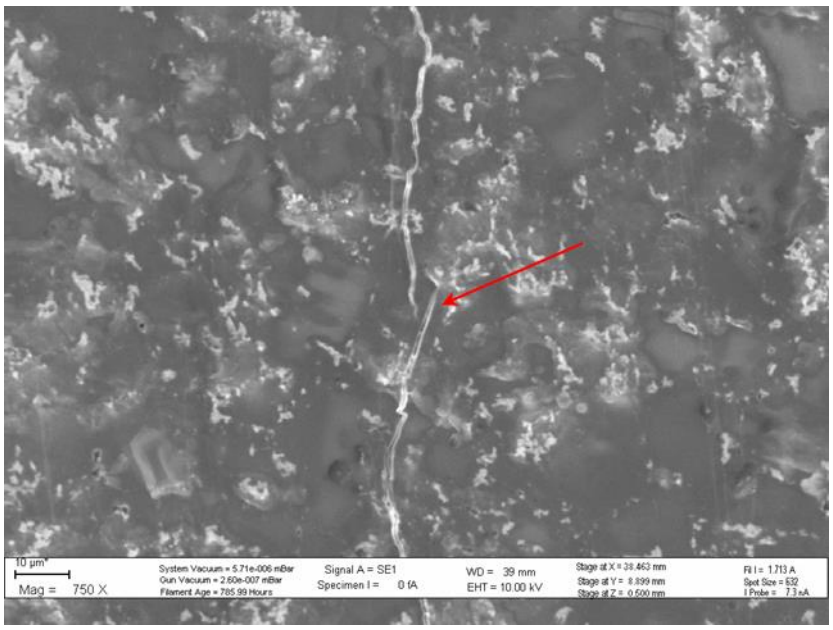

Figure 5.41 – SEM micrograph depicting the crack propagation in specimen 30µm-2, highlighting a crack "jump" feature. The crack terminates in what appears to be a diamond crystal and re-initiates along an energetically preferential path (arrow).

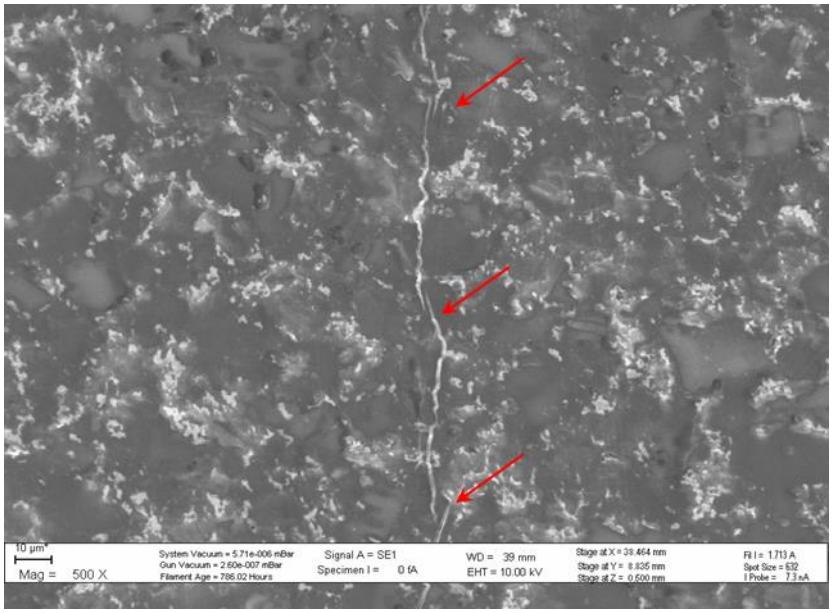

Figure 5.42 – SEM micrograph depicting further crack "jumps" during propagation in specimen 30µm-2.

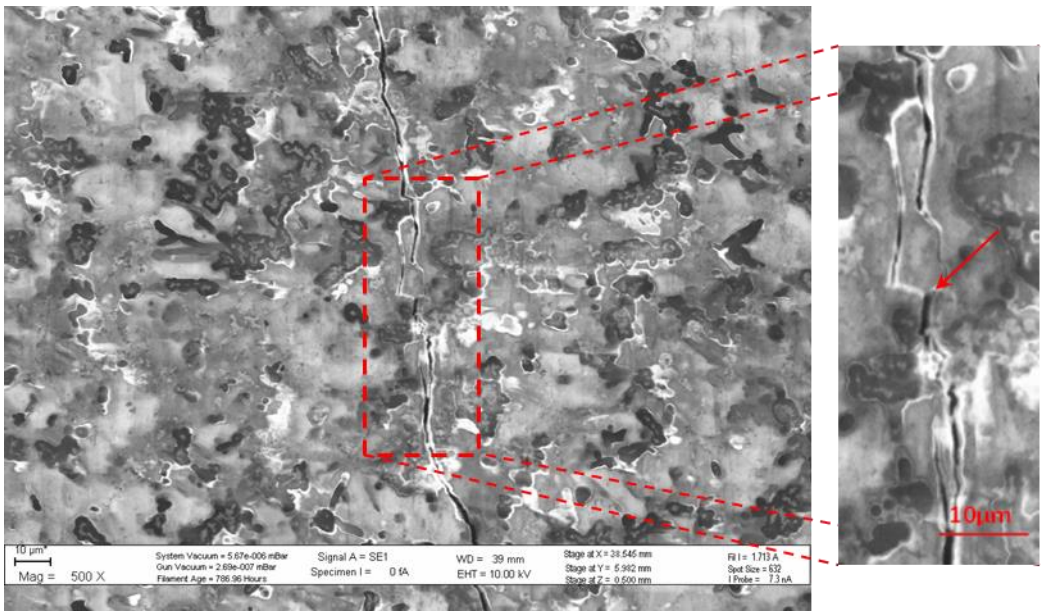

Figure 5.43 – SEM micrograph depicting a crack branching feature in specimen 30µm-2 (arrows).

5.4.4.3 Inspection of the closed crack

Inspection of the unloaded specimen 30µm-2 revealed a very tightly shut crack, Figure 5.44. Comparing the crack path to the crack paths observed in the finer grained specimens, Figure 5.27 and Figure 5.34, a much tighter crack was observed. Observation of the crack in the coarser grain specimen also better revealed the propagation of the crack as a function of the microstructural features. Both transgranular and intergranular propagation features could be observed, Figure 5.45.

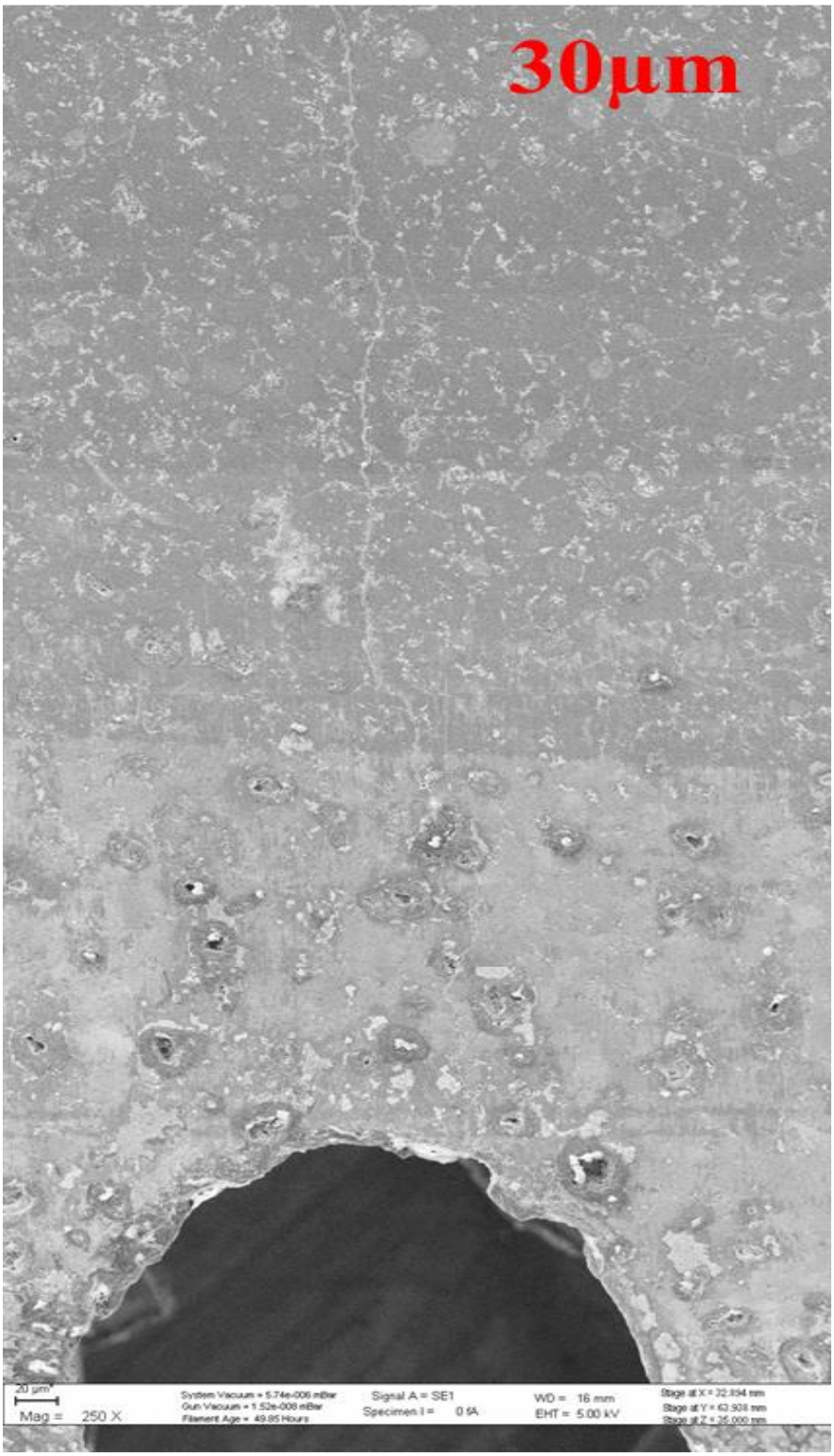

Figure 5.44 – SEM micrograph collage depicting the global view of the crack after specimen 30µm-2 unloading.

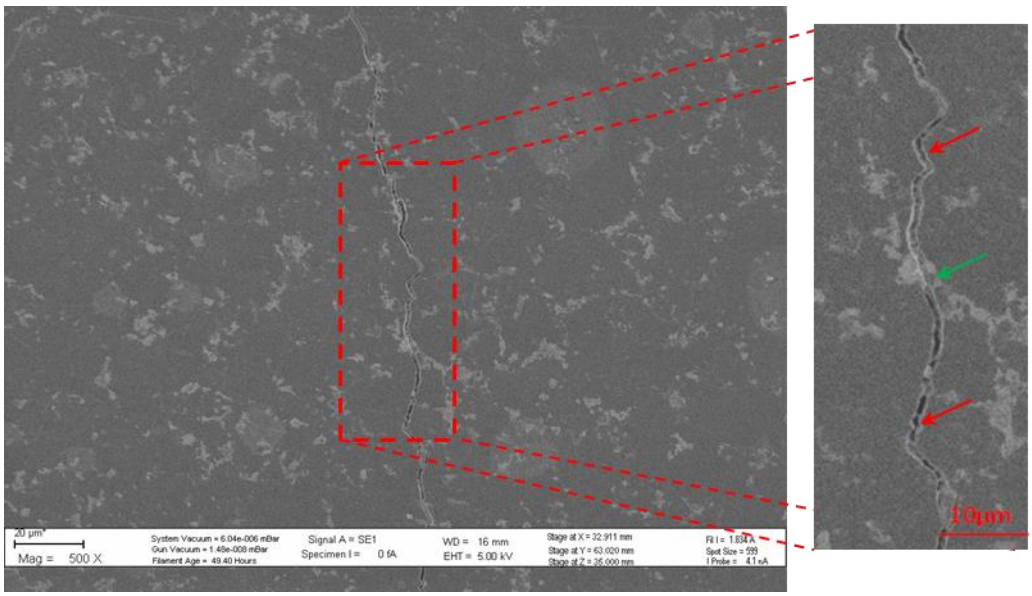

Figure 5.45 - SEM micrograph depicting the propagation features in specimen 30µm-2 after unloading. The red arrows highlight the positions where the crack propagates through diamond grains. The green arrow highlights a deviation of the crack to the left, seeking a preferential path in the binder pool – between diamond grains.

5.4.5 **30-4µm starter particle size**

5.4.5.1 Notch geometry and crack initiation

The notch geometries of specimens 30-4µm-1 and 30-4µm-2 are depicted in Figure 5.46 and Figure 5.47. The notch of specimen 30-4µm-1 had an irregular shape, however, it did not appear to significantly affect the crack initiation process. Pitting, believed to be caused by EDM machining, was evident adjacent to starter notches of both specimens. The 30-4µm material appeared to have a more smeared surface appearance and further proved to be more challenging to image in-situ SEM. Changes in the accelerating voltage in the range of 2.5-10 kV did not appear to have a significant improvement, neither did variation of other microscope parameters.

Both cracks initiated controllably, at the roots of the starter notches, Figure 5.48 and Figure 5.49. In the case of specimen 30-4µm-2, the FIB marks were closer than the other specimens that were pre-mapped. In order to frame the FIB marks, demarcating the pre-mapped EBSD region, a magnification, lower than that for specimen 30-4µm-1 was employed.

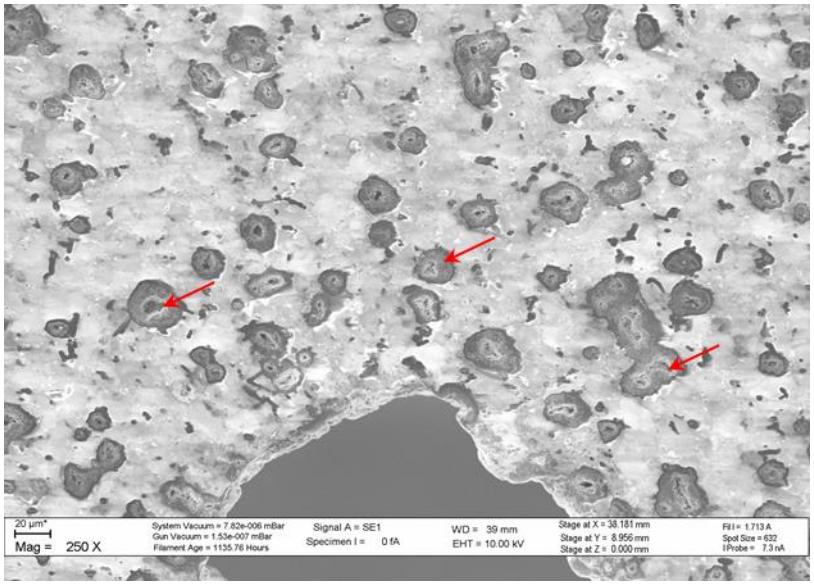

Figure 5.46 - SEM micrograph depicting the starter notch of specimen 30-4µm-1. The root of the notch had irregular geometry. Regions of cobalt pool removal due to EDM machining were observed adjacent to the notch (red arrows).

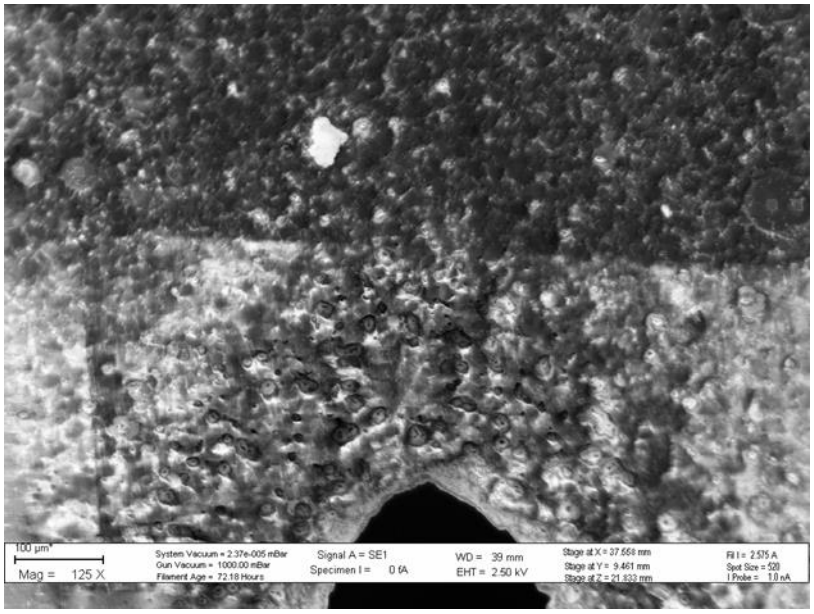

Figure 5.47 - SEM micrograph depicting the starter notch of specimen 30-4µm-2. The root of the notch had irregular geometry with regions of cobalt pool removal due to EDM machining (red arrows).

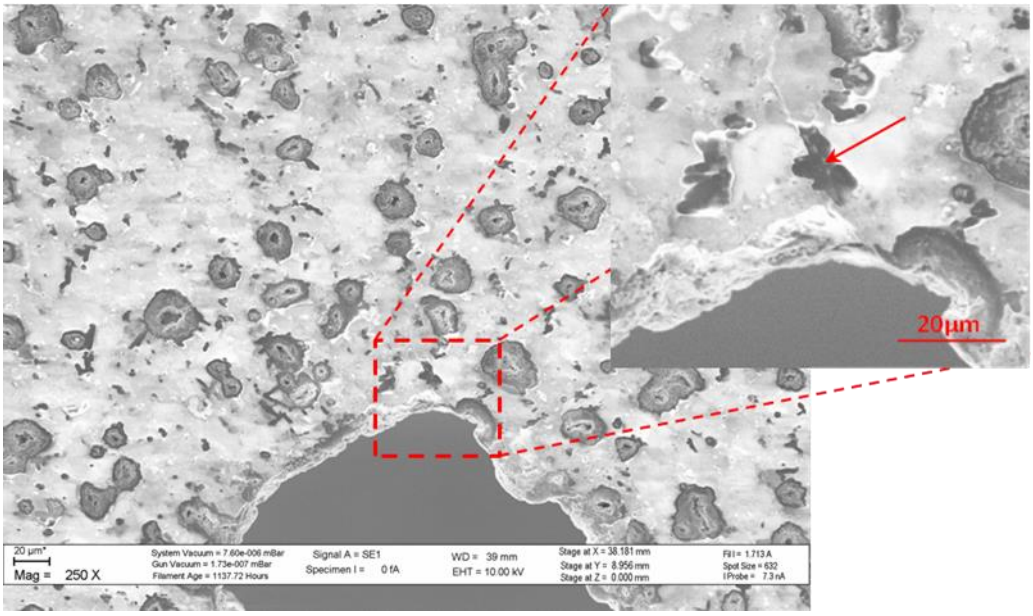

Figure 5.48 - SEM micrograph depicting the crack initiation region in specimen 30-4µm-1. The crack initiated at the root of the notch, adjacent to an EDM erosion defect.

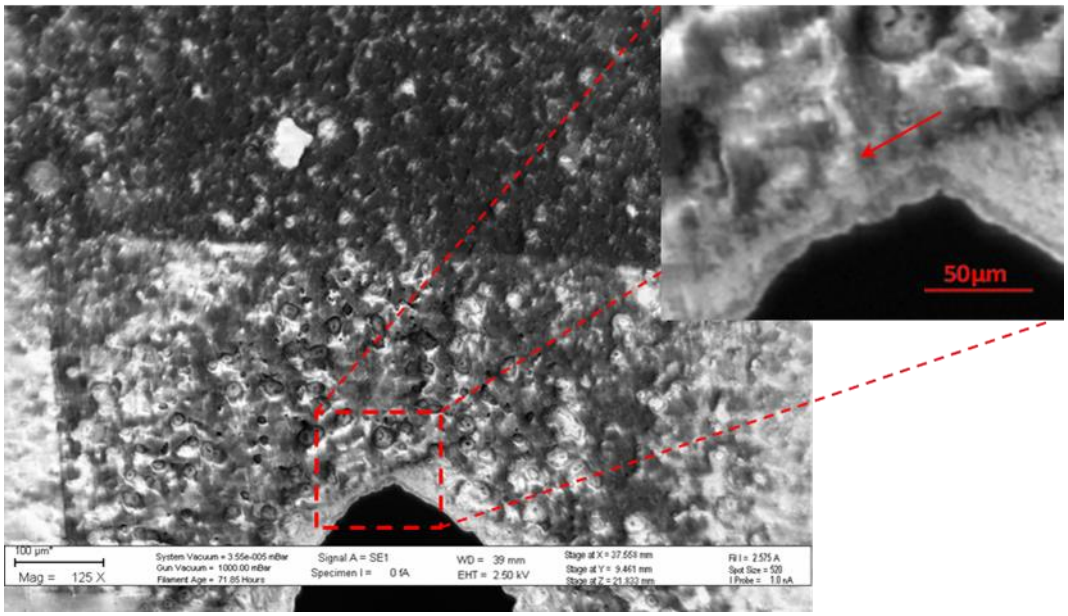

Figure 5.49 - SEM micrograph depicting the starter notch of specimen 30-4µm-2. Crack initiation occurred at one of the EDM machining defects in the root of the starter notch (red arrow). The magnification was halved in order to frame the FIB marks.

5.4.5.2 Crack propagation

The cracks were controllably initiated and propagated in both specimens. The crack in specimen 30-4µm-2 was incrementally propagated through the EBSD pre-mapped region, Figure 5.50. Observation of the crack propagation process further revealed crack bridging and deflection features similar to those observed in the finer grain specimens. The degree of deflection appeared to have increased, which would be consistent with the higher deflection potential of the coarse grain microstructure.

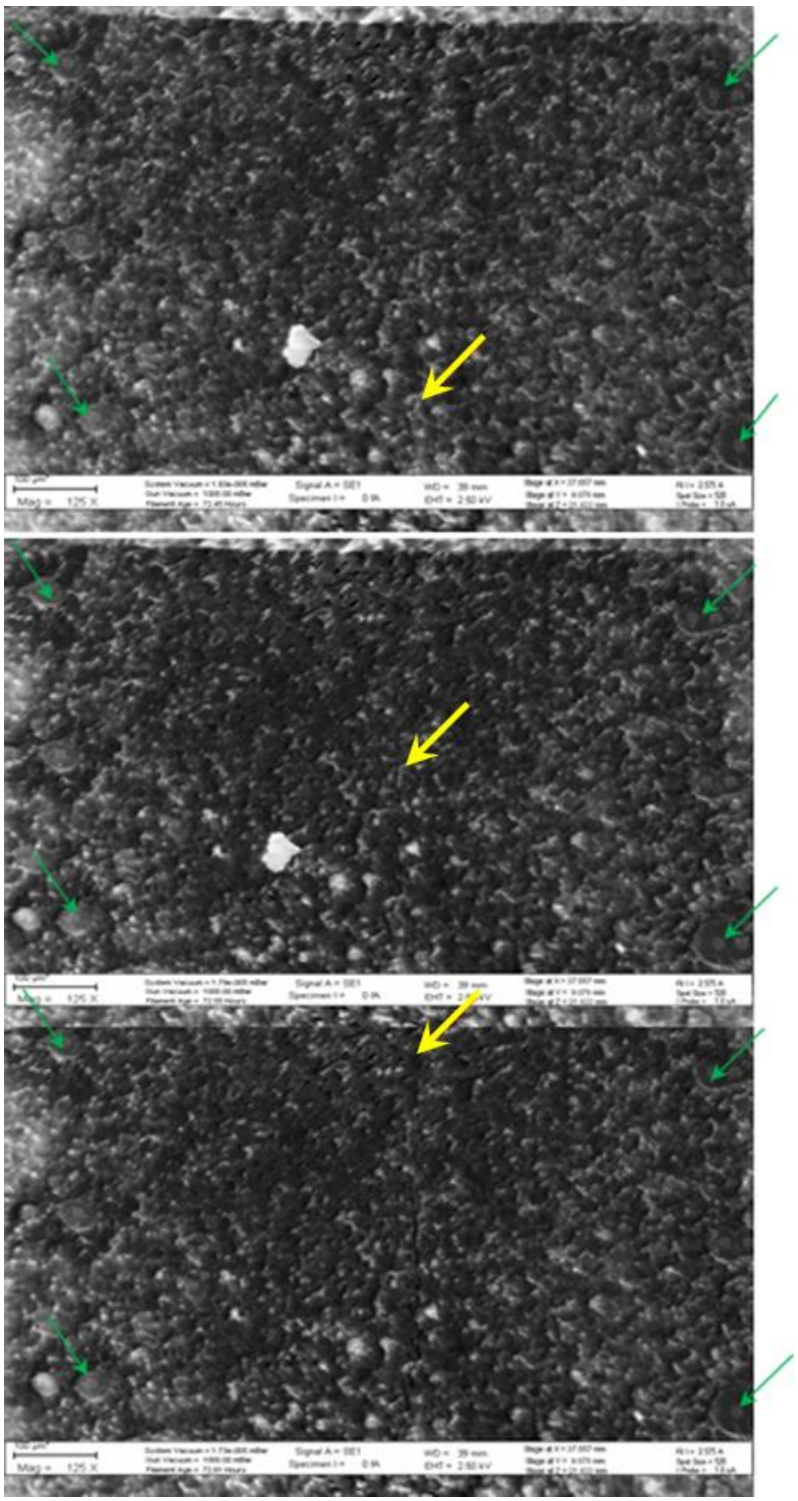

Figure 5.50 - SEM micrograph collage depicting three stages of crack propagation through the EBSD mapped region of specimen 30-4µm-2 (green arrows highlight FIB marks and red arrows highlight the crack tip position).

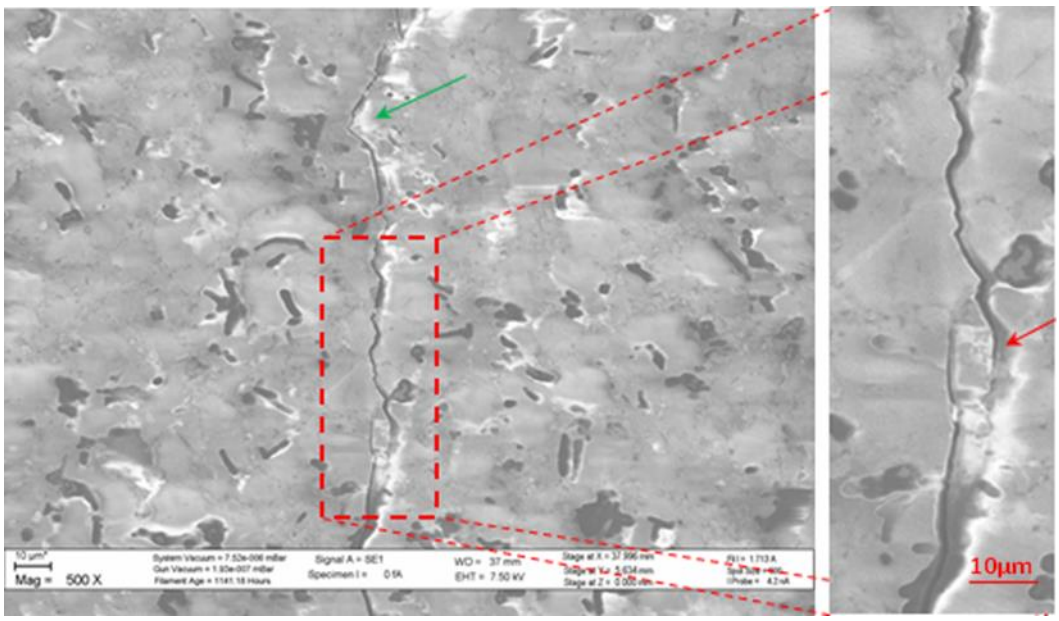

Figure 5.51 - SEM micrograph depicting a crack branching feature in specimen 30-4µm-1 (arrow). Significant crack path deflection was also observed (green arrow, main image).

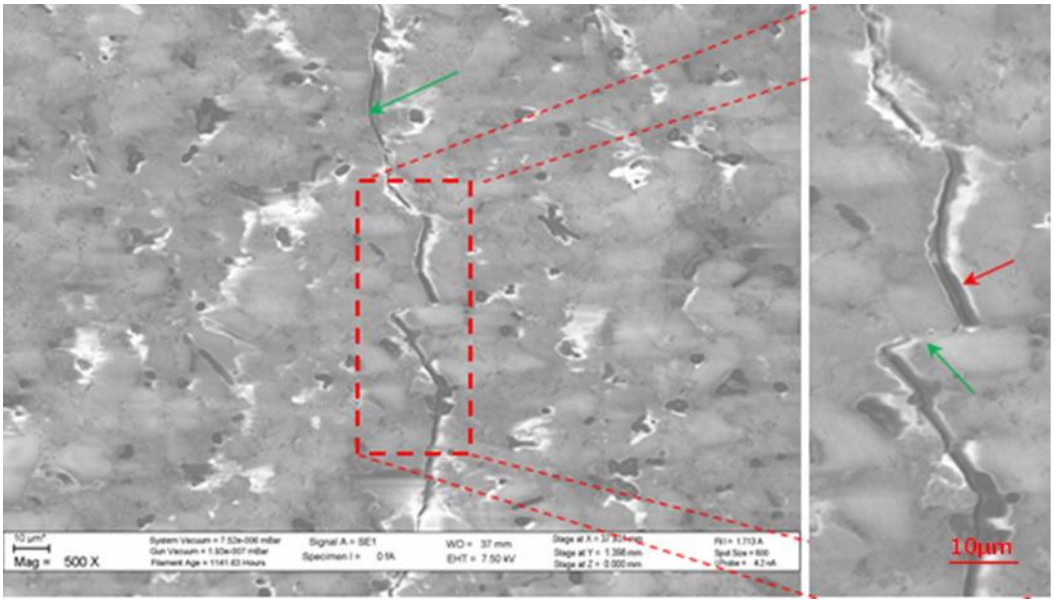

Figure 5.52 - SEM micrograph depicting a crack deflection feature in specimen 30-4µm-1 (arrow). The feature appears to have been generated by a relative slip between two diamond grains (green arrow) with subsequent fracture of a grain along a preferential cleavage plane (red arrow).

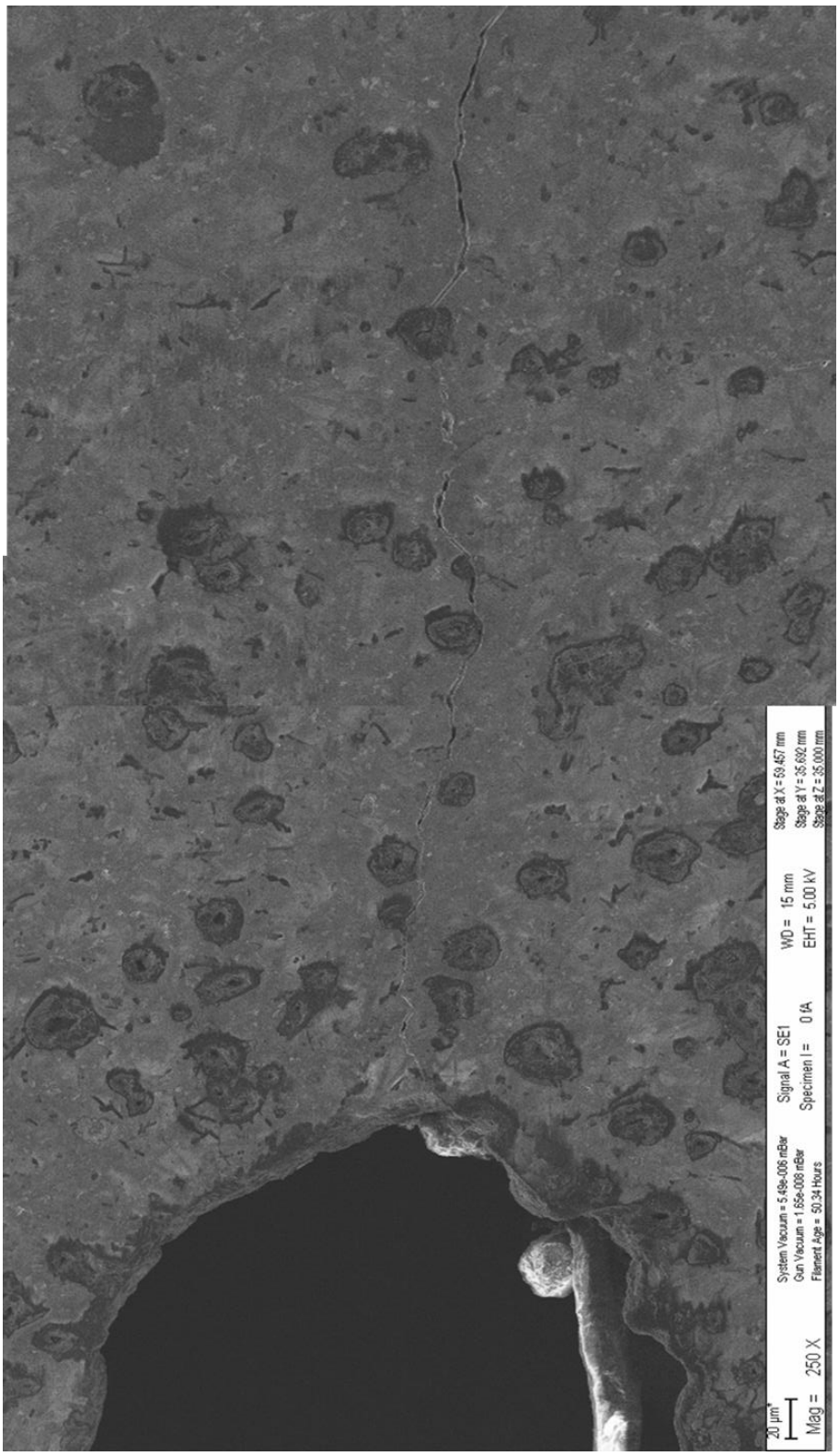

Figure 5.53 – Micrograph collage depicting the crack in specimen 30-4µm after unloading.

5.5 Fractography

The following subsections detail the findings of the fractographic analyses performed perpendicular and parallel to the fracture surfaces of the broken miniature DT specimens as well as fractographic feature observations during the EBSD post-mapping experiments on the pre-cracked specimens. The results of the inspection of the pre-cracked specimens resemble those obtained during the live in-situ fracture process observation. However, they key difference is the use of a field emission SEM microscope which allowed for better quality imaging employing optimum working distance.

5.5.1 Broken specimen fractography

In order to examine the fracture surfaces of the broken specimens, the specimens were fitted into a special stub holder where the 0.5 mm thick plates could be set on their long edge, exposing the fracture surface to the electron beam. As shown in the Figure 5.54 and Figure 5.55, the specimens were inserted into two separate stub holder slots, with 4 µm and 30 µm and the 12 µm and 30-4 µm specimens being inserted adjacent to each other.

Initial observation of the fracture surfaces revealed a clear difference in the appearance of the fracture surfaces of the different grades of the PCD material. The fracture surface of the 4µm-1 specimen appeared smooth and devoid of any significant relief. By comparison, the fracture surface of the 30µm-1 specimen was much rougher, having significant topological relief, Figure 5.54. Inspection of the fracture surfaces of the 12µm-1 and 30-4µm-1 specimens, depicted in Figure 5.55, resulted in similar observation. The fracture surface of the finer grain 12 µm material was significantly smoother when compared to the 30-4 µm material. The more pronounced topological relief in the coarser grain specimens is consistent with the theory of a more tortuous crack path. The coarse diamond grains result in more crack tip deflection, resulting in longer crack path and hence higher energy requirement for crack development. These observations are further consistent with the quantitative double torsion fracture test results detailed in section 5.2, where the coarse grained material revealed higher fracture toughness properties than the fine grained material.

Further inspection of the fracture surface of the 4 µm specimen revealed a feature consistent with a propagation arrest mark, Figure 5.56. Inspection of the fracture surface at the arrest mark boundary revealed a difference in the

appearance of the fracture diamond grains and cobalt pools, Figure 5.57. The observed change in appearance is believed to be related to the rate of crack propagation, where higher propagation velocity results in a less tortuous path and an increase in cleaved grains.

Inspection of the fracture surfaces further revealed a difference in the appearance of the cobalt pools. The fine grained PCD materials showed a higher ratio of cobalt to diamond on the fracture surfaces, Figure 5.58 to Figure 5.61. This is consistent with the microstructural analyses performed in section 5.1.1 which revealed that the fine grained specimens had the highest cobalt content. The finest starter particle size grades of PCD tend to require add-mixing of cobalt into the diamond grit as cobalt diffusion during sintering is not as efficient as that observed in the case of coarser starter particle sizes [46]. Inspection of the fracture surfaces of the 30 µm and 30-4 µm specimens revealed that the cobalt phase is clearly defined at the grain boundaries of the diamond grains. This feature is well described in Figure 5.62, where a lower magnification micrograph clearly highlights the cobalt phase at the boundaries of the diamond grains. Therefore, any preferential propagation along these cobalt features would require higher energies to circumnavigate the diamond grains. In case of the 4 µm material and the relative abundance of the cobalt pools within the microstructure, the crack deflection and hence the toughening mechanism is reduced. This is again consistent with material toughness findings, detailed in section 5.2, which revealed that the 30 µm and 30-4 µm materials had higher fracture toughness properties. The higher fracture toughness can be further attributed to higher levels of contiguity between the coarser diamond crystals as supported by the discontinuous nature of the cobalt phase along the diamond grain boundaries, Figure 5.63.

In an attempt to verify the observation of more intergranular fractographic features at slow crack propagation rates versus more transgranular features at faster crack propagation rates, EDS mapping of surface cobalt was undertaken. The mapping approach and the results obtained are discussed in the following section.

Over the course of the fractographic analysis, the 30µm material was identified to have a number of deleterious porosity features, Figure 5.64. Evidence of these defects helps to explain the deflection of the crack from the centreline of the miniature DT specimen. Similar defects were not observed in the remaining three PCD grades investigated.

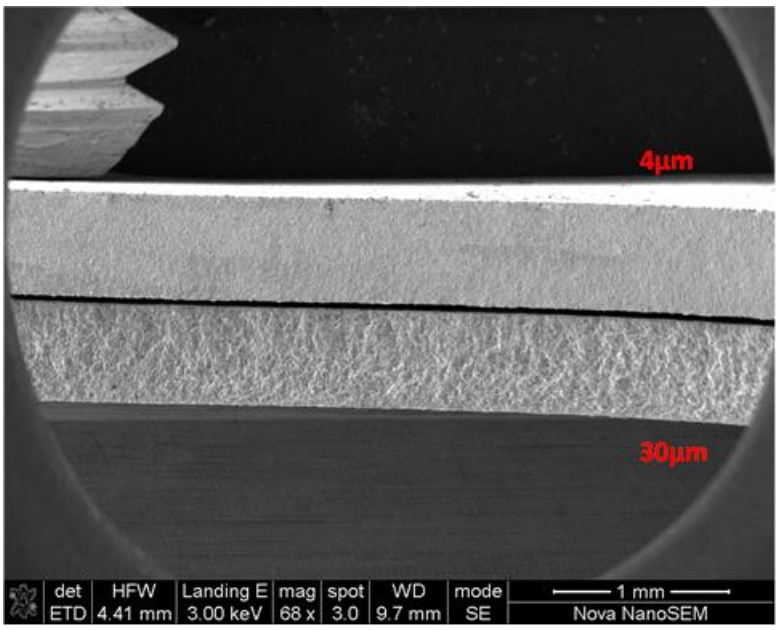

Figure 5.54 – SEM micrograph depicting the fracture surfaces of specimens 4µm-1 and 30µm-1. The specimens are mounted adjacent to each other, held in by a grub screw visible in the top left corner of the micrograph.

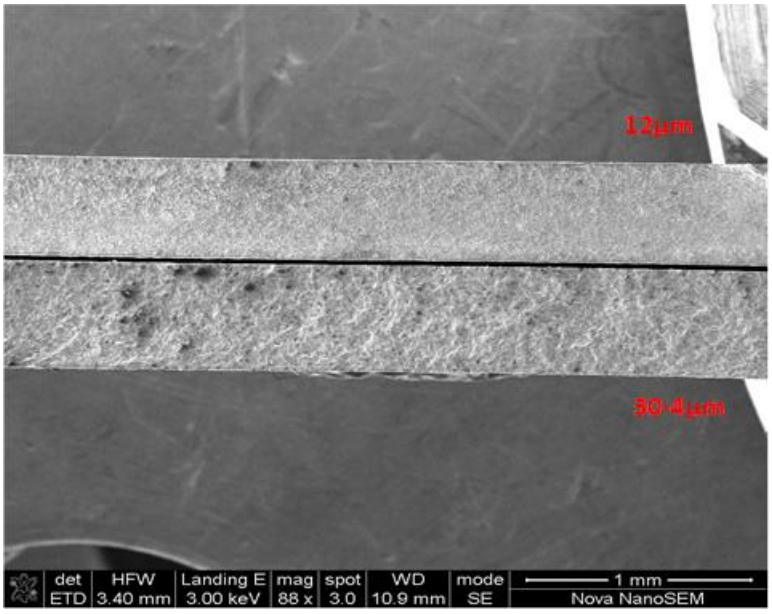

Figure 5.55 - SEM micrograph depicting the fracture surfaces of specimens 12µm-1 and 30-4µm-1. The specimens are mounted adjacent to each other, held in by a grub screw visible in the top left corner of the micrograph.

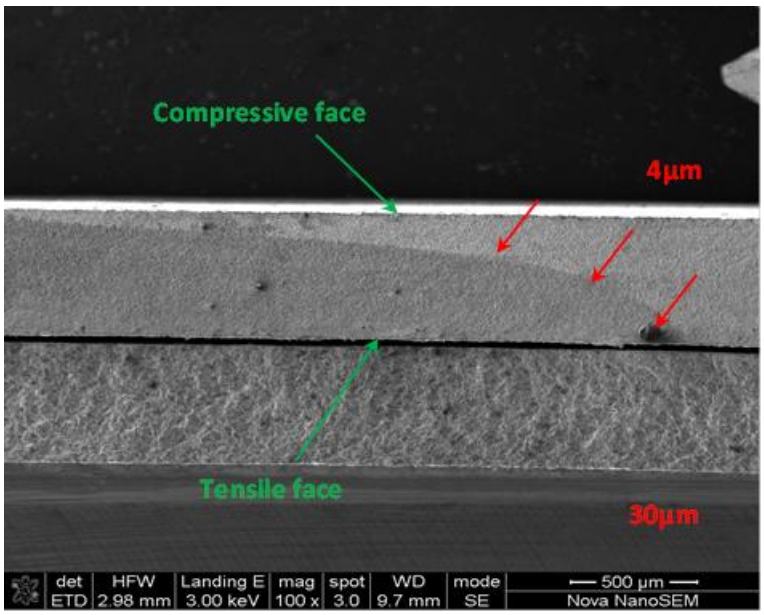

Figure 5.56 – SEM micrograph depicting the fracture surfaces of specimens 4µm-1 and 30µm-1. The red arrows highlight the contour of the arrest mark believed to be consistent with the shape of the crack front.

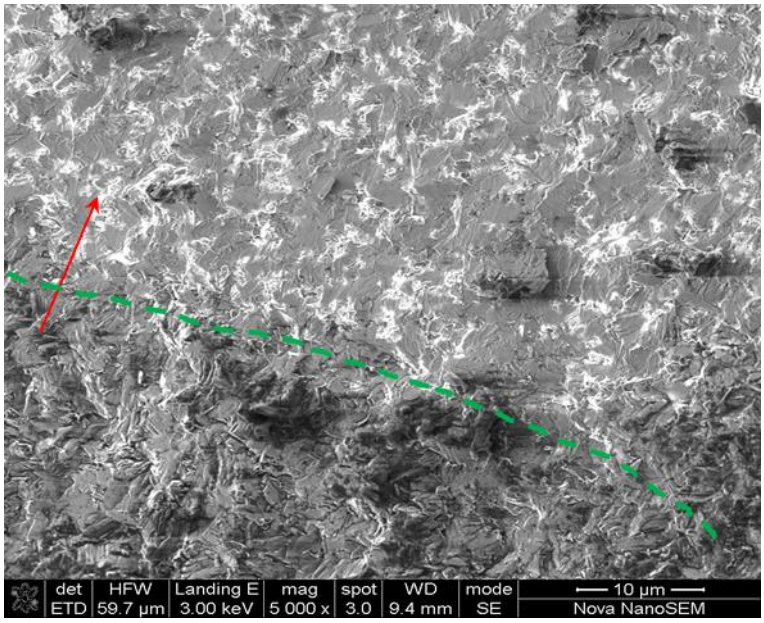

Figure 5.57 – SEM micrograph depicting the arrest boundary in specimen 4µm-1, highlighting the change in the appearance of the fractographic features of the diamond grains as well as the appearance of the cobalt pools. The red arrow shows the direction of crack propagation.

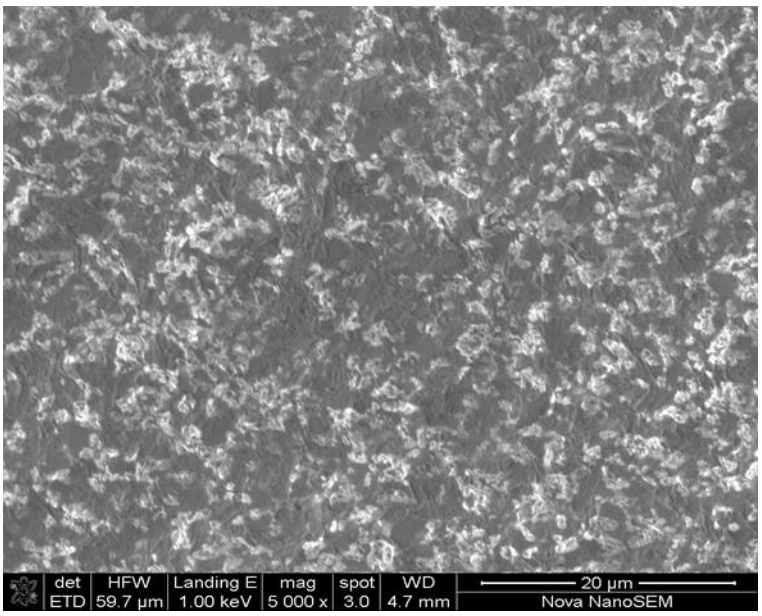

Figure 5.58 – SEM micrograph depicting the fracture surface of the 4µm-1 specimen, highlighting the morphology of the cobalt pools (white constituent) and the diamond phase (grey constituent).

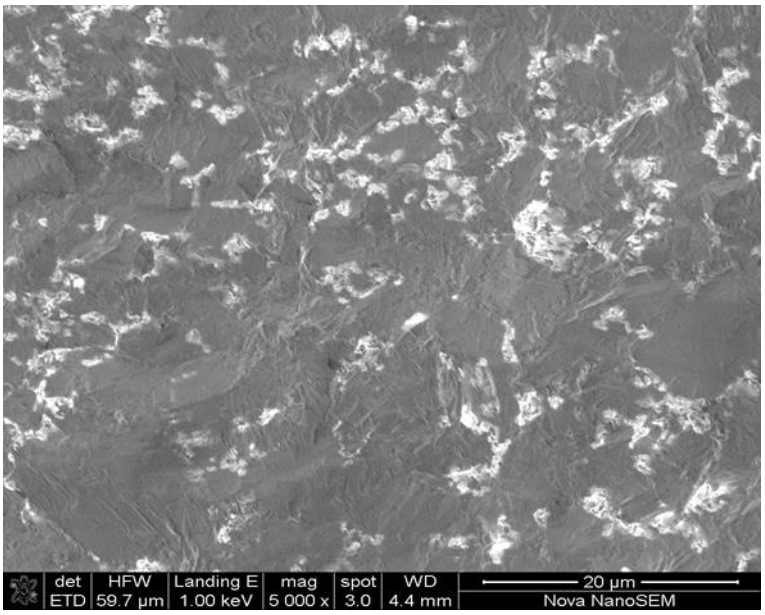

Figure 5.59 – SEM micrograph depicting the fracture surface of the 12µm-1 specimen, highlighting the morphology of the cobalt pools (white constituent) and the diamond phase (grey constituent). Compared to the 4 µm specimen, distinct diamond grains are better defined with a clear reduction in the number of cobalt pool features.

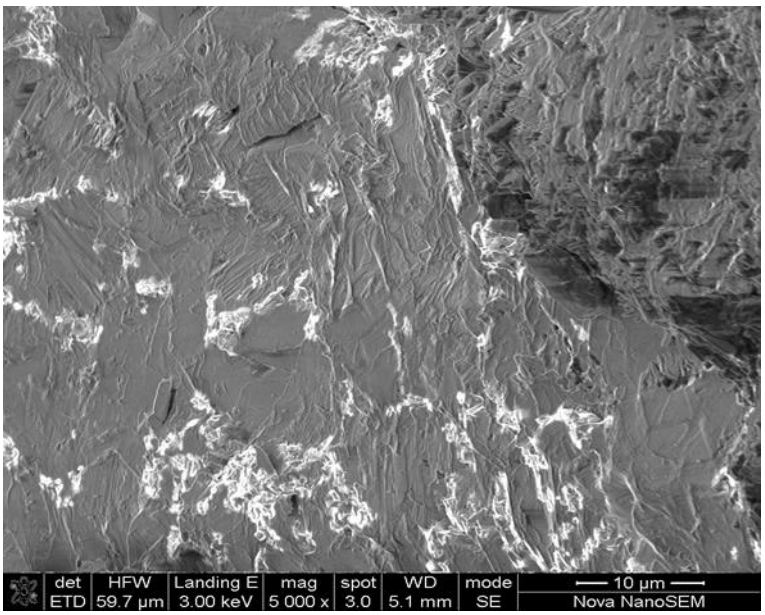

Figure 5.60 – SEM micrograph depicting the fracture surface of the 30µm-1 specimen, highlighting the morphology of the cobalt pools (white constituent) and the diamond phase (grey constituent). The cobalt pool positions can be attributed to the boundary regions of adjacent diamond grains.

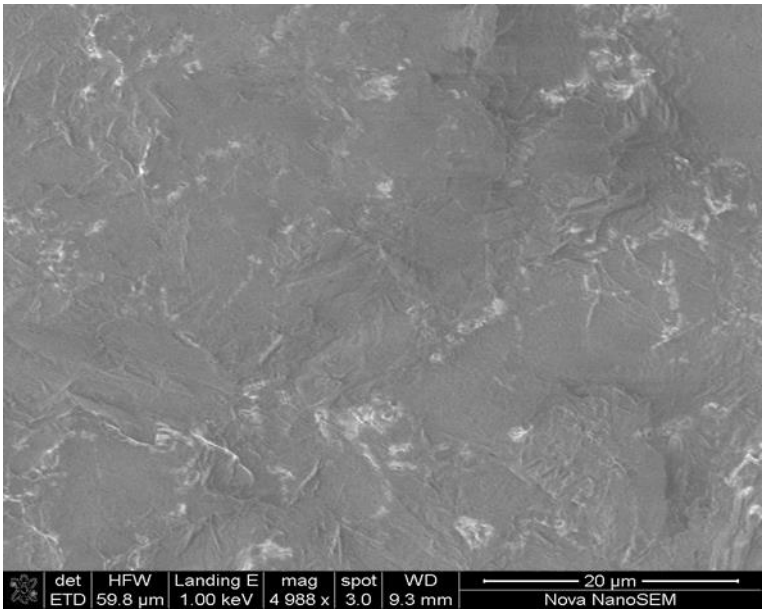

Figure 5.61 - SEM micrograph depicting the fracture surface of the 30-4µm-1 specimen, highlighting the morphology of the cobalt pools (white constituent) and the diamond phase (grey constituent). Similar to 30 µm specimen, the cobalt pools are isolated at the grain boundaries, showing further reduction in cobalt phase.

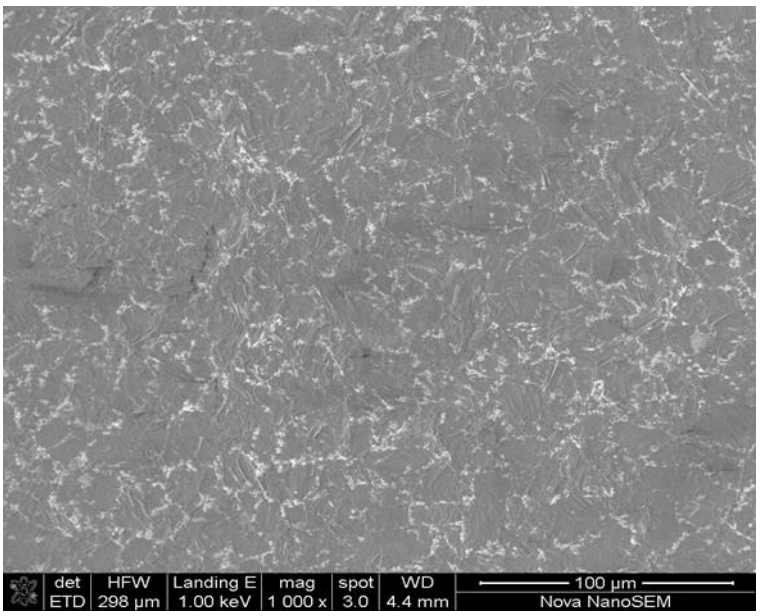

Figure 5.62 – SEM micrograph depicting the fracture surface of specimen 30-4µm-1, highlighting the cobalt phase (white constituent) clearly isolated at the grain boundaries between diamond particles (grey phase).

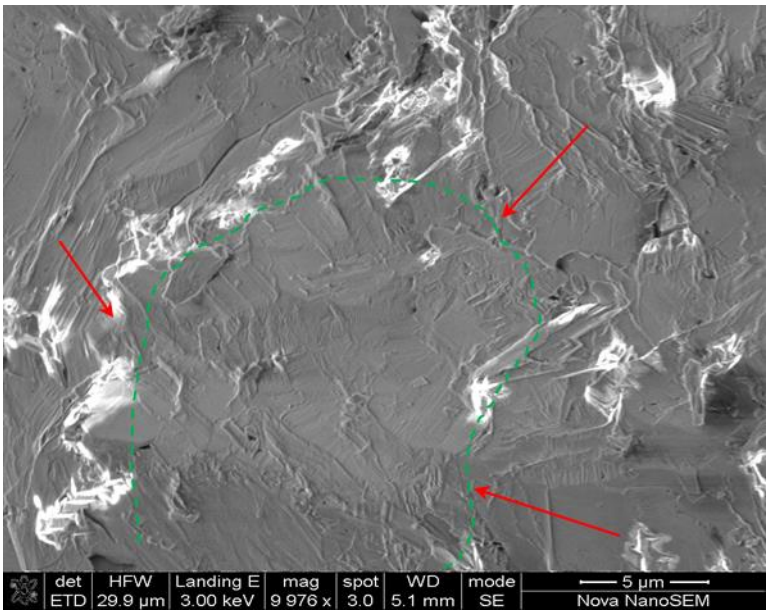

Figure 5.63 – SEM micrograph depicting the fracture surface of specimen 30µm-1, highlighting a diamond grain (bounded by the green dashed line) and the diamond-to-diamond connections (red arrows) separated by intermittent grain boundary cobalt pools.

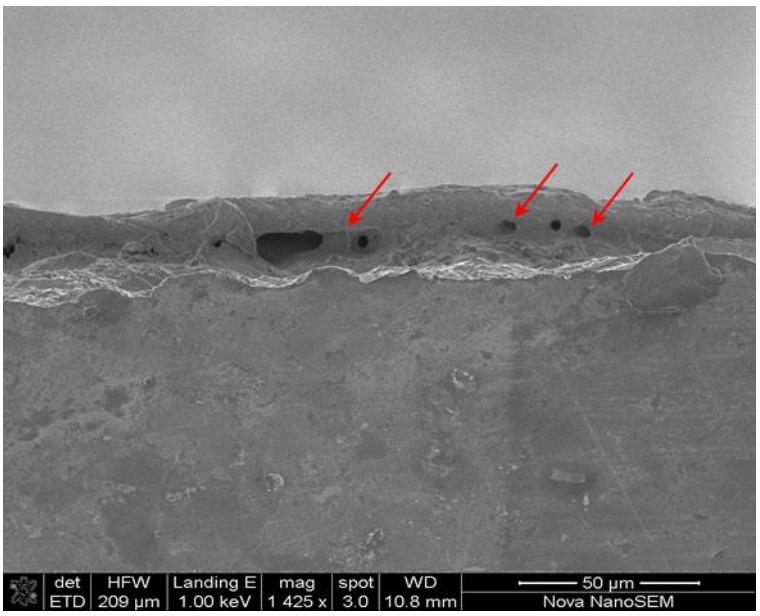

Figure 5.64 – SEM micrograph depicting a step in the fracture surface (in the plane of the page) of specimen 30µm-2, caused by internal porosity defects.

5.5.2 **Surface cobalt mapping**

Surface cobalt mapping was performed employing the FEI NanoSEM equipped with an Oxford X-Max EDS detector running INCA software. The cobalt was mapped in regions of 200x200 µm at equivalent secondary electron imaging magnification of x1500 and working distance of 5.5 mm. The regions selected were immediately adjacent to the crack initiation region where the slowest, most controlled propagation occurred and on the opposite end of the specimen where fast fracture occurred. The resolution employed was an average of 12 frames at 512x448 points at 100 µs dwell time, resulting in a spatial resolution in the order of 0.4 µm and total point count of 2.7 million points per scan.

The results of the mapping performed revealed that the cobalt content on the fracture surfaces was consistently higher in the slow crack propagation region than in the fast crack propagation region, consistent with fractographic observations. The results obtained for the four grades of material are presented in Table 5.5. These findings support the hypothesis that at the slower crack propagation speeds the crack propagation has a larger intergranular component which is reduced when the crack speed and available energy are increased.

It is worth bearing in mind that the orientation of the specimens with respect to the parent PCD "billet" are not known and these may have an effect on the observations obtained.

Cobalt content (%) present on the surface of the PCD fracture surface			
Designation	**Crack initiation region (slow propagation)**	**Final fracture region (Fast propagation)**	**Cobalt content difference (%)**
Grade 4	12.1	10.3	1.8
Grade 12	8.3	5.9	2.4
Grade 30	6.2	6.1	0.1
Grade 4/30	6.2	4.7	1.5

Table 5.5 – Fracture surface cobalt content.

5.6 EBSD mapping of the propagation regions

5.6.1 Pre-mapping

All four grades of PCD were pre-mapped by EBSD. None of the specimens revealed any preferential surface grain orientation, this is expected for randomly mixed (and sintered) PCD material. Due to fine grain size of the 4 µm and 12 µm specimens, crack path overlay was only possible in the case of the 30µm-1 and 30-4µm-1 specimens. The crack paths are transferred from the SEM micrographs by matching the positions of the FIB marks in IrfanView and Microsoft office photo editing software. The 30 µm crack path overlay is depicted in Figure 5.65 and that for the 30-4 µm is depicted in Figure 5.66.

The overlay of the crack paths onto the mapped regions indicates that the crack path in the 30 µm specimen followed regions of finer grain size. The 30-4 µm overlay does not appear to highlight any preferential crack path features. It should be borne in mind that these observation are made based on surface grain

orientation only and subsurface features may play a more significant role (such as the porosity identified within specimen 30µm-2).

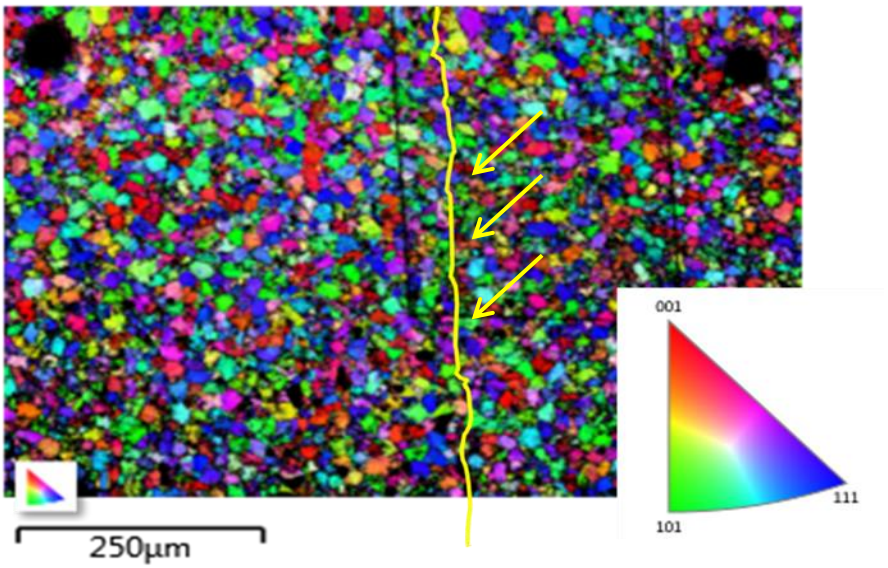

Figure 5.65 – EBSD map in the starter region of the 30 µm specimen containing an overlaid crack path (yellow line) obtained during the in-situ SEM fracture experiments. It appears that the crack path coincides with regions of finer/crushed grains (yellow arrows).

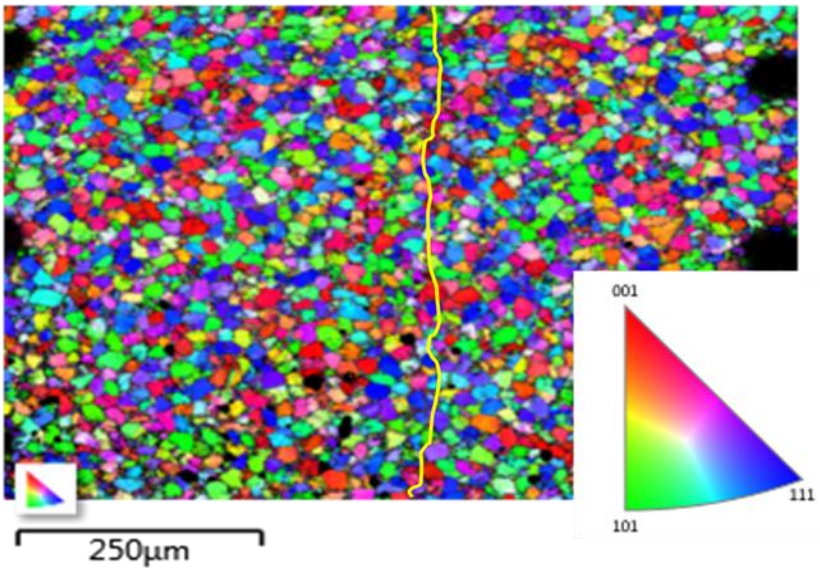

Figure 5.66 - EBSD map in the starter region of the 30-4 µm specimen containing an overlaid crack path (yellow line) obtained during the in-situ SEM fracture

experiments. No preferential features are evident from the map and crack path overlay.

5.6.2 EBSD mapping of crack paths

The EBSD approach, in addition to its ability to provide crystallographic orientation, provided a clear identification of the diamond crystals and cobalt constituents. Looking at the sample EBSD map images depicted in Figure 5.67 and Figure 5.68, the EBSD approach assists in confirming that the mode of crack propagation the 4 µm and 12 µm materials is mainly intergranular, while that in the 30 µm and 30-4 µm is mixed mode with features of both inter and transgranular propagation. This experiment was made possible by the ability of the miniature DT methodology to introduce controllably a crack into the specimen and then unload it in order to map the crack path as a function of the crystallographic orientation.

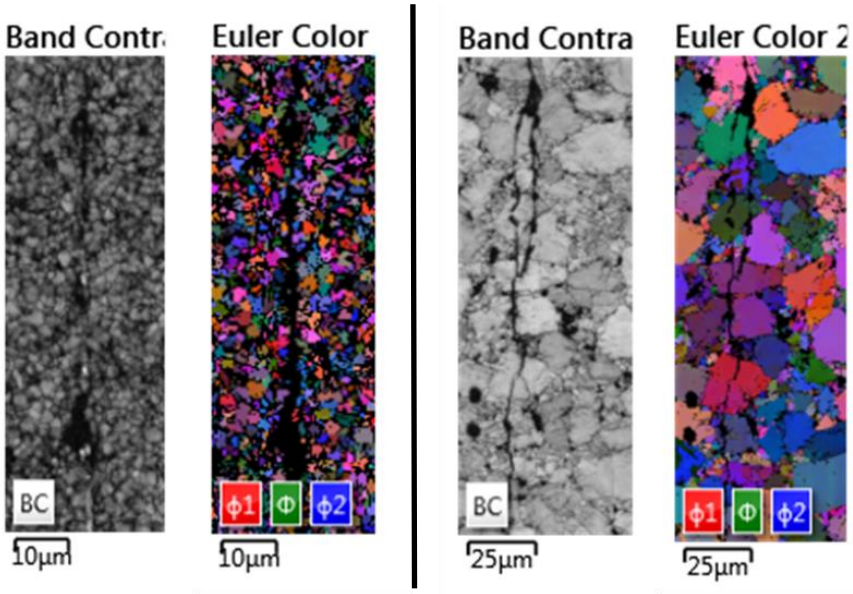

Figure 5.67 – EBSD map collage for the 4 µm specimen (left) and 30-4 µm (right). The 4µm specimen is difficult to index due to the very small grains as well as the intergranular cobalt pools which have high a degree of deformation. The 30-4 µm map has better indexing and the crack path is clearly visibly as a function of the microstructure.

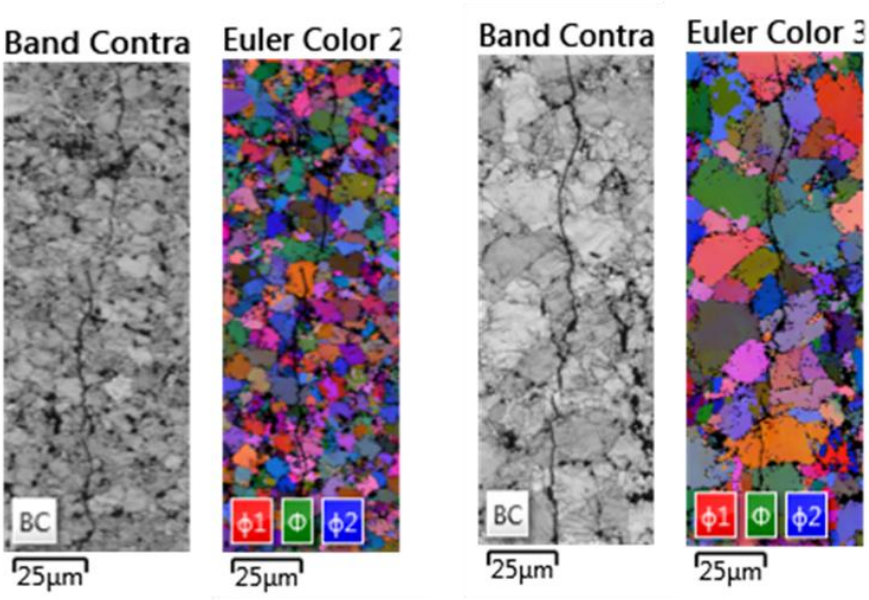

Figure 5.68 - EBSD map collage for the 12 µm specimen (left) and 30 µm (right). The indexing in 12 µm specimen is improved when compared to the 4 µm but it still lacks the quality obtained in the case of the 30 µm and 30-4 µm specimens.

5.6.3 **Microstructural observations in coarse grain specimens**

Mapping of the microstructural features and crystallographic orientations was best achieved in the coarse grain specimens. Observation of the crack paths as a function of microstructure revealed that, in a number of instances, the crack preferentially passed within the diamond grain structure rather than the nearby grain boundary. Examples of such crack path features are depicted in Figure 5.69. This is believed to be related to the growth of new diamond structures at the grain boundaries, which results in the contiguity of the diamond phase. The newly regrown diamond has no deformation associated with the HPHT process and may possess higher crack resistance than the deformed parent crystal. This would also depend on the orientation of the parent crystal with respect to the approaching crack front. Evidence of such new diamond regrowth has been described by a number of authors [35,44], sample image of the **regrown diamond** which exhibits no plastic deformations associated with the HPHT process is depicted in Figure 5.70. Therefore it is believed that the extent of diamond regrowth at the grain boundaries may significantly affect the fracture toughness and crack propagation mechanisms in the PCD material.

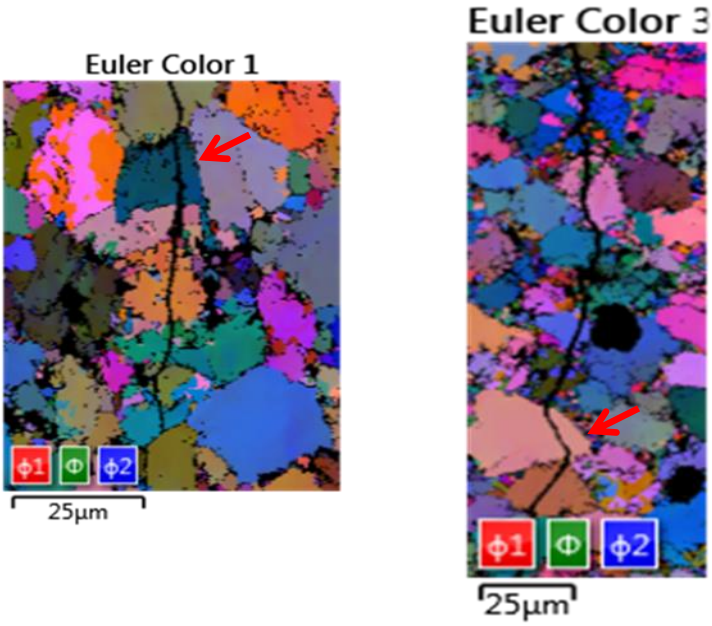

Figure 5.69 - EBSD map collage depicting the 30 µm specimen (left) and the 30-4 µm specimen (right). Red arrows highlight regions where the crack paths tend to avoid the grain boundaries to preferentially pass through the diamond crystals.

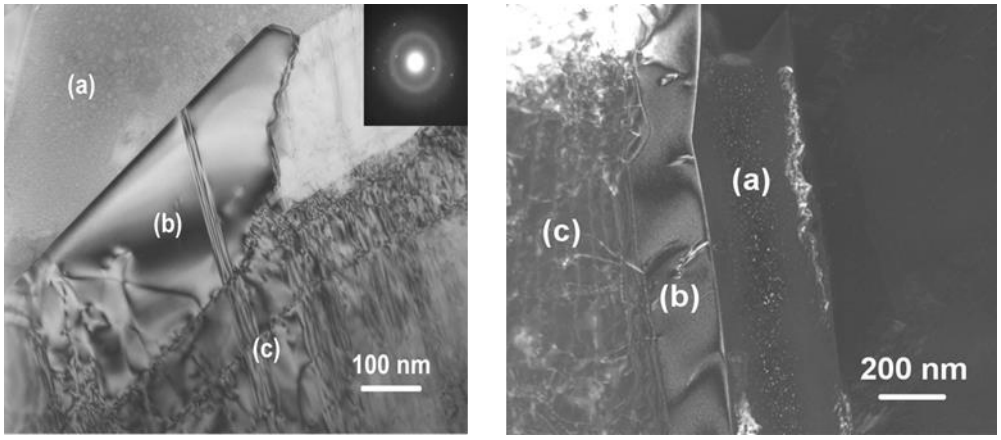

Figure 5.70 – Transmission electron microscopy images of the regrown diamond at the grain boundary, highlighting the constituents as – a) non-metallic bonding agent, b) regrown diamond and c) plastically deformed diamond[46].

5.6.4 EBSD mapping of unloaded cracked specimens

Mapping of the unloaded cracked specimens revealed similar findings in terms of the lack of clear information in the fine grained specimens. The quality of the

obtained maps is depicted in Figure 5.71. The difficulties in mapping the finer microstructures are associated with the significant deformations in the cobalt pools as well as polishing damage.

Mapping of the coarser grain structures revealed useful information. It highlighted that the cracking process does not result in significant change in crystallographic orientation of the grains adjacent/split by the crack front, Figure 5.72. Inspection of the coarse grain maps further highlights mixed mode propagation with both transgranular and intergranular crack propagation.

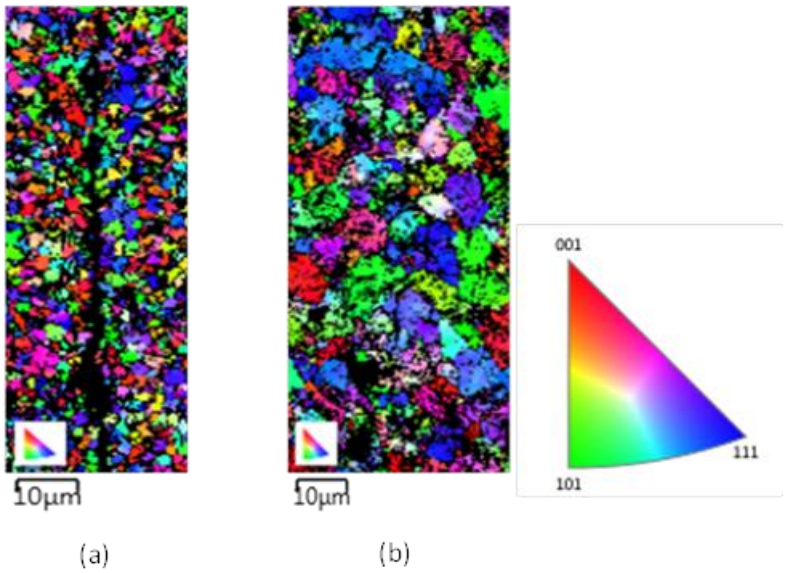

Figure 5.71 – EBSD maps depicting the maps performed around the closed cracks in specimen with 4 µm microstructure (a), and the 12 µm microstructure (b). As highlighted by the images, it is difficult to extract useful information from these maps.

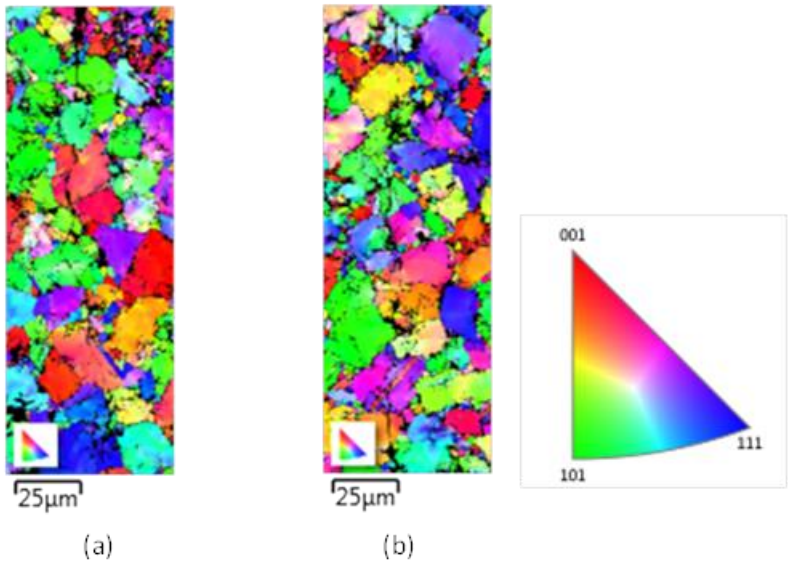

Figure 5.72 - EBSD maps depicting the maps performed around the closed cracks in specimen with 30 µm microstructure (a), and the 30-4 µm microstructure (b). The maps indicate the grain orientation remains nominally the same after the crack splits the crystal. The maps further highlight both trans and intergranular crack propagation.

Summary

Analysis of the fractographic features, both on the fracture surfaces and parallel to the crack wake, revealed clear differences in propagation mechanisms of the four grades of PCD material. The fine grained materials, having the smallest diamond particle sizes and higher cobalt content, resulted in the least crack path tortuosity. By comparison, the coarse grained specimens resulted in the highest degree of tortuosity. These results are consistent with the higher fracture toughness properties recorded for the coarser grade materials as well as the fact that the larger diamond particles have a greater potential to deflect the crack tip. The analysis further revealed what is believed to be an arrest mark (beach mark) in the 4 µm specimen, which reveals the shape of the crack front in the 4 µm specimen. Similar marks were not observed in the other grades of PCD and this result may be attributed to the cobalt content which is highest in the 4µm specimen. Inspection of the 30 µm material revealed evidence of significant porosity which may serve as the explanation for the crack path deviation from the centreline in one of the miniature DT experiments in this grade of material. Fracture surface inspection further revealed a clear difference in the appearance

and distribution of the cobalt pools between the primary diamond phase. The fine grained specimens had the most homogeneous cobalt pool distribution whereas the coarse grain specimens had the cobalt pools isolated at the diamond grain boundaries.

Inspection of the crack wakes after pre-cracking of the DT specimens revealed presence of crack bifurcation and surface particle breakout in all grades of PCD material investigated. In the 4 µm specimen, secondary cracking occurred more than two grain sizes to the side of the main crack. Crack bifurcation observed in the coarser grades did not deviate by more than a single grain interaction adjacent to the primary crack. Inspection of the crack paths did not highlight a clear difference in the intergranular versus transgranular propagation mechanisms. While the coarse grain specimens had an increase in the transgranular fracture, intergranular propagation was also observed. Therefore it is believed that the obvious propagation mechanism switch over does not occur with the range of the microstructures investigated. In an attempt to better quantify these observations, cobalt content mapping was performed on the fracture surfaces. This mapping revealed a trend where more cobalt was present on the fracture surfaces characterised by slow propagation speeds than those characterised by fast crack propagation speeds. This observation indicates that the intergranular propagation component appears to be reduced as the crack propagation speed increases.

6 Discussion

The following chapter details the discussion around the experimental research programme performed. The research objectives, set out at the start of the project, are briefly reintroduced below and are individually addressed as the chapter develops.

The key objectives of this research project were separated into four distinct groups, namely, i) the development and testing of the miniature double torsion test rig for testing of PCD materials, ii) extraction of the PCD fracture mechanics parameters by classical DT equations during live observation in-situ in the SEM, iii) qualitative characterisation of the surface grain orientation with respect to crack propagation mechanism observations and documentation of the resultant fractographic features and iv) non-contact strain measurement techniques employing the novel JMAN procedure for J-integral calculation. These four fundamental objectives are described in the following sections.

Once the discussion of the developed experimental techniques and results obtained is presented, the results of the experimental programme are discussed in the context of the published experimental approaches to PCD fracture studies. The current understanding of the fracture mechanics based parameters for the PCD material is also presented. The chapter is concluded with a discussion of the contribution the current work has made to the development of the experimental techniques applicable to the study of brittle materials such as PCD as well as the understanding of the fracture phenomena occurring in PCD.

6.1 Miniature double torsion methodology

6.1.1 System concept overview

The most important aspect of the miniature DT rig development has been the facilitation of rig “use” for live microcrack observation in-situ with SEM microscopes, with the aim of observing the fracture process live. This has been achieved by designing a miniature, DT loading geometry in a rig body assembly allowing full rig insertion into an SEM chamber. Such design resulted in the following key advantages, i) the rig system could easily be adapted to various SEM microscopes by simply changing the interface base plate and ii) the rig

could be externally controlled via electronics precluding the need for mechanical penetrations in the SEM chamber door. Furthermore, attachment of the drive motor to the gearbox body enabled reaction of the motor torques within the rig body, preventing the need for overly robust fastening of the rig, simplifying the use of the rig when observed, either with i) benchtop conventional optical stereomicroscopes or ii) with digital image correlation camera systems. In prior versions of the rig, motor torques had the potential to disturb the rig position within the field of view of the selected observation instrument. In the case of the DIC experiments this resulted in rigid body motions which negatively affected the quality of the data measured.

The miniature DT system was operated in-situ in the SEM, optical stereo microscopes together with 2D and 3D DIC systems. In all instances, valuable experimental data could be reliably extracted from the system, highlighting a high degree of versatility but also repeatability. This is believed to be important in the development of future experimental systems as a multitude of imaging systems is possible when employing the current miniature rig concept.

6.1.2 Miniature DT system parameters

In order to achieve stable and controllable crack propagation in extremely stiff and brittle PCD materials, possessing Young's modulus properties in the range of 1000 GPa, a stiff rig is required. Any spring compliance in the load path results in potential energy storage which negatively affects the control over the incremental crack extension process.

The final design iteration of the miniature DT rig employed in the current research had a load path stiffness of 2.54 MN/m while maintaining an applied load indication resolution of 0.5 N. An incremental crosshead displacement resolution of 26 nm per step of the stepper motor or 1.25 µm per revolution of the input shaft, was achieved. Improved data logging was enabled by employing a dedicated Vishay Micromeasurements P3 strain gauge amplifier and indicator unit which incorporates high levels of noise protection and filtering. However, the resolution of the cross-head position measuring system was coarser than the possible actuation increment. A resolution of 1.7 µm was obtained for the crosshead position.

The system showed very good (i.e. low) levels of drift consistency which were considered important in the context of in-situ SEM tests which lasted up to, and in some experiments in excess of, three hours per specimen. Signal noise levels

during experiments were identified to be within 1-2 µm of cross head displacement and a force range of 0.5-1 N and a total system drift per hour was within 2-4 µm and no more than 1-2 N.

A cross-head displacement logging methodology was developed to detect cross-head movement directly above the saddle centreline, minimizing the potential errors associated with employing the motor revolution monitoring approach which is susceptible to errors associated with the clearances and deflections of the components in the load path.

The system developed showed promise in its potential to be applied to the testing of the stiff and brittle PCD materials. However, due to the limited number of available PCD specimens and the need to extract the maximum information, the DT rig system was tested in a series of tests using “Perspex” PMMA materials.

6.1.3 Miniature DT testing of PMMA specimens

PMMA material was chosen as the test material for the rig validation experiments. It was selected due to its nominally isotropic properties and the tendency to undergo brittle fracture. While significantly more compliant than PCD, PMMA specimens could be easily obtained, through laser cutting, from a standard sheet of 2 mm ISO 7823-2 standard Perspex. The choice of the 2 mm Perspex sheet was guided by the fact that the 2 mm PMMA miniature DT specimen developed cracking at approximately the same critical load range as the 0.5 mm PCD material. Therefore the rig was operating in a similar load state as would be the case during the PCD fracture experiments.

Over a hundred PMMA tests were carried out in the development of the experimental procedures such as specimen alignment, load and displacement bridge testing as well as the data acquisition system. Once all system components were tested and a reliable methodology was developed, a series of ten miniature DT PMMA specimens were tested to evaluate the miniature DT rig performance. The average fracture toughness for the ten specimen test series of PMMA material was determined to be 0.99 MPa√m. The statistical analysis of the results revealed a very good degree of consistency in the results, indicating that the rig produced repeatable experimental data. The standard mean error for the series of the experiments was calculated to be 0.017 MPa√m with the standard deviation being equal to 0.051 MPa√m.

In order to reduce the degree of scatter and improve the consistency of the PMMA results, the specimens employed were cut from the **same area** on the parent material sheet. After laser cutting, the specimen dimensions were refined to a geometrical tolerance of 0.05 mm employing 1000 grit water paper. Particular care was applied when developing the specimen geometry in order to successfully centre the notch.

The results obtained in the PMMA series provided the confidence in the miniature DT rig and the experimental methodology to proceed with the experiments in PCD specimens.

6.1.4 In-situ SEM experimental approach

Completion of the rig development process and validation of the miniature DT methodology in PMMA specimens was followed by the in-situ SEM experiments on PCD materials. Prior to the fracture experiments, the material grain orientation, immediately ahead of the starter notches of four of the eight available PCD specimens, was mapped by EBSD techniques (the detailed discussion about the EBSD mapping process can be found in Section 5.6). This provided the information about the relative crystallographic orientation of the surface grains of the PCD material. EBSD mapping was undertaken prior to the fracture experiments because it was not known at the time, whether slow, controllable crack growth initiation would be possible and whether a cracked specimen could be successfully unloaded after partial crack propagation. Thus pre-mapping of the specimens had the potential to provide some information about the crack path as a function of microstructure in case of catastrophic failure (i.e. crack propagation features in the two halves of the specimen). At this stage it is worth noting that controllable crack initiation and propagation was possible in all specimens tested.

The in-situ SEM experiments provided two streams of information i) the load-displacement data and ii) imaging of the fracture process. Such observation of the micro-fracture process enabled better understanding of the cracking process and mechanisms. For example, it was identified that cracking of the starter notch wedge, where the material is thinned to aid controllable initiation, initiated at approximately 60 % of the maximum load associated with the notch toughness of the full thickness specimen. Processing the surface deformation data captured by DIC and employing the JMAN routine, revealed critical levels in the stress intensity of surface material – confirming onset of cracking. These

results did not agree with the stress intensity results calculated from load-displacement data due to local thinning of the starter wedge and an unknown thickness correction factor which would be required to determine the surface stress intensity in the non-standard wedge geometry. This example serves to highlight the advantages of such in-situ SEM and in-situ DIC experiments.

The in-situ SEM experiments were successful in controllably initiating, propagating and unloading cracks in the miniature DT specimens while observing the fracture process. Experiments in all eight PCD specimens, four individual grades, generated the load displacement data which enabled characterisation of the fracture toughness properties of the four grades of the PCD material by means of classical DT equations (discussed in further detail in section 6.2.1). The fracture process could be observed in all specimens. Six of the eight specimens were successfully unloaded for further investigation by EBSD and DIC-JMAN techniques. Of the two specimens which were not unloaded, one 30µm grade failed due to microstructural porosity confirmed during the fractographic investigations (Section 5.5) and one 12 µm specimen was broken by propagating the crack to failure in order to confirm the fact that the stress intensity had indeed reached a plateau.

It can therefore be said that the miniature DT methodology provided a successful and robust approach to characterisation of PCD material fracture mechanics properties as well as observation of crack development phenomena while in-situ in the SEM.

6.2 PCD fracture toughness properties

6.2.1 Miniature DT fracture toughness results obtained in-situ SEM tests of PCD materials

The load-displacement data obtained during the in-situ SEM experiments was processed employing the classical DT formulation, equation (2.30), to obtain the fracture toughness properties for the four grades of PCD materials analysed. The results revealed a clear and consistent difference between the four material grades. The fracture toughness levels obtained for the four grades were – i) 8.10±0.3 MPa√m for 4 µm grade, ii) 9.5±0.3 MPa√m for 12 µm grade, iii) 10.6±0.5 MPa√m for 30 µm grade and iv) 11.9±0.6 MPa√m for 30/4 µm grade.

In order to measure the fracture toughness properties detailed above, a through-thickness crack front has to be developed. Such developed crack front is

consistent with the constant stress intensity region of the DT load-displacement curve. A sample plot highlighting stress-intensity versus displacement obtained during crack propagation in the 4 µm specimen is depicted in Figure 6.1. The plot highlights the fact that the notch toughness at the start of crack front development significantly exceeds the stress-intensity associated with the constant stress-intensity region which is employed to determine the fracture toughness, K_{IC}, of the material. Comparison of these phenomena in the four grades of PCD materials revealed that on average the apparent notch toughness exceeded the fracture toughness of the material by 2.2 MPa√m, while the individual results for the four material grades were as follows – i) 2.1MPa√m in 4 µm material, ii) 1.9 MPa√m in 12 µm material, iii) 2.45 MPa√m in 30 µm material and iv) 2.3 MPa√m in 30-4 µm material.

These findings highlight the importance of establishing a sufficiently long and stable crack in a controllable manner in order to obtain an accurate measurement of the material fracture toughness. It is believed that crack dependent fracture toughness methodologies lack the necessary control after crack initiation and may therefore measure elevated fracture toughness properties.

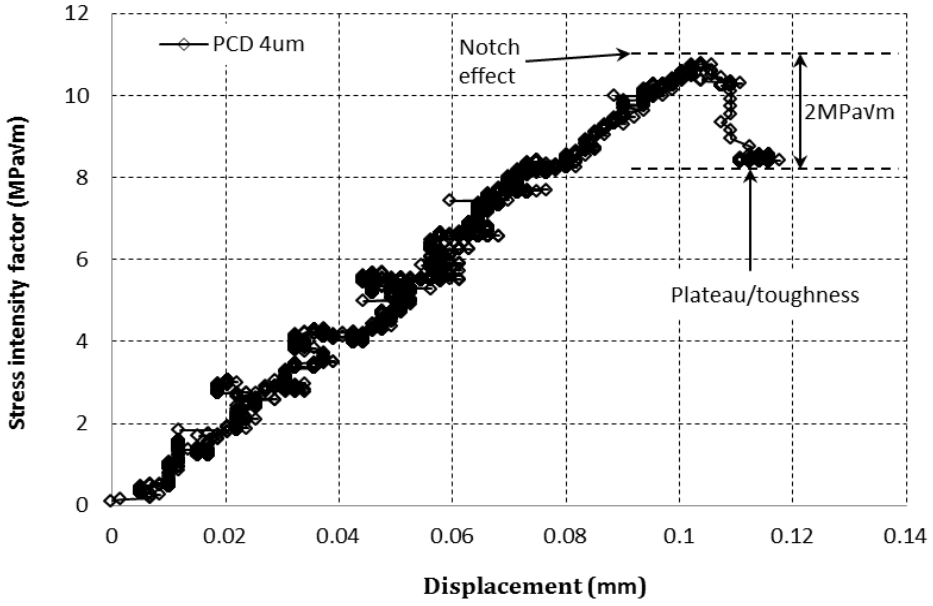

Figure 6.1 – Plot depicting the stress intensity plotted against the crosshead displacement during an experiment in a 4 µm PCD specimen, highlighting the

elevated stress intensity associated with establishment of the stable crack front from a notch and a plateau region characterising the toughness of the material.

6.2.2 Microstructural effects on fracture toughness

In order to investigate the effects of the various PCD microstructural parameters on fracture toughness levels, the measured particle size, cobalt content and diamond phase contiguity were plotted against the obtained fracture toughness results. Although the range of the available material starter particle sizes was quite narrow, the microstructural features were clearly different and therefore would have an effect on the crack propagation mechanisms within the material.

Figure 6.2 depicts the relationship between the fracture toughness of the material and the measured grain size. Measured grain size was employed in this instance as it is believed to be important to compare the fracture toughness to the grain size resulting after the sintering process where significant grain damage and alteration due to the dissolution of finer grains occurs[111]. Also, as proprietary sintering processes may differ significantly, the resultant particle sizes may vary and it is therefore believed more appropriate to compare the toughness with actual grain size measured. The plot reveals that the fracture toughness increases with increasing grain size, which is consistent with the published material for the PCD grades of similar starter particle sizes[8], [20], [29]. It is worth noting a marked difference in the fracture toughness of the bi-modal 30-4µm material as compared to the 30 µm material. While the measured equivalent circle diameter grain sizes for the two materials were 20.3 µm and 20.1 µm respectively, the fracture toughness of the bi-modal 30-4 µm material was 11.2 % higher than that of the 30 µm material. This observation suggests that a further mechanism, believed to manifest itself during packing and sintering of the bi-modal grade material, is responsible for the improved toughness properties of the 30-4 µm grade.

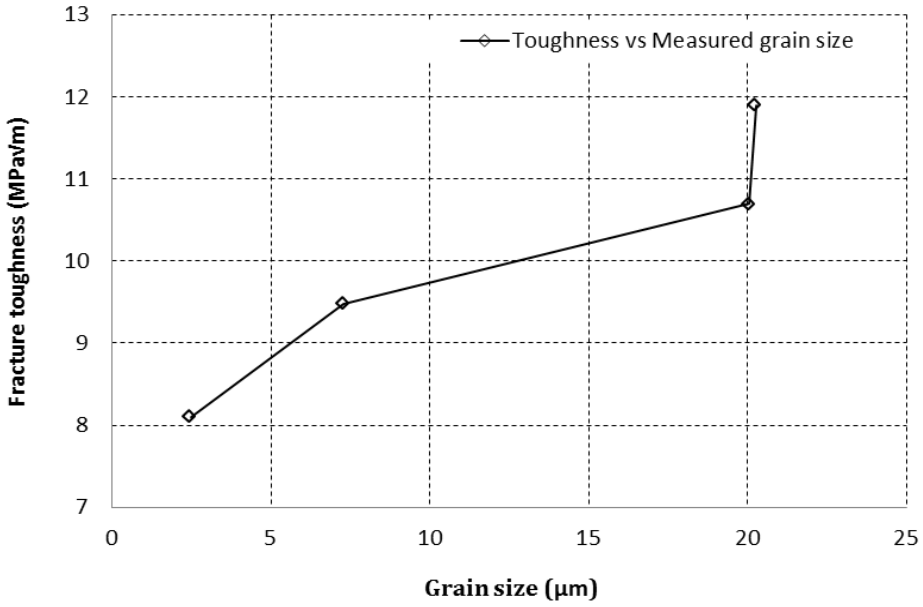

Figure 6.2 – Plot depicting the relationship between the fracture toughness and the measured grain size of the four grades of PCD materials tested.

Plotting the cobalt content of the PCD specimens versus the fracture toughness, Figure 6.3, revealed that the fracture toughness property is inversely proportional to the cobalt content. This result also agrees with published data [20], [37]. The presence of cobalt, which, among other elements, is required as a catalyst during sintering, affects the degree of diamond to diamond bonds. The degree of diamond to diamond bonding in a PCD material is referred to as diamond contiguity. As cobalt content is increased, the degree of diamond to diamond bonding is decreased by virtue of cobalt presence between the diamond grains. The importance of the diamond to diamond bonding is best highlighted by the properties of the so-called thermo-stabilised PCD materials, where cobalt is leached from the PCD material through hot acid boiling yet the remaining diamond network remains sufficiently strong to perform well under extreme loading conditions[18], [46].

It is believed that it is through this mechanism that cobalt affects the toughness properties of PCD materials rather than through a direct effect of the cobalt pool size and inter-diamond distribution. The effect contiguity has on toughness is

depicted in

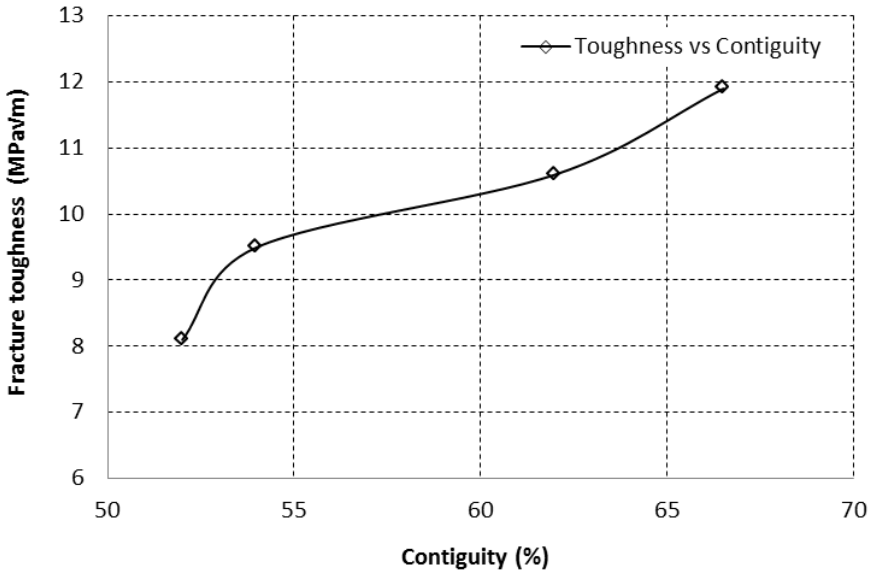

Figure 6.4. With increasing diamond phase contiguity the toughness of the PCD material is increased. Therefore it is believed that the contiguity of the polycrystalline diamond phase is the key mechanism responsible for the toughness of the PCD material. It is worth noting that the polycrystalline nature of the PCD compacts, along with increased contiguity, provide the favourable toughening effects. Taking monocrystalline diamond phase contiguity to the upper limit would result in the fracture properties of the single crystal diamond, with its orientation sensitive crystallographic properties[7].

The experimental observations discussed above indicate that the fracture toughness of PCD compacts is not a simple function of grain size or cobalt content. Optimum toughness is obtained through a complex interaction, explanation of which is beyond the scope of the current thesis and which is often proprietary. It is believed that improved toughness properties in PCD can be obtained by optimising the polycrystalline contiguity of the diamond phase. The diamond phase plasticity and degree of introduced dislocations would play a further role in the development of the crack path[37],[116],[117].

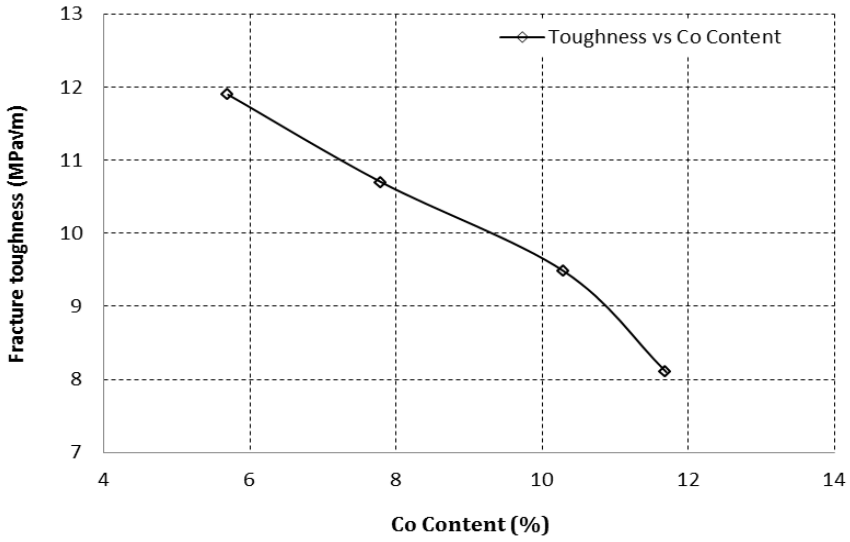

Figure 6.3 - Plot depicting the relationship between the fracture toughness and the cobalt content of the four grades of PCD materials tested.

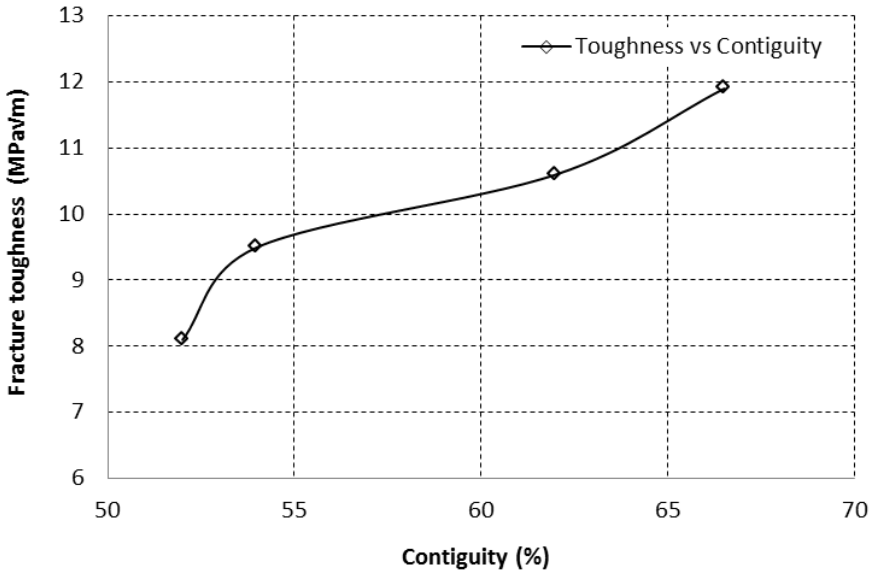

Figure 6.4 - Plot depicting the relationship between the fracture toughness and the diamond phase contiguity of the four grades of PCD materials tested. In the four PCD grades analysed, contiguity increases with increasing grain sizes and decreases with increasing cobalt content.

6.3 Fracture process observations

6.3.1 In-situ SEM live process observations

As highlighted in the previous sections, the miniature DT rig was designed to facilitate the observation of the tensile face of the specimen. Previous experimental research, where in-situ observation was not the primary aim of the experiment, highlighted that DT experiments were performed with the tensile face in either top or bottom orientation [29,101]. In the current research project, the in-situ study of the fracture process revealed the following key observations – i) crack initiation in the tapered starter wedge occurred at approximately half the maximum experimental load level (this was further confirmed by the 2D DIC experiments), ii) the appearance of the crack and its propagation features differed significantly in the four material grades tested and iii) propagation in the constant stress intensity region resulted in significant crack extension increments for very small crosshead displacements.

The cracking process in the tapered starter notch region initiated at 38-45% of the maximum load recorded in the DT experiments (peak load is associated with notch toughness). No clear difference was observed as a function of the material grain size, as crack initiation typically occurred from microstructural defects at the root of the notch. This finding, while confirmed by the in-situ images, was initially unexpected as the load-displacement curve did not reveal the initiation of micro cracking in the notch root. Initiation of the cracks at subcritical loading was confirmed during the 2D DIC experiments discussed in the following sections. During the initial experiments, it was not well understood why a significant discrepancy in the measured stress intensity was observed in the initiation stages of the experiment and yet the correlation between the DT formulation and the DIC results improved as the cracks developed. These experimental observations underlined the value of in-situ SEM observation of the crack propagation process.

The in-situ experiments further revealed markedly different appearances of the crack wakes. The crack wakes in the 4 µm and 12 µm material grades revealed less tortuosity than the wakes observed for the 30 µm and 30-4 µm. The finer grades, especially the 4 µm PCD material, revealed a degree of breakout of the diamond particles adjacent to the faces of the main crack, refer to Figure 5.27. The coarser grade specimens did not have similar adjacent grain pull-out/damage, as evidenced by Figure 5.44. This indicated that in addition to the

formation of the main crack fracture surfaces, additional energy is dissipated in the fracture process by the formation of secondary damage. Based on the observed evidence it is believed that the secondary cracking development, which can be referred to as the process zone, absorbs a large portion of energy in the finer grains than it does in the coarse grain materials.

A further observation with regard to the miniature DT crack propagation development was the nature of the incremental crack propagation. The crack initiation process occurred in a very slow and controllable mechanism in all grades of material. As already highlighted, initiation occurred at less than half the maximum load applied during the experiment due to the EDM/laser sharpened starter wedges introduced. As the cracks propagated through the wedge region and extended into the bulk thickness of the specimen, having overcome the geometrical notch effects, propagation occurred in longer crack extension increments. This was the result of the load bridge relaxation which occurred every time a crack extended incrementally. As the crack extended, the torsion arms of the specimen became more compliant, leading to incremental relaxation of the load bridge. The load-displacement data revealed that such load relaxation increments were in the order of 0.5 N or approximately 1 % (0.2 µm upward bridge displacement) of the load applied to the PCD materials in the constant stress intensity region. It is worth noting that these phenomena were of the same order of magnitude as the resolution capability of the system, which may have masked some of the details associated with the propagation process. Following relaxation, additional load was applied to overcome the propagation threshold, leading to the dynamic crack extension until the stress intensity level was reduced. The control over such propagation process is difficult given the magnitudes of the displacements involved. This is further complicated by the microstructural properties of the material as the crack tends to arrest at the toughest features. Subsequent increase in the stress intensity required to re-initiate propagation may exceed the crack resistance of the material ahead of the tougher arrest feature and lead to larger incremental propagation. Furthermore, dynamic propagation effects, beyond the scope of the current analysis, have the potential to affect the incremental crack extension until the stress intensity level drops beyond the propagation threshold.

6.3.2 Fractographic observations

Further to the observations made during the in-situ SEM experiments, the cracked specimens were inspected after unloading and their fracture surfaces were inspected once the specimens were broken in the DIC experiments.

Inspection of the unloaded, pre-cracked specimens revealed an important finding which highlighted that all grades of PCD material, from fine to coarse, experienced both **intergranular** and **transgranular** cracking failure and in both instances experienced a significant degree of secondary damage – the development of a process zone. This zone was small and intermittent as compared to the classical process zone formulations in materials like ceramics and graphite [13,55,94,95]. Therefore the ability to have a specimen pre-cracked and inspected after unloading, before damaged material was lost, was critical to the identification of these features. Once the specimens are broken, the secondary fracture process features close up or small fragments breakaway and the useful features are mostly lost. An example of the process zone cracking developed in one of the coarse grain specimens is depicted in Figure 6.5.

Inspection of the fracture surfaces of the broken specimens revealed markedly different appearance as a function of the starter particle size. Samples of the fracture surface of the four material grades are depicted in Figure 6.6. It can be seen that the fracture surface relief increases significantly as the starter particle size of the material increases. This indicates that the coarser grade materials force the advancing crack front to circumnavigate the tough polycrystalline microstructural features and result in an increased total surface area generated. Generation of such extra microcracking area results in **higher energy expenditure and a tougher material**.

Inspection of the fracture surface of the 4 µm specimen also revealed a fractographic feature characterising the shape of the crack front Figure 6.7. This is the first record of such double torsion crack front shape in PCD material and is significant as the crack front shape factor, according to Leevers analysis[118], relates the rate of crack extension on the surface of the specimen to the rate of the crack front advance. This information can be useful in the study of crack velocities in PCD materials. None of the other grades of PCD revealed similar clear features and this is believed to be related to the fine grain structure of the 4µm material, cobalt content of the specimen as well as, in particular, the time that the specimen was exposed to the atmosphere between the introduction of

the crack and final fracture. The specimen was pre-cracked, unloaded and the unloaded crack wake was studied. Following this, the design of the DIC experiment occurred, resulting in the total time between crack introduction and specimen failure of approximately ten months. Such extended storage may have resulted in the darkening of the cobalt phase and therefore easier identification of the features when exposed to the electron beam of an SEM microscope.

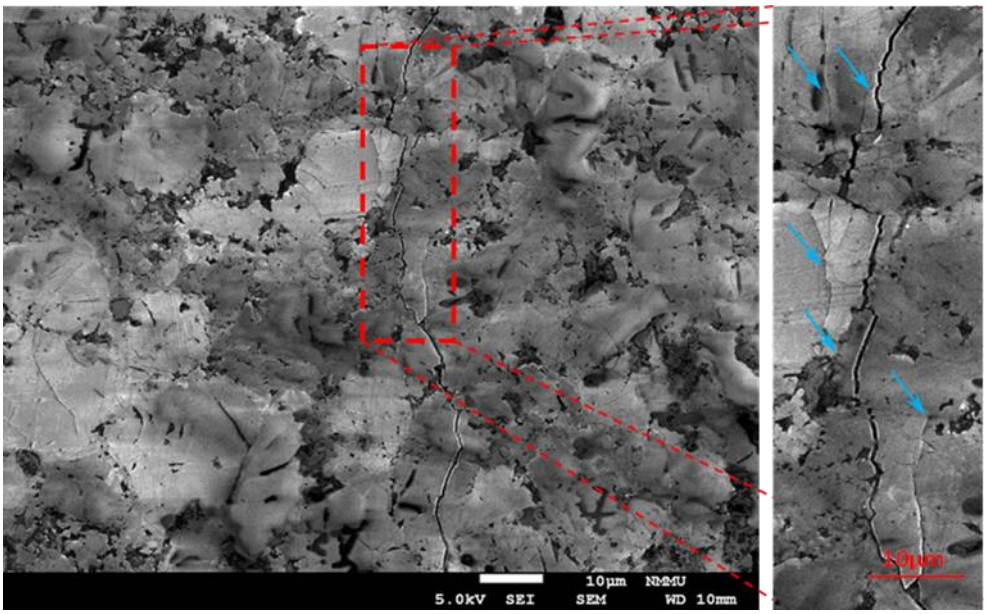

Figure 6.5 – Fractograph depicting the pre-cracked region in the 30 µm specimen after the load was removed, highlighting the presence of the process zone around the main crack wake.

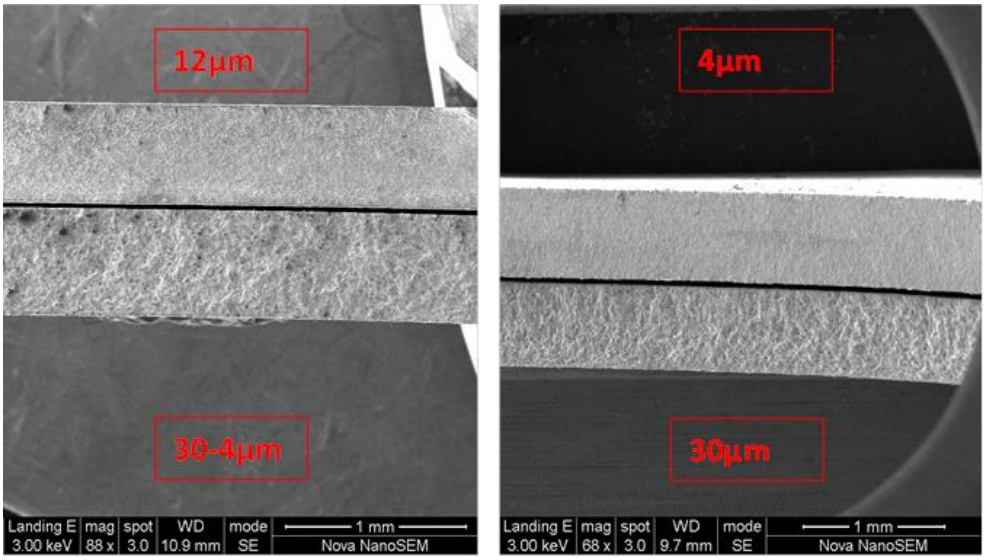

Figure 6.6 – Collage depicting the fracture surface of the four specimens of the four grades tested, highlighting the difference in the appearance of the tortuosity/relief of the fracture surface.

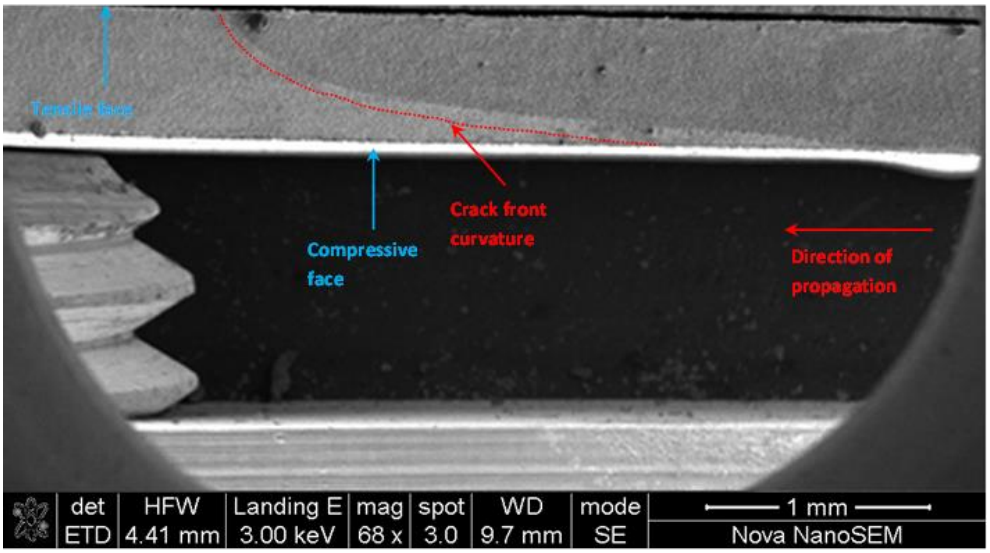

Figure 6.7 – SEM micrograph depicting the shape of crack front developed during the double torsion experiment in the 0.5 mm PCD specimen.

6.4 Characterising toughness by DIC and JMAN routine

An attempt was made to characterise the fracture toughness properties of the PCD specimens through non-contact optical techniques. Three approaches were employed – i) two-dimensional displacement field capture, ii) three-dimensional displacement field capture. These approaches are discussed individually below.

6.4.1.1 2D DIC JMAN based results

The two-dimensional approach yielded the best results of the three approaches highlighted. The images captured employing an optical stereo microscope resulted in the most consistent characterisation of the surface pattern, which enabled accurate mapping of the surface deformations. As discussed in the previous sections, the high stiffness of the PCD material and the loading bridge, result in very little deflection of the specimen and bridge. This in turn minimises the error associated with out of plane displacement of the whole specimen which, when significant, would result in an erroneous bulk compression artefact

(when moving away from the focal point). Therefore in PCD specimens under double torsion loading, the crack region remains nominally on the same level, and was therefore well suited to the 2D microscope image capture for DIC post processing.

The 2D DIC experiment was performed on a specimen of a multimodal industrial grade PCD. The exact specimen composition was not disclosed, however, it is believed to be a blend of grit sizes isolated in the current research. These industrial grade specimens were initially supplied to investigate the potential to carry out the research project and were used in the initial experiments to develop the methodology. The surface texture of the specimen as well as the additional paint speckle added, are depicted in Figure 6.8. An additional image of the specimen surface is provided in Figure 6.9, highlighting the specimen after the crack has been fully developed. The image aims to highlight the difficulty associated with fracture observation in the opaque PCD material, especially when it is partially leached and has a surface texture.

The same surface texture provides an advantage when performing DIC analyses. The overview of the process employed to determine the surface stress intensity associated with crack propagation is depicted in Figure 6.10. The deformation fields are extracted from the images captured during the DT experiment and the J-integral is numerically integrated employing MATLAB.

The results obtained through this process were in good agreement with those obtained by the classical DT equations employing the load data. The DIC determined stress intensity values were typically 6-8 % higher than those obtained from load data. This may be explained by the fact that the DIC based measurements are surface based and therefore account for the plane stress condition rather than the plane strain condition employed in the DT equations.

The experiments further revealed that the fracture surface in the tilted wedge of the starter notch initiates at approximately 38-45 % of the peak experimental load. In this instance, the DT equations would indicate a proportionally low stress intensity level (stress intensity is directly proportional to the applied load in DT geometry). However, the stress intensity results based on the full field deformations of the surface material at the notch highlights that the material has reached a critical level of stress intensity, Figure 6.11. This result was confirmed during the live in-situ SEM experiments where crack initiation in the starter wedge was identified at these low loads.

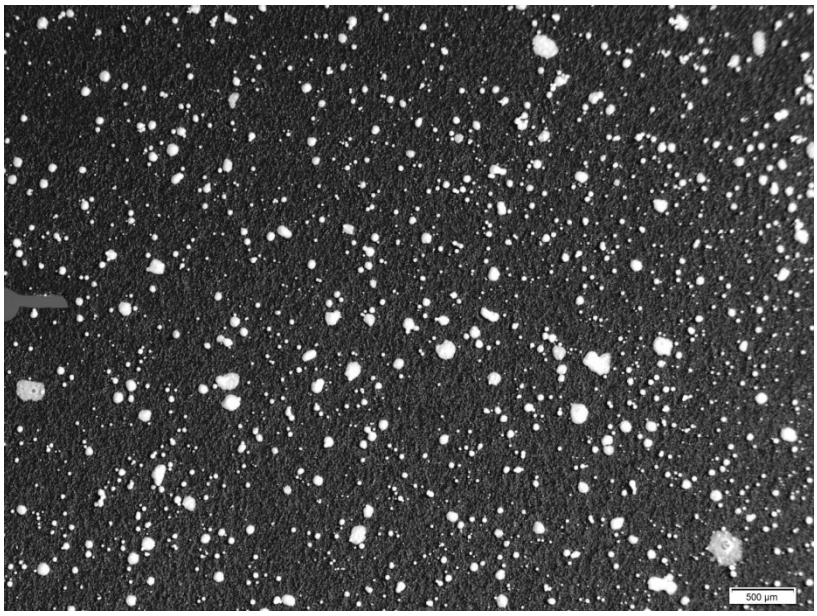

Figure 6.8 – Optical micrograph depicting the surface of a leached PCD specimen, highlighting the natural surface texture (dark grey) and the additional paint speckles (white globules). For illustration purposes, depicts the same image at the end of the experiment with the crack having fully traversed the field of view from the notch, left to right.

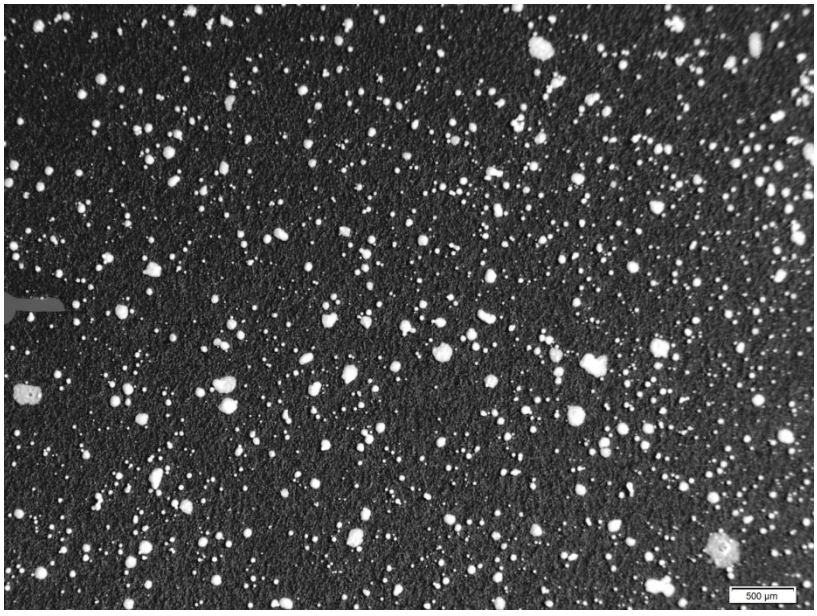

Figure 6.9 – Optical micrograph depicting the same field of view as Figure 6.8 after the crack was propagated fully across the field of view and can be considered “wide open”. It is evident that the crack is difficult to identify.

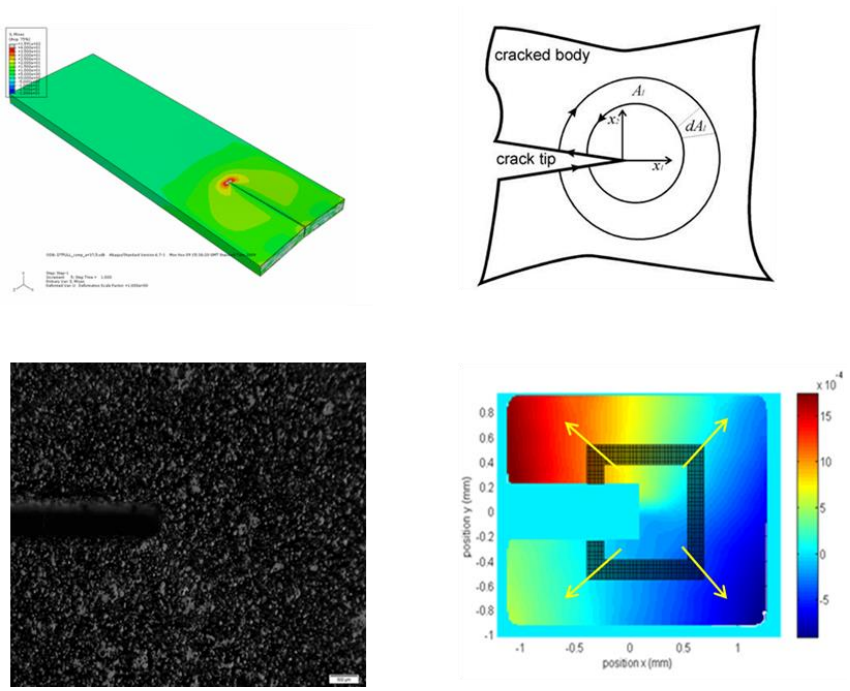

Figure 6.10 – Illustration collage depicting a miniature DT specimen (top left) experiencing crack propagation. The surface of the specimen has a speckle pattern (bottom left). The J-integral is evaluated around the crack tip for deformation field determined by DIC. The image in the bottom right corner depicts the MATLAB implementation of the contour integral.

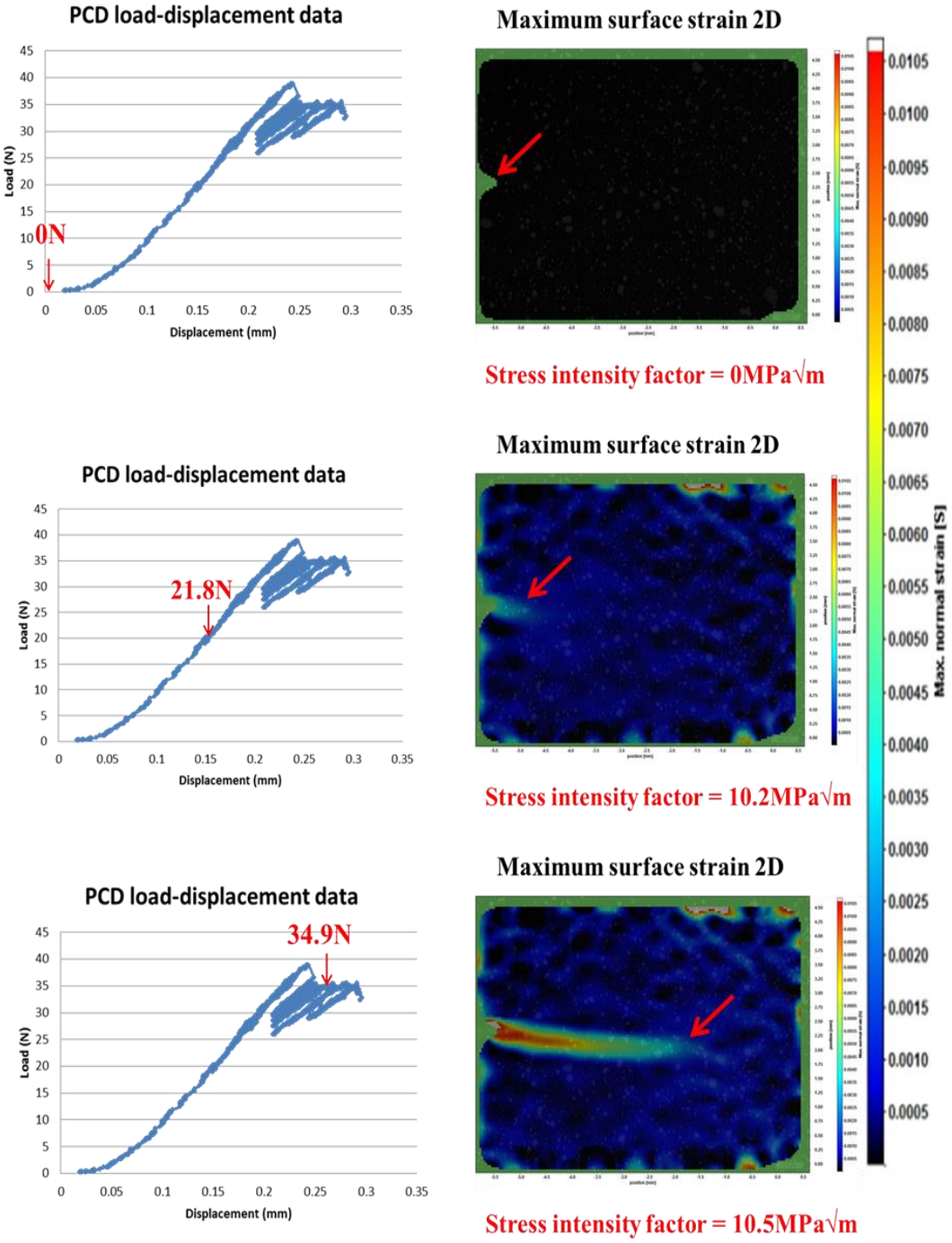

Figure 6.11 – Collage depicting the correlation between the applied load and the stress intensity level determined by DIC and Jman techniques. It is important to note that the optical approach correctly identifies critical stress intensity levels in the starter wedge at what is nominally half the load associated with the critical stress intensity as characterised by the classical DT equations. (The global

sidebar applies to all three images as the strain range is fixed in the individual plots).

6.4.2 3D DIC-JMAN based results

The 3D DIC approach was attempted on the pre-cracked specimens in order to evaluate the potential of the approach to characterise the fracture toughness of the PCD material in a non-contact manner while quantifying the out of plane displacements not included in the 2D analysis.

The results obtained revealed that the approach can indeed characterise the fracture toughness of the material. However, large variation in the measured results, up to 20-25 % highlighted that the experimental factors such as selection of the appropriate lenses, specimen dimensions and specimen surface texture are required to optimise the experiment. Adjustment of all of these parameters was not possible within the course of the current research project.

Nonetheless, the experimental investigation revealed that the non-contact approach to characterisation of surface stress intensity levels and hence toughness properties are possible employing the combination of DIC and JMAN techniques. Even in the material as stiff and brittle as PCD, benchtop characterisation of fracture toughness was possible. This provides a sound basis for further research into non-contact approaches to fracture toughness studies of brittle materials enabling experiments in various tailor made environmental conditions such as acids or high temperatures - conditions which preclude, or make difficult, the use of standard techniques and specimen geometries.

6.5 EBSD based microstructural observations

The EBSD mapping experiments assisted in developing the understanding of the microstructural parameters affecting the crack propagation. The pre-mapping and post-mapping approaches were developed in order to insure that some information would be gained should the DT fracture experiments not be sufficiently controllable. However, as all experiments were successful, the following observations were made.

The ability of the EBSD technique to clearly distinguish between individual diamond crystals, revealed an important observation.

6.5.1 **Pre-mapping**

The results obtained from the experiments performed in the pre-mapped specimens, revealed that, importantly, the cracks could be successfully propagated through the small pre-mapped region. The orientation of the diamond grains did not appear to be significantly altered after the cracks had been grown through the mapped region. However, the maps revealed that in the finer grain specimens, the path of the crack could hardly be related to the microstructural orientation of the individual grains. The propagation mechanism appeared to be mostly intergranular with the crack path causing significant damage in the crack wake.

These observations indicate a significant degree of secondary damage in the fine grain specimens. Observations made in the coarse grain specimens better showed the crack path with respect to the surrounding microstructure. However, little damage could be observed in the wake of the crack. Compared to the fine grain specimens, the propagation mechanism had a significantly larger transgranular component than the one which could be determined in the fine grain specimens.

6.5.2 **Post-mapping**

Inspection of the closed cracks in unloaded miniature DT specimens revealed that most information could be obtained from the coarse grain specimens. The experiments revealed that the crack path in the unloaded specimen could be clearly related to the surrounding microstructure. A key observation was made that in instances where the crack was approaching a region of intergranular propagation “opportunity”, the crack would pass in transgranular mode, near the grain boundary, but within one of the parent grains. This is believed to be related to the strength/toughness properties of the diamond regrown in the regions where intergranular contact is made under HPHT conditions.

These observations require further study, with the technique providing the potential to perform fracture experiments in-situ EBSD studies. Furthermore, the presented discussion highlights the potential tool in developing a PCD material where the properties of the parent grain as well as those of the regrown region, are employed to develop a material with tailor made fracture properties.

6.6 Results in the context of the current state of the art

6.6.1 Fracture toughness results

The fracture toughness results obtained during the current research project were compared to those in the published literature which can be considered the current state of the art in the field of fracture mechanics studies in PCD materials. The results obtained by Lammer[20], Field[105], McNamara[16], Novikov[21], Achilles[19] and Morrell[17] all fall within the range of 5-11 MPa√m (For detailed values refer to section 3.1). The fracture toughness levels obtained in the current research project were in the range of 8.1-11.9 MPa√m.

It is worth noting that the results obtained in the current research project are considered reliable based on the two following arguments. The stability and control of the crack initiation and propagation enabled the measurement of the load, and hence stress intensity, associated with the extension of the crack from an atomically sharp condition. This was controllably performed in the middle one third section of the miniature DT specimen length, which is considered to be the most stable region for obtaining constant stress intensity values for DT experiments[61,66]. Furthermore, the results revealed a clear and consistent difference between the toughness measurements obtained for the four distinct grades of PCD material tested. While the difference in toughness can be considered small in terms of an absolute range of toughness, with a full range of difference in toughness measurements spanning only 4 MPa√m, the percentage differences were significant. The 30-4 µm bi-modal PCD material was found to be 47 % tougher than the unimodal 4µm PCD material. In contrast, Lin, Cooper and Hood[29] experimented on PCD compacts with specimen microstructures characterised by grain size ranges of 5-15 µm, 10-30 µm and 20-50 µm. No significant difference in the critical stress intensity levels for the different microstructures was obtained during their experiments. Lammer[20], in his experiments involving 12 µm and 30 µm grain size specimens also did not observe significant differences in the fracture toughness of the materials of the finer grain sizes. However, clear differences were observed in the experiments extended to coarser grain sizes.

Davies and Field[95] studied the toughness properties of optical quality CVD diamond employing the double torsion technique. While microstructurally different, the CVD diamond is polycrystalline. It is worth noting that a similar

experimental strategy to that of the current test programme was employed by Davies and Field in that they calibrated their experimental equipment and methodology by employing readily available alumina specimens. Once confidence was obtained in the fact that the results were in good agreement with the published data, the experiments were extended to CVD specimens. The experiments revealed that the CVD material had a toughness level of 8.3 MPa√m, which is of the same order of magnitude as the current results.

The results obtained by McNamara[16] are also in good agreement with those obtained in the current work. McNamara and his colleagues employed three point bending test geometry to study the fracture toughness of 4 µm and 30 µm grain size PCD materials. Notches of known root radii were employed in the experiments and the results were corrected for the notch root radius apparent toughening effect. As an example, the 30 µm grain size PCD revealed critical stress intensity levels of 15.3-17.2 MPa√m prior to the correction for the blunt notch effects. The corrected results for the 30 µm specimens were determined to be 8.5-9.5 MPa√m. These are in good agreement with the results obtained in the current work, although they do depend on the correct determination of the analytical parameters such as the critical distance and accurate measurement and interpretation of the root notch size[16].

The present discussion highlights that the current results are in good agreement with the published research. Based on the developed methodology and the length of controlled cracks propagated (several millimetres), it is proposed that the current results are more accurate than those that require significant analytical corrections. Bearing in mind the assumptions and limitations associated with the derivation of the double torsion methodology.

6.6.2 Experimental solutions

The methodology developed in the current research project has shown itself to be experimentally robust in characterising the fracture mechanics properties and studying fracture mechanisms in PCD materials.

Fracture mechanics studies in PCD are complicated by the extreme stiffness of the material, difficulty of producing specimens and the cost associated with destructive testing of the expensive material. For these reasons, crack length dependant geometries provide little valuable information with regard to both the real fracture toughness properties and the associated fracture mechanisms. This is due to the fact that the cracks become unstable almost immediately and

hence little data and opportunity for propagation mechanism observation are generated. Sudden and complete fracture of the specimens immediately after the onset of propagation provides little confidence in the results obtained.

It is proposed that the methodology developed in this research project provides an elegant solution to the abovementioned problems. A miniature DT rig placed inside an SEM microscope enables simultaneous – i) generation of the load displacement data, ii) observation and measurement of the fracture processes, iii) unloading of the crack to study the wake features and iv) extraction of full field deformations from the images obtained.

The capability of extracting the J-integral and associated stress intensity data from the full field displacement data captured during the DT experiments further enables the analysis and cross-correlation of the obtained results. The current experimental programme has provided a foundation for the application of DIC techniques in the experiments with low strains associated with onset of fracture. Nonetheless, the optical approach was successful in characterising the stress intensity of the PCD material with good agreement between the classical DT formulations and the JMAN non-contact approach. The non-contact approach further provides a multitude of opportunities to extend the experimental scope as the deformations can be captured while the specimen is heated, subjected to environmental effects and many more.

Finally, the cost associated with the realisation of the miniature DT rig design is low and the rig is relatively simple to construct. This can lead to a proliferation of in-situ SEM research in PCD as well as other brittle materials such as a wide range of engineering ceramics.

6.6.3 Improving PCD material toughness

The results obtained during the experimental programme performed have provided insight into the relationship between the microstructural properties of the material and fracture toughness and the fracture mechanisms observed. The results indicate that increasing grain size and contiguity increase the fracture toughness of the material. In turn, increased cobalt content leads to the reduction in the fracture toughness of the PCD material.

It is important to note that the microstructure of a PCD material is generated in a complex process where interactions of chemical constituents, high pressures and high temperatures lead to the formation of a specific microstructure.

Therefore it is not trivial to change the properties of a single parameter in isolation. The starter grit size affects the ability of the cobalt to interpenetrate the microstructure, the packing order of the grit affects the degree of crushing and inter-crystal strain during sintering, the hold time affects the degree of diamond regrowth which is at the same time affected by the quantity of available cobalt. These complex interactions need to be well understood in order to generate a PCD material with improved/increased toughness properties.

Further to simply aim at increasing the toughness properties of the PCD material is not sufficient and it is often sought to control the crack path, by controlling material properties ahead of the crack. Increasing the tortuosity of the crack path can increase the apparent toughness of the material. Predictable crack propagation paths can also provide the component designer with the tools necessary to develop a functionally graded material which is purpose fit. Based on the observations made during the analysis of the EBSD maps of the crack wake, it is believed that one method of creating a functionally graded PCD material with variable toughness properties is by means of diamond crystal deformation and plasticity.

While limited, research has been published by Dyer and Conradi[119], and Mukhin[120], where exposure of PCD to a heat treatment process at temperatures in the range of 1100-1400 K, resulted in a loss of strength of about 35 % for fine grain PCD materials and as much as 65 % for coarse grain PCD materials. Gasc and Wang[117], performing deformation experiments at 1273 K and 6 GPa, highlighted that diamond grits with reduced defect density generated better diamond-to-diamond bonds. Exposing the diamond grit to higher thermal damage would lead to graphitisation and formation of surface defects which could further control the diamond-to-diamond bonding. Based on the above, it appears that both the degree of diamond-to-diamond bonding and the strength of the individual crystals can be controlled by prior deformation and heat treatment of the grit, notwithstanding all parameters which need to be considered for successful HPHT sintering of PCD compacts. Thus it is entirely plausible that the process of developing functionally graded PCD materials can start by manipulating the starter grits, and specifically the degree of plastic deformation within the crystal and on the interface surfaces. Arranging the grits of varying properties, would enable the control over the local contiguity of the global specimen. Development of such techniques would enable crack propagation along preferential paths. This in turn could enable development of tools which undergo damage in a predictable manner, “self-sharpen” and

prevent premature macrocrack propagation into the bulk of the material which typically leads to early loss of the tool performance.

Summary

In summary, the results of the research programme performed have revealed that the DT technique is a valuable technique in the study of the fracture mechanics properties of PCD materials. Given the extreme stiffness and brittleness of the material and the successful application of the technique to all specimens employed, it can be concluded that the DT technique is indeed a robust facility in the study of brittle materials. The ability to develop miniature test rigs which would suit most SEM microscope stages/chambers, makes the DT technique widely accessible to anyone involved in the study of brittle material fracture.

The controlled propagation, arrest and then continued propagation of the crack in the middle one third of the specimen length provides confidence in the obtained PCD material fracture toughness properties. This is due to the fact that the crack propagation process is restarted from what can be considered an atomically sharp crack front.

In addition to the fracture toughness properties obtained through classical DT approach, non-contact characterisation of the PCD surface stress intensity levels was successfully achieved. Specifically, the 2D approach revealed good agreement between the material fracture toughness properties obtained through classical DT equations using load-displacement data and that determined from the full field displacements of the specimen surface. Given the extreme stiffness of PCD, it is considered very promising that the small, localized surface strains were sufficient to evaluate the J-integral and determine the PCD material properties.

In-situ SEM studies enabled observation of the crack propagation while capturing the load displacement data as well as the full field surface deformation images. Such in-situ studies provide the ability to study the effects various microstructural features and/or variations, especially those introduced intentionally, have on the behaviour of the crack and the associated fracture mechanics properties.

The results of the current research programme revealed, in agreement with published research, that the toughness of the PCD material, in the range of grain sizes tested, increases with increasing grain size and contiguity and decreases with increasing cobalt content. It was further observed that the crack propagation process develops a larger transgranular crack path as the grain size increases. This is consistent with the fact that the intergranular path requires more and more energy as the grain size increases and the transgranular mechanism becomes energetically favourable. In addition, these cracks with the longer grains follow crystal slip planes and are thus more tortuous – resulting in increased toughness.

EBSD pre-mapping of the microstructure revealed that crack propagation in PCD has a very small fracture process zone (FPZ). While the material with the finest diamond grain size and highest cobalt content showed evidence of damage in the wake of the crack. Analyses of the coarse grained specimens revealed that there was practically no change in orientation of the fractured grain segments, on either side of that crack, occurs when a crack splits a grain. Furthermore, it was observed that in some instances, the crack path appeared to propagate preferentially inside the grain rather than through a grain boundary between the two grains. This may be explained by the fact that the regrown diamond, which develops during the sintering process, possesses higher crack resistance. This leads to the crack propagation along the boundary between the deformed/damaged parent grain and the new regrown diamond.

Finally, only a small number of diamond specimens was (typically) available for destructive fracture mechanics testing. This is the result of the high cost as well as specialist equipment and personnel required to make such specimens. Taking the scarcity of the specimens available, the current experimental approach provides a methodology capable of extracting the maximum amount of useful information from the limited number of specimens available. Furthermore, the optical, non-contact fracture mechanics parameter evaluation techniques demonstrated in this research can facilitate the development of new specimen geometries. Development of more economical specimens would enable a wider study of the fascinating material that is PCD.

7 Conclusions and Recommendations

7.1 Conclusions

The aim of this project was to contribute new techniques, methodologies and understanding in the fracture mechanisms, crack propagation behaviour and fracture properties in PCD. The work was split into four key sections which entailed the following – i) development of the miniature DT rig which could be operated in-situ in the SEM, ii) characterisation of the fracture mechanics properties of four grades of PCD material of varying, known composition, iii) qualitative observation of the micromechanical cracking processes and microstructural features affecting them and iv) an attempt to quantify simultaneously the fracture toughness parameters by using a novel non-contact optical approach employing DIC and JMAN MATLAB routines.

i) A miniature DT rig was successfully developed such that it could be employed for both bench top optical and SEM microscope observation of the live fracture experiments. In addition, the bench top operation enabled the fracture process observation and quantification by means of 2D and 3D DIC optical imaging systems. The crack propagation region of interest is not obstructed by any of the miniature DT loading rig components.

The rig provides the capability for **controlled** initiation and propagation of cracks in PCD as well as other brittle materials. The miniature DT methodology was robust in that all experiments were successful in characterising the material properties without loss of specimens.

ii) Four PCD material grades, of known composition, were characterised employing this approach. The results revealed clear distinction between the toughness properties of the four PCD particle size grades, specifically, the average toughness values obtained were – i) 4 µm at 8.1 MPa√m±0.3, ii) 12 µm at 9.5 MPa√m±0.3, iii) 30 µm at 10.6 MPa√m±0.5 and iv) 30/4 µm at 10.6 MPa√m±0.6. This highlights the accuracy and repeatability of the DT technique. The fact that the specimens could be unloaded and then re-loaded again to propagate the crack from an atomically sharp condition, provides confidence in the obtained fracture toughness results.

The results revealed that the fracture toughness properties increased with increasing grain size, increasing contiguity and decreasing cobalt content.

iii) In-situ SEM experiments revealed that in all four grades of material tested, secondary cracking had occurred, highlighting that a FPZ does exist in PCD and serves as a toughening mechanism. EBSD mapping of cracked, coarse grained specimens revealed crack paths in diamond grains of known crystallographic orientation. The two observation techniques highlighted that transgranular crack front propagation increases with increasing grain size and diamond phase contiguity.

The EBSD data further highlighted a feature/mechanism where the crack would approach a grain boundary of relatively large grain but propagate inside the grain, slightly below the surface. This mechanism may be related to the newly regrown diamond at the diamond-to-diamond grain interfaces, where new, undamaged diamond is formed during the sintering process.

iv) The DIC/JMAN approach revealed excellent agreement with the classical DT formulation when applied to the optical 2D microscope data and a leached specimen surface with significant texture. Good agreement was

further aided by very small out-of-plane displacements characteristic to the very stiff PCD material.

The 3D DIC experiments showed some correlation with SIF data determined from the load displacement data by classical DT equation. The correlation was within 20-25 %. The poor correlation and poor JMAN convergence were a result of the relatively small data set obtained during 3D DIC, further affected by the small strains to failure characteristic of the PCD material with a Young's modulus in the order of 1000 GPa.

The application of the techniques and methodologies developed and presented in the current project provide new tools and information in the development of the understanding of the fracture mechanisms in PCD material. The techniques presented can be better used to quantify, observe and understand the fracture mechanisms in PCD materials made by new sintering methodologies and new binder/catalyst compositions. The ability to observe and understand the effects microstructural features have on crack resistance, may enable the development of functionally graded materials which employ the principles of biomimicry to develop toughening mechanisms resembling those found in nature.

7.2 Recommendations

Based on the research presented, the following recommendations are made:

- Further refinement of the miniature DT rig can lead to the standardisation of the miniature DT approach as a fracture mechanics property and mechanism evaluation technique for brittle materials.

- Development of the in-situ SEM imaging for DIC is an ongoing research topic. Future work is recommended in combining the in-situ SEM DT imaging experiments with DIC processing in order to develop further tools for micro-fracture mechanism studies.

- Further development of 3D DIC systems for non-contact extraction of fracture mechanics properties from the miniature DT geometry. Such research will provide the tools for testing of materials in tailored environments, especially those poorly suited for refined electronics and mechanisms.

- Application of the techniques presented in the current work, along with others available, can be employed to better understand and control the parameters and mechanisms which lead to improved toughness properties in polycrystalline diamond. Further research on the effects of the regrown diamond and HPHT diamond properties on the cracking behaviour of the polycrystalline bulk material appear to be of particular interest.

References

[1] C. S. Trueb, L.F., Barrett, “American Mineralogist (1972) Vol. 57, pp. 1664-7680,” *Am. Mineral.*, vol. 57, p. pp.1664-1680, 1972.

[2] Y. Moriyoshi, M. Kamo, N. Setaka, and Y. Sato, “The microstructure of natural polycrystal diamond, carbonado and ballas,” *J. Mater. Sci.*, vol. 18, no. 1, pp. 217–224, 1983.

[3] W. C. Trueb, L.F., Butterman, “Carbonado: a microstructural study,” *Am. Mineral.*, vol. 54, pp. 412–425, 1969.

[4] R. H. Wentorf, R. C. Devries, and F. P. Bundy, “Sintered superhard materials.,” *Science*, vol. 208, no. 4446, pp. 873–80, 1980.

[5] H. T. Hall, “Sintered diamond: a synthetic carbonado.,” *Science (New York, N.Y.)*, vol. 169, no. 3948. pp. 868–9, 1970.

[6] E. M. Wilks and J. Wilks, “The abrasion resistance of natural and synthetic diamond,” *Wear*, vol. 81, no. 2. pp. 329–346, 1982.

[7] J. E. Field and C. S. J. Pickles, “Strength, fracture and friction properties of diamond,” *Diam. Relat. Mater.*, vol. 5, no. 6–8, pp. 625–634, 1996.

[8] J. E. Field, “The mechanical and strength properties of diamond.,” *Rep. Prog. Phys.*, vol. 75, no. 12, p. 126505, 2012.

[9] D. Scott, “The history and impact of synthetic diamond cutters and diamond enhanced inserts on the oil and gas industry,” *Ind. Diam. Rev.*, vol. 66, no. 1, pp. 48–55, 2006.

[10] K. Zacny and G. Cooper, “Considerations, constraints and strategies for drilling on Mars,” *Planet. Space Sci.*, vol. 54, no. 4, pp. 345–356, 2006.

[11] A. Ersoy and M. D. Waller, “Drilling Detritus and the Operating Parameters of Thermally Stable PDC Core Bits,” *Int. J. Rock Mech. Min. Sci.*, vol. 34, no. 7, pp. 1109–1123, 1997.

[12] S. G. Moseley, K. P. Bohn, and M. Goedickemeier, “Core drilling in reinforced concrete using polycrystalline diamond (PCD) cutters: Wear and fracture mechanisms,” *Int. J. Refract. Met. Hard Mater.*, vol. 27, no. 2, pp. 394–402, 2009.

[13] J. Chevalier, C. Olagnon, G. Fantozzi, and B. Cales, “Subcritical crack growth and thresholds in a 3Y-TZP ceramic under static and cyclic loading conditions,” *Ceram. Int.*, vol. 23, no. 3, pp. 263–266, 1997.

[14] A. Ersoy and M. D. Waller, “Wear Characteristics of PDC Pin and Hybrid Core Bits in Rock Drilling,” *Wear*, vol. 188, no. 1–2, pp. 150–165, 1995.

[15] R. R. O. Drory, M.D., Dauskardt, R.H., Kant, A., “Frcature of synthetic diamond,” *J. Appl. Phys.*, vol. 78, no. 5, pp. 3083–3088, 1995.

[16] D. McNamara, P. Alveen, D. Carolan, N. Murphy, and a. Ivanković, “Fracture toughness evaluation of polycrystalline diamond as a function of microstructure,” *Eng. Fract. Mech.*,

vol. 143, pp. 1–16, 2015.

[17] R. Morrell, R. Danzer, P. Supancic, W. Harrer, S. Puchegger, and H. Peterlik, “Meso-scale mechanical testing methods for diamond composite materials,” *Int. J. Refract. Met. Hard Mater.*, vol. 28, no. 4, pp. 508–515, 2010.

[18] D. Miess and G. Rai, “Fracture toughness and thermal resistance of polycrystalline diamond compacts,” *Mater. Sci. Eng. A*, vol. 209, no. 1–2, pp. 270–276, 1996.

[19] R. D. Achilles, “Development of a Procedure for Fatigue Crack Growth in PCD,” in *International Industrial Diamond Conference, Rome.*, 2007.

[20] A. Lammer, “Mechanical Properties of Polycrystalline diamonds,” *Materials Science and Technology*, vol. 4, no. 11. pp. 949–955, 1988.

[21] M. V. Novikov, V. N. Maistrenko, and V. N. Kulakowski, *Fracture Resistance of Superhard Composite Materials*. Naukova Dumka Publications (Translated from Russian), 1993.

[22] K. J. Dunn and M. Lee, “The fracture and fatigue of sintered diamond compact,” *J. Mater. Sci.*, vol. 14, pp. 882–890, 1979.

[23] V. Kanyanta, A. Dormer, N. Murphy, and A. Invankovic, “Impact fatigue fracture of polycrystalline diamond compact (PDC) cutters and the effect of microstructure,” *Int. J. Refract. Met. Hard Mater.*, vol. 46, pp. 145–151, 2014.

[24] M. V. Sneddon and D. R. Hall, “Polycrystalline Diamond : Manufacture , Wear Mechanisms , and Implications for Bit Design,” *J. Pet. Technol.*, vol. 40, no. 12, pp. 1593–1601, 1988.

[25] T. H. Becker, T. J. Marrow, and R. B. Tait, “An Evaluation of the Double Torsion Technique,” *Exp. Mech.*, vol. 51, no. 9, pp. 1511–1526, Feb. 2011.

[26] R. B. Tait, P. R. Fry, and G. G. Garrett, “Review and evaluation of the double-torsion technique for fracture toughness and fatigue testing of brittle materials,” *Exp. Mech.*, no. 27, pp. 14–22, 1987.

[27] A. Shyam and E. Lara-Curzio, “The double-torsion testing technique for determination of fracture toughness and slow crack growth behavior of materials: A review,” *J. Mater. Sci.*, vol. 41, no. 13, pp. 4093–4104, Jun. 2006.

[28] A. Evans, “A method for evaluating the time-dependent failure characteristics of brittle materials—and its application to polycrystalline alumina,” *J. Mater. Sci.*, vol. 7, pp. 1137–1146, 1972.

[29] T.-P. Lin, G. a. Cooper, and M. Hood, “Measurement of the fracture toughness of polycrystalline diamond using the double- torsion test ill,” *J. Mater. Sci.*, vol. 29, pp. 4750–4756, 1994.

[30] Amanda S. Barnard, *The Diamond Formula: Diamond Synthesis - A gemmological perspective*. Butterworth-Heinemann, 2008.

[31] Wikipedia, “ASEA,” 2019. [Online]. Available: https://en.wikipedia.org/wiki/ASEA. [Accessed: 25-Jun-2019].

[32] Wikipedia, “Baltzar Von Platen (Inventor),” 2018. [Online]. Available: https://en.wikipedia.org/wiki/Baltzar_von_Platen_(inventor). [Accessed: 25-Jun-2019].

[33] R. H. Bundy, F.P., Hall, H.T., Strong, H.M., Wentorf, “Man-Made Diamonds,” *Nature*, vol. 176, pp. 51–55, 1955.

[34] M. Akaishi, H. Kanda, Y. Sato, N. Setaka, T. Ohsawa, and O. Fukunaga, “Sintering behaviour of the diamond-cobalt system at high temperature and pressure,” *J. Mater. Sci.*, vol. 17, pp. 193–198, 1982.

[35] S. Naka, H. Itoh, and T. Tsutsui, “Reaction sintering of diamond using a binary solvent-catalyst of the Fe-Ti system,” *J. Mater. Sci.*, vol. 22, pp. 1753–1757, 1987.

[36] F. Bellin, A. Dourfaye, W. King, and M. Thigpen, “The current state of PDC bit technology - Part 3,” *World Oil*, vol. 231, no. 11, pp. 67–71, 2010.

[37] J. E. Field, *The Properties of Natural and Synthetic Diamond*. Academic Press, 1992.

[38] F. Bellin, A. Dourfaye, W. King, and M. Thigpen, “The current state of PDC bit technology - Part 1,” *World Oil*, vol. 231, no. 11, pp. 41–46, 2010.

[39] F. Bellin, A. Dourfaye, W. King, and M. Thigpen, “The current state of PDC bit technology - Part 2,” *World Oil*, vol. 231, no. 11, pp. 53–58, 2010.

[40] F. G. Marro, A. Mestra, E. Jiménez-Piqué, S. Ozbayraktar, and L. Llanes, “Damage induced by monotonic and cyclic spherical indentation in polycrystalline diamond (PCD),” *Int. J. Refract. Met. Hard Mater.*, vol. 49, no. 1, pp. 292–301, 2015.

[41] C. T. Peters, “The relationship between Palmqvist indentation toughness and bulk fracture toughness for some WC-Co cemented carbides,” *J. Mater. Sci.*, vol. 14, no. X, pp. 1619–1623, 1979.

[42] Astakhov, P., *Drills: Science and Technology of Advanced Operations*. CRC Press, 2014.

[43] Heath, P.J., “Ultrahard Tool Materials,” in *ASM Handbook Volume 16*, ASM International, 1989, pp. 105–117.

[44] H. Robard, “Hughes Christensen - Drill Bit catalog.”

[45] M. V. Novikov, A. L. Maystrenko, and V. I. Kushch, “Effect of metal catalyst thermal expansion on thermal stability of synthetic diamonds,” *Comput. Mater. Sci.*, vol. 53, no. 1, pp. 409–415, 2012.

[46] J. E. Westraadt, I. Sigalas, and J. H. Neethling, “Characterisation of thermally degraded polycrystalline diamond,” *Int. J. Refract. Met. Hard Mater.*, vol. 48, pp. 286–292, 2015.

[47] T. L. Anderson, *Fracture mechanics: fundamentals and applications*. CRC press, 2005.

[48] D. Broek, *Elementary Engineering Fracture Mechanics*. New York: McGraw-Hill, 1978.

[49] S. Suresh, *Fatigue of Materials*, 2nd Editio. Cambridge University Press, 1998.

[50] J. F. Knott, *Elementary engineerign fracture mechanics*. Butterworth & Co, London, 1973.

[51] A. A. Griffith, “The Phenomena of Rupture and Flow in Soldis,” *Philos. Trans. R. Soc. London, Ser. A,* vol. 221, pp. 163–198, 1921.

[52] C. E. Inglis, “Stresses in a plate due to the presnce of cracks and sharp corners,” *Trans. Inst. Naval Architects*, vol. 55(1). pp. 219-241 Plate XXVIII, 1913.

[53] G. R. Irwin, “Fracture Dynamics,” *Fract. Dyn. "Fracturing Met. Am. Soc. Met. Cleveland, OH.*, pp. 147–166, 1948.

[54] E. Orowan, “Fracture and strength of solids,” *Reports Prog. Phys.*, vol. 12, pp. 185–232, 1949.

[55] H. L. Ewalds and R. J. H. Wanhill, *Fracture mechanics*, 1st Editio. Edward Arnold, 1991.

[56] B. R. Lawn and T. R. Wilshaw, *Fracture of brittle solids*. Cambridge: Cambridge University Press, 1975.

[57] T. H. Becker, “Understanding and modelling damage and fracture in nuclear grade graphite,” PhD Thesis, University of Cape Town, 2011.

[58] J. Rice, “A Path Independent Integral and the Approximate Analysis of Strain Concentration by Notches and Cracks,” *J. Appl. Mech.*, vol. 35, pp. 379–386, 1968.

[59] L. M. Barker, “A simplified method for measuring plane strain fracture toughness,” *Eng. Fract. Mech.*, vol. 9, no. 2, pp. 361–369, 1977.

[60] ASTM E1304-97, “Standard Test Method for Plane Strain (Chevron Notch) Fracture Toughness of Metallic Materials,” *ASTM Int. West Conshohocken, PA, USA*, vol. 97, no. Reapproved, pp. 1–12, 2014.

[61] L. Chuck, E. R. Fuller, and S. W. Freiman, *Chevron-Notch bend testing in glass: Some experimental problems, in "Chevron-Notched Specimens: Testing and Stress Analysis, ed. J.H. Underwood, S.W. Freiman, E.R. Fuller*. 1984.

[62] J. O. Outwater, M. C. Murphy, R. G. Kumble, and J. T. Berry, “Double Torsion Technique as a Universal Fracture Toughness Test Method, ed. P.Paris, G.R. Irwin,” *ASTM STP 559, Am. Soc. Test. Mater.*, pp. 127–138, 1974.

[63] J. A. Kies and A. B. J. Clark, “Fracture propagation rates and times to fail proof stresses in bulk glass, in Fracture 1969, ed. P.l. Pratt, E.H. Andrews, N.E. Frost, R.W. Nichols, and E. Smith,” *Proc. Second Int. Conf. Fract.*, pp. 483–492.

[64] E. R. Fuller, “An evaluation of double-torsion testing—analysis,” in *Fracture mechanics applied to brittle materials, ASTM STP 678*, New York: ASTM International, 1979, pp. 3–18.

[65] B. J. Pletka, E. R. Fuller, and B. G. Koepke, “An evaluation of double-torsion testing—experimental,” in *Fracture mechanics applied to brittle materials, ASTM STP 678*, Philadelphia: ASTM International, 1979, pp. 19–37.

[66] G. G. Trantina, “Stress Analysis of the Double-Torsion Specimen,” *J. Am. Ceram. Soc.*, vol. 60, no. 7–8, pp. 338–341, 1977.

[67] D. R. Biswas and V. K. Pujari, “Verification of the Double-Torsion Equation by Using Different Thickness Samples of a Machinable Glass-Ceramic,” *J. Am. Ceram. Soc.*, vol. 64, pp. C98–C99, 1981.

[68] K. R. McKinney and H. L. Smith, “Method of studying subcritical cracking of opaque materials,” *J. Am. Ceram. Soc.*, vol. 56, no. 1, pp. 30–32, 1973.

[69] D. K. Shetty and A. V Virkar, “Determination of the useful range of crack lengths in double torsion specimens,” *J. Am. Ceram. Soc.*, vol. 61, no. 1–2, pp. 93–94, 1978.

[70] J. A. Salem, M. Radovic, E. Lara-Curzio, and G. Nelson, “Fracture Toughness of Thin Plates by the Double-Torsion Test Method, in Mechanical Properties and Performance of Engineering Ceramics and Composites. 2, ed. R. Tandon,” pp. 63–73, 2006.

[71] R. B. Tait and G. G. Garrett, “In situ double torsion fracture studies of cement mortar and cement paste inside a scanning electron microscope,” *Cem. Concr. Res.*, vol. 16, no. 2, pp. 143–155, 1986.

[72] G. Vekinis, M. F. Ashby, and P. W. R. Beaumont, “R-curve behaviour of Al 2 O 3 ceramics,” *Acta Metall. Mater.*, vol. 38, no. 6, pp. 1151–1162, 1990.

[73] K. Rosie, “A method for in-situ SEM fracture studies of brittle materials using the double torsion technique: application to nuclear graphite,” MSc Thesis, University of Cape Town, 2011.

[74] R. Tait and K. Rosie, “Microstructural Crack Behaviour Studies of Nuclear Graphite Using an in situ Double Torsion Rig Inside a Scanning Electron Microscope,” 2010, no. 271, pp. 12–18.

[75] P. Reu., “Introduction to digital image correlation: Best practices and applications,” *Exper. Tech.*, no. 36(1), pp. 3–4, 2012.

[76] H. Bruck, S. McNeill, M. Sutton, and W. P. Iii, “Digital image correlation using Newton-Raphson method of partial differential correction,” *Exper. Mech.*, vol. 29, pp. 261–267, 1989.

[77] M. Sutton, S. McNeill, J. Helm, and Y. J. Chao, “Advances in two-dimensional and three-dimensional computer vision,” *Top. Appl. Phys.*, vol. 77, pp. 323–372, 2000.

[78] B. Pan, K. Qian, H. Xie, and A. Asundi, “Two-dimensional digital image correlation for in-plane displacement and strain measurement : a review,” *Meas. Sci. Technol.*, vol. 20, no. 062001, pp. 1–17, 2009.

[79] Y. Wang, M. Sutton, H. Bruck, and H. Schreier, “Quantitative error assessment in pattern matching: effects of intensity pattern noise, interpolation, strain and image contrast on motion measurements,” *Strain*, vol. 45, pp. 160–178, 2009.

[80] J. D. Carroll, “Relating Fatigue Crack Growth to Microstructure Via Multiscale Digital Image Correlation,” PhD Thesis, Univ. of Illinois at Urbana-Champaign, 2011.

[81] D. Lecompte *et al.*, “Quality assessment of speckle patterns for digital image correlation,” *Opt. Lasers Eng.*, vol. 44, no. 11, pp. 1132–1145, Nov. 2006.

[82] T. H. Becker, M. Mostafavi, R. B. Tait, and J. Marrow, “An approach to calculate the J-integral using digital image correlation displacement field data,” *Fatigue Fract. Mater. Struct.*, vol. 35, no. 10, pp. 971–984, 2012.

[83] T. Maitland and S. Sitzman, “Electron Backscatter Diffraction (EBSD) Technique and Materials Characterization Examples,” in *Scanning Microscopy and Nanotechnology Techniques and Applications, ed. W. Zhou and Z.L. Wang*, W. Zhou and Z. L. Wang, Eds. New York, Springer., 2007, pp. 41–75.

[84] C. Hammond, *The basics of crystallography and diffraction*, vol. 12. Oxford University Press Oxford, 2009.

[85] A. A. Kelly and K. M. Knowles, *Crystallography and crystal defects*. John Wiley & Sons, 2012.

[86] A. Mckie, M. Herrmann, I. Sigalas, K. Sempf, and R. Nilen, “Suppression of abnormal grain growth in fi ne grained polycrystalline diamond materials (PCD),” *Int. J. Refract. Met. Hard Mater.*, vol. 41, pp. 66–72, 2013.

[87] B. S. El-dasher *et al.*, “Crystallographic anisotropy of wear on a polycrystalline diamond surface,” *Appl. Phys. Lett.*, vol. 241915, no. 88, pp. 11–14, 2006.

[88] T. Shin, J. Oh, K. Hwan, and D. Nyung, “The mechanism of abnormal grain growth in polycrystalline diamond during high pressure-high temperature sintering,” *Diam. Relat. Mater.*, vol. 13, pp. 488–494, 2004.

[89] H. Itoh, S. Tajima, M. Tamaki, and S. Naka, “Effects of starting carbon and solvent-catalyst on the reaction sintering of diamond,” *J. Mater. Sci.*, vol. 23, no. 8, pp. 2877–2881, 1988.

[90] M. Wolfer *et al.*, “Diamond & Related Materials Crystallographic anisotropy of growth and etch rates of CVD diamond,” *Diam. Relat. Mater.*, vol. 18, no. 5–8, pp. 713–717, 2009.

[91] Q. Meng, S. Guo, X. Zhao, and S. Veintemillas-Verdaguer, “Bulk metastable cobalt in fcc crystal structure,” *J. Alloys Compd.*, vol. 580, pp. 187–190, 2013.

[92] A. A. Salem, M. G. Glavicic, and S. L. Semiatin, “A coupled EBSD/EDS method to determine the primary- and secondary-alpha textures in titanium alloys with duplex microstructures,” *Mater. Sci. Eng. A*, vol. 494, no. 1–2, pp. 350–359, 2008.

[93] J. Nohava, P. Haušild, M. Karlík, and P. Bompard, “Electron backscattering diffraction analysis of secondary cleavage cracks in a reactor pressure vessel steel,” *Mater. Charact.*, vol. 49, no. 3, pp. 211–217, 2002.

[94] L. W. Yin *et al.*, “Investigation on defects in HPHT-grown diamond single crystals,” *J. Mater. Sci.*, vol. 36, no. 23, pp. 5585–5588, 2001.

[95] A. R. Davies, J. E. Field, K. Takahashi, and K. Hada, “The toughness of free-standing CVD diamond,” *J. Mater. Sci.*, vol. 39, no. 5, pp. 1571–1574, 2004.

[96] D. C. Roberts, “SYNDITE: Its mechanical and physical properties,” *Ind. Diam. Rev.*, vol. 39, pp. 237–241, 1979.

[97] P. D. Gigl, “The strength of polycrystalline diamond compacts,” in *High-Pressure Science*

and Technology, Springer, 1979, pp. 914–922.

[98] R. W. Rice, “Elastic anisotropy and the grain size dependence of ceramic fracture energies,” *J. Mater. Sci.*, vol. 19, pp. 1267–1271.

[99] R. W. Rice, “Fractographic identification of strength-controlling flaws and microstructure,” in *Concepts, Flaws, and Fractography*, Springer, 1974, pp. 323–345.

[100] ASTM, “Standard Test Method for Linear-Elastic Plane-Strain Fracture Toughness K1C of Metallic Material,” pp. 1–33, 2013.

[101] ISO 23146, “ISO 23146 Fine ceramics (advanced ceramics , advanced technical ceramics) — Test methods for fracture toughness of monolithic ceramics - Single-edge V-notch beam (SEVNB) method,” *ISO*. 2008.

[102] D. Carolan, P. Alveen, A. Ivanković, and N. Murphy, “Effect of notch root radius on fracture toughness of polycrystalline cubic boron nitride,” *Eng. Fract. Mech.*, vol. 78, no. 17, pp. 2885–2895, 2011.

[103] E. J. Brookes, P. Greenwood, and G. Xing, “The plastic deformation and strain-induced fracture of natural and synthetic diamond,” *Diam. Relat. Mater.*, vol. 8, no. 8–9, pp. 1536–1539, 1999.

[104] B. Lawn and R. Wilshaw, “Indentation fracture: principles and applications,” *J. Mater. Sci.*, vol. 10, no. 6, pp. 1049–1081, 1975.

[105] A. R. Davies, J. E. Field, K. Takahashi, and K. Hada, “Tensile and fatigue strength of free-standing CVD diamond,” *Diam. Relat. Mater.*, vol. 14, no. 1, pp. 6–10, 2005.

[106] M. Ciccotti, N. Negri, G. Gonzato, and F. Mulargia, “Practical application of an improve methodology for the double torsion load relaxation method,” *Int. J. Rock Mech. Min. Sci.*, vol. 38, no. 4, pp. 569–576, 2001.

[107] M. R. Ayatollahi, M. R. M. Aliha, and M. M. Hassani, “Mixed mode brittle fracture in PMMA - An experimental study using SCB specimens,” *Mater. Sci. Eng. A*, vol. 417, no. 1–2, pp. 348–356, 2006.

[108] D. A. Forsyth and J. Ponce, *Computer vision: a modern approach*. Prentice Hall Professional Technical Reference, 2002.

[109] M. Van Rooyen, “Thermal Power Plant Steel Creep Deformation Measurement Using Stereo Digital Image Correlation,” MSc Thesis, University of Stellenbosch, 2016.

[110] Olympus Inc., “Olympus Stream Micro-Imaging Analysis Software.”

[111] V. F. Britun, G. S. Oleynik, and N. P. Semenenko, “Deformation processes during high-pressure sintering of the diamond powders produced by catalytic synthesis,” *J. Mater. Sci.*, vol. 27, pp. 4472–4476, 1992.

[112] G. J. Davies, M. C. Nzama, and R. W. Nilen, “Patent No. US20160207168A1 - polycrystalline diamond composite compact element and tols incorporating same and method for making same,” 2016.

[113] H. T. Hall, “Sintered diamond: a synthetic carbonado.,” *Science*, vol. 169, no. 3948, pp. 868–9, 1970.

[114] H. Kanda, K. Suzuki, O. Fukunaga, and N. Setaka, “Growth of polycrystalline diamond,” *J. Mater. Sci.*, vol. 11, no. 12, pp. 2336–2338, 1976.

[115] V. T. Golovchan, N. V Litoshenko, and V. Wc, “On the contiguity of carbide phase in WC – Co hardmetals,” *Int. J. Refract. Met. Hard Mater.*, vol. 21, pp. 241–244, 2003.

[116] D. Howell *et al.*, “Quantitative characterization of plastic deformation of single diamond crystals: A high pressure high temperature (HPHT) experimental deformation study combined with electron backscatter diffraction (EBSD),” *Diam. Relat. Mater.*, vol. 30, pp. 20–30, 2012.

[117] J. Gasc *et al.*, “High-pressure, high-temperature plastic deformation of sintered diamonds,” *Diam. Relat. Mater.*, vol. 59, pp. 95–103, 2015.

[118] P. S. Leevers, “Crack-front shape effects in the double torsion test,” *J. Mater. Sci.*, vol. 17, no. 9, pp. 2469–2480, 1982.

[119] H. B. Dyer and V. R. Conradi, “Properties of natural debdust and its use in diamond saw blades,” *Ind. Diam. Rev.*, vol. 32, no. 381, p. 335, 1972.

[120] M. E. Mukhin, M. F. Yarmak, and V. V Popov, “Strength properties of type CAM synthetic diamonds of different grit sizes,” *Almazy Sverkh. Mater.*, 1974.

[121] P. Crawford, “K179 - Unipolar steppermotor driver,” *http://kitsrus.com/pdf/k179.pdf*, 2004.

[122] T. A. Scott, “The influence of microstructure on the mechanical properties of polycrystalline diamond : a literature review *,” vol. 117, no. 3, pp. 161–176, 2018.

[123] J. C. Walmsley and a. R. Lang, “Characteristics of diamond regrowth in a synthetic diamond compact,” *J. Mater. Sci.*, vol. 23, pp. 1829–1834, 1988.

[124] Q. Jiang, J. C. Li, and G. Wilde, “The size dependence of the diamond-graphite transition,” *J. Physics. Condens. matter*, vol. 12, pp. 5623–5627, 2000.

Appendix A Miniature DT rig drawings and control circuit diagrams.

A.1 Miniature DT rig drawings

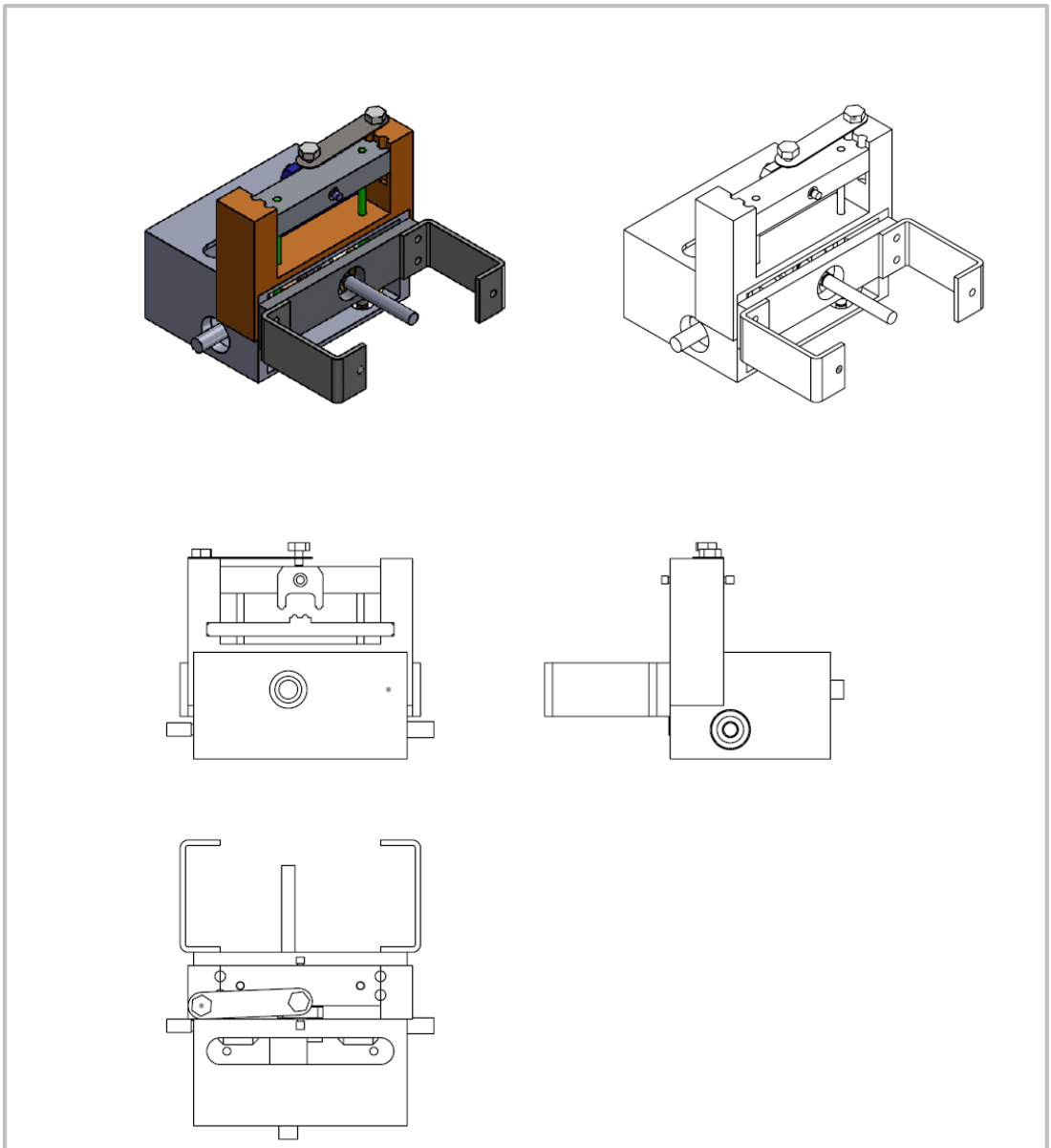

UNLESS OTHERWISE SPECIFIED: DIMENSIONS ARE IN MILLIMETERS SURFACE FINISH: TOLERANCES: LINEAR: ANGULAR:		FINISH:		DEBUR AND BREAK SHARP EDGES		DO NOT SCALE DRAWING	REVISION
	NAME	SIGNATURE	DATE			TITLE:	
DRAWN	S. Petrov		10/14			Miniature DT rig assembly	
CHK'D							
APPV'D							
MFG							
Q.A				MATERIAL:		DWG NO. 1000-001	A4
				WEIGHT:		SCALE:1:2	SHEET 1 OF 1

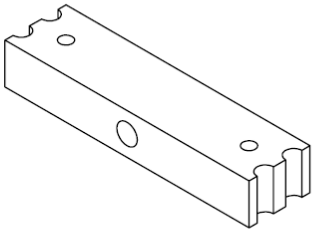

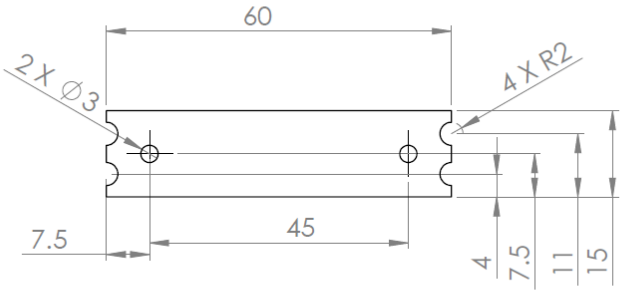

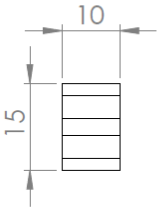

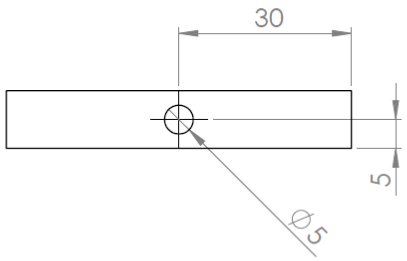

UNLESS OTHERWISE SPECIFIED: DIMENSIONS ARE IN MILLIMETERS SURFACE FINISH: TOLERANCES: LINEAR: ANGULAR:	FINISH:				DEBUR AND BREAK SHARP EDGES	DO NOT SCALE DRAWING	REVISION
	NAME	SIGNATURE	DATE			TITLE:	
DRAWN	S. Petrov		10/14			Cross Head	
CHK'D							
APPV'D							
MFG							
Q.A				MATERIAL:		DWG NO.	A4
				Aluminium		1000 - 002	
				WEIGHT:		SCALE:1:1	SHEET 1 OF 1

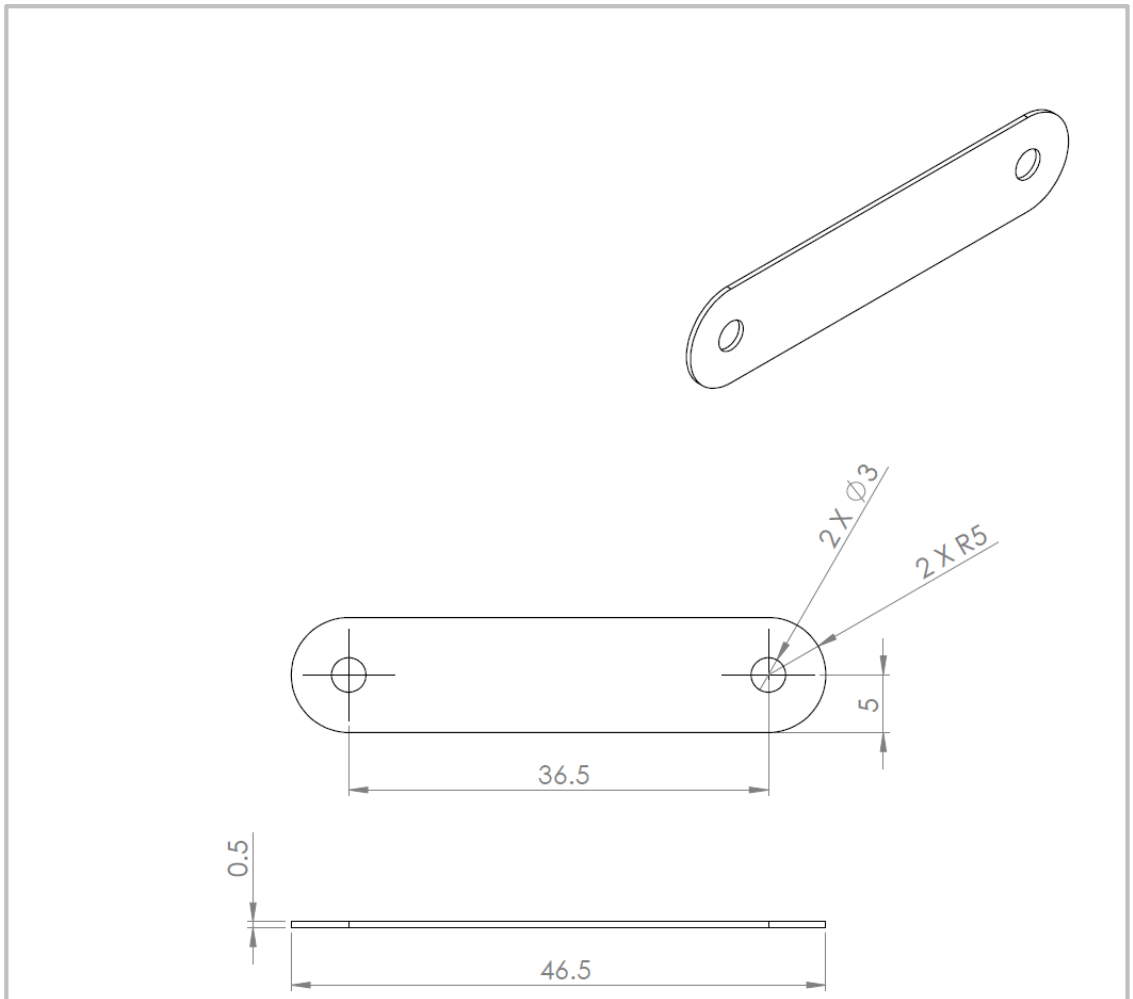

UNLESS OTHERWISE SPECIFIED: DIMENSIONS ARE IN MILLIMETERS SURFACE FINISH: TOLERANCES: LINEAR: ANGULAR:		FINISH:			DEBUR AND BREAK SHARP EDGES	DO NOT SCALE DRAWING	REVISION
	NAME	SIGNATURE	DATE			TITLE:	
DRAWN	S. Petrov		10/14			Gauge beam	
CHK'D							
APPV'D							
MFG							
Q.A				MATERIAL:		DWG NO.	A4
				Spring steel		1000 - 003	
				WEIGHT:		SCALE:2:1	SHEET 1 OF 1

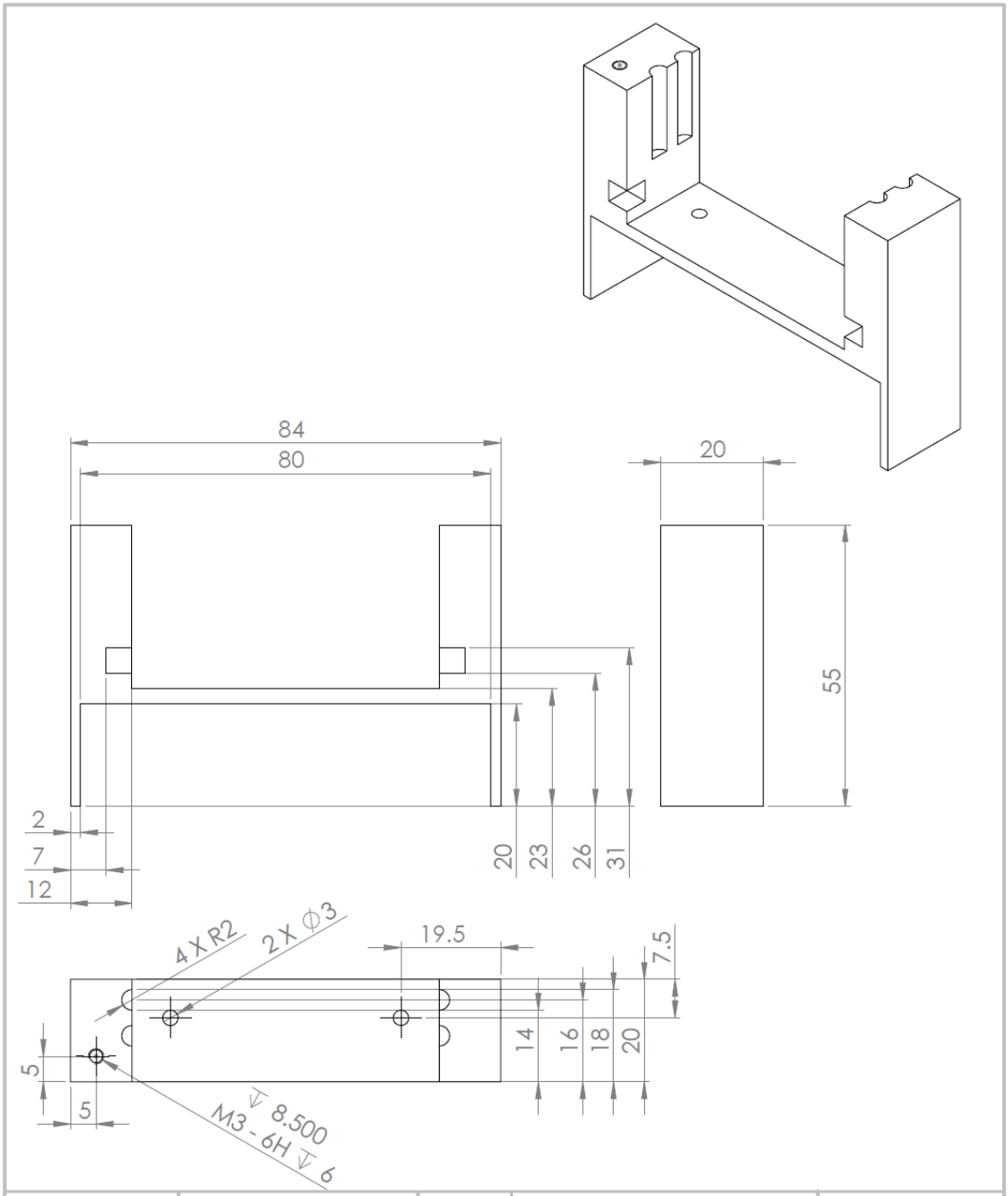

UNLESS OTHERWISE SPECIFIED: DIMENSIONS ARE IN MILLIMETERS SURFACE FINISH: TOLERANCES: LINEAR: ANGULAR:	FINISH:		DEBUR AND BREAK SHARP EDGES	DO NOT SCALE DRAWING	REVISION	
	NAME	SIGNATURE	DATE	TITLE:		
DRAWN	S. Petrov		10/14	Crosshead guide		
CHK'D						
APPV'D						
MFG						
Q.A				MATERIAL: Aluminium	DWG NO. 1000 - 004	A4
				WEIGHT:	SCALE:1:1	SHEET 1 OF 1

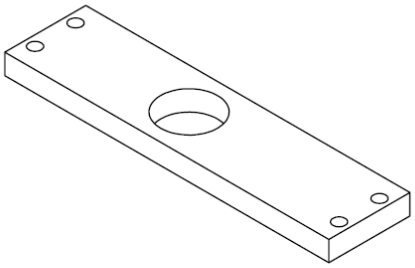

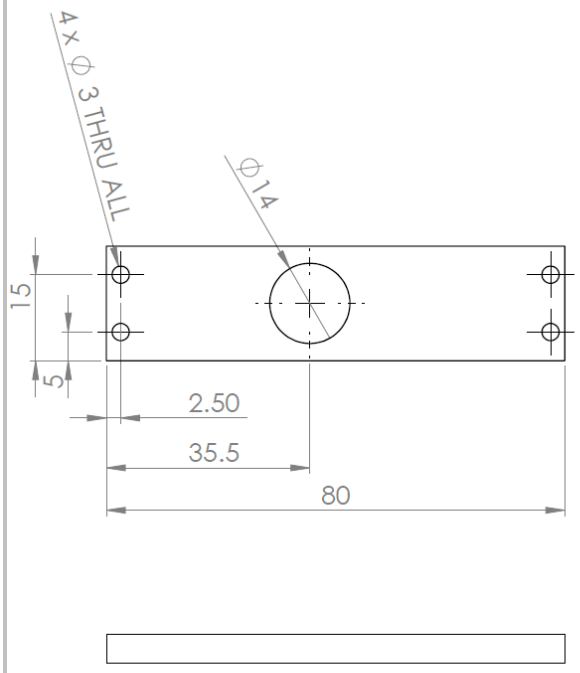

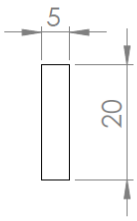

UNLESS OTHERWISE SPECIFIED: DIMENSIONS ARE IN MILLIMETERS SURFACE FINISH: TOLERANCES: LINEAR: ANGULAR:		FINISH:			DEBUR AND BREAK SHARP EDGES	DO NOT SCALE DRAWING	REVISION
	NAME	SIGNATURE	DATE			TITLE:	
DRAWN	S. Petrov		10/14			Drive bearing plate	
CHK'D							
APPV'D							
MFG							
Q.A				MATERIAL: Aluminium		DWG NO. 1000 - 005	A4
				WEIGHT:		SCALE:1:1	SHEET 1 OF 1

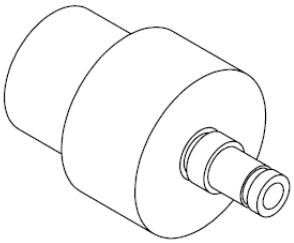

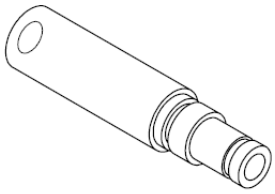

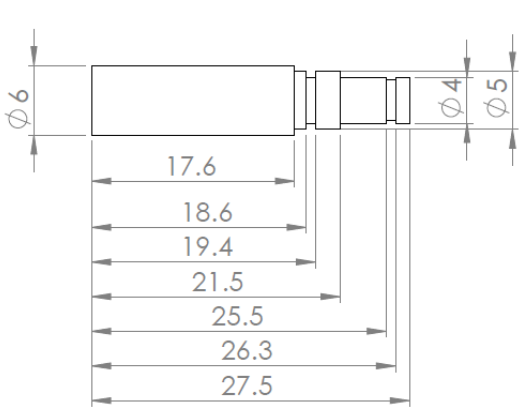

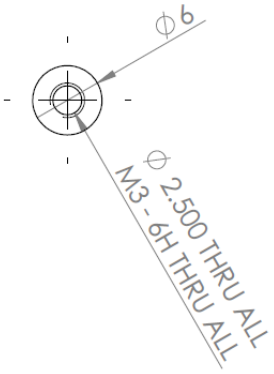

Note: The gear wheel is machined out to 6mm OD of gear nut.
Gear specification: Module 0.8; Teeth 20; Pressure angle 20 degrees.
RS Article Reference: 5216834

UNLESS OTHERWISE SPECIFIED: DIMENSIONS ARE IN MILLIMETERS SURFACE FINISH: TOLERANCES: LINEAR: ANGULAR:		FINISH:				DEBUR AND BREAK SHARP EDGES	DO NOT SCALE DRAWING	REVISION
	NAME	SIGNATURE	DATE				TITLE:	
DRAWN	S. Petrov		10/14				Gear nut	
CHK'D								
APPV'D								
MFG								
Q.A				MATERIAL:			DWG NO.	A4
				Mild steel			1000 - 006	
				WEIGHT:			SCALE:2:1	SHEET 1 OF 1

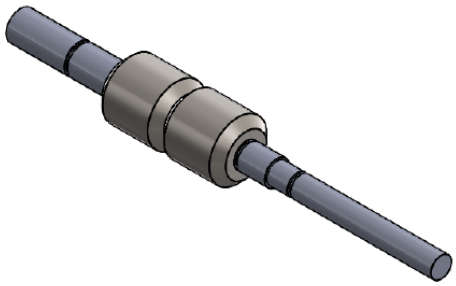

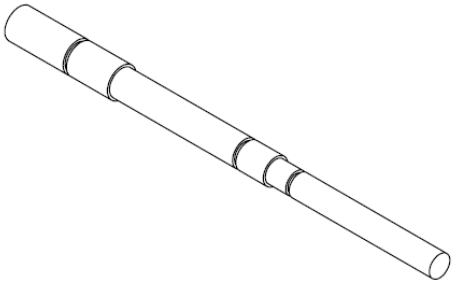

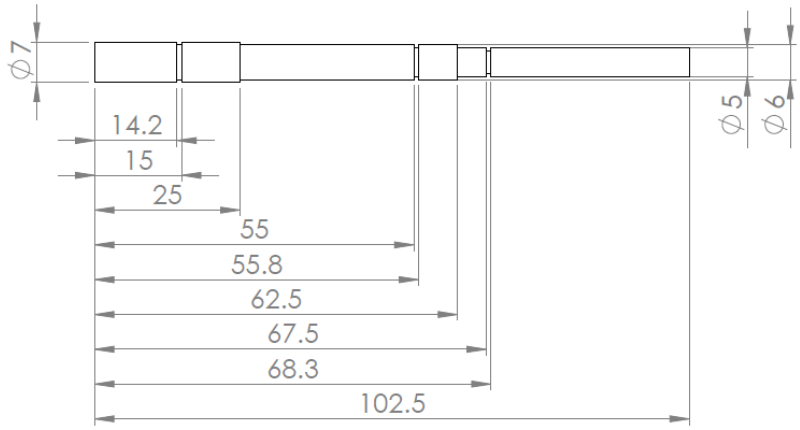

Note: Worm gear mashined out to 6mm input shaft OD.
Worm gear specification: Module 0.8; 30mm long; Pressure angle 20 degrees
RS Article reference: 5218559

UNLESS OTHERWISE SPECIFIED: DIMENSIONS ARE IN MILLIMETERS SURFACE FINISH: TOLERANCES: LINEAR: ANGULAR:		FINISH:			DEBUR AND BREAK SHARP EDGES		DO NOT SCALE DRAWING	REVISION
	NAME	SIGNATURE	DATE				TITLE:	
DRAWN	S. Petrov		10/14				Input shaft	
CHK'D								
APPV'D								
MFG								
Q.A				MATERIAL:			DWG NO.	A4
				BMS			1000 - 007	
				WEIGHT:			SCALE:1:1	SHEET 1 OF 1

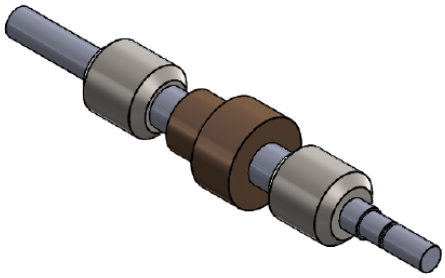

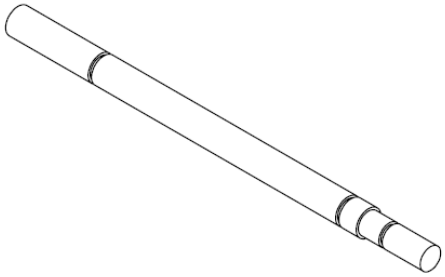

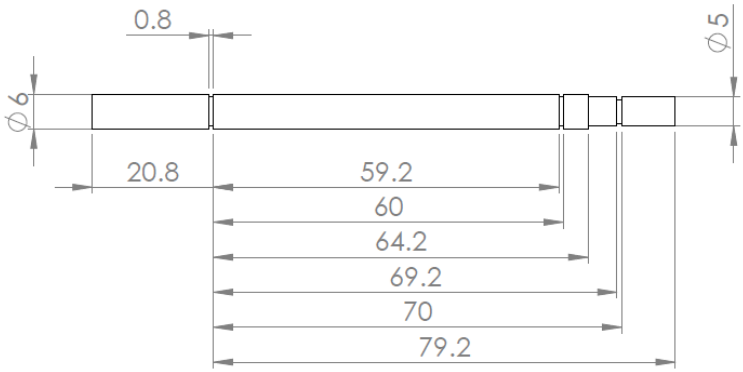

Note: The shaft is equipped with worm gear wheel and 2 worm gears. For gear wheel refer to drawing 1000-006. The worm gear i sdetailed in drawing 1000-007. Worm gear length to be reduced to 15mm for assembly.

UNLESS OTHERWISE SPECIFIED: DIMENSIONS ARE IN MILLIMETERS SURFACE FINISH: TOLERANCES: LINEAR: ANGULAR:		FINISH:			DEBUR AND BREAK SHARP EDGES		DO NOT SCALE DRAWING	REVISION
	NAME	SIGNATURE	DATE				TITLE:	
DRAWN	S. Petrov		10/14				Intermediate shaft	
CHK'D								
APPV'D								
MFG								
Q.A				MATERIAL:			DWG NO.	A4
				BMS			1000 - 008	
				WEIGHT:			SCALE:1:1	SHEET 1 OF 1

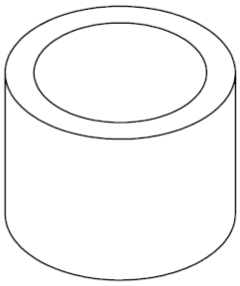

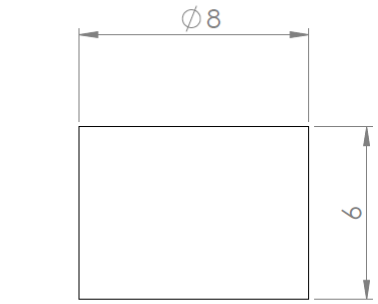

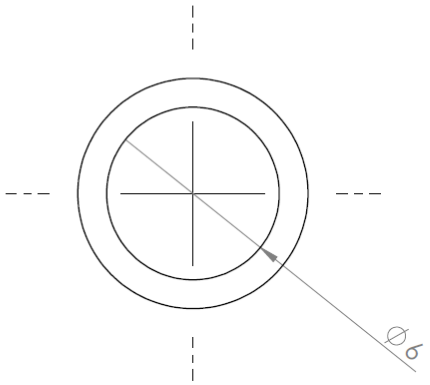

UNLESS OTHERWISE SPECIFIED: DIMENSIONS ARE IN MILLIMETERS SURFACE FINISH: TOLERANCES: LINEAR: ANGULAR:		FINISH:				DEBUR AND BREAK SHARP EDGES	DO NOT SCALE DRAWING / REVISION
	NAME	SIGNATURE	DATE				TITLE: Intermediate shaft gear spacer
DRAWN	S. Petrov		10/14				
CHK'D							
APPV'D							
MFG							
Q.A				MATERIAL: BMS			DWG NO. 1000 - 009 / A4
				WEIGHT:			SCALE:5:1 / SHEET 1 OF 1

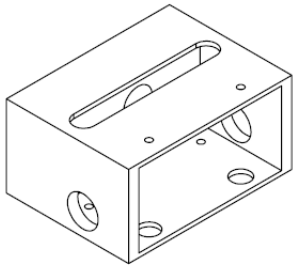

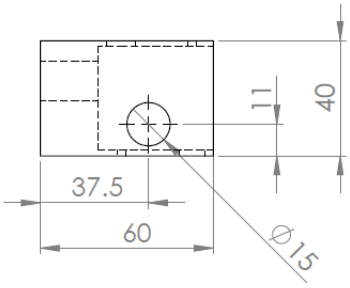

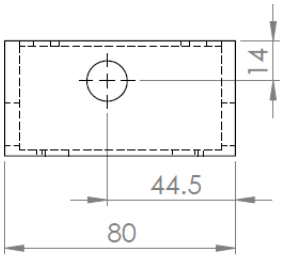

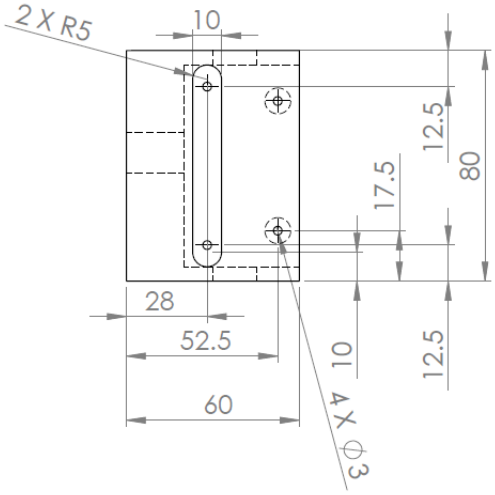

UNLESS OTHERWISE SPECIFIED: DIMENSIONS ARE IN MILLIMETERS SURFACE FINISH: TOLERANCES: LINEAR: ANGULAR:		FINISH:		DEBUR AND BREAK SHARP EDGES		DO NOT SCALE DRAWING	REVISION
	NAME	SIGNATURE	DATE			TITLE:	
DRAWN	S. Petrov		10/14			Main housing	
CHK'D							
APPV'D							
MFG							
Q.A				MATERIAL:		DWG NO.	A4
				Aluminium		1000 - 010	
				WEIGHT:		SCALE:1:2	SHEET 1 OF 1

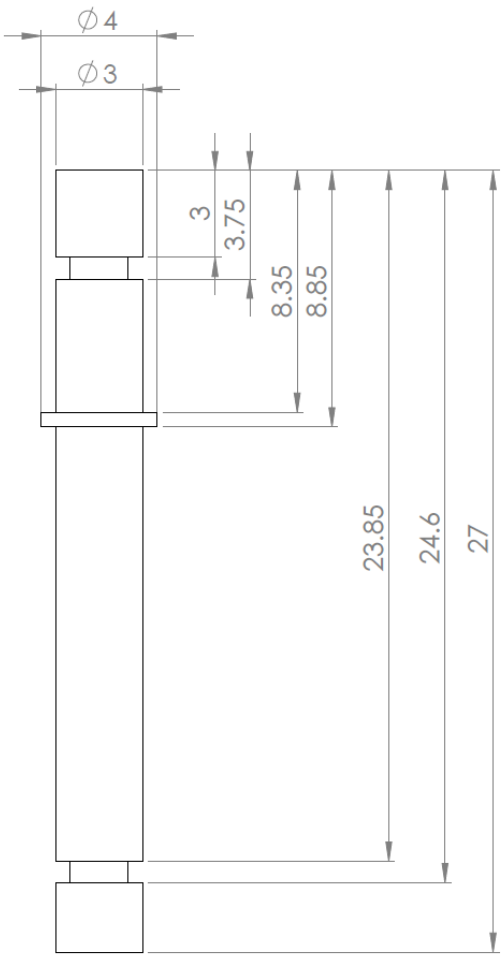

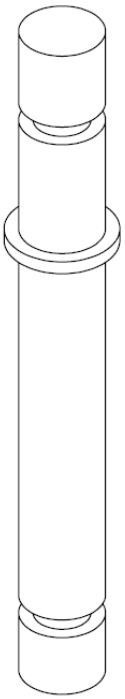

UNLESS OTHERWISE SPECIFIED: DIMENSIONS ARE IN MILLIMETERS SURFACE FINISH: TOLERANCES: LINEAR: ANGULAR:		FINISH:		DEBUR AND BREAK SHARP EDGES		DO NOT SCALE DRAWING	REVISION
	NAME	SIGNATURE	DATE			TITLE:	
DRAWN	S. Petrov		10/14			Yoke pin	
CHK'D							
APPV'D							
MFG							
Q.A				MATERIAL:		DWG NO.	A4
				BMS		1000 - 011	
				WEIGHT:		SCALE:5:1	SHEET 1 OF 1

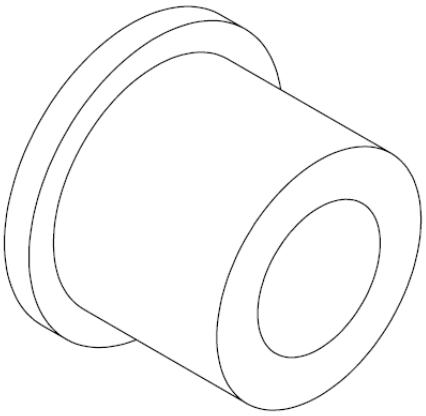

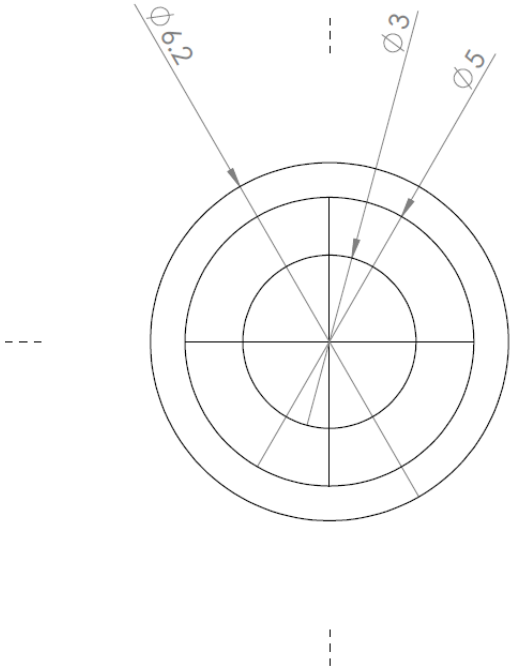

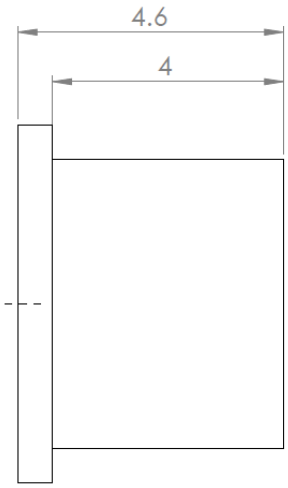

UNLESS OTHERWISE SPECIFIED: DIMENSIONS ARE IN MILLIMETERS SURFACE FINISH: TOLERANCES: LINEAR: ANGULAR:		FINISH:			DEBUR AND BREAK SHARP EDGES	DO NOT SCALE DRAWING	REVISION
	NAME	SIGNATURE	DATE			TITLE:	
DRAWN	S. Petrov		10/14			Yoke pin bush	
CHK'D							
APPV'D							
MFG							
Q.A				MATERIAL:		DWG NO.	A4
				PB 1		1000 - 012	
				WEIGHT:		SCALE:10:1	SHEET 1 OF 1

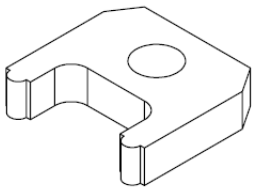

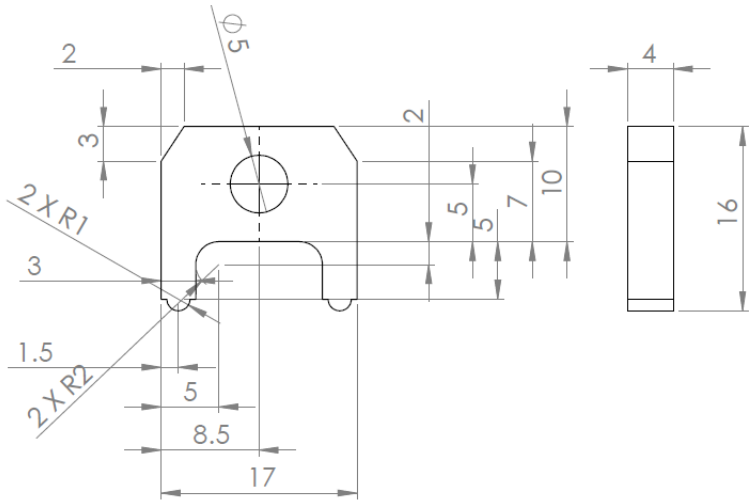

UNLESS OTHERWISE SPECIFIED: DIMENSIONS ARE IN MILLIMETERS SURFACE FINISH: TOLERANCES: LINEAR: ANGULAR:		FINISH:			DEBUR AND BREAK SHARP EDGES		DO NOT SCALE DRAWING	REVISION
	NAME	SIGNATURE	DATE				TITLE:	
DRAWN	S. Petrov		10/14				Loading yoke	
CHK'D								
APPV'D								
MFG								
Q.A				MATERIAL:			DWG NO.	A4
				Key steel			1000 - 013	
				WEIGHT:			SCALE:2:1	SHEET 1 OF 1

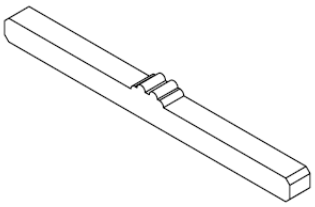

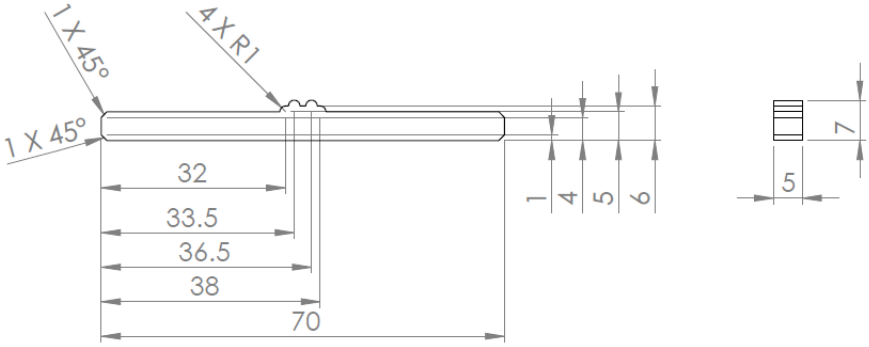

UNLESS OTHERWISE SPECIFIED: DIMENSIONS ARE IN MILLIMETERS SURFACE FINISH: TOLERANCES: LINEAR: ANGULAR:		FINISH:				DEBUR AND BREAK SHARP EDGES	DO NOT SCALE DRAWING	REVISION
	NAME	SIGNATURE	DATE				TITLE:	
DRAWN	S. Petrov		10/14				Load bridge	
CHK'D								
APPV'D								
MFG								
Q.A				MATERIAL:			DWG NO.	A4
				Key steel			1000 - 014	
				WEIGHT:			SCALE:1:1	SHEET 1 OF 1

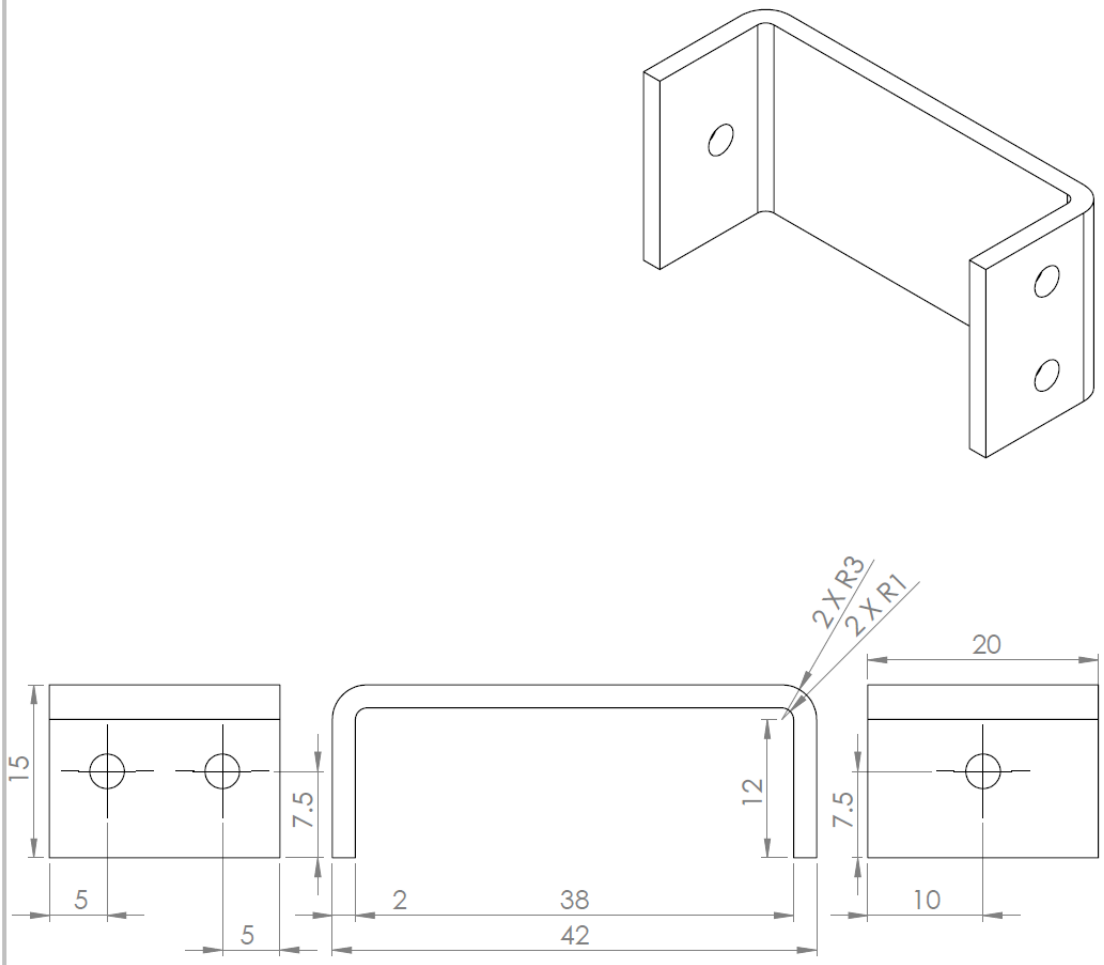

UNLESS OTHERWISE SPECIFIED: DIMENSIONS ARE IN MILLIMETERS SURFACE FINISH: TOLERANCES: LINEAR: ANGULAR:		FINISH:				DEBUR AND BREAK SHARP EDGES	DO NOT SCALE DRAWING	REVISION
	NAME	SIGNATURE	DATE				TITLE:	
DRAWN	S. Petrov		10/14				Left motor bracket	
CHK'D								
APPV'D								
MFG								
Q.A				MATERIAL:			DWG NO.	A4
				Aluminium			1000 - 015	
				WEIGHT:			SCALE:2:1	SHEET 1 OF 1

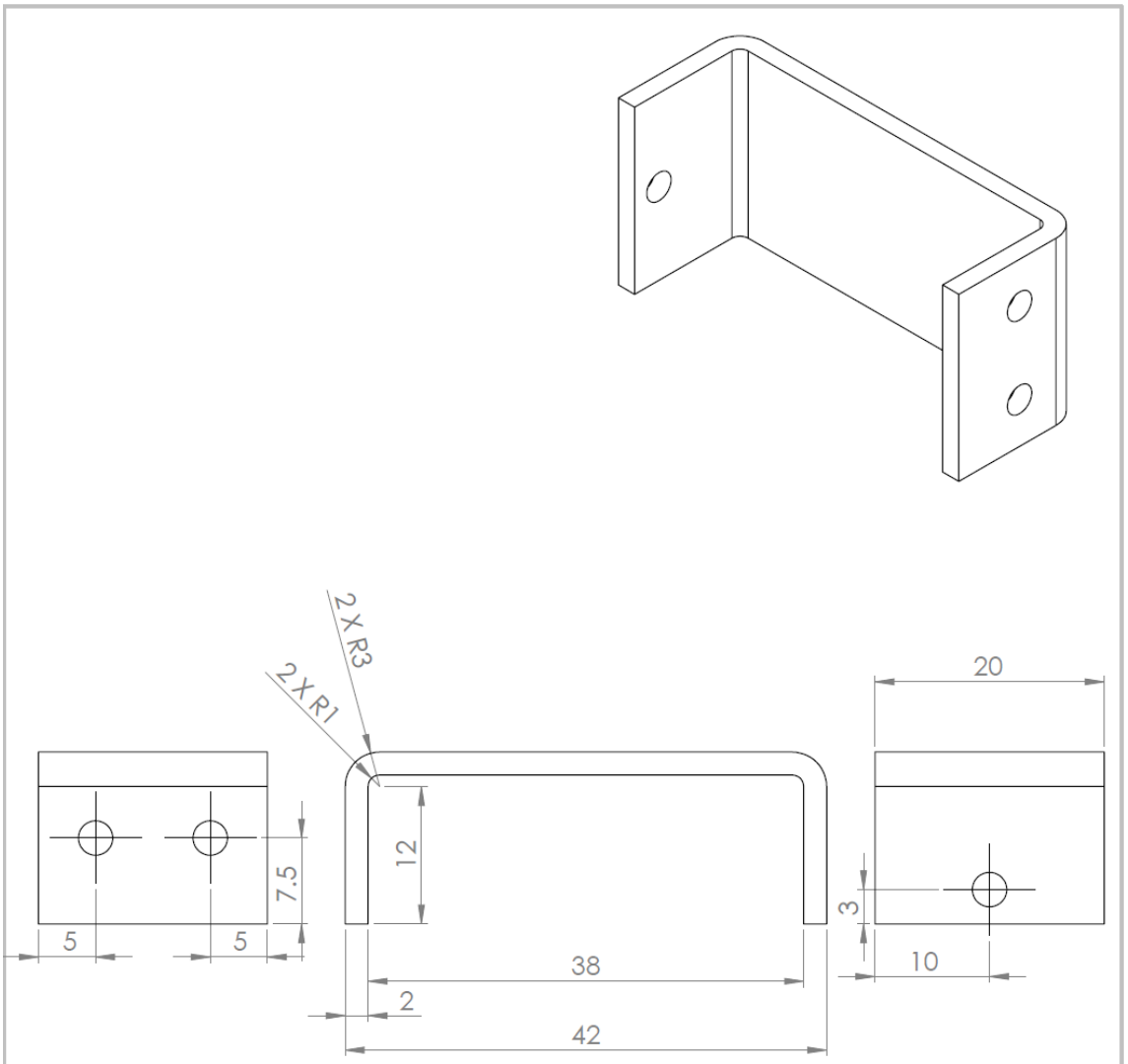

UNLESS OTHERWISE SPECIFIED: DIMENSIONS ARE IN MILLIMETERS SURFACE FINISH: TOLERANCES: LINEAR: ANGULAR:		FINISH:				DEBUR AND BREAK SHARP EDGES	DO NOT SCALE DRAWING	REVISION
	NAME	SIGNATURE	DATE				TITLE:	
DRAWN	S. Petrov		10/14				Right motor bracket	
CHK'D								
APPV'D								
MFG								
Q.A				MATERIAL:			DWG NO.	A4
				Aluminium			1000 - 016	
				WEIGHT:			SCALE:2:1	SHEET 1 OF 1

A.2 Control circuit diagrams

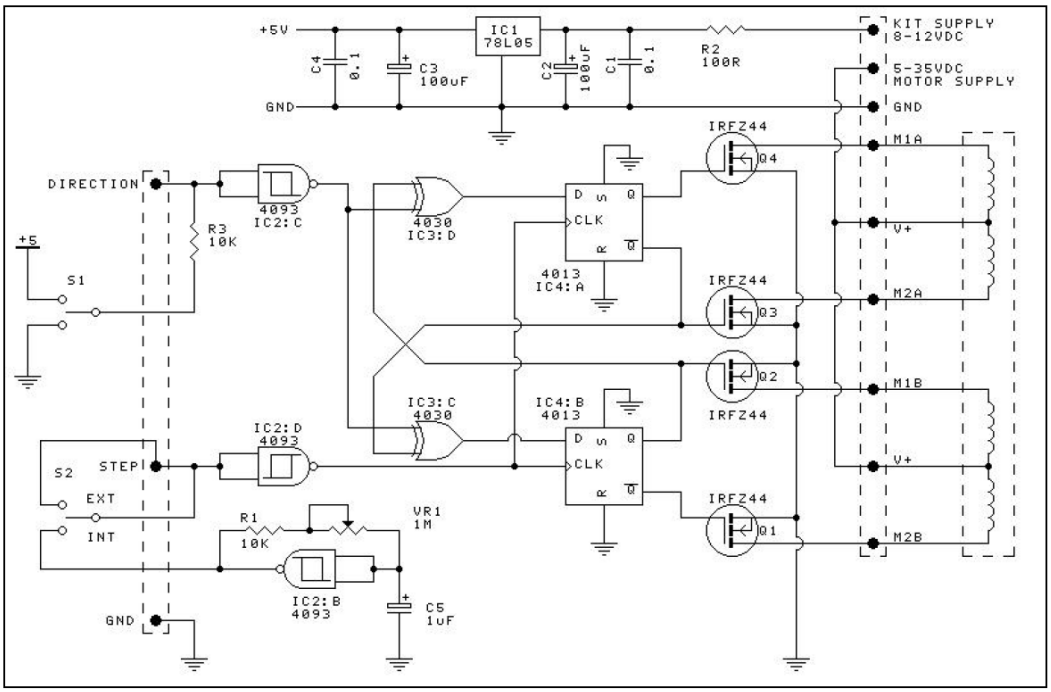

Figure A2-1 – Stepper motor control circuit [121].

Appendix B Images employed in the analyses.

B.1 Cobalt content analysis

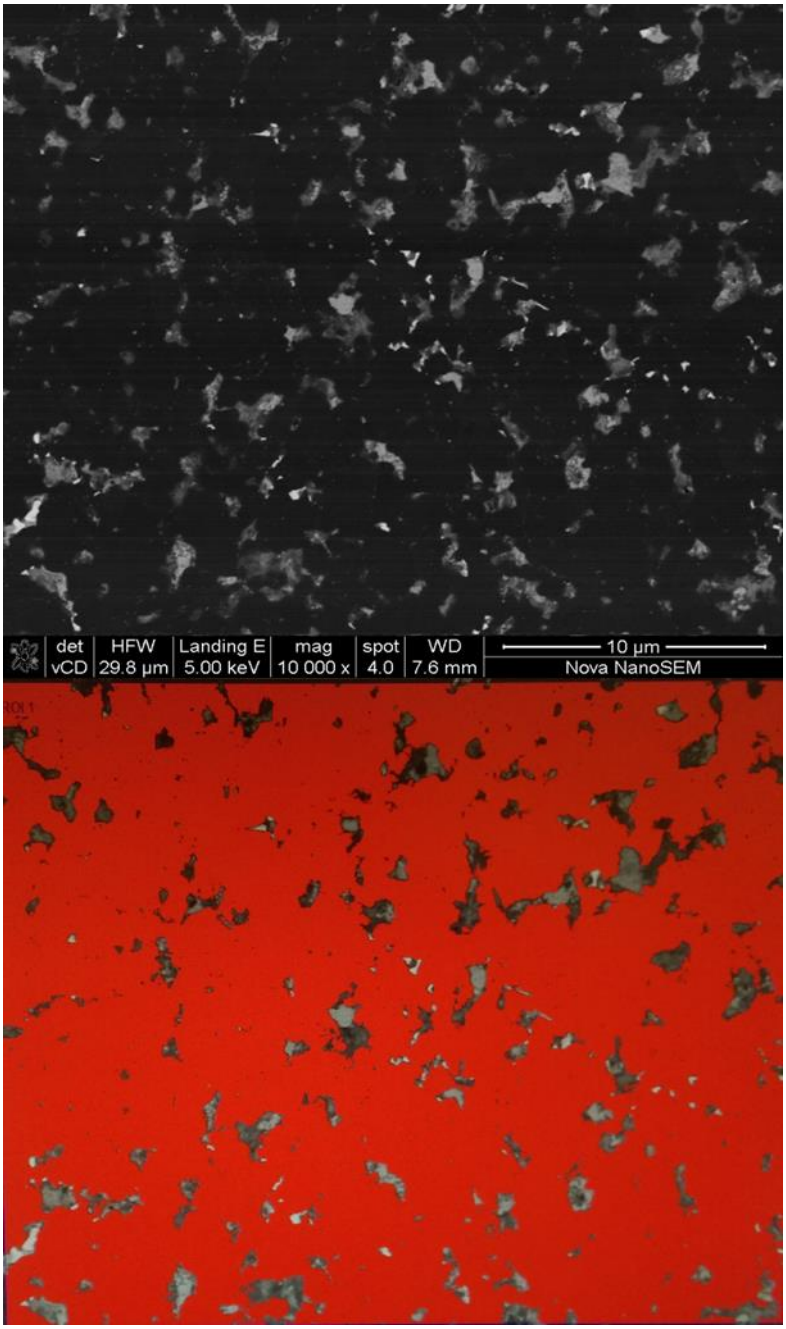

Figure B1-1 - Two phase composition analysis (bottom) of the BSD image (top) of the cobalt phase in a 4µm specimen. All data below the intensity level equal to 50 is considered to be diamond and is highlighted red, the remaining areas are considered to be cobalt.

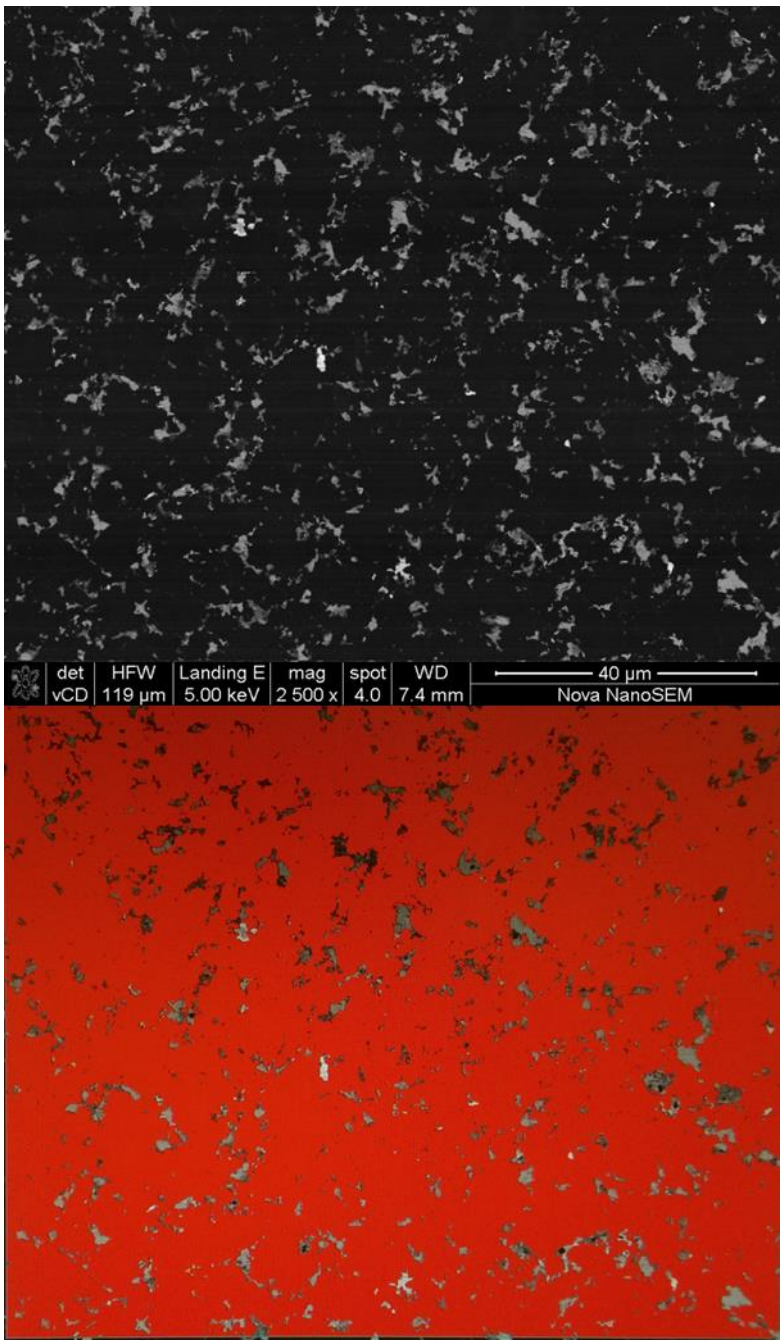

Figure B1-2 - Two phase composition analysis (bottom) of the BSD image (top) of the cobalt phase in a 12µm specimen. All data below the intensity level equal to 50 is considered to be diamond and is highlighted red, the remaining areas are considered to be cobalt.

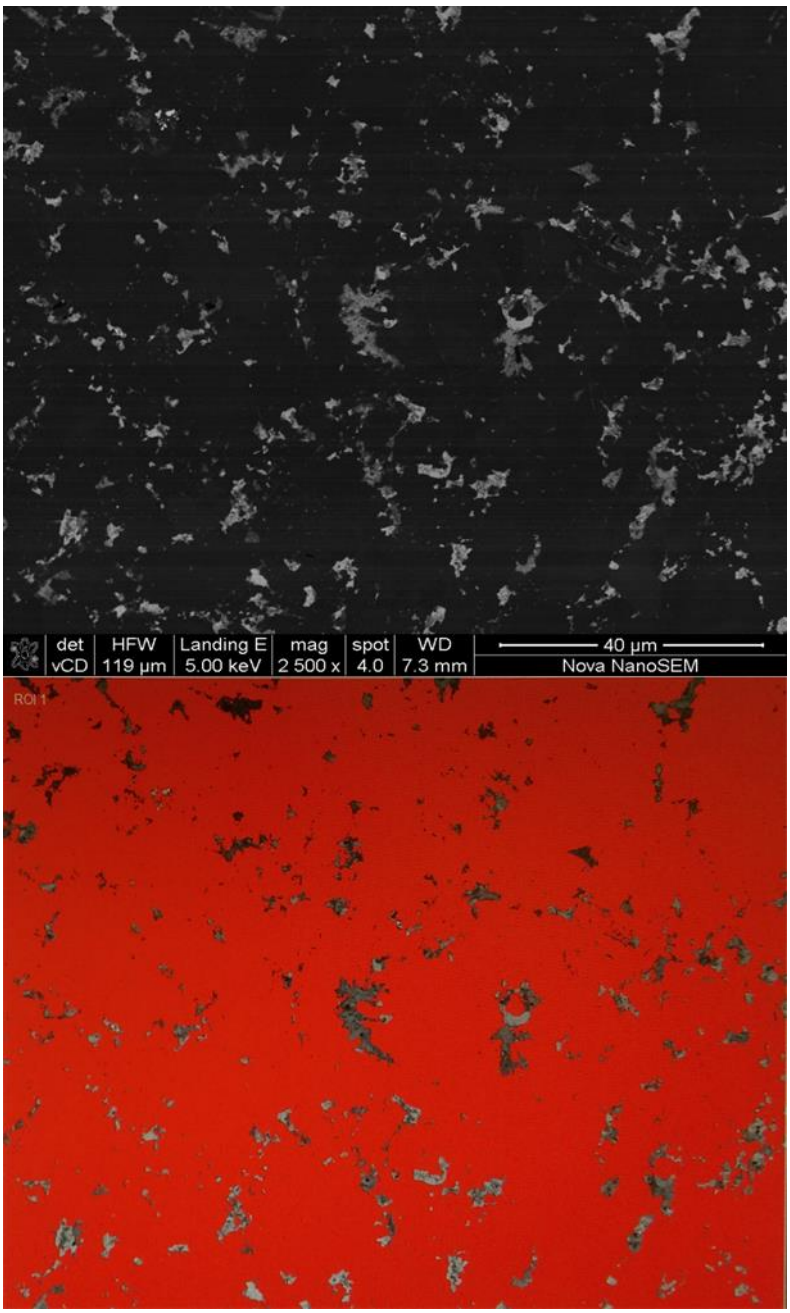

Figure B1-3 - Two phase composition analysis (bottom) of the BSD image (top) of the cobalt phase in a 30µm specimen. All data below the intensity level equal to 50 is considered to be diamond and is highlighted red, the remaining areas are considered to be cobalt.

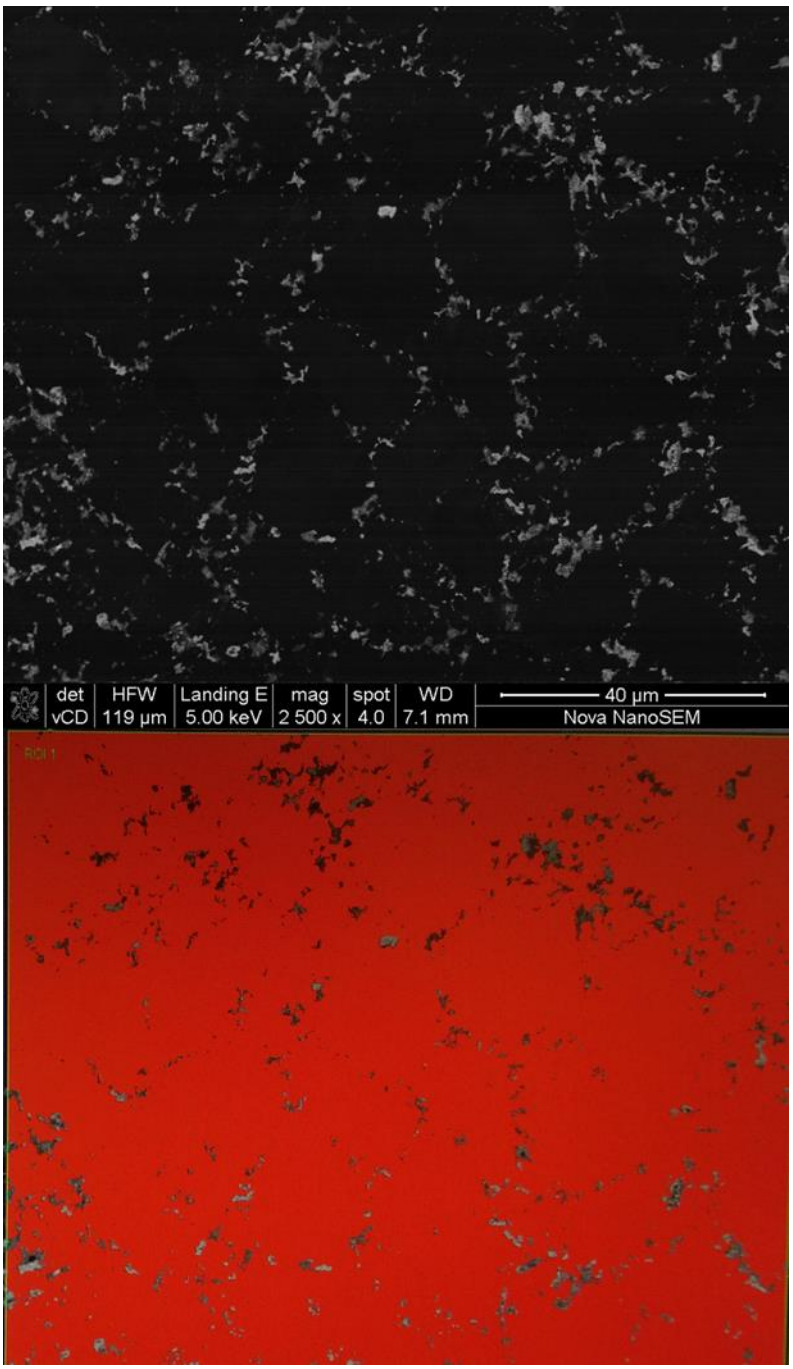

Figure B1-4 – Two phase composition analysis (bottom) of the BSD image (top) of the cobalt phase in a 30-4µm specimen. All data below the intensity level equal to 50 is considered to be diamond and is highlighted red, the remaining areas are considered to be cobalt.

B.2 Grain size analysis

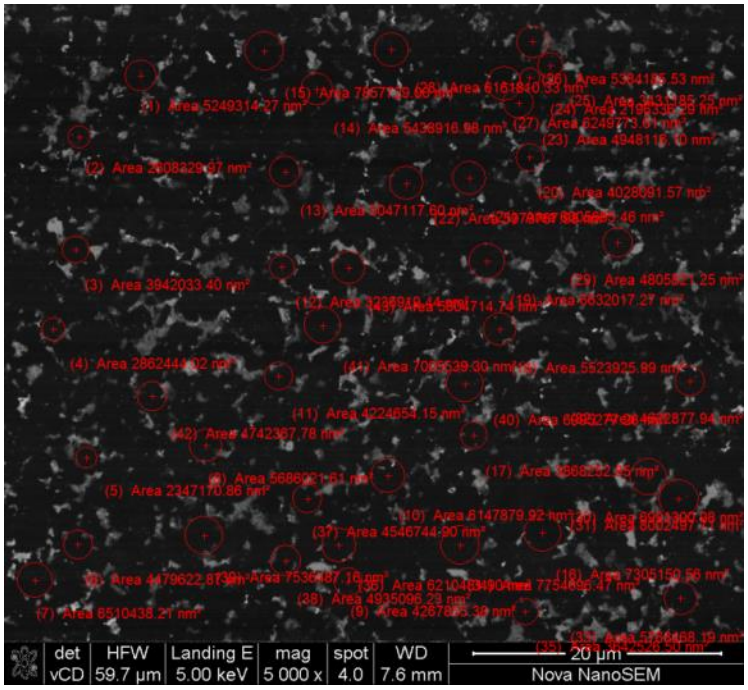

Figure B2-1 – BSD micrograph depicting the microstructure of the 4µm grade PCD specimen, highlighting the regions where measurements were taken.

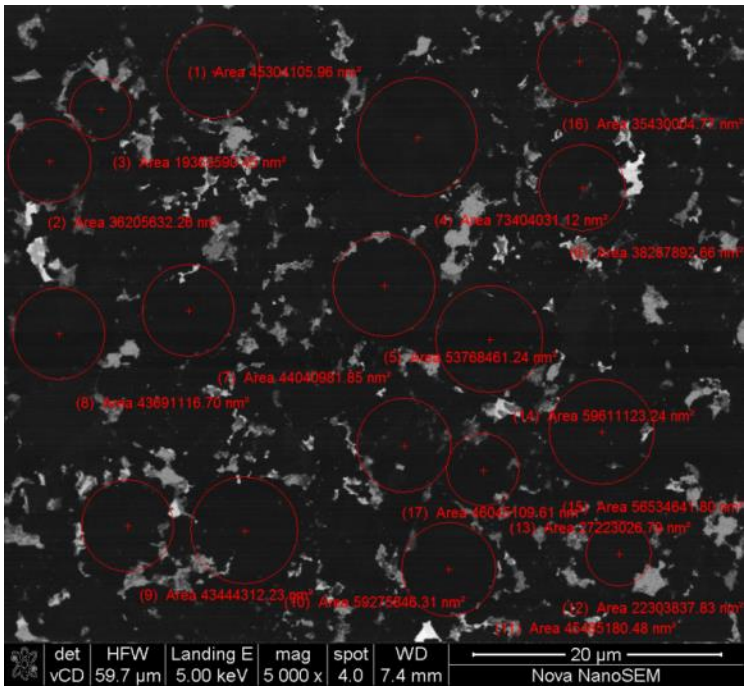

Figure B2-2 - BSD micrograph depicting the microstructure of the 12µm grade PCD specimen, highlighting the regions where measurements were taken.

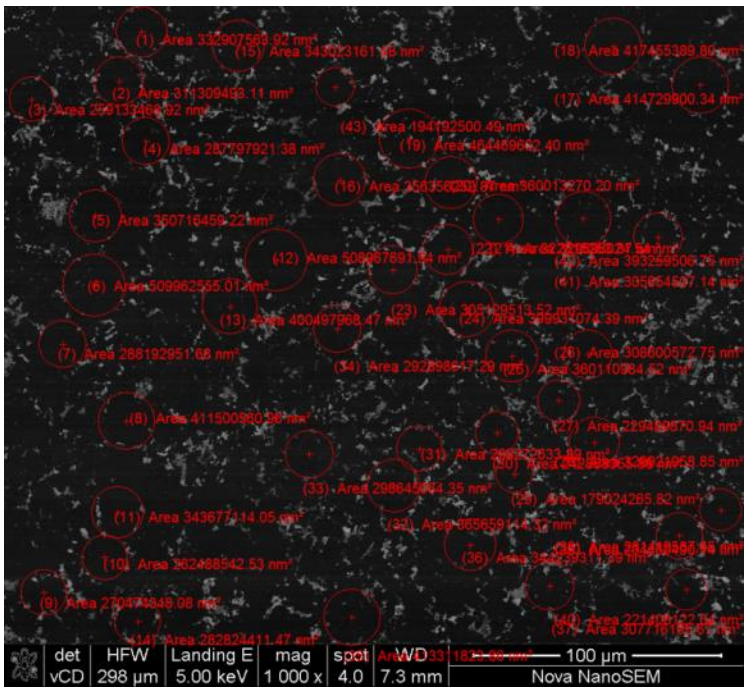

Figure B2-3 - BSD micrograph depicting the microstructure of the 30µm grade PCD specimen, highlighting the regions where measurements were taken.

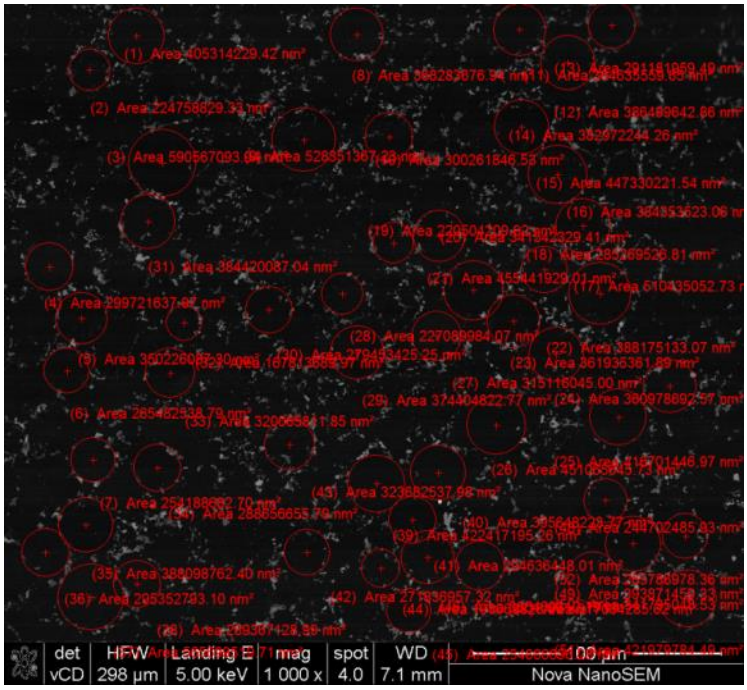

Figure B2-4 - BSD micrograph depicting the microstructure of the 30-4µm grade PCD specimen, highlighting the regions where measurements were taken.

B.3 Contiguity analysis

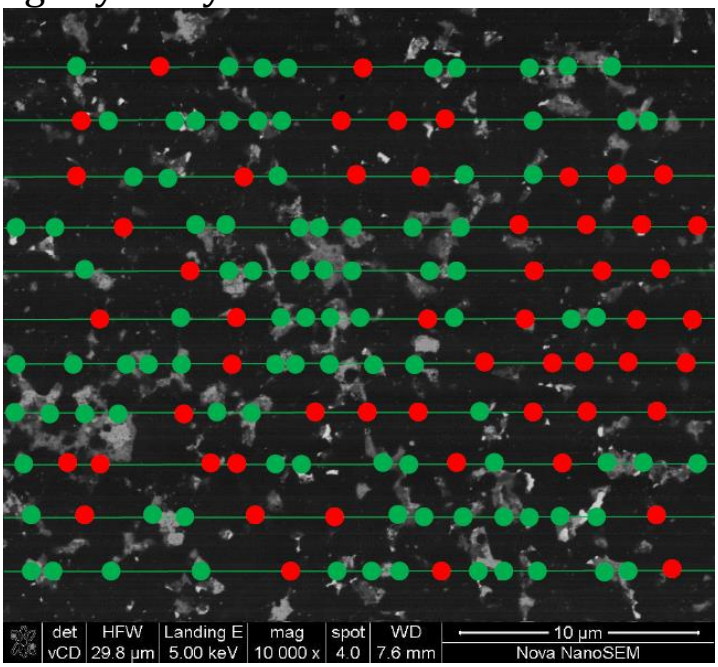

Figure B3-1 – BSD micrograph depicting the microstructure of the 4µm grade PCD specimen, highlighting an example of the line intercept count employed to evaluate the microstructural contiguity.

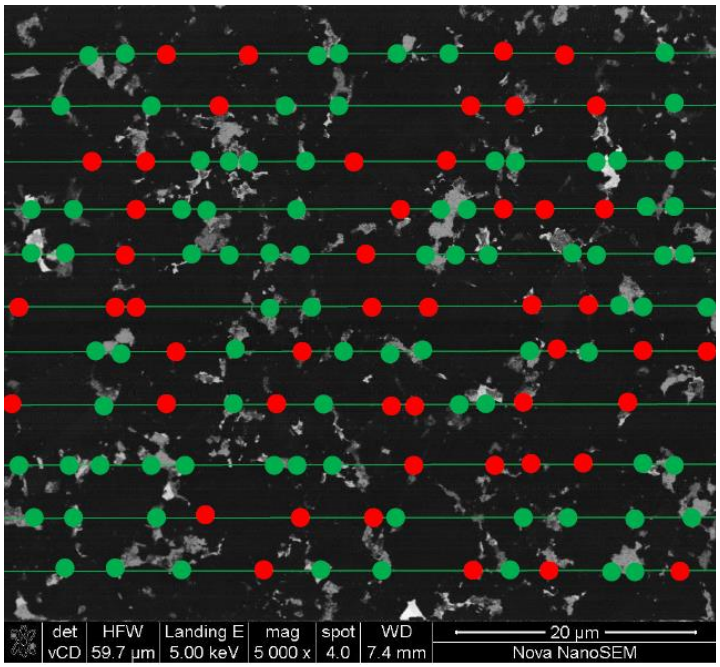

Figure B3-2 – BSD micrograph depicting the microstructure of the 12µm grade PCD specimen, highlighting an example of the line intercept count employed to evaluate the microstructural contiguity.

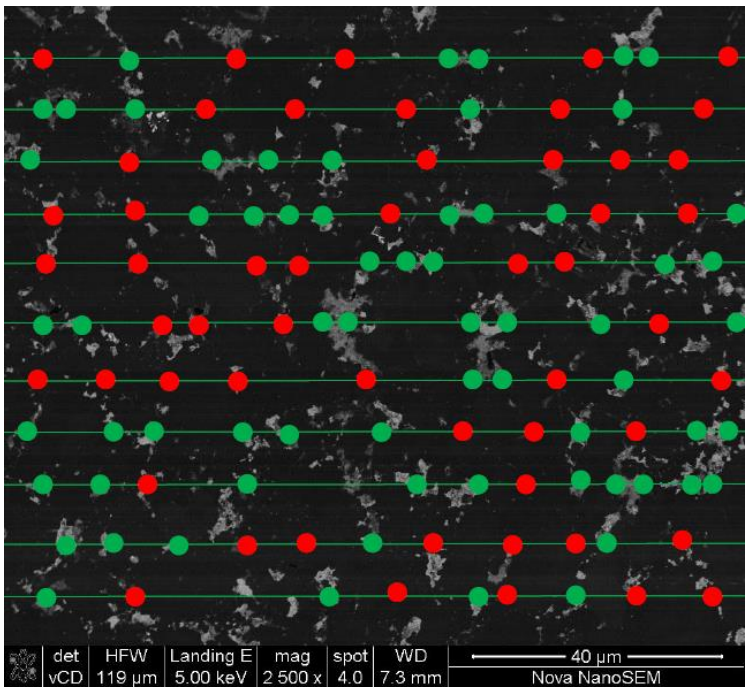

Figure B3-3 – BSD micrograph depicting the microstructure of the 30µm grade PCD specimen, highlighting an example of the line intercept count employed to evaluate the microstructural contiguity.

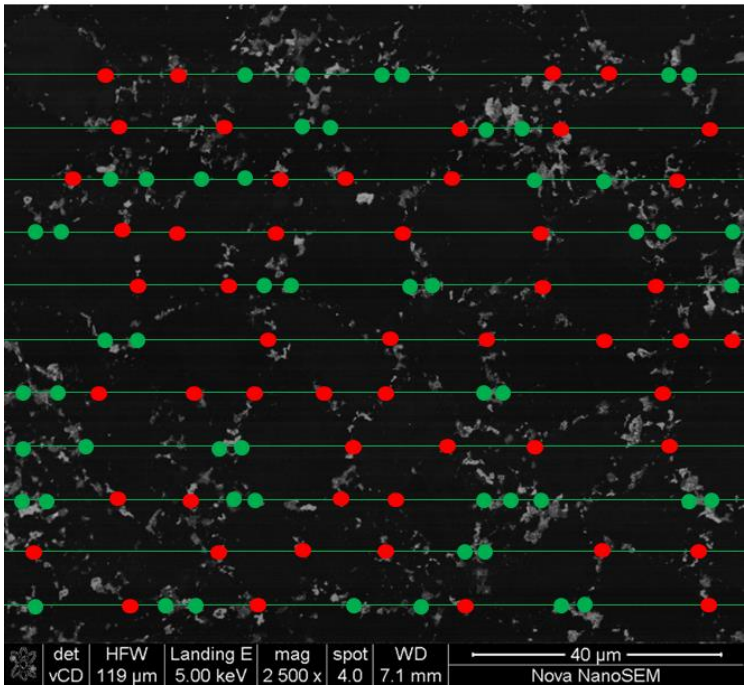

Figure B3-4 – BSD micrograph depicting the microstructure of the 30-4µm grade PCD specimen, highlighting an example of the line intercept count employed to evaluate the microstructural contiguity.

Appendix C –HPHT Sintering and Leaching of PCD

C. 1 - PCD Synthesis

Polycrystalline diamond materials are sintered from starter powders consisting of diamond grains which are sintered atop of a cemented tungsten carbide cobalt (WC-Co) substrate. These diamond grains can be of uniform size, or alternatively, mixtures of various grain sizes can be utilized. A capsule is made of the starter grit atop a substrate. The capsule designs may vary, but they key function is to enable even thermal and hydrostatic pressure distribution in order achieve good sintering conditions. The production process typically involves four key stages, which are – i) cold compaction, ii) hot compaction, iii) cobalt infiltration and iv) liquid phase sintering. These stages are further illustrated in Figure 1, [122]. During the cold compaction process, the grits are tightly packed, and some grit fracturing occurs, which results in the finer grit sizes as the hot compaction stage is approached. A challenge exists with compacting particles as hard as diamond. The contact points between diamonds are able to sustain very high contact pressures while the voids between the diamond grits remain unpressurized. As shown in the temperature-pressure diagram in Figure 2, diamond is not stable at high temperatures unless very high pressures are applied. Therefore, as the temperature is increased, "unpressurized" diamond surfaces experience graphitisation. However, as the pressure and temperature are increased further and further, typically in the range of 1500-2000 °C and pressures between 5-10 GPa, the diamond grits compact further, with some plastic grain deformation occurring in the diamond grits. At the set design temperatures and pressures, the cobalt from the substrate "sweeps" through the diamond grit. The cobalt has an important function of dissolving the carbon in the graphitised regions, which prevents graphite entrapment between sintered grains and enables the formation of new diamond-to-diamond bonds between starter diamond particles [123]. The new diamond is formed during the liquid phase sintering, where new diamond precipitates form the carbon reach cobalt pools. Upon completion of the sintering process, the material consists of inter-grown diamond particles surrounded by a network of residual,

interconnected cobalt pools. The original diamond grains typically reveal slip and micro-twinning deformations while the newly re-grown diamond regions do not.

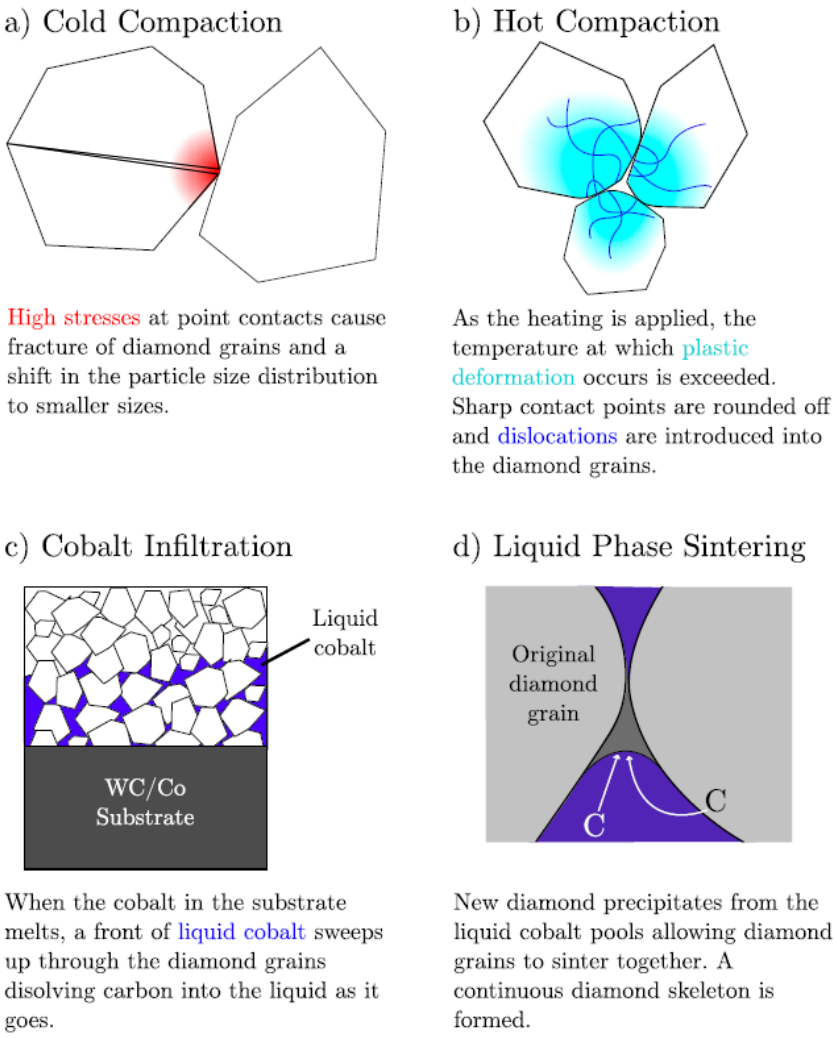

Figure 1 – Schematic illustration of the four key stages of PCD sintering process [122].

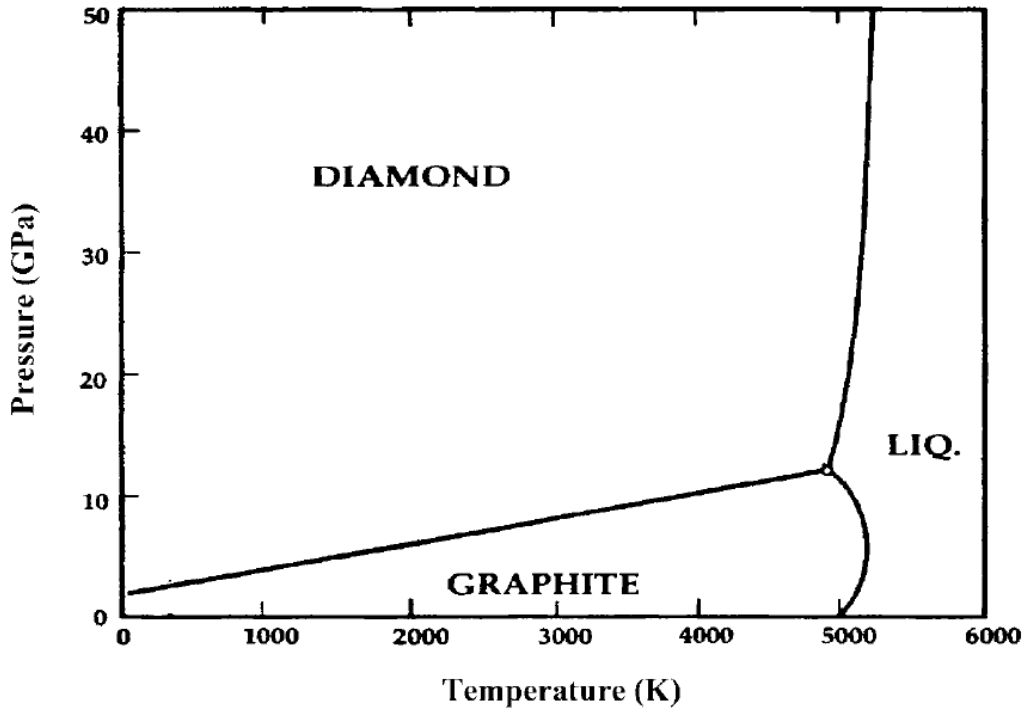

Figure 2 – The basic temperature-pressure diagram for carbon [124].

C.2 - PCD Leaching

Presence of residual cobalt in the PCD material can have significant disadvantages when elevated service temperatures are encountered. The deleterious effects are caused by two mechanisms, namely – i) different thermal expansion coefficients of Cobalt and Diamond and ii) the catalytic effect Cobalt can have at elevated temperatures which can promote graphitisation, leading to damage of diamond-diamond bonds and loss of microstructural integrity. In addition, in the absence of cobalt, diamond alone possesses higher thermal conductivity, which also allows better temperature distribution in abrasive machining operations. As highlighted, it often becomes desirable to remove the cobalt from the PCD material. This can be achieved by exposing the region of interest to strong acid solutions. Typical acids employed are nitric and hydrofluoric, but other strong acids may be used. In the case of PCD drill bit "buttons", the substrate/body has to be well protected

from the effects of the strong acids. Various ways exists to mask the cutter body and expose the PCD region of interest to be leached.

The leaching process, depending on the required leaching depth, can be a very time consuming process. It can take 7-12 days to achieve a leach of a depth sufficient to yield what can be considered a thermally stable PCD (TSP) material. In order to increase the leaching speeds, temperature and pressure can be increased, employing a pressure vessel, to increase the cobalt removal rates. Depending on the particular design requirements, cobalt is not fully leached from the PCD material as this leads to a reduction in mechanical strength properties. It is worth noting that even in the regions considered leached, some cobalt may remain trapped interstitially or adhering to the diamond grains [16], [39], [46].